## UNIVERSIDADE DE BRASÍLIA INSTITUTO DE FÍSICA

VICTOR VENDRAMINI RODRIGUES PEREIRA

SIMULAÇÕES COMPUTACIONAIS DE CRISTAIS 2D
COMPUTATIONAL SIMULATIONS OF 2D CRYSTALS

BRASÍLIA SEPTEMBER 19, 2025

### Victor Vendramini Rodrigues Pereira

### Simulações Computacionais de Cristais 2D

### **Computational Simulations of 2D Crystals**

Dissertation submitted in partial fulfillment of the requirements for the Master's degree in Physics at the Institute of Physics, University of Brasília.

Supervisor: D. L. Azevedo

Universidade de Brasília – UnB Instituto de Física

> Brasília September 19, 2025

Victor Vendramini Rodrigues Pereira Simulações Computacionais de Cristais 2D Computational Simulations of 2D Crystals / Victor Vendramini Rodrigues

Pereira. – Brasília, September 19, 2025-187 p. : il. (algumas color.) ; 30 cm.

Supervisor: D. L. Azevedo

Dissertação – Universidade de Brasília – UnB Instituto de Física, September 19, 2025.

 $1.~\rm MX_{\rm enes}.~2.~\rm DFT.~3.$  Semiconductors 4. Electronic Structure 5. Thermodynamics 6. Optical Properties 7. Effective Mass I. D. L. Azevedo. II. Universidade de Brasília. III. Instituto de Física. IV. Title

CDU 02:141:005.7

### Victor Vendramini Rodrigues Pereira

# Simulações Computacionais de Cristais 2D

## **Computational Simulations of 2D Crystals**

Dissertation submitted in partial fulfillment of the requirements for the Master's degree in Physics at the Institute of Physics, University of Brasília.

Dissertation approved. Brasília, 21/08/2025:

D. L. Azevedo Supervisor

Professor

Mariana Malard Sales Andrade

Professor

Geraldo Magela da Silva

Brasília 21/08/2025

献给老师



### Resumo

### Simulações Computacionais de Cristais 2D

As tecnologias quânticas baseiam-se no entendimento mais sofisticado da matéria que possuímos e, para buscar esse desenvolvimento tecnológico, precisamos continuar aprimorando nossos métodos de exploração e ser criativos ao imaginar materiais além dos que já fomos capazes de sintetizar. Este estudo propõe uma investigação teórica de classes modernas de materiais bidimensionais (2D): os dicalcogenetos de metais de transição (DMTs) e os carbonetos, nitretos e carbonitretos de metais de transição (MXenes). Este viés exploratório é sustentado pela teoria de perturbação do funcional de densidade (TPFD) para prever a estabilidade e a caracterização de materiais não sintetizados, e pela teoria do funcional de densidade (TFD) para propriedades eletrônicas, sendo estas posteriormente refinadas com métodos pós-TFD baseados em funções de Wannier. Nesta abordagem mais refinada, discutimos os fundamentos da teoria quântica e do estado sólido para obter resultados de grande relevância para o desenvolvimento de tecnologias quânticas, como a massa efetiva dos portadores de carga e bandas eletrônicas planas encontradas em Y<sub>2</sub>CCl<sub>2</sub>, propriedades ópticas com efeitos excitônicos significativos encontrados sobre as bandas planas em Y<sub>2</sub>CCl<sub>2</sub> e também nos vales K em MoS<sub>2</sub>, e ainda propriedades topológicas reveladas pela curvatura de Berry na estrutura de bandas em MoS<sub>2</sub>. O foco deste estudo não se restringe a exploração de materiais, dedicando-se também ao desenvolvimento de técnicas computacionais que aprimorem nossos métodos atuais de simulação.

Palavras-chave: DFT. MXenes. DMTs. Materiais 2D. Simulação Computacional. Estabilidade. Bandas planas. Éxciton. Curvatura de Berry.

## **Abstract**

Quantum technologies are grounded in the most sophisticated understanding of matter we have so far, and to pursue this technological development we must keep pushing our methods of exploration and be creative in imagining materials beyond what have already been synthesized. This study presents a theoretical investigation of modern classes of twodimensional (2D) materials; the transition metal dichalcogenides (TMDs) and transition metal carbides, nitrides, and carbonitrides (MXenes). Such exploration is underpinned by density functional perturbation theory (DFPT) to predict the stability and characterization of unsynthesized materials, and density functional theory (DFT) for electronic properties, which are further refined with post-DFT methods based on Wannier functions. In this finer approach we discuss the fundamentals of quantum theory and solid-state systems to achieve results of great relevance to the development of quantum technologies, such as charge carrier effective mass and flat band behavior in Y<sub>2</sub>CCl<sub>2</sub>, optical properties with significant excitonic effects which are created in the flat bands of Y<sub>2</sub>CCl<sub>2</sub> and in the valleys of MoS<sub>2</sub>, and also possible topological properties revealed by the Berry curvature in the  $MoS_2$  band structure. The focus of the study goes beyond materials exploration, to also dedicate on developing computational techniques that improve our current methods of simulation.

**Key-words**: DFT. MXenes. TMDs. 2D Materials. Computational Simulation. Stability. Flat band. Exciton. Berry Curvature.

# List of Figures

Figure 1 –	Electron states in carbon atom. Valence electrons are those with $n = 2$ . All states with $n > 2$ are excited states	2
Figure 2 –	H <sub>2</sub> molecule energy states, constructed from hydrogen valence states. Both electrons occupies the bonding state, while the antibonding state	
	is left empty	2
Figure 3 –	Electron states in sp <sup>3</sup> hybridization of carbon atom	1
Figure 4 –	Carbon atom (pink) in $sp^3$ hybridization bonding with four atomic species (blue) in tetrahedral geometry. Illustration made in BIOVIA	
	Materials Studio	1
Figure 5 –	Illustrations containing symmetries of the mirror type (m) or rotation axis	
	$C_n \ (n = 1, 2,, 6). $ 55	5
Figure 6 –	The planar lattices, and next to them, their characterizations based on	
	their respective symmetry elements	
	Some examples of crystalline directions	3
Figure 8 –	Examples of crystalline planes	)
Figure 9 –	Illustration showing the optical path difference in the process of crystalline diffraction	)
Figure 10 –	Illustration of the planar hexagonal crystal lattice of M <sub>2</sub> X 63	3
Figure 11 –	Illustration of the reciprocal lattice of $M_2X$ , containing the K and K'	_
	points	
	Wave scattering at the origin and in a volume positioned at $r$ 66	
	Generation of the first Brillouin zone for the hexagonal lattice 68	
	Illustration of a periodic potential in an one-dimensional lattice 70	
	Illustration of the real part of a Bloch wave function	
	Cutoff vector representation	1
Figure 17 –	High symmetry points of the two-dimensional hexagonal lattice Brillouin zone	3
Figure 18 –	Mapping between potentials, ground states, and ground state electron	
	densities sets	L
Figure 19 –	Mapping between the external potentials and the corresponding set of	
	ground states and ground state densities, considering degenerate cases. 93	}
Figure 20 –	a) Crystal structure of 2H-MoS <sub>2</sub> viewed along the x-axis. b) Crystal	
	structure of 2H-MoS <sub>2</sub> viewed along the z-axis	2

Figure 21 –	First Brillouin zone of $MoS_2$ and its distinct K and K' valleys, where bright exciton states are formed with opposite spins, induced by different light polarization
Figure 22 –	General chemical exfoliation for the synthesis process of an $M_2XT_2$ MXene derived from its precursor MAX phase
Figure 23 –	a) Real space unit cell for $Y_2C_1T_2$ MXenes in the trigonal p-3m1 spacegroup. b) First Brillouin zone representation, showing $\Gamma$ , M and K points of high symmetry (the top view of the real lattice in the center is not in true proportion in relation to the reciprocal lattice). c) Side view of the $Y_2CT_2$ monolayer. d) Top view of the $Y_2CT_2$ monolayer 117
Figure 24 –	Phonon dispersion curves of $Y_2CF_2$ (red), $Y_2CCl_2$ (blue) and $Y_2CBr_2$ (green) in the frequency range from 0 to $600\mathrm{cm}^{-1}$ , calculated with the GGA-PBE exchange-correlation functional
Figure 25 –	a) Thermodynamic properties for $Y_2CT_2$ MXenes: Enthalpy $[H(T)]$ (blue), temperature times entropy, $T \times S(T)$ (red), and free energy $[G(T)]$ (green). b) Constant volume heat capacity, $C_V$ , for the $Y_2CF_2$ (red), $Y_2CCl_2$ (blue) and $Y_2CBr_2$ (green) monolayers as a function of the temperature (K), using the GGA-PBE functional 129
Figure 26 –	Energy level diagram representing IR absorption, Stokes Raman scattering, and anti-Stokes Raman scattering
Figure 27 –	a) Infrared spectrum for $Y_2CF_2$ (red), $Y_2CCl_2$ (blue) and $Y_2CBr_2$ (green). b) Raman spectrum for the $Y_2CF_2$ (red), $Y_2CCl_2$ (blue) and $Y_2CBr_2$ (green)
Figure 28 –	Electronic band structure of $Y_2CF_2$ (red), $Y_2CCl_2$ (blue) and $Y_2CBr_2$ (green). a) using GGA-PBE exchange-correlation functional along the 2D Brillouin high symmetry pathand, b) using HSE06 hybrid functional. c) and d) are the same energy bands of a) and b), but zoomed near Fermi level in $M \to \Gamma$ path
Figure 29 –	Highest occupied energy bands for $Y_2CF_2$ (red), $Y_2CCl_2$ (blue) and $Y_2CBr_2$ (green), between two $\Gamma$ points, with correspondent effective mass (black) as a multiple of the electron mass $m_e$
Figure 30 –	Crystalline sites localized by its position vectors $\mathbf{R}_{n_1n_2}$ . Each site correspond to the origin of a crystalline cell identified with the coordinates of it's origin
Figure 31 –	Unit cell shaped grid, equivalent to the Brillouin Zone
Figure 32 –	Grid for the Brillouin zone in the 2D hexagonal system
Figure 33 –	Valence and conduction energy levels of Y <sub>2</sub> CCl <sub>2</sub> Brillouin Zone 147

	a) Higher valence state effective mass along $\hat{y}$ mapped in Y <sub>2</sub> CCl <sub>2</sub> Brillouin Zone (30 $m_e$ is set as threshold for numerical precision). b) Higher valence state group velocity along $\hat{y}$ mapped in Y <sub>2</sub> CCl <sub>2</sub> Brillouin Zone	8
	Both perspectives on energy eigenstates along path in first Brillouin zone. The energy levels or bands are distinguished by color in both cases. a) Energy levels addressed according to energy hierarchy. b) Energy bands addressed according to wave function continuity. The green, red and yellow are the first to third higher valence bands, respectively; while the blue, cyan and pink bands are the first to third lower conduction bands, respectively. The ordering of the bands considered the	1
Figure 36 –	higher/lower value of each valence/conduction band	1
	color	2
Figure 37 –	$MoS_2$ energy bands after index correction	3
Figure 38 –	2D mapping of the $MoS_2$ valence bands in the hexagonal unit cell 15	4
0	Y <sub>2</sub> CCl <sub>2</sub> Momentum matrix element in both index configurations, considering the bands/levels in the vicinity of the Fermi level	6
_	MoS <sub>2</sub> Momentum matrix elements in both index configurations. Each	
	element along the momentum space is distinguished by color 15	8
_	$MoS_2$ momentum matrix elements with both circular polarizations, coupling spin up or spin down bands	0
	$Y_2CCl_2$ momentum matrix elements with $\hat{x}$ and $\hat{y}$ polarization, showing regions of optical activity	1
	Illustration of the numeric integral around the singularity point 16	
_	Squared absolute value of the wave functions for the degenerated pair	•
	of exciton states in $MoS_2$	5
Figure 45 –	Squared absolute value of the first exciton state wave function in $Y_2CCl_2.16$	6
	Excitonic Optical absorption spectra of monolayer MoS <sub>2</sub> under right-handed circularly polarized light. a) considers hierarchical energy states,	
	while b) considers continuous energy bands	7
Figure 47 –	Excitonic Optical absorption spectra of monolayer $Y_2CCl_2$ under $\hat{x}$ polarized light	
		Э
	Real part of Berry curvature contributions for each band interactions in both pictures of index configurations. The contribution from each	
	pair of bands is distinguished by color, and both scenarios considers	
	$= x \text{ and } \beta = y.$	2
Figure 49 –	Real part of Berry curvature tensor components	3

Figure 50 – Spin up and down contributions to the Berry curvature within the un	nit	
cell (Berry curvature units in $Å^2$ )		174

## List of Tables

Table 1 –	Pseudo atoms configurations used for geometry optimization 121
Table 2 -	Lattice parameters for the studied systems, according to the DFT GGA-
	PBE geometry optimization
Table 3 -	Cohesive energy $(E_{coh})$ for the studied systems, according to the DFT
	GGA-PBE geometry optimization
Table 4 -	Zero-point energy $(E_{zp})$ for the studied systems
Table 5 -	Frequency of the modes of vibration generated from infrared light ab-
	sorption in MXenes, in $cm^{-1}$
Table 6 -	Frequency of the Raman modes of vibration for MXenes, in ${\rm cm}^{-1}$ 133
Table 7 -	Direct and indirect band gaps, obtained for $Y_2CF_2$ , $Y_2CCl_2$ and $Y_2CBr_2$ ,
	using both PBE and HSE06 functionals
Table 8 -	Mass ratio for electron and holes associated with the indirect transition
	from $\Gamma$ to M, obtained for $Y_2CF_2$ , $Y_2CCl_2$ and $Y_2CBr_2$

# Contents

	Introduction	. 23
ı	THE UNDERLYING PHYSICAL THEORY	25
1	QUANTUM THEORY	. 27
1.1	Physical Systems	. 27
1.2	Mixed States	. 30
1.3	Multiple Particle Systems	. 33
1.4	Fermions	. 35
1.5	Bosons	. 40
1.6	Change of Basis	. 40
1.7	Number of Particles	. 42
1.8	One-Body Operators	. 43
1.9	Two-Body Operators	. 45
2	SOLID STATE	. 51
2.1	Chemical Introduction	. 51
2.2	Symmetry	. 55
2.3	Crystalline Lattices	. 56
2.3.1	Bravais Lattices	. 56
2.3.2	Lattice Planes and Crystalline Directions	. 58
2.4	Diffraction	. 59
2.5	Fourier Analysis	. 60
2.6	Reciprocal Lattice	. 62
2.6.1	Vectors in the Reciprocal Lattice	. 62
2.6.2	Diffraction Condition	. 65
2.6.3	The First Brillouin Zone	. 67
2.7	Periodic Functions	. 68
2.7.1	Lattice Translations	. 68
2.7.2	Bloch's Theorem	. 69
2.7.3	Counting States	. 72
2.7.4	Plane Wave Basis	. 73
2.7.5	Wannier Functions	. 74
2.8	Discrete Symmetries	. 75
2.8.1	Space Inversion	

2.8.2	Time Reversion
2.8.3	High Symmetry Points and Degeneracy
2.9	Schrödinger Equation for Many-electron Systems
2.10	Phonons
3	DFT
3.1	What is Density Functional Theory
3.2	The Many-Body Problem
3.3	Hohenberg-Kohn Theorem
3.4	Kohn-Sham Equations
3.5	Exchange and Correlation
3.5.1	The Exact Functionals
3.5.2	The Approximated Functionals
П	MATERIALS 109
3.6	Of Two-Dimensional Materials
3.7	Of Transition Metal Dichalcogenides
3.8	Of MXenes
Ш	OF COMPUTATIONAL SIMULATIONS 119
4	NOVEL MXENES PREDICTIONS
4.1	<b>DFT with CASTEP</b>
4.2	Lattice Stability and Characterization
4.2.1	Cohesive Energy
4.2.2	Phonon Energy States
4.2.3	Thermodynamics
4.2.4	Vibrational Spectroscopy
4.3	Electronic Properties
4.3.1	Band Structure
4.3.2	Effective Mass
5	ADVANCED ELECTRONIC PROPERTIES OF MXENES AND TMDS141
5.1	Quantum Espresso and Wannier90
5.2	Tight-Binding in Wannier Basis
5.3	Energy States in Crystals
5.4	Grids
5.5	Addressing Band-States
5.6	Momentum Matrix

5.7	Optics
5.8	<b>Exciton States</b>
5.9	<b>Berry Curvature</b>
	Conclusions
	REFERENCES
	ANNEX A – MATERIALS TODAY COMMUNICATIONS ARTI- CLE:
	ANNEX B – E-BOLETIM DA FÍSICA ARTICLE:

### Introduction

Humanity relies on the technology of its era. We continuously push the boundaries of our understanding and, consequently, the boundaries of the technology we can achieve. The electronic properties of materials are associated with groundbreaking developments in technology which unquestionably lead to major transformations in society; we live in the electronic age. From early studies of conductors, insulators, and later semiconductors, these and other electronic phases of matter have become fundamental to the advancement of cutting-edge electronic technologies. Technology which was always sustained in quantum mechanics, even before we knew it, though now we know, and now our knowledge grows, and as time goes on, more exotic properties are entering our repertoire of technologies.

Nowadays, these modern devices are being labeled as "quantum technology", bringing this mystery out of the scientific shell and growing popularity in the media. Many of these quantum technologies are rising with advanced topological phases of matter, spintronics and valleytronics exploration, quantum information processing, growing efficiency in photovoltaic cells, and as much as our understanding of the electron states can provide. As scientists continue to push the boundaries of knowledge, opening the path for further technology development, a necessity to refine our methods of studying the electron in solid state systems also increase, as we want to simulate the most exotic phenomena we can think of.

Quantum mechanics is not trivial, and solutions for many-body systems are as complex as they can get. For dealing with such complexity, computational simulations have been a key tool in the study of the electronic properties of materials. DFT simulations revolutionized the range and accuracy of physical properties that could now be theoretically proposed independently of experiments, but there is still more to grasp. Post-DFT methods are able to refine even further the electronic description and thus, prediction. Wannier functions give an elegant description of the electron states in the crystalline environment, and can serve as a great path to improve our computational description of reality.

Independently of the methods we use, it is crucial to evaluate how well the natural description is being constructed. Quantum mechanics concepts are sometimes elusive, but with careful pondering, the data-structure contained in their mathematics is surprisingly

24 Introduction

computationally oriented. Operators are represented as matrices, quantum states as vectors, and many properties appear in tensor form. In solid-state simulation, it's usual to map these properties in a unit cell that is represented on a discrete grid. All of these structures must be carefully constructed in computational language. Here we discuss the methodology used for this purpose, and show how physical properties can be better studied with proper information treatment. We go from quantum mechanics first principles, through DFT and the most relevant computational methodologies for simulating solid systems, into refined techniques for obtaining state-of-the-art properties of synthesized and even unsynthesized crystals. Predicting the existence of a crystal before giving it birth is possible due to simulations of the stability and characterization of the material, which then invites us into exploring advanced electronic and optical properties, such as excitonic and topological phenomena.

The structure of this dissertation is composed of three main parts, the first being a complete theoretical review endorsed by the best literature references, which is recommended as optional for the reader that is already comfortable with their knowledge in the first and second quantization languages, and fundamental solid-state representations. The second part connects physics with reality, exhibiting, discussing, and justifying the materials which are targeted for our simulations; we work with a transition metal dichalcogenide (TMD) and the newborn family of transition metal carbides, nitrides, and carbonitrides (MXenes). The third, and last part, is the heart of this study, being where we develop our computational methods, exhibiting and discussing the properties we were able to simulate and the technologies that may come with it.

# Part I

The Underlying Physical Theory

## 1 Quantum Theory

Deepening in condensed matter physics will require strong foundations of the theory that describes the lower scales of reality. Crystals are sets of atoms, and to understand them, we need quantum theory. This section begins with the fundamental concepts of quantum mechanics and crosses to the second quantization of many-body systems.

### 1.1 Physical Systems

Associated to any physical system, there is a complex Hilbert space  $\mathscr{H}$ , also known as the state space of the system. In any system, a state is represented by a state vector, which is an unitary vector in Hilbert space  $|\Psi\rangle \in \mathscr{H}$ . All unit vectors in a finite Hilbert space correspond to a possible physical state of the system (MANZANO, 2020). For obtaining physical information about that system, we make use of operators, which act on the Hilbert space of the state vectors as follows:

$$\hat{Q} |\Psi\rangle = q |\Psi\rangle \,, \tag{1.1}$$

where  $\hat{Q}$  is an operator that acts in  $|\Psi\rangle$  to produce  $q|\Psi\rangle$ , being q the measurement of the physical observable. The action of an operator in a state vector is given by an eigenvalue and eigenvector equation (1.1), where the eigenvectors are called eigenstates. It is important to keep in mind that, despite all physical observables being represented by operators, not all operators are related to a physical observable.

Quantum theory does not allow every observable to be measured simultaneously. According to Heisenberg's uncertainty relation (HEISENBERG, 1927), some operators are incompatible, that is, measuring a state with an operator may cause loss of information about some previous measurement. The compatibility of operators is defined by their commutator, where compatible operators have necessarily to commute, that is,

$$[\hat{Q}_1, \hat{Q}_2] = \hat{Q}_1 \hat{Q}_2 - \hat{Q}_2 \hat{Q}_1 = 0.$$

A set containing the maximum amount of commuting observable operators  $\hat{Q}_1,...,\hat{Q}_j$  is called a complete experiment. When acting on a state vector, the operators produce a set of eigenvalues  $q_1,...,q_j$ , which is the maximum amount of information that can be obtained from the system. The state vector is then written as  $|q_1,...,q_j\rangle$ .

The existence of complete experiments causes the notion of sates of maximum information. This states are called pure states, and are represented by unit vectors. For presenting the maximum information allowed by the uncertainty relation, they are quantum analogs to the classical states where is known all positions and momentum of a system.

The choice for some complete set of commuting operators is not necessarily unique. As an example, let's consider a quantity k of physical systems, where in each of them we have a complete experiment with a quantity j of operators. Be then the set of operators  $\hat{Q}_1, ..., \hat{Q}_j$ , that acting on the k state vectors lead us to  $\{|\Psi_1\rangle, ..., |\Psi_k\rangle\} = \{|q_{11}, ..., q_{1j}\rangle, ..., |q_{k1}, ..., q_{kj}\rangle\}$ . For another set of operators  $\hat{Q}'_1, ..., \hat{Q}'_j$ , we have the eigenstates as  $\{|\phi_1\rangle, ..., |\phi_k\rangle\} = \{|q'_{11}, ..., q'_{1j}\rangle, ..., |q'_{k1}, ..., q'_{kj}\rangle\}$ , where at least one of the operators in the second set does not commute with the first set, despite being both complete sets. If a system is represented by the state vector  $|\Psi_n\rangle$ , this can always be written as a linear combination of all eigenstates from  $\hat{Q}'_1, ..., \hat{Q}'_j$  (MANZANO, 2020),

$$|\Psi_n\rangle = \sum_{\alpha}^{j} a_{n\alpha} |\phi_{\alpha}\rangle.$$
 (1.2)

This equation is the mathematical representation for the notion of superposition. The vectors  $|\phi_{\alpha}\rangle$  above are the basis vectors, and the system  $|\Psi_{n}\rangle$  is said to be in the  $\{|\phi_{\alpha}\rangle\}$  representation. In general, every pure state can be written as a linear combination of any set of vectors that form a basis for the Hilbert space. Here,  $a_{n\alpha}$  are complex numbers that represent the probability amplitude of measuring the system  $|\Psi_{n}\rangle$  in the state  $|\phi_{\alpha}\rangle$ .

It's convenient to use a basis set with properties of orthonormality

$$\langle \phi_{\alpha} | \phi_{\beta} \rangle = \delta_{\alpha\beta},\tag{1.3}$$

and completeness

$$\sum_{\alpha} |\phi_{\alpha}\rangle \langle \phi_{\alpha}| = 1. \tag{1.4}$$

One can represent the adjoint state of  $|\Psi_n\rangle$  as

$$\langle \Psi_n | = \sum_{\alpha} a_{n\alpha}^* \langle \phi_{\alpha} |,$$
 (1.5)

so we can write the normalization as

$$\langle \Psi_n | \Psi_n \rangle = \sum_{\alpha} |a_{n\alpha}|^2 = 1, \tag{1.6}$$

being  $|a_{n\alpha}|^2$  the probability to measure the system  $|\Psi_n\rangle$  in the state  $|\phi_{\alpha}\rangle$ .

For a pure state  $|\Psi_n\rangle$  that is not an eigenstate of some observable  $\hat{Q}$ , measurements of that observable may have different results, i.e., each measurement might be a distinct eigenvalue of  $\hat{Q}$ . In general, if the number of identical particles is sufficiently large, all eigenvalues will eventually be measured. The average of the measurements, also called the expectation value  $\langle \hat{Q} \rangle$  of the observable  $\hat{Q}$ , is

$$\langle \hat{Q}_n \rangle = \langle \Psi_n | \hat{Q} | \Psi_n \rangle. \tag{1.7}$$

In a simple system of an nonrelativistic electron in an atom, the maximum information is described by four quantum numbers  $n, l, m_l, ms$ . Thus, any state  $|\phi_{\tau}\rangle$  can be written as  $|n \ l \ m_l \ m_s\rangle$ , which are the electron states in the energy representation, i.e., they are eigenstates of the energy operator. States are not limited to one representation. The vector  $|x\rangle \equiv |r\sigma\rangle$  is an eigenstate of the position operator  $\hat{r}$  and the spin projection operator  $\hat{s}_z$ . We have

$$\hat{\boldsymbol{r}}|x\rangle = \boldsymbol{r}|x\rangle \tag{1.8}$$

$$\hat{s}_z |x\rangle = \sigma \frac{\hbar}{2} |x\rangle \,, \tag{1.9}$$

where  $\sigma = \pm 1$ . The states  $|x\rangle$  satisfy the improper orthogonality relation

$$\langle x|x'\rangle = \delta_{\sigma\sigma'}\delta(r-r') \equiv \delta(x,x').$$
 (1.10)

Since space is a continuous, the state vectors  $|x\rangle$  are not properly normalizable, thus they are not elements of the Hilbert space of one particle  $\mathcal{H}_1$ . Nevertheless, they still can be used to represent the elements of  $\mathcal{H}_1$  in the sense of a basis set, since they form a complete basis in a vector space which contains  $\mathcal{H}_1$  (ENGEL; DREIZLER, 2011). To see this, we start by

$$|\phi_{\alpha}\rangle = \mathbb{1} |\phi_{\alpha}\rangle$$

$$= \sum_{x} |x\rangle \langle x|\phi_{\alpha}\rangle$$

$$= \sum_{x} \langle x|\phi_{\alpha}\rangle |x\rangle, \qquad (1.11)$$

and then we may rescue our notion of space as a continuous, to better describe nature, rewritten the equation above in the integral form

$$\int dx \left\langle x | \phi_{\alpha} \right\rangle | x \rangle \,, \tag{1.12}$$

where the ingeral  $\int dx$  abbreviates integration over space and summation over all internal degrees of freedom, as e.g. in the case of spin- $\frac{1}{2}$  fermions

$$\int dx \equiv \sum_{\sigma=\uparrow,\downarrow} \int d^3r. \tag{1.13}$$

The scalar product of the state vector  $|x\rangle$  and the single particle state  $|\phi_{\alpha}\rangle$  is interpreted as the wavefunction of the particle  $\phi_{\alpha}(x) \equiv \langle x|\phi_{\alpha}\rangle$ , so we have

$$\int dx \phi_{\alpha}(x) |x\rangle. \tag{1.14}$$

Based on this concept, we may find the orthonormality relation written as

$$\langle \phi_{\alpha} | \phi_{\beta} \rangle = \sum_{x} \langle \phi_{\alpha} | x \rangle \langle x | \phi_{\beta} \rangle$$

$$= \int dx \phi_{\alpha}(x)^{*} \phi_{\beta}(x) = \delta_{\alpha\beta}. \tag{1.15}$$

#### 1.2 Mixed States

In most cases, however, we do not know with certainty the pure state  $|\Psi_n\rangle$  in which the system is found, but rather a set of possible pure states  $|\Psi_1\rangle$ , ...,  $|\Psi_k\rangle$ . Due to statistical uncertainty, it is impossible to represent the state of these systems with a single state vector, as they are described with classical probabilities  $W_1, ..., W_k$  of being in pure states  $|\Psi_1\rangle$ , ...,  $|\Psi_k\rangle$ . For these systems, whose states are called mixed states, it is necessary to use a statistical description analogous to what occurs in classical systems, while still preserving the statistical component of quantum nature. To determine  $\langle \hat{Q} \rangle$  for a mixture  $|\Psi_1\rangle$ , ...,  $|\Psi_k\rangle$ , each expectation value  $\langle \hat{Q}_n\rangle$  is obtained through  $\langle \hat{Q}_n\rangle = \langle \Psi_n|\hat{Q}|\Psi_n\rangle$  and then multiplied by a probabilistic weight  $W_n$  in a summation, where  $W_n$  is a real number equal to the probability that any given particle in the set is in the pure state  $|\Psi_n\rangle$ :

$$\langle Q \rangle = \sum_{n} W_n \langle \Psi_n | Q | \Psi_n \rangle.$$
 (1.16)

By doing so, a classical probability is incorporated into a particle that is a priori in a pure state  $|\Psi_n\rangle$ , and upon measuring it, there is the quantum probabilistic effect of

1.2. Mixed States 31

finding it in one of the basis states  $|\phi_{\tau}\rangle$ .

We consider a set of independent states  $|\Psi_1\rangle, ..., |\Psi_k\rangle$  and their respective statistical weights  $W_1, ..., W_k$ . Using these, the density operator is defined as:

$$\hat{n} = \sum_{n} W_n |\Psi_n\rangle \langle \Psi_n|. \tag{1.17}$$

To write this operator in matrix form, another orthonormal and complete basis  $|\phi_{1'}\rangle, ..., |\phi_{k'}\rangle$  is chosen, so that we can use the principle of superposition  $|\Psi_n\rangle = \sum_{\tau'} a_{n\tau'} |\phi_{\tau'}\rangle$  to obtain:

$$\hat{n} = \sum_{n,\tau,\tau'} W_n a_{n\tau'} a_{n\tau}^* |\phi_{\tau'}\rangle \langle \phi_{\tau}|. \tag{1.18}$$

The elements  $n_{ji}$  of the density matrix, between the states  $\langle \phi_j |$  and  $|\phi_i \rangle$ , can be defined using  $\langle \phi_j | \phi_{\tau'} \rangle = \delta_{j\tau'}$  and  $\langle \phi_\tau | \phi_i \rangle = \delta_{\tau i}$ :

$$\langle \phi_j | \, \hat{n} \, | \phi_i \rangle = \sum_n W_n a_{nj}^* a_{ni}. \tag{1.19}$$

The elements found in the equation above are elements of the density matrix in the  $|\phi_{\tau}\rangle$  representation, such that the density matrix is explicitly written as:

$$\hat{n} \doteq \begin{pmatrix} \langle \phi_{1} | \hat{n} | \phi_{1} \rangle & \langle \phi_{1} | \hat{n} | \phi_{2} \rangle & \dots & \langle \phi_{1} | \hat{n} | \phi_{k} \rangle \\ \langle \phi_{2} | \hat{n} | \phi_{1} \rangle & \langle \phi_{2} | \hat{n} | \phi_{2} \rangle & \dots & \langle \phi_{2} | \hat{n} | \phi_{k} \rangle \\ \vdots & \vdots & \ddots & \vdots \\ \langle \phi_{k} | \hat{n} | \phi_{1} \rangle & \langle \phi_{k} | \hat{n} | \phi_{2} \rangle & \dots & \langle \phi_{k} | \hat{n} | \phi_{k} \rangle \end{pmatrix}.$$

Analyzing the matrix elements, we find some properties, such as the fact that  $\hat{n}$  is Hermitian, that is:

$$n_{ji} = n_{ij}^*,$$
 (1.20)

as we can verify,

$$\langle \phi_j | \, \hat{n} \, | \phi_i \rangle = \sum_n W_n a_{ni} a_{nj}^* = \left( \sum_n W_n a_{ni}^* a_{nj} \right)^* = \left( \langle \phi_i | \, \hat{n} \, | \phi_j \rangle \right)^*. \tag{1.21}$$

Since  $W_n$  represents the probability of finding one of the systems  $|\Psi_n\rangle$ , and  $|\Psi_n\rangle$  has the probability of being found in the state  $|\phi_{\tau}\rangle$  given by  $a_{n\tau}^2$ , the diagonal elements of the matrix combine these probabilities, resulting in the probability of finding the system in  $|\phi_{\tau}\rangle$ :

$$\hat{n}_{\tau\tau} = \sum_{n} W_n |a_{n\tau}|^2, \tag{1.22}$$

which provides a physical interpretation of the diagonal elements of the density matrix, also known as populations. In complement, the off-diagonal elements represent coupling terms between the states. This operator also obeys the following properties (MANZANO, 2020):

$$Tr[\hat{n}] = 1, \qquad \qquad \hat{n} > 0. \tag{1.23}$$

Given a density matrix, it is possible to verify whether it represents a pure or mixed state. This can be determined using the trace of  $\hat{n}^2$ :  $Tr[\hat{n}^2] = 1$  implies that the state is pure, and  $Tr[\hat{n}^2] < 1$  implies that the system is in a mixed state. The quantity  $Tr[\hat{n}^2]$  is referred to as the purity of the states, and it satisfies the condition:

$$\frac{1}{d} \le Tr[\hat{n}^2] \le 1,\tag{1.24}$$

where d is the number of dimensions of the Hilbert space.

The expected value  $\langle \hat{Q} \rangle$  of an observable  $\hat{Q}$  can be written as:

$$\langle \hat{Q} \rangle = Tr[\hat{Q}\hat{n}] \tag{1.25}$$

For example, we can perform measurements of the energies of a system. Consider a simple two-level system with  $E_0$  and  $E_1$ , where the operator corresponding to this measurement is the Hamiltonian:

$$\hat{H} = E_0 |0\rangle \langle 0| + E_1 |1\rangle \langle 1|. \tag{1.26}$$

This operator has two eigenvalues  $E_0, E_1$  with the corresponding eigenvectors  $|0\rangle, |1\rangle$ , which represent the ground state and excited state of the system.

For a pure state  $|\Psi\rangle = a_0 |0\rangle + a_1 |1\rangle$ , the probability of measuring the energy at  $E_0$  is given by  $P(E_0) = \langle 0|\Psi\rangle^2 = a_0^2$ , and analogously for  $E_1$ ,  $P(E_1) = \langle 1|\Psi\rangle^2 = a_1^2$ . Applying equation (1.7),  $\langle H\rangle = E_0 a_0^2 + E_1 a_1^2$ .

In the case of a mixed state represented by the operator  $\hat{n} = \hat{n}_{00} |0\rangle \langle 0| + \hat{n}_{01} |0\rangle \langle 1| + \hat{n}_{10} |1\rangle \langle 0| + \hat{n}_{11} |1\rangle \langle 1|$ , the probability of finding the ground state is given by  $P(0) = Tr[|0\rangle \langle 0| \hat{n}] = \hat{n}_{00}$ . Using (1.25), the expected value of the energy is obtained as:

$$\langle \hat{H} \rangle = Tr[\hat{H}\hat{n}] = E_0 \hat{n}_{00} + E_1 \hat{n}_{11}$$
 (1.27)

### 1.3 Multiple Particle Systems

The Hilbert space of N identical particles  $\mathscr{H}_N$  is the tensor product of N single-particle Hilbert spaces,

$$\mathcal{H}_N = \mathcal{H}_1^1 \otimes \mathcal{H}_1^2 \otimes \dots \otimes \mathcal{H}_1^N, \tag{1.28}$$

and it is spanned by the product states

$$|\phi_{\alpha_1}...\phi_{\alpha_N}\rangle' = |\phi_{\alpha_1}\rangle \otimes ... \otimes |\phi_{\alpha_N}\rangle. \tag{1.29}$$

In this form of N-particle states, the k-th particle is in state  $|\phi_{\alpha_k}\rangle$ , and the N-particle state characterizes the whole system. The same construction method is valid for

$$|x_1...x_N\rangle' = |x_1\rangle \otimes ... \otimes |x_N\rangle,$$
 (1.30)

giving the product wavefunction as

$$\Phi'_{\alpha_1...\alpha_N}(x_1...x_N) = \langle x_1...x_N |' | \phi_{\alpha_1}...\phi_{\alpha_N} \rangle'.$$
(1.31)

The wavefunctions  $\Phi'_{\alpha_1...\alpha_N}$  are ordered with respect to the particles and their labels, which is only possible if the individual particles can be distinguished. However, in the case of N identical particles, their bosonic or fermionic nature has to be taken into account, so that the corresponding subspaces  $\mathscr{B}_N$  and  $\mathscr{F}_N$  of  $\mathscr{H}_N$  presents symmetric or antisymmetric behavior.

For discussing symmetric or antisymmetric states, we must first understand the concept of particle permutations. A permutation of particles involves rearranging the positions or labels of the particles while ensuring that the state of the system remains unchanged. As e.g., the following states are permutations of particles:

$$|\phi_{\alpha_1}\phi_{\alpha_2}\phi_{\alpha_3}\rangle'$$
,  $|\phi_{\alpha_1}\phi_{\alpha_3}\phi_{\alpha_2}\rangle'$ ,  $|\phi_{\alpha_2}\phi_{\alpha_1}\phi_{\alpha_3}\rangle'$ ,  $|\phi_{\alpha_2}\phi_{\alpha_3}\phi_{\alpha_3}\rangle'$ ,  $|\phi_{\alpha_3}\phi_{\alpha_1}\phi_{\alpha_2}\rangle'$ ,  $|\phi_{\alpha_3}\phi_{\alpha_2}\phi_{\alpha_1}\rangle'$ . (1.32)

We introduce the permutation operator  $\hat{P}_{P_N}$ , which acts on a state vector, doing a permutation of particles. Equation (1.32) shows the six states corresponding to permutations  $P_1, ..., P_6$  of a system of three particles. For a system of N particles, there are N!possible permutations, thus, we say that

$$\sum_{P_N \in S_N} \hat{P}_{P_N} \left| \phi_{\alpha_1} ... \phi_{\alpha_N} \right\rangle' \tag{1.33}$$

is a sum of all N! possible permutations of the state vector  $|\phi_{\alpha_1}...\phi_{\alpha_N}\rangle'$ , where this set of summed permutations constitutes the symmetric group  $S_N$ .

We say that if  $\hat{P}_{P_N} |\Psi\rangle = |\Psi\rangle$ , for any permutation, then  $|\Psi\rangle$  is a totally symmetric state. If  $\hat{P}_{P_N} |\Psi\rangle = (-1)^P |\Psi\rangle$ , the state is totally antisymmetric. The sign of the permutations  $(-1)^P$  corresponds to the property even (+) or odd (-), according to the number P of pairwise transpositions necessary to restore the original order, where a transposition is a permutation of a pair of particles.

For a system of identical particles, the only vectors of its state space that can describe physical states are totally symmetric vectors with respect to permutations of identical particles and totally antisymmetric vectors with respect to permutations of identical particles. Particles of each specific nature are labeled, respectively, bosons and fermions.

The last step before we can finally define the fermionic and bosonic states is the symmetrizer and antisymmetrizer operators

$$\hat{S}_{+} = \frac{1}{N!} \sum_{P_N \in S_N} \hat{P}_{P_N} \tag{1.34}$$

$$\hat{S}_{-} = \sum_{P_N \in S_N} (-1)^P \hat{P}_{P_N}. \tag{1.35}$$

With these operators, we gain access to the occupation number representation, which suits both fermionic and bosonic systems. state vectors in this representation can be easily written as groups of particles in each individual state:

$$|n_1, ..., n_k, ...\rangle = A_{\pm} \hat{S}_{\pm} |\phi_{\alpha_1}\rangle_1 \otimes |\phi_{\alpha_1}\rangle_2 \otimes ... \otimes |\phi_{\alpha_1}\rangle_{n_1} \otimes ... \otimes |\phi_{\alpha_k}\rangle_1 \otimes ... \otimes |\phi_{\alpha_k}\rangle_{n_k} \otimes ..., (1.36)$$

being the occupation numbers  $n_k$  the number of particles in each state  $|\phi_{\alpha_k}\rangle$ , and  $A_{\pm}$  the normalization factor in each symmetric or antisymmetric case.

For bosons we have the symmetric case:

$$A_{+} = \sqrt{\frac{N!}{n_1! n_2! \dots n_k! \dots}},\tag{1.37}$$

1.4. Fermions 35

while for fermions, the antisymmetric case:

$$A_{-} = \begin{cases} \sqrt{N!}, & \text{if all states } |\phi_{\alpha_{k}}\rangle \text{ are different,} \\ 0, & \text{if any two states } |\phi_{\alpha_{k}}\rangle \text{ are equal.} \end{cases}$$
 (1.38)

The total number of particles N is obtained as the sum over all occupation numbers  $n_k$ , as

$$N = \sum_{k} n_k. \tag{1.39}$$

For a more general space, which contains all subspaces of any number of particles, we define the Fock space of fermions  $\mathscr{F}$ , and the Fock space of bosons  $\mathscr{B}$ , as the direct sum of  $\mathscr{F}_N$  or  $\mathscr{B}_N$ , in each case, for all particle numbers N,

$$\mathscr{F} = \mathscr{F}_0 \oplus \mathscr{F}_1 \oplus \dots \oplus \mathscr{F}_N \oplus \dots \tag{1.40}$$

$$\mathscr{B} = \mathscr{B}_0 \oplus \mathscr{B}_1 \oplus \dots \oplus \mathscr{B}_N \oplus \dots, \tag{1.41}$$

where the  $\mathscr{F}_0$  and  $\mathscr{B}_0$  subspaces are such that they contain no particles at all, where the only possible state is called the vacuum state  $|0\rangle$ . Vectors from different  $\mathscr{F}$  and  $\mathscr{B}$  subspaces are necessarily orthogonal. For navigating in each subspace, we shall later define the correspondent creation and annihilation operators. What we are doing is digging into the second quantization format, where not only the observables are written in form of operators, but also the state vectors.

#### 1.4 Fermions

For discussing fermions, we start from the wavefunctions, which must be totally antisymmetric, i.e. any wavefunction  $\Psi$  describing N identical fermions satisfies the relation

$$\Psi(x_{n_1}...x_{n_N}) = (-1)^P \Psi(x_1...x_N). \tag{1.42}$$

This relation is known as the Pauli principle.

A basis in  $\mathcal{F}_N$  can be constructed from the canonical basis by explicit antisymmetrization,

$$\Phi_{\alpha_{1}...\alpha_{N}}(x_{1}...x_{N}) = \frac{1}{\sqrt{N!}} \sum_{P_{N} \in S_{N}} (-1)^{P} \Phi'_{\alpha_{p_{1}}...\alpha_{p_{N}}}(x_{1}...x_{N})$$

$$= \frac{1}{\sqrt{N!}} \sum_{P_{N} \in S_{N}} (-1)^{P} \phi_{\alpha_{p_{1}}}(x_{1})...\phi_{\alpha_{p_{N}}}(x_{N})$$

$$= \frac{1}{\sqrt{N!}} \sum_{P_{N} \in S_{N}} (-1)^{P} \phi_{\alpha_{1}}(x_{p_{1}})...\phi_{\alpha_{N}}(x_{p_{N}}).$$
(1.43)

The last lines indicate that the basis functions of  $\mathscr{F}_N$  take the form of a determinant that considers permutations in labels and coordinates, which is called a Slater determinant.

The antisymmetrized wavefunctions  $\Phi_{\alpha_1...\alpha_N}$  do no longer associate a particular single-particle quantum number with a given particle. Their determinantal structure is a direct manifestation of the Pauli principle, and the function  $\Phi_{\alpha_1...\alpha_N}$  vanishes if two of the labels  $\alpha_1...\alpha_N$  are identical. This allows a definite ordering of the quantum numbers in  $\Phi_{\alpha_1...\alpha_N}$  in the form  $\alpha_1 < ... < \alpha_N$ . This basis functions are orthonormal and complete in  $\mathscr{F}_N$ , as the 1-particle basis used in its construction is orthonormal and complete in  $\mathscr{H}_N$ .(ENGEL; DREIZLER, 2011)

For spanning  $\mathscr{F}_N$  with state vectors, we use the antisymmetrized states

$$|n_1, ..., n_N\rangle = |\phi_{\alpha_1} ... \phi_{\alpha_N}\rangle = \frac{1}{\sqrt{N!}} \sum_{P_N \in S_N} (-1)^P |\phi_{\alpha_{p_1}} ... \phi_{\alpha_{p_N}}\rangle'.$$
 (1.44)

We notice that, as fermions have all occupation numbers  $n_k$  as one or zero, we may still represent the state vectors  $|n_1, ..., n_N\rangle$  as  $|\phi_{\alpha_1}...\phi_{\alpha_N}\rangle$ . This antisymmetric states, as happened to the wavefunction form, does not relate the positions of quantum numbers with particular states, i.e. a given particle is not in a particular single-particle state.

The antisymmetric N-fermion state vectors satisfy the orthonormality relation,

$$\langle \phi_{\alpha_1} ... \phi_{\alpha_N} | \phi_{\beta_1} ... \phi_{\beta_N} \rangle = \delta_{\alpha_1 \beta_1} ... \delta_{\alpha_N \beta_N}. \tag{1.45}$$

Similarly, the completeness relations have the form

$$\frac{1}{N!} \sum_{\alpha_1 \dots \alpha_N} |\phi_{\alpha_1} \dots \phi_{\alpha_N}\rangle \langle \phi_{\alpha_1} \dots \phi_{\alpha_N}| = \mathbb{1}_{\mathscr{F}_N}$$
(1.46)

$$\sum_{\alpha_1 < \dots < \alpha_N} |\phi_{\alpha_1} \dots \phi_{\alpha_N}\rangle \langle \phi_{\alpha_1} \dots \phi_{\alpha_N}| = \mathbb{1}_{\mathscr{F}_N}, \tag{1.47}$$

1.4. Fermions 37

where  $\mathbb{1}_{\mathscr{T}_N}$  represents the unit operator in the N-fermionic subspace.

A complete and orthonormal basis of  $\mathscr{F}$  is obtained as the sum of the basis sets from all N-particle subspaces, including  $|0\rangle$ . The completeness relation is then

$$|0\rangle\langle 0| + \sum_{N=1}^{\infty} \frac{1}{N!} \sum_{\alpha_1...\alpha_N} |\phi_{\alpha_1}...\phi_{\alpha_N}\rangle\langle \phi_{\alpha_1}...\phi_{\alpha_N}| = \mathbb{1}_{\mathscr{F}}.$$
 (1.48)

For fermions, it is forbidden for multiple particles to occupy the same state. Still, the creation operator  $\hat{c}^{\dagger}_{\alpha}$  acting on a  $\mathscr{F}_N$  state vector generates a  $\mathscr{F}_{N+1}$  state vector, as

$$\hat{c}_{\alpha}^{\dagger} |0\rangle = |\phi_{\alpha}\rangle, \qquad (1.49)$$

$$\hat{c}_{\alpha}^{\dagger} |\phi_{\alpha_1} ... \phi_{\alpha_N}\rangle = |\phi_{\alpha} \phi_{\alpha_1} ... \phi_{\alpha_N}\rangle. \tag{1.50}$$

This new tool, the creation operator, allows us to create any state from vacuum,

$$|\phi_{\alpha_1}...\phi_{\alpha_N}\rangle = \hat{c}_{\alpha_1}^{\dagger}...\hat{c}_{\alpha_N}^{\dagger}|0\rangle. \tag{1.51}$$

The antisymmetry property of fermion states, as e.g.,

$$|\phi_{\alpha_1}\phi_{\alpha_2}...\phi_{\alpha_N}\rangle = -|\phi_{\alpha_2}\phi_{\alpha_1}...\phi_{\alpha_N}\rangle, \qquad (1.52)$$

demand specific commutation relations, as we see:

$$|\phi_{\alpha_1}\phi_{\alpha_2}...\phi_{\alpha_N}\rangle = \hat{c}_{\alpha_1}^{\dagger}\hat{c}_{\alpha_2}^{\dagger}...\hat{c}_{\alpha_N}^{\dagger} |0\rangle$$

$$= -|\phi_{\alpha_2}\phi_{\alpha_1}...\phi_{\alpha_N}\rangle = -\hat{c}_{\alpha_2}^{\dagger}\hat{c}_{\alpha_1}^{\dagger}...\hat{c}_{\alpha_N}^{\dagger} |0\rangle, \qquad (1.53)$$

which indicate us the anticommutation relation:

$$\{\hat{c}_{\alpha}^{\dagger}, \hat{c}_{\beta}^{\dagger}\} = 0. \tag{1.54}$$

We may notice that if the fermionic creation operator creates a state that is already occupied, the interchange of those particle states must be equal to the previous state with a minus sign, signifying that the state must be zero.

$$\hat{c}_{\alpha_1}^{\dagger} |\phi_{\alpha_1}\rangle = |\phi_{\alpha_1}\phi_{\alpha_1}\rangle, \qquad (1.55)$$

and then

$$|\phi_{\alpha_1}\phi_{\alpha_1}\rangle = -|\phi_{\alpha_1}\phi_{\alpha_1}\rangle = 0. \tag{1.56}$$

With creation  $\hat{c}_{\alpha}^{\dagger}$ , there is annihilation  $\hat{c}_{\alpha}$ . One is not without the other; a duality of existence, as we see from definition:

$$\hat{c}_{\alpha} \coloneqq (\hat{c}_{\alpha}^{\dagger})^{\dagger}. \tag{1.57}$$

Consequently,

$$\langle \phi_{\alpha_1} | = \langle 0 | \hat{c}_{\alpha_1} \tag{1.58}$$

$$\langle \phi_{\alpha_1} ... \phi_{\alpha_N} | = \langle 0 | \hat{c}_{\alpha_N} ... \hat{c}_{\alpha_1}, \tag{1.59}$$

where we should notice that any new state is written in the left edge for both bras and kets.

In the same way that an anticommutation relation was found for the creation operator, it can be found for annihilation:

$$\{\hat{c}_{\alpha}, \hat{c}_{\beta}\} = 0.$$
 (1.60)

The annihilation operator destroys a state on the left edge of the ket representation, acting in the Fock space as  $\mathscr{F}_N \to \mathscr{F}_{N-1}$ . It is important to notice that if the annihilated state is not in the left edge of the ket representation, it must be first reallocated while respecting the interchanging minus sign, as

$$\hat{c}_{\beta} |\phi_{\alpha}\phi_{\beta}\rangle = -\hat{c}_{\beta} |\phi_{\beta}\phi_{\alpha}\rangle = -|\phi_{\alpha}\rangle. \tag{1.61}$$

It makes sense that particles cannot be annihilated if there are no particles at all, so for the vacuum state,

$$\hat{c}_{\beta} |0\rangle = 0. \tag{1.62}$$

Let us now derive the commutation relation between the creation  $\hat{c}^{\dagger}_{\alpha}$  and annihilation  $\hat{c}_{\beta}$  operators. For that, we must first apply both operators, in both orders, to some state vector  $\hat{c}^{\dagger}_{\gamma}|0\rangle$ . Consider first the case where  $\alpha \neq \beta$ ,  $\gamma = \alpha$ :

1.4. Fermions 39

$$\hat{c}_{\alpha}\hat{c}_{\beta}^{\dagger} |\phi_{\alpha}\rangle = \hat{c}_{\alpha} |\phi_{\beta}\phi_{\alpha}\rangle = -\hat{c}_{\alpha} |\phi_{\alpha}\phi_{\beta}\rangle = -|\phi_{\beta}\rangle, \qquad (1.63)$$

$$\hat{c}_{\beta}^{\dagger}\hat{c}_{\alpha}|\phi_{\alpha}\rangle = \hat{c}_{\beta}^{\dagger}|0\rangle = |\phi_{\beta}\rangle. \tag{1.64}$$

The sum of these two equations results in

$$(\hat{c}_{\alpha}\hat{c}_{\beta}^{\dagger} + \hat{c}_{\beta}^{\dagger}\hat{c}_{\alpha})|\phi_{\alpha}\rangle = 0, \tag{1.65}$$

i.e., for  $\alpha \neq \beta$ , and  $\gamma \neq \alpha$ ,  $\{\hat{c}_{\alpha}, \hat{c}^{\dagger}_{\beta}\} = 0$ .

For  $\alpha \neq \beta$ ,  $\gamma \neq \alpha$ :

$$\hat{c}_{\alpha}\hat{c}_{\beta}^{\dagger}|\phi_{\gamma}\rangle = \hat{c}_{\alpha}|\phi_{\beta}\phi_{\gamma}\rangle = 0, \tag{1.66}$$

$$\hat{c}_{\beta}^{\dagger}\hat{c}_{\alpha}\left|\phi_{\gamma}\right\rangle = 0. \tag{1.67}$$

So for  $\alpha \neq \beta$ ,  $\{\hat{c}_{\alpha}, \hat{c}^{\dagger}_{\beta}\} = 0$ .

Now we consider the case where  $\beta = \alpha$ . For,  $\gamma = \alpha$ :

$$\hat{c}_{\alpha}\hat{c}_{\alpha}^{\dagger} |\phi_{\alpha}\rangle = 0, \tag{1.68}$$

$$\hat{c}_{\alpha}^{\dagger}\hat{c}_{\alpha}\left|\phi_{\alpha}\right\rangle = \hat{c}_{\alpha}^{\dagger}\left|0\right\rangle = \left|\phi_{\alpha}\right\rangle. \tag{1.69}$$

The sum of the two equations gives that for  $\beta = \alpha$ , and  $\gamma = \alpha$ ,  $\{\hat{c}_{\alpha}, \hat{c}^{\dagger}_{\beta}\} = 1$ . Now, finally, when  $\beta = \alpha$ , and  $\gamma \neq \alpha$ ,

$$\hat{c}_{\alpha}\hat{c}_{\alpha}^{\dagger} |\phi_{\gamma}\rangle = \hat{c}_{\alpha} |\phi_{\alpha}\phi_{\gamma}\rangle = |\phi_{\gamma}\rangle, \qquad (1.70)$$

$$\hat{c}_{\alpha}^{\dagger}\hat{c}_{\alpha}\left|\phi_{\gamma}\right\rangle = 0. \tag{1.71}$$

Again, the sum of the equations gives  $\{\hat{c}_{\alpha}, \hat{c}_{\alpha}^{\dagger}\} = 1$ . All we obtained from every possible scenario can be expressed in a single generalized statement,  $\{\hat{c}_{\alpha}, \hat{c}_{\beta}^{\dagger}\} = \delta_{\alpha\beta}$ .

The set of tools containing the fermionic creation and annihilation operators, as well as their relations, is resumed in:

$$\{\hat{c}_{\alpha}, \hat{c}_{\beta}\} = 0$$
  $\{\hat{c}_{\alpha}^{\dagger}, \hat{c}_{\beta}^{\dagger}\} = 0$   $\{\hat{c}_{\alpha}, \hat{c}_{\beta}^{\dagger}\} = \delta_{\alpha\beta},$  (1.72)

which is enough to handle all possible operations in the fermionic Fock space  $\mathscr{F}$ . (ENGEL; DREIZLER, 2011)

### 1.5 Bosons

Bosons are not the main focus of this work, but of course, for completeness of information, let us briefly show this particles subspace.

The bosonic creation operator  $\hat{a}^{\dagger}_{\alpha}$  acting on a  $\mathscr{B}_{N}$  state vector generates a  $\mathscr{B}_{N+1}$  state vector, as

$$\hat{a}_{\alpha}^{\dagger} | n_1, n_2, ..., n_{\alpha}, ... \rangle = \sqrt{n_{\alpha} + 1} | n_1, n_2, ..., n_{\alpha} + 1, ... \rangle.$$
 (1.73)

For its adjoint operator, the annihilation operator  $(\hat{a}^{\dagger}_{\alpha})^{\dagger} = \hat{a}_{\alpha}$ :

$$\hat{a}_{\alpha} | n_1, n_2, ..., n_{\alpha}, ... \rangle = \sqrt{n_{\alpha}} | n_1, n_2, ..., n_{\alpha} - 1, ... \rangle.$$
 (1.74)

Associated with those, the very important commutation properties may be derived in a similar fashion we did for the fermionic operators, and we get:

$$[\hat{a}_{\alpha}, \hat{a}_{\beta}] = 0 \qquad \qquad [\hat{a}_{\alpha}^{\dagger}, \hat{a}_{\beta}^{\dagger}] = 0 \qquad \qquad [\hat{a}_{\alpha}, \hat{a}_{\beta}^{\dagger}] = \delta_{\alpha\beta}. \tag{1.75}$$

## 1.6 Change of Basis

We showed that any state can be written in terms of creation and annihilation operators, so for changing basis in the second quantization format, we must see how these operators transform. The basis set used until now is one with labels  $\phi_{\alpha}$ . How about particles in a given coordinates  $\boldsymbol{x}$ ? We may remember the concept of transforming basis vectors in  $\mathcal{H}_1$ ,

$$|\boldsymbol{x}\rangle = \mathbb{1} |\boldsymbol{x}\rangle = \sum_{\alpha} |\phi_{\alpha}\rangle \langle \phi_{\alpha}|\boldsymbol{x}\rangle = \sum_{\alpha} \phi_{\alpha}^{*}(\boldsymbol{x}) |\phi_{\alpha}\rangle = \sum_{\alpha} \phi_{\alpha}^{*}(\boldsymbol{x}) c_{\alpha}^{\dagger} |0\rangle.$$
 (1.76)

This suggests the definition of new operators  $\hat{\Psi}^{\dagger}(\boldsymbol{x})$  and  $\hat{\Psi}(\boldsymbol{x})$ . These are usually called field operators and are responsible for the creation and annihilation of particles at coordinates  $\boldsymbol{x}$ ,

1.6. Change of Basis

$$\hat{\Psi}^{\dagger}(\boldsymbol{x}) = \sum_{\alpha} \phi_{\alpha}^{*}(\boldsymbol{x}) \hat{c}_{\alpha}^{\dagger}$$
 (1.77)

$$\hat{\Psi}(\boldsymbol{x}) = \sum_{\alpha} \phi_{\alpha}(\boldsymbol{x})\hat{c}_{\alpha}, \tag{1.78}$$

with inverse transformation

$$\hat{c}_{\alpha}^{\dagger} = \int d\boldsymbol{x} \phi_{\alpha}(\boldsymbol{x}) \hat{\Psi}^{\dagger}(\boldsymbol{x})$$
 (1.79)

$$\hat{c}_{\alpha} = \int d\boldsymbol{x} \phi_{\alpha}^{*}(\boldsymbol{x}) \hat{\Psi}(\boldsymbol{x}). \tag{1.80}$$

With those we may write

$$|\boldsymbol{x}\rangle = \hat{\Psi}^{\dagger}(\boldsymbol{x})|0\rangle$$
 and  $\langle \boldsymbol{x}| = \langle 0|\hat{\Psi}(\boldsymbol{x}).$  (1.81)

In case of spin- $\frac{1}{2}$  fermions, the field operator is divided into components,

$$\hat{\Psi}(oldsymbol{x}) = \hat{\Psi}(oldsymbol{r}oldsymbol{\sigma}) = egin{cases} \hat{\Psi}(oldsymbol{r},rac{1}{2}) & ext{if } oldsymbol{\sigma} = rac{1}{2} \ \hat{\Psi}(oldsymbol{r},-rac{1}{2}) & ext{if } oldsymbol{\sigma} = -rac{1}{2} \end{cases}.$$

The commutation or anticommutation relations of bosons and fermions are preserved for their respective field operators, for e.g. the fermionic case produces relations similar to (1.72),

$$\{\hat{\Psi}(\boldsymbol{x}), \hat{\Psi}(\boldsymbol{x}')\} = 0 \qquad \{\hat{\Psi}^{\dagger}(\boldsymbol{x}), \hat{\Psi}^{\dagger}(\boldsymbol{x}')\} = 0 \qquad \{\hat{\Psi}(\boldsymbol{x}), \hat{\Psi}^{\dagger}(\boldsymbol{x}')\} = \delta(\boldsymbol{x}, \boldsymbol{x}').$$
 (1.82)

In general, transformation of basis conserves the commutation or anticommutation relations. These properties gather the symmetric and antisymmetric nature of bosonic and fermionic particles. The general basis transformation is written as:

$$\hat{c}_{v_j}^{\dagger} = \sum_{i} \langle u_i | v_j \rangle \, \hat{c}_{u_i}^{\dagger} \qquad \qquad \hat{c}_{v_j} = \sum_{i} \langle v_j | u_i \rangle \, \hat{c}_{u_i}, \qquad (1.83)$$

where  $|v_j\rangle$  and  $|u_i\rangle$  correspond to different basis sets. These relations, despite being written in terms of the fermionic notation for operators, are general for both bosons and fermions.

### 1.7 Number of Particles

To obtain the number  $n_{\alpha}$  of particles in a particular state  $|\phi_{\alpha}\rangle$ , we define the occupation number operator  $\hat{n}_{\alpha} = \hat{c}_{\alpha}^{\dagger}\hat{c}_{\alpha}$ , where  $\hat{n}_{\alpha}|n_{\alpha}\rangle = n_{\alpha}|n_{\alpha}\rangle$ . For fermions, the occupation number can only be one or zero, and for bosons, it is easy to check that this indeed gives the number of particles in a specific state,

$$\hat{a}_{\alpha}^{\dagger} \hat{a}_{\alpha} | n_{1}, n_{2}, ..., n_{\alpha}, ... \rangle = \hat{a}_{\alpha}^{\dagger} \sqrt{n_{\alpha}} | n_{1}, n_{2}, ..., n_{\alpha} - 1, ... \rangle 
= \sqrt{n_{\alpha} - 1 + 1} \sqrt{n_{\alpha}} | n_{1}, n_{2}, ..., n_{\alpha}, ... \rangle = n_{\alpha} | n_{1}, n_{2}, ..., n_{\alpha}, ... \rangle.$$
(1.84)

Then, the operator for the total number of particles in the system is  $\hat{N} = \sum_{\alpha} \hat{n}_{\alpha}$ . We may also write this operator in the x-basis, so we obtain the number of particles in some region of space. For spin- $\frac{1}{2}$  particles we have

$$\hat{N} = \sum_{\alpha} \int d\mathbf{x}' d\mathbf{x} \phi_{\alpha}(\mathbf{x}) \hat{\Psi}^{\dagger}(\mathbf{x}) \phi_{\alpha}^{*}(\mathbf{x}') \hat{\Psi}(\mathbf{x}')$$

$$= \int d^{3}\mathbf{x} d^{3}\mathbf{x}' \sum_{\alpha} \langle \mathbf{x} | \phi_{\alpha} \rangle \langle \phi_{\alpha} | \mathbf{x}' \rangle \hat{\Psi}^{\dagger}(\mathbf{x}) \hat{\Psi}(\mathbf{x}')$$

$$= \sum_{\sigma, \sigma' = \uparrow, \downarrow} \int d^{3}\mathbf{r} d^{3}\mathbf{r}' \delta_{\sigma\sigma'} \delta(\mathbf{r} - \mathbf{r}') \hat{\Psi}^{\dagger}(\mathbf{r}\boldsymbol{\sigma}) \hat{\Psi}(\mathbf{r}'\boldsymbol{\sigma}')$$

$$= \sum_{\sigma = \uparrow, \downarrow} \int d^{3}\mathbf{r} \hat{\Psi}^{\dagger}(\mathbf{r}\boldsymbol{\sigma}) \hat{\Psi}(\mathbf{r}\boldsymbol{\sigma}). \tag{1.85}$$

We might write this in the form

$$\hat{N} = \int d^3 \mathbf{r} \hat{n}(\mathbf{r}), \tag{1.86}$$

where

$$\hat{n}(\mathbf{r}) = \sum_{\sigma = \uparrow, \downarrow} \hat{\Psi}^{\dagger}(\mathbf{r}\boldsymbol{\sigma})\hat{\Psi}(\mathbf{r}\boldsymbol{\sigma})$$
(1.87)

is the particle density operator, which gives the number of particles contained in an infinitesimal region of space around r.

So far, we have been intentionally considering spin- $\frac{1}{2}$  particles, so we stay close to the concept of electron density, which will be central in the DFT section.

## 1.8 One-Body Operators

Now, it is time to write in the second quantized form, i.e. in terms of annihilation and creation operators, the quantum operators that act on one particle at a time. Operators as such include the position and momentum operators,  $\hat{x}$  and  $\hat{p}$ .

In a N body system, we wrote the correspondent space as a tensor product of all N single particle spaces,  $\mathscr{H}_N = \mathscr{H}_1^1 \otimes \mathscr{H}_1^2 \otimes ... \otimes \mathscr{H}_1^N$ . Thus, an operator  $\hat{o}_q$  of some subspace  $\mathscr{H}_1^q$ , which acts only in the particle of that subspace, is written as  $\mathbb{1}_1 \otimes ... \otimes \hat{o}_q \otimes ... \otimes \mathbb{1}_N$ .

For a system of N identical particles, exchanging any two particles leads to the exact same physics, so we work not with  $\mathscr{H}_N$  but with the totally symmetric subspace  $\mathscr{G}_N$  or the totally antisymmetric subspace  $\mathscr{F}_N$ . For maintaining the physics of the system under particle exchange, we need symmetric operators. They, called one-body operators, are obtained as the sum over all single particle operators,

$$\hat{O} = \sum_{q=1}^{N} \hat{o}_q. \tag{1.88}$$

We can write  $\hat{o}_q$  as

$$\hat{o}_{q} = \mathbb{1}\hat{o}_{q}\mathbb{1} = \sum_{\alpha\beta} |\phi_{\alpha}\rangle_{q} \langle \phi_{\alpha}|\hat{o}_{q}|\phi_{\beta}\rangle_{q} \langle \phi_{\beta}| = \sum_{\alpha\beta} o_{\alpha\beta} |\phi_{\alpha}\rangle_{q} \langle \phi_{\beta}|, \tag{1.89}$$

where  $o_{\alpha\beta}$  is  $_{q}\langle\phi_{\alpha}|\hat{o}_{q}|\phi_{\beta}\rangle_{q}=\langle\phi_{\alpha}|\hat{o}|\phi_{\beta}\rangle$ , since the operator elements must be identical for identical particles. That can be inserted in equation (1.88), resulting in

$$\hat{O} = \sum_{\alpha,\beta} o_{\alpha\beta} \sum_{q=1}^{N} |\phi_{\alpha}\rangle_{q} \, _{q} \langle \phi_{\beta}|. \tag{1.90}$$

This is the one-body operator written in terms of the first quantization language. We must now proceed for second quantization, and for that, let us write the action of the operator in a state vector, in terms of tensor products:

$$\hat{O}A_{\pm}\hat{S}_{\pm} |\phi_1\rangle_1 \otimes |\phi_1\rangle_2 \otimes \dots \otimes |\phi_1\rangle_{n_1} \otimes |\phi_2\rangle_{n_1+1} \otimes \dots |\phi_2\rangle_{n_1+n_2} \otimes \dots \otimes |\phi_k\rangle_q \otimes \dots$$
 (1.91)

Since the one-body operator is symmetric, it necessarily commutes with the permutation operator, and thus also with the symmetrizer and antisymmetrizer operators, allowing

$$A_{\pm}\hat{S}_{\pm}\hat{O} |\phi_{1}\rangle_{1} \otimes |\phi_{1}\rangle_{2} \otimes ... \otimes |\phi_{1}\rangle_{n_{1}} \otimes |\phi_{2}\rangle_{n_{1}+1} \otimes ... |\phi_{2}\rangle_{n_{1}+n_{2}} \otimes ... \otimes |\phi_{k}\rangle_{q} \otimes ....$$
 (1.92)

For simplicity, from now on we may omit the symbol of the tensor product and the operator terms  $\sum_{\alpha,\beta} o_{\alpha\beta}$ , leading to

$$A_{\pm}\hat{S}_{\pm}\left(\sum_{q=1}^{N}\left|\phi_{\alpha}\rangle_{q} \left\langle\phi_{\beta}\right|\right)\left|\phi_{1}\rangle_{1}\left|\phi_{1}\rangle_{2} \dots\left|\phi_{1}\rangle_{n_{1}}\left|\phi_{2}\rangle_{n_{1}+1} \dots\left|\phi_{2}\rangle_{n_{1}+n_{2}} \dots\left|\phi_{k}\rangle_{q} \dots\right.\right.\right)$$

$$(1.93)$$

We may notice that the subindex q contained in the tensor product states is explicit, for it represents the particle related to the operator action. From all N states in the sum, it will not vanish only those which  $\langle \phi_{\beta} | \phi_k \rangle = 1$ , i.e., there will be exactly  $n_{\beta}$  states. Then,

$$A_{\pm}\hat{S}_{\pm}\left(\sum_{q=1}^{N}|\phi_{\alpha}\rangle_{q}\,_{q}\langle\phi_{\beta}|\right)|\phi_{1}\rangle_{1}|\phi_{1}\rangle_{2}\dots|\phi_{1}\rangle_{n_{1}}|\phi_{2}\rangle_{n_{1}+1}\dots|\phi_{2}\rangle_{n_{1}+n_{2}}\dots|\phi_{k}\rangle_{q}\dots$$

$$=n_{\beta}A_{\pm}\hat{S}_{\pm}|\phi_{1}\rangle_{1}|\phi_{1}\rangle_{2}\dots|\phi_{1}\rangle_{n_{1}}|\phi_{2}\rangle_{n_{1}+1}\dots|\phi_{2}\rangle_{n_{1}+n_{2}}\dots|\phi_{\alpha}\rangle_{q}\dots$$
(1.94)

Despite looking like a totally symmetrized or antisymmetrized state, the last line is not such. The terms  $n_{\beta}A_{\pm}=n_{\beta}\sqrt{\frac{N!}{n_{1}!...n_{\beta}!...n_{\alpha}!...}}$  are not in accordance with the tensor product states since the correct normalization factor would be correct only with  $n_{\beta}=1$ . We may write the last equation in a way that the normalization factor fits the new state, as

$$n_{\beta} \sqrt{\frac{n_{\alpha}+1}{n_{\beta}}} \sqrt{\frac{N!}{n_{1}!...(n_{\beta}-1)!...(n_{\alpha}+1)!...}} \hat{S}_{\pm} |\phi_{1}\rangle_{1} ... |\phi_{1}\rangle_{n_{1}} |\phi_{2}\rangle_{n_{1}+1} ... |\phi_{2}\rangle_{n_{1}+n_{2}} ... |\phi_{\alpha}\rangle_{q} ...,$$

$$(1.95)$$

so when we rewrite in terms of the occupation number representation,

$$\sqrt{n_{\alpha} + 1} \sqrt{n_{\beta}} |n_1...n_{\beta} - 1...n_{\alpha} + 1...\rangle = a_{\alpha}^{\dagger} a_{\beta} |n_1...n_{\beta}...n_{\alpha}...\rangle.$$
 (1.96)

The result we just achieved is remarkable. The term  $\sum_{q=1}^{N} |\phi_{\alpha}\rangle_{q} \langle \phi_{\beta}|$  is equivalent to  $a_{\alpha}^{\dagger} a_{\beta}$ . Notice that despite the usage of creation and annihilation operators with bosonic notation, this result is valid for both bosons and fermions; the math is exactly the same. Finally, we may write the one-body operator in the second quatization format,

$$\hat{O} = \sum_{\alpha,\beta} o_{\alpha\beta} a_{\alpha}^{\dagger} a_{\beta}. \tag{1.97}$$

Despite the absence of the summation, previously stated as necessary for the symmetrization of the one-body operator, this is compensated by the pair of creation and annihilation operators with the respective commutation or anticommutation relations, which are enough for the symmetry of the operator. It should be clear that the last expression shows the action of the operator  $\hat{O}$  as the transitioning of particles from states  $|\phi_{\beta}\rangle$  to states  $|\phi_{\alpha}\rangle$ , with amplitude  $o_{\alpha\beta}$  related to these transitions.

## 1.9 Two-Body Operators

As seen before, for a N body system,

$$\mathcal{H}_{N} = \mathcal{H}_{1}^{1} \otimes ... \otimes \mathcal{H}_{1}^{q} \otimes ... \otimes \mathcal{H}_{1}^{q'} \otimes ... \otimes \mathcal{H}_{1}^{N}. \tag{1.98}$$

Now we shall work with  $\hat{w}_{qq'}$ , which is an operator of some subspace  $\mathscr{H}_1^q \otimes \mathscr{H}_1^{q'}$ , responsible for the interaction between particles of such subspace. We maintain notation, but when acting in N particle states, we need to consider this operator as

$$\hat{w}_{qq'} = \mathbb{1}_1 \otimes \dots \otimes \hat{w}_{qq'} \otimes \dots \otimes \mathbb{1}_N. \tag{1.99}$$

If particles are identical, physics is unchanged in the exchange of particles, so we work not with  $\mathcal{H}_N$  but with the totally symmetric subspace  $\mathcal{F}_N$  or totally antisymmetric subspace  $\mathcal{F}_N$ . Not surprisingly, as one-body operators, two-body operators must also be symmetric, so the totally symmetric operator defined in first quantization format is

$$\hat{W} = \frac{1}{2!} \sum_{\substack{q,q'=1\\q \neq q'}}^{N} \hat{w}_{qq'}, \tag{1.100}$$

where the factor  $\frac{1}{2!}$  is responsible for redundancy of interactions.

Now we shall see how to write this operator in second quantized format, so before that, let's check some important features of the commutation and anticommutation relations of bosons and fermions. We have

$$[\hat{a}_{\alpha}, \hat{a}_{\beta}^{\dagger}] = \delta_{\alpha\beta} \qquad \{\hat{c}_{\alpha}, \hat{c}_{\beta}^{\dagger}\} = \delta_{\alpha\beta}, \qquad (1.101)$$

or,

$$\hat{a}_{\alpha}\hat{a}_{\beta}^{\dagger} = \hat{a}_{\beta}\hat{a}_{\alpha}^{\dagger} + \delta_{\alpha\beta} \tag{1.102}$$

$$\hat{c}_{\alpha}\hat{c}_{\beta}^{\dagger} = -\hat{c}_{\beta}\hat{c}_{\alpha}^{\dagger} + \delta_{\alpha\beta}. \tag{1.103}$$

The following discussion considers the same notation  $\hat{a}_{\alpha}$ ,  $\hat{a}_{\beta}^{\dagger}$ , for both bosons and fermions, using

$$\hat{a}_{\alpha}\hat{a}_{\beta}^{\dagger} = \eta \hat{a}_{\beta}\hat{a}_{\alpha}^{\dagger} + \delta_{\alpha\beta}, \tag{1.104}$$

where  $\eta$  is -1 for fermions, and 1 for bosons.

Similarly,

$$\hat{a}_{\alpha}\hat{a}_{\beta} = \hat{a}_{\beta}\hat{a}_{\alpha} \tag{1.105}$$

$$\hat{c}_{\alpha}\hat{c}_{\beta} = -\hat{c}_{\beta}\hat{c}_{\alpha},\tag{1.106}$$

SO

$$\hat{a}_{\alpha}\hat{a}_{\beta} = \eta \hat{a}_{\beta}\hat{a}_{\alpha}. \tag{1.107}$$

Having reviewed the properties of the creation and annihilation operators, we proceed to the two-body operator in the second quantized format, where we shall maintain the same notation for the creation and annihilation of bosons and fermions. The mathematics should be equivalent in both cases.

We can always write a two-particle operator  $\hat{w}_{qq'}$  as an expansion of two single-particle operators

$$\hat{w}_{qq'} = \sum_{ij} C_{i,j} \hat{f}_q^i \hat{g}_{q'}^j, \tag{1.108}$$

where  $C_{ij}$  are coefficients of the expansion. Including this in definition (1.100), we get

$$\hat{W} = \frac{1}{2} \sum_{\substack{q,q'=1\\q \neq q'}}^{N} \sum_{ij} C_{i,j} \hat{f}_{q}^{i} \hat{g}_{q'}^{j} = \frac{1}{2} \sum_{ij} C_{i,j} \sum_{\substack{q,q'=1\\q \neq q'}}^{N} \hat{f}_{q}^{i} \hat{g}_{q'}^{j}.$$
(1.109)

We continue our derivation focusing on the summation over q and q'. For this, we shall temporally omit the superscripts i, j in the one-particle operators to write

$$\sum_{\substack{q,q'=1\\q\neq q'}}^{N} \hat{f}_q \hat{g}_{q'} = \sum_{q=1}^{N} \hat{f}_q \sum_{q'=1}^{N} \hat{g}_{q'} - \sum_{q=1}^{N} \hat{f}_q \hat{g}_q.$$
 (1.110)

Now we apply the second quantized format for the one-body operator (1.97),

$$\sum_{\substack{q,q'=1\\q\neq q'}}^{N} \hat{f}_{q} \hat{g}_{q'} = \sum_{\alpha_{1},\beta_{1}} f_{\alpha_{1}\beta_{1}} \hat{a}_{\alpha_{1}}^{\dagger} \hat{a}_{\beta_{1}} \sum_{\alpha_{2},\beta_{2}} g_{\alpha_{2}\beta_{2}} \hat{a}_{\alpha_{2}}^{\dagger} \hat{a}_{\beta_{2}} - \sum_{\alpha_{3},\beta_{3}} (\hat{f}\hat{g})_{\alpha_{3}\beta_{3}} \hat{a}_{\alpha_{3}}^{\dagger} \hat{a}_{\beta_{3}}$$

$$= \sum_{\alpha_{1},\beta_{1},\alpha_{2},\beta_{2}} f_{\alpha_{1}\beta_{1}} g_{\alpha_{2}\beta_{2}} \hat{a}_{\alpha_{1}}^{\dagger} (\eta \hat{a}_{\alpha_{2}}^{\dagger} \hat{a}_{\beta_{1}} \hat{a}_{\alpha_{2}}^{\dagger} \hat{a}_{\beta_{2}} - \sum_{\alpha_{3},\beta_{3}} (\hat{f}\hat{g})_{\alpha_{3}\beta_{3}} \hat{a}_{\alpha_{3}}^{\dagger} \hat{a}_{\beta_{3}}$$

$$= \sum_{\alpha_{1},\beta_{1},\alpha_{2},\beta_{2}} f_{\alpha_{1}\beta_{1}} g_{\alpha_{2}\beta_{2}} \hat{a}_{\alpha_{1}}^{\dagger} (\eta \hat{a}_{\alpha_{2}}^{\dagger} \hat{a}_{\beta_{1}} + \delta_{\alpha_{2}\beta_{1}}) \hat{a}_{\beta_{2}} - \sum_{\alpha_{3},\beta_{3}} (\hat{f}\hat{g})_{\alpha_{3}\beta_{3}} \hat{a}_{\alpha_{3}}^{\dagger} \hat{a}_{\beta_{3}}$$

$$= \sum_{\alpha_{1},\beta_{1},\alpha_{2},\beta_{2}} f_{\alpha_{1}\beta_{1}} g_{\alpha_{2}\beta_{2}} \eta \hat{a}_{\alpha_{1}}^{\dagger} \hat{a}_{\alpha_{2}}^{\dagger} \hat{a}_{\beta_{1}} \hat{a}_{\beta_{2}} + \delta_{\alpha_{2}\beta_{1}} f_{\alpha_{1}\beta_{1}} g_{\alpha_{2}\beta_{2}} \hat{a}_{\alpha_{1}}^{\dagger} \hat{a}_{\beta_{2}} - \sum_{\alpha_{3},\beta_{3}} (\hat{f}\hat{g})_{\alpha_{3}\beta_{3}} \hat{a}_{\alpha_{3}}^{\dagger} \hat{a}_{\beta_{3}}$$

$$= \sum_{\alpha_{1},\beta_{1},\alpha_{2},\beta_{2}} f_{\alpha_{1}\beta_{1}} g_{\alpha_{2}\beta_{2}} \hat{a}_{\alpha_{1}}^{\dagger} \hat{a}_{\alpha_{2}}^{\dagger} \hat{a}_{\beta_{2}} \hat{a}_{\beta_{1}} + \delta_{\alpha_{2}\beta_{1}} f_{\alpha_{1}\beta_{1}} g_{\alpha_{2}\beta_{2}} \hat{a}_{\alpha_{1}}^{\dagger} \hat{a}_{\beta_{2}} - \sum_{\alpha_{3},\beta_{3}} (\hat{f}\hat{g})_{\alpha_{3}\beta_{3}} \hat{a}_{\alpha_{3}}^{\dagger} \hat{a}_{\beta_{3}}$$

$$= \sum_{\alpha_{1},\beta_{1},\alpha_{2},\beta_{2}} f_{\alpha_{1}\beta_{1}} g_{\alpha_{2}\beta_{2}} \hat{a}_{\alpha_{1}}^{\dagger} \hat{a}_{\alpha_{2}}^{\dagger} \hat{a}_{\beta_{2}} \hat{a}_{\beta_{1}} + \delta_{\alpha_{2}\beta_{1}} f_{\alpha_{1}\beta_{1}} g_{\alpha_{2}\beta_{2}} \hat{a}_{\alpha_{1}}^{\dagger} \hat{a}_{\beta_{2}} - \sum_{\alpha_{3},\beta_{3}} (\hat{f}\hat{g})_{\alpha_{3}\beta_{3}} \hat{a}_{\alpha_{3}}^{\dagger} \hat{a}_{\beta_{3}}.$$

$$= \sum_{\alpha_{1},\beta_{1},\alpha_{2},\beta_{2}} f_{\alpha_{1}\beta_{1}} g_{\alpha_{2}\beta_{2}} \hat{a}_{\alpha_{1}}^{\dagger} \hat{a}_{\alpha_{2}}^{\dagger} \hat{a}_{\beta_{2}} \hat{a}_{\beta_{1}} + f_{\alpha_{1}\alpha_{2}} g_{\alpha_{2}\beta_{2}} \hat{a}_{\alpha_{1}}^{\dagger} \hat{a}_{\beta_{2}} - \sum_{\alpha_{3},\beta_{3}} (\hat{f}\hat{g})_{\alpha_{3}\beta_{3}} \hat{a}_{\alpha_{3}}^{\dagger} \hat{a}_{\beta_{3}}.$$

$$= \sum_{\alpha_{1},\beta_{1},\alpha_{2},\beta_{2}} f_{\alpha_{1}\beta_{1}} g_{\alpha_{2}\beta_{2}} \hat{a}_{\alpha_{1}}^{\dagger} \hat{a}_{\alpha_{2}} \hat{a}_{\beta_{2}} \hat{a}_{\beta_{1}} + f_{\alpha_{1}\alpha_{2}} g_{\alpha_{2}\beta_{2}} \hat{a}_{\alpha_{1}}^{\dagger} \hat{a}_{\beta_{2}} - \sum_{\alpha_{3},\beta_{3}} (\hat{f}\hat{g})_{\alpha_{3}\beta_{3}} \hat{a}_{\alpha_{3}}^{\dagger} \hat{a}_{\beta_{3}}.$$

$$= \sum_{\alpha_{1},\beta_{1},\alpha_{2},\beta_{2}} f_{\alpha_{1}\beta_{1}} g_{$$

That was a lot, but we can reduce this expression by realizing that

$$\sum_{\alpha_{1},\alpha_{2},\beta_{2}} f_{\alpha_{1}\alpha_{2}} g_{\alpha_{2}\beta_{2}} \hat{a}_{\alpha_{1}}^{\dagger} \hat{a}_{\beta_{2}} = \sum_{\alpha_{1},\alpha_{2},\beta_{2}} \langle \phi_{\alpha_{1}} | \hat{f} | \phi_{\alpha_{2}} \rangle \langle \phi_{\alpha_{2}} | \hat{g} | \phi_{\beta_{2}} \rangle \hat{a}_{\alpha_{1}}^{\dagger} \hat{a}_{\beta_{2}}$$

$$= \sum_{\alpha_{1},\beta_{2}} \langle \phi_{\alpha_{1}} | \hat{f} \hat{g} | \phi_{\beta_{2}} \rangle \hat{a}_{\alpha_{1}}^{\dagger} \hat{a}_{\beta_{2}} = \sum_{\alpha_{1},\beta_{2}} (fg)_{\alpha_{1}\beta_{2}} \hat{a}_{\alpha_{1}}^{\dagger} \hat{a}_{\beta_{2}}. \tag{1.112}$$

Using this, we may cancel the second and the last term of equation (1.111), and substitute all back into (1.109) to finally obtain

$$\hat{W} = \frac{1}{2} \sum_{ij} C_{i,j} \sum_{\alpha_1,\beta_1,\alpha_2,\beta_2} f^i_{\alpha_1\beta_1} g^j_{\alpha_2\beta_2} \hat{a}^{\dagger}_{\alpha_1} \hat{a}^{\dagger}_{\alpha_2} \hat{a}_{\beta_2} \hat{a}_{\beta_1}.$$
(1.113)

We may still make further simplification, by considering the canonical matrix element

$$W_{\alpha_1 \alpha_2 \beta_1 \beta_2} = {}_{q} \langle \phi_{\alpha_1} | {}_{q'} \langle \phi_{\alpha_2} | \hat{q}_{qq'} | \phi_{\beta_1} \rangle_{q} | \phi_{\beta_2} \rangle_{q'}, \qquad (1.114)$$

and expanding  $\hat{q}_{qq'}$ ,

$$W_{\alpha_{1}\alpha_{2}\beta_{1}\beta_{2}} = \sum_{i,j} C_{ij} \langle \phi_{\alpha_{1}} | \hat{f}_{q}^{i} | \phi_{\beta_{1}} \rangle \langle \phi_{\alpha_{2}} | \hat{g}_{q'}^{j} | \phi_{\beta_{2}} \rangle = \sum_{i,j} C_{ij} f_{\alpha_{1}\beta_{1}}^{i} g_{\alpha_{2}\beta_{2}}^{j}.$$
(1.115)

Inserting this in the expression for the two-body operator,

$$\hat{W} = \frac{1}{2} \sum_{\alpha_1, \beta_1, \alpha_2, \beta_2} W_{\alpha_1 \alpha_2 \beta_1 \beta_2} \hat{a}_{\alpha_1}^{\dagger} \hat{a}_{\alpha_2}^{\dagger} \hat{a}_{\beta_2} \hat{a}_{\beta_1}. \tag{1.116}$$

This is the final expression for the two-body operator in the second quantized form. The action of such is to annihilate one particle from each state  $|\phi_{\alpha_1}\rangle$  and  $|\phi_{\alpha_2}\rangle$ , and then create one particle in each state  $|\phi_{\beta_1}\rangle$  and  $|\phi_{\beta_2}\rangle$ . The matrix element  $W_{\alpha_1\alpha_2\beta_1\beta_2}$ , represented in the two-particle sector of Fock space, indicates the amplitude associated with this transition of states. We may also write it in the x-representation as

$$\langle \boldsymbol{x}_1' | \langle \boldsymbol{x}_2' | \hat{W} | \boldsymbol{x}_1 \rangle | \boldsymbol{x}_2 \rangle$$
. (1.117)

A good example is the interaction between two particles, which is usually local with respect to the coordinates of the pair of particles,

$$\langle \boldsymbol{x}_1' | \langle \boldsymbol{x}_2' | \hat{W} | \boldsymbol{x}_1 \rangle | \boldsymbol{x}_2 \rangle = \delta(\boldsymbol{x}_1, \boldsymbol{x}_1') \delta(\boldsymbol{x}_2, \boldsymbol{x}_2') w(\boldsymbol{x}_1, \boldsymbol{x}_2).$$
 (1.118)

The function  $w(\boldsymbol{x}_1, \boldsymbol{x}_2)$  has to be symmetric and real, as the operator  $\hat{W}$  is hermitian. If the interaction is spin-independent, we may write  $w(\boldsymbol{x}_1, \boldsymbol{x}_2) = w(\boldsymbol{r}_1, \boldsymbol{r}_2)$ , e.g. in the very important case of the Coulomb interaction. Coulomb force is also Galilei invariant, i.e.,

$$w(\mathbf{r}_1, \mathbf{r}_2) = w(\mathbf{r}_1 - \mathbf{r}_2). \tag{1.119}$$

The  $\alpha$ -representation may be obtained through the completeness relation,

$$\langle \phi_{\beta_1} | \langle \phi_{\beta_2} | \hat{W} | \phi_{\alpha_1} \rangle | \phi_{\alpha_2} \rangle =$$

$$= \int d\mathbf{x}_1' d\mathbf{x}_2' d\mathbf{x}_1 d\mathbf{x}_2 \langle \phi_{\beta_1} | \langle \phi_{\beta_2} | \mathbf{x}_1' \rangle | \mathbf{x}_2' \rangle \langle \mathbf{x}_1' | \langle \mathbf{x}_2' | \hat{W} | \mathbf{x}_1 \rangle | \mathbf{x}_2 \rangle \langle \mathbf{x}_1 | \langle \mathbf{x}_2 | \phi_{\alpha_1} \rangle | \phi_{\alpha_2} \rangle, \quad (1.120)$$
which, if being local,

$$\langle \phi_{\alpha_1} | \langle \phi_{\alpha_2} | \hat{W} | \phi_{\beta_1} \rangle | \phi_{\beta_2} \rangle = \int d\boldsymbol{x}_1' d\boldsymbol{x}_2' d\boldsymbol{x}_1 d\boldsymbol{x}_2 \phi_{\beta_1}^*(\boldsymbol{x}_1) \phi_{\beta_2}^*(\boldsymbol{x}_2) \hat{W} \phi_{\alpha_1}(\boldsymbol{x}_1) \phi_{\alpha_2}(\boldsymbol{x}_2). \quad (1.121)$$

The matrix elements must satisfy the symmetry relations:

$$W_{\alpha_1 \alpha_2 \beta_1 \beta_2} = W_{\alpha_2 \alpha_1 \beta_2 \beta_1} = W_{\beta_1 \beta_2 \alpha_1 \alpha_2}^*. \tag{1.122}$$

For fermionic particles, the matrix elements still inherit the antisymmetric relation  $W_{\alpha_1\alpha_2\beta_1\beta_2} = -W_{\alpha_2\alpha_1\beta_1\beta_2}$ . The action of two-body operators on antisymmetric two-particle states can, once again, be found with aid from the completeness relation,

$$\hat{W} |\phi_{\alpha_{1}}\phi_{\alpha_{2}}\rangle$$

$$= \frac{1}{2!} \sum_{\beta_{1},\beta_{2}} |\phi_{\beta_{1}}\phi_{\beta_{2}}\rangle \langle \phi_{\beta_{1}}\phi_{\beta_{2}}| \hat{W} |\phi_{\alpha_{1}}\phi_{\alpha_{2}}\rangle = \frac{1}{2} \sum_{\beta_{1},\beta_{2}} \langle \phi_{\beta_{1}}\phi_{\beta_{2}}| \hat{W} |\phi_{\alpha_{1}}\phi_{\alpha_{2}}\rangle |\phi_{\beta_{1}}\phi_{\beta_{2}}\rangle, \quad (1.123)$$

where we must be careful with the antisymmetric matrix element  $\langle \phi_{\beta_1} \phi_{\beta_2} | \hat{W} | \phi_{\alpha_1} \phi_{\alpha_2} \rangle$ , which can be expressed in terms of the canonical matrix elements,

$$\langle \phi_{\beta_{1}}\phi_{\beta_{2}}|\hat{W}|\phi_{\alpha_{1}}\phi_{\alpha_{2}}\rangle = \frac{1}{2!}(\langle \phi_{\beta_{1}}|\langle \phi_{\beta_{2}}|-\langle \phi_{\beta_{2}}|\langle \phi_{\beta_{1}}|)\hat{W}(|\phi_{\alpha_{1}}\rangle|\phi_{\alpha_{2}}\rangle - |\phi_{\alpha_{2}}\rangle|\phi_{\alpha_{1}}\rangle)$$

$$= \langle \phi_{\beta_{1}}|\langle \phi_{\beta_{2}}|\hat{W}|\phi_{\alpha_{1}}\rangle|\phi_{\alpha_{2}}\rangle - \langle \phi_{\beta_{2}}|\langle \phi_{\beta_{1}}|)\hat{W}|\phi_{\alpha_{2}}\rangle|\phi_{\alpha_{1}}\rangle$$

$$= W_{\beta_{1}\beta_{2}\alpha_{1}\alpha_{2}} - W_{\beta_{2}\beta_{1}\alpha_{2}\alpha_{1}} = 2W_{\beta_{1}\beta_{2}\alpha_{1}\alpha_{2}}. \quad (1.124)$$

Inserting this relation in (1.123), the action on an antisymmetric two-particle becomes

$$\hat{W} |\phi_{\alpha_1} \phi_{\alpha_2}\rangle = \sum_{\beta_1, \beta_2} W_{\beta_1 \beta_2 \alpha_1 \alpha_2} |\phi_{\beta_1} \phi_{\beta_2}\rangle.$$
(1.125)

The same conclusion is verified with the second quantization format (1.116),

$$\hat{W} |\phi_{\alpha_{1}}\phi_{\alpha_{2}}\rangle = \frac{1}{2} \sum_{\gamma_{1},\gamma_{2},\beta_{1},\beta_{2}} W_{\beta_{1}\beta_{2}\gamma_{1}\gamma_{2}} \hat{c}_{\beta_{1}}^{\dagger} \hat{c}_{\beta_{2}}^{\dagger} \hat{c}_{\gamma_{2}} \hat{c}_{\gamma_{1}} |\phi_{\alpha_{1}}\phi_{\alpha_{2}}\rangle 
= \frac{1}{2} \sum_{\gamma_{1},\gamma_{2},\beta_{1},\beta_{2}} W_{\beta_{1}\beta_{2}\gamma_{1}\gamma_{2}} \hat{c}_{\beta_{1}}^{\dagger} \hat{c}_{\beta_{2}}^{\dagger} \hat{c}_{\gamma_{2}} \hat{c}_{\gamma_{1}} \hat{c}_{\alpha_{1}}^{\dagger} \hat{c}_{\alpha_{2}}^{\dagger} |0\rangle 
= \frac{1}{2} \sum_{\gamma_{1},\gamma_{2},\beta_{1},\beta_{2}} W_{\beta_{1}\beta_{2}\gamma_{1}\gamma_{2}} \hat{c}_{\beta_{1}}^{\dagger} \hat{c}_{\beta_{2}}^{\dagger} (\delta_{\alpha_{1}\gamma_{1}}\delta_{\alpha_{2}\gamma_{2}} - \delta_{\alpha_{1}\gamma_{2}}\delta_{\alpha_{2}\gamma_{1}}) |0\rangle 
= \sum_{\beta_{1},\beta_{2}} W_{\beta_{1}\beta_{2}\alpha_{1}\alpha_{2}} \hat{c}_{\beta_{1}}^{\dagger} \hat{c}_{\beta_{2}}^{\dagger} |0\rangle = \sum_{\beta_{1},\beta_{2}} W_{\beta_{1}\beta_{2}\alpha_{1}\alpha_{2}} |\phi_{\beta_{1}}\phi_{\beta_{2}}\rangle.$$
(1.126)

The second quantized form of a two-particle operator in the x-representation is obtained with aid of the completeness relation. We also consider locality (1.118), to simplify

$$\begin{split} \hat{W} &= \frac{1}{2} \sum_{\alpha_1,\beta_1,\alpha_2,\beta_2} W_{\alpha_1\alpha_2\beta_1\beta_2} \hat{a}_{\alpha_1}^{\dagger} \hat{a}_{\alpha_2}^{\dagger} \hat{a}_{\beta_2} \hat{a}_{\beta_1} \\ &= \frac{1}{2} \int d\boldsymbol{x}_1 d\boldsymbol{x}_2 \sum_{\alpha_1,\beta_1,\alpha_2,\beta_2} \left\langle \phi_{\alpha_1} | \left\langle \phi_{\alpha_2} | \boldsymbol{x}_1 \right\rangle | \boldsymbol{x}_2 \right\rangle w(\boldsymbol{x}_1,\boldsymbol{x}_2) \left\langle \boldsymbol{x}_1 | \left\langle \boldsymbol{x}_2 | \phi_{\beta_1} \right\rangle | \phi_{\beta_2} \right\rangle \hat{a}_{\alpha_1}^{\dagger} \hat{a}_{\alpha_2}^{\dagger} \hat{a}_{\beta_2} \hat{a}_{\beta_1} \\ &= \frac{1}{2} \int d\boldsymbol{x}_1 d\boldsymbol{x}_2 \sum_{\alpha_1,\beta_1,\alpha_2,\beta_2} \phi_{\alpha_1}^*(\boldsymbol{x}_1) \phi_{\alpha_2}^*(\boldsymbol{x}_2) w(\boldsymbol{x}_1,\boldsymbol{x}_2) \phi_{\beta_1}(\boldsymbol{x}_1) \phi_{\beta_2}(\boldsymbol{x}_2) \hat{a}_{\alpha_1}^{\dagger} \hat{a}_{\alpha_2}^{\dagger} \hat{a}_{\beta_2} \hat{a}_{\beta_1} \\ \hat{W} &= \frac{1}{2} \int d\boldsymbol{x}_1 d\boldsymbol{x}_2 \sum_{\alpha_1,\beta_1,\alpha_2,\beta_2} \phi_{\alpha_1}^* \hat{a}_{\alpha_1}^{\dagger}(\boldsymbol{x}_1) \phi_{\alpha_2}^*(\boldsymbol{x}_2) \hat{a}_{\alpha_2}^{\dagger} w(\boldsymbol{x}_1,\boldsymbol{x}_2) \phi_{\beta_2}(\boldsymbol{x}_2) \hat{a}_{\beta_2} \phi_{\beta_1}(\boldsymbol{x}_1) \hat{a}_{\beta_1}, \end{split}$$

where in the last line we have ordered the terms so that the transformation of basis (1.78) becomes clear, leading to the final form as: (ENGEL; DREIZLER, 2011)

$$\hat{W} = \frac{1}{2} \int d\boldsymbol{x}_1 d\boldsymbol{x}_2 \hat{\Psi}^{\dagger}(\boldsymbol{x}_1) \hat{\Psi}^{\dagger}(\boldsymbol{x}_2) w(\boldsymbol{x}_1, \boldsymbol{x}_2) \hat{\Psi}(\boldsymbol{x}_2) \hat{\Psi}(\boldsymbol{x}_1). \tag{1.127}$$

# 2 Solid State

#### 2.1 Chemical Introduction

Before we get deeper into systems of many atoms, we shall first discuss the atom. From our knowledge of quantum mechanics, the maximum information of an electron in an atom is described by states containing four quantum numbers  $|n \ l \ m_l \ m_s\rangle$ . The first three are information concerning the probabilistic region where the electron may be found, being the state  $|n \ l \ m_l\rangle$  an atomic orbital.

In an atomic orbital, the integer n is called principal, as it is responsible for the main contribution of the energy level of the electron. The principal quantum number obeys the relation:  $n \geq 1$ . The azimuthal quantum number l is information about the angular momentum of the electron, having its value confined in the relation  $0 \leq l \leq (n-1)$ , being the values 0, 1, 2, 3 commonly called s, p, d, f orbitals, respectively. Each orbital is also restricted to the relation  $-l \leq m_l \leq l$ , being  $m_l$  the magnetic quantum number, which gives the angular momentum projection vector over some axis, usually z. As e.g., a possible electron state  $|100\rangle$  is called 1s orbital, and  $|210\rangle$  is 2p; the latter being energetically degenerated for the three possible  $m_l$  numbers,  $2p_x$ ,  $2p_y$ ,  $2p_z$ . Each atomic orbital can contain two antiparallel electrons, i.e., with opposite spin quantum numbers. The spin quantum number  $m_s$  obeys the relation  $-m_s \leq s \leq -m_s$ , being  $s = \frac{1}{2}$  the total spin of an electron. Then, each possible electron state is called a spin-orbital, which is a pure state containing maximum information about the electron.

The electrons in an atom will occupy the lowest available energy states, but they might be excited to higher states if they absorb the correspondent energy. The occupied states with greater value of n are called valence states, as they represent the most external orbitals of the atom, and all states above those are called excited states. As e.g., the six electrons in the carbon atom are illustrated in figure (1):

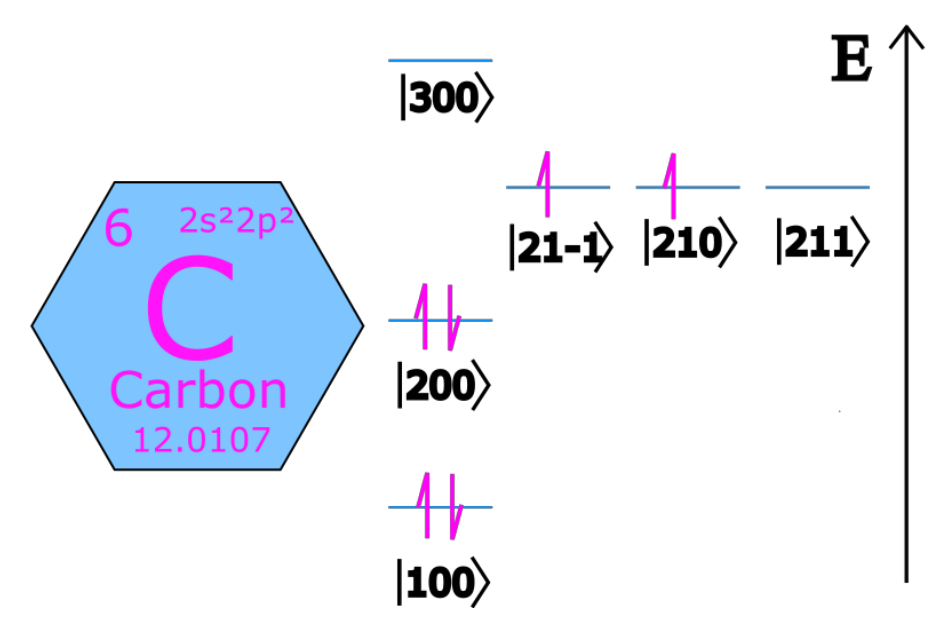


Figure 1 – Electron states in carbon atom. Valence electrons are those with n=2. All states with n>2 are excited states.

So far, we discussed electron states in a single atom, but when a system considers a plural of atoms in a short distance, these electron states might overlap and reshape into orbitals around the whole set of atoms. These wave function interactions might be in phase or out of phase. In the former, we have a symmetric linear combination of atomic orbitals called bonding molecular orbitals, while the latter is an antisymmetric linear combination of atomic orbitals, or antibonding molecular orbitals. A simple example of the  $H_2$  molecule is illustrated in figure (2):

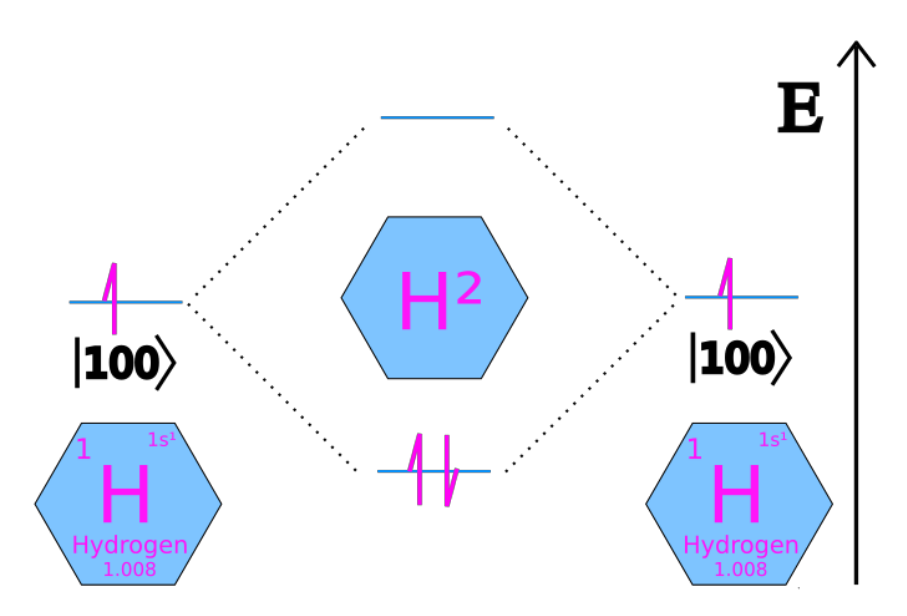


Figure 2 – H<sub>2</sub> molecule energy states, constructed from hydrogen valence states. Both electrons occupies the bonding state, while the antibonding state is left empty.

In the bonding states, the electron density (in the form of 1.87) is strongly localized in the region between the nuclei, which gives rise to chemical bonds; these are the lower energy states of the electrons. The antibonding states are of higher energy, as the region between the nuclei is of low electron density and the outside region is high, resulting in low localization of the electron; that is the opposite of a chemical bond. The difference in electronegativity of the atoms is the cause of polarization in the covalent bond. If the difference is too big, it is the case of an ionic bond, where we might consider it as if one atom is taking one electron from another.

In Figure 2 is not obvious, but in bigger atoms, where the core atomic orbitals are much tighter into the nuclei, we consider only the valence states for the constitution of molecular orbitals. The number of initial (valence) atomic orbitals is equal to the number of resulting molecular orbitals, so if we increase the number of atoms in the system, extra states will appear as combinations of bonding and antibonding states, and those are energetically placed between the completely antibonding and completely bonding states. If the number of atoms in the system is very large, as in crystals, the discrete energy states become a set of continuous energy regions which we call energy bands. All valence orbitals of each atom will interact, thus we may find a set of energy bands as a result.

In molecular orbitals, just as in single atoms, electrons can be excited from lowenergy states into higher states if an energy equivalent to the gap between states is absorbed from some source. That is a good reason for investing in solar energy, and for using sunscreen before sunlight breaks the bonds of your molecules. In case of energy bands, if the electrons completely fill a band, there is an energy gap between the highest occupied state and the lowest unoccupied state, so the material is an insulator. If the highest occupied state is inside an energy band, even small temperatures might cause electrons to go into excited states, where they become unlocalized, and able to transport charge; that is a conductor, i.e., a metal. A semiconductor is simply an insulator with a gap small enough; the line is not well defined, or is defined by practical purposes. The unlocalized electrons in metals are shared between all atoms in the structure, giving rise to the concept of a "sea of electrons", which is essentially a shared electron density from where all the positively charged nuclei are bound; these are the metallic bonds.

Figure 1 shows how electrons are distributed in the carbon atom, however, when bonding is to occur, the valence states might combine in different forms which we call hybridized orbitals. Carbon might be hybridized in sp,  $sp^2$  and  $sp^3$  forms, but we shall only discuss the  $sp^3$  form for the scope of this study. Figure 3 illustrates the energy levels in this configuration.

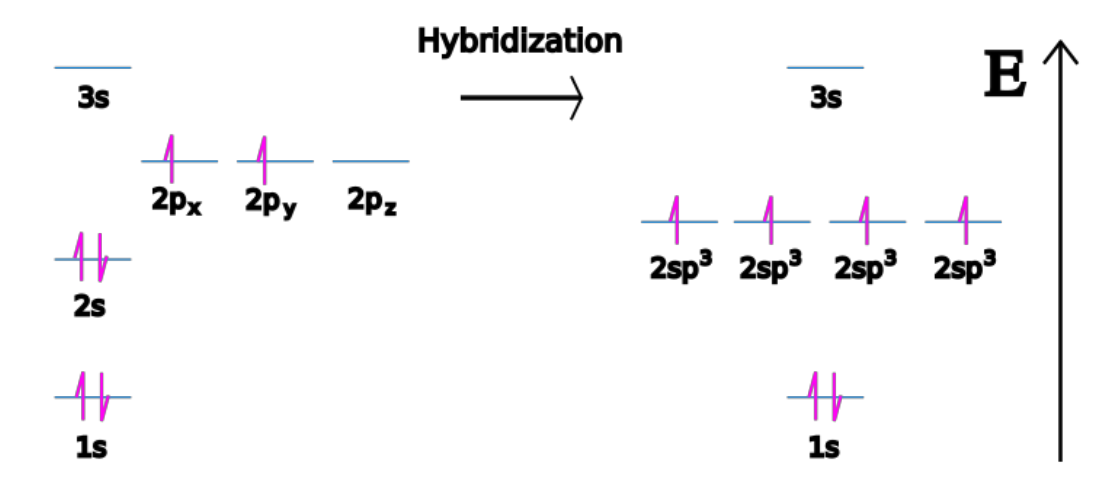


Figure 3 – Electron states in sp<sup>3</sup> hybridization of carbon atom.

In  $sp^3$  hybridization, the s valence state is merged with all three p valence states, resulting in four degenerated  $sp^3$  orbitals. Since all four states are degenerated, the four chemical bonds are equidistant from one another by electron repulsion, giving rise to a tetrahedral geometry, illustrated in Figure 4. In general, the orbital's geometry will give rise to the geometry of the structure, which is the essence of crystals, which we are now in good position to discuss.

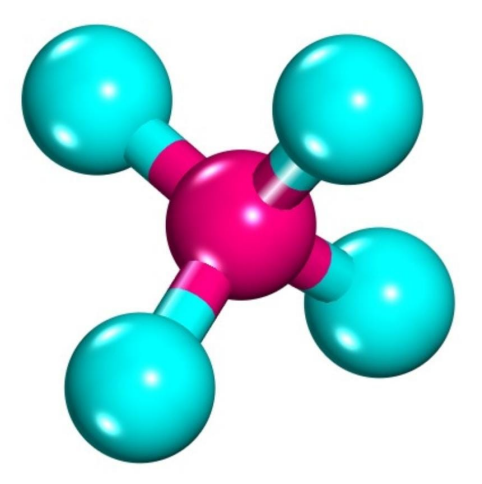


Figure 4 – Carbon atom (pink) in  $sp^3$  hybridization bonding with four atomic species (blue) in tetrahedral geometry. Illustration made in BIOVIA Materials Studio.

A deeper understanding of chemistry is unnecessary for this oversimplified introduction to the theory of solids, but it is left for reference (FLEMING, 2011).

2.2. Symmetry 55

## 2.2 Symmetry

The physical properties of matter depend not only on the constituent elements but also on the way these constituents organize themselves. When studying crystalline structures, we work with the periodic atomic organization that constitutes the crystal. To conceptualize this organization, we use the fundamental concepts of the lattice and the basis of the crystalline structure.

When characterizing physical objects, we use notions of symmetry to develop the fundamental concepts which we work with. The study of symmetries is necessary for the characterization of both the bases and the crystalline lattices.

An asymmetric element, such as the letter R, essentially has only one symmetry, a rotation of  $2\pi$ . Elements of this type are characterized by the number 1. A mirror symmetry, characterized by the letter m, reflects with regards to a line in the two-dimensional (2D) case or a plane in the three-dimensional (3D) case, where every part of the element has an image at the same distance from the mirror but on the opposite side. Rotation axes include symmetries in which the element is rotated by some angle around an axis. For a rotation of  $\pi$ , two rotations are necessary to return to the original position, thus, these are characterized by the number 2. Similarly, ternary axes  $(\frac{2\pi}{3})$  are characterized by the number 3, quaternary axes  $(\frac{\pi}{2})$  by the number 4, and hexagonal axes  $(\frac{\pi}{3})$  by the number 6.

The *glide* is a symmetry element characterized by the letter g, whose operation combines a mirror reflection with a translation in a certain direction.

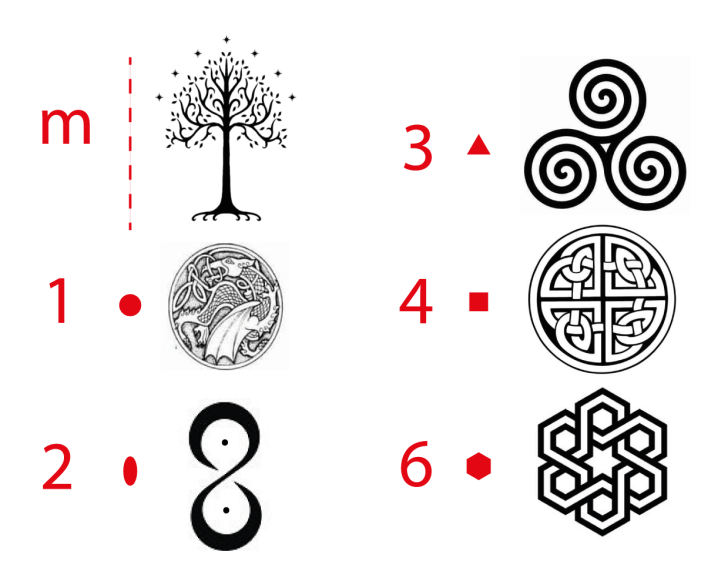


Figure 5 – Illustrations containing symmetries of the mirror type (m) or rotation axis  $C_n$  (n = 1, 2, ..., 6).

## 2.3 Crystalline Lattices

As redes de Bravais são definidas como o conjunto de pontos discretos que geram uma geometria periódica onde a vizinhança de cada ponto é idêntica. Podemos representar esta como o infinito conjunto de pontos representados pelo vetor de posição

$$r = n_1 a_1 + n_2 a_2 + n_3 a_3, \tag{2.1}$$

onde  $n_1, n_2$  e  $n_3$  são números inteiros arbitrários e  $\boldsymbol{a_1}, \boldsymbol{a_2}$  e  $\boldsymbol{a_3}$  são vetores não coplanares, chamados de vetores de base. Os vetores de base são ditos como os que geram a rede cristalina.

Em uma rede, a célula unitária é um volume de espaço contendo átomos, capaz de reproduzir por translação toda a estrutura cristalina do sólido, sem que haja sobreposições ou espaços vazios. Quando o volume da célula unitária é o mínimo possível, ela é denominada primitiva. (ASHCROFT et al., 1976)

Bravais lattices are defined as the set of discrete points that generate a periodic geometry where the neighborhood of each point is identical. This can be represented as an infinite set of points described by the position vector:

$$r = n_1 a_1 + n_2 a_2 + n_3 a_3, (2.2)$$

where  $n_1, n_2$ , and  $n_3$  are arbitrary integers, and  $a_1, a_2$ , and  $a_3$  are non-coplanar vectors, referred to as basis vectors. Basis vectors are known as those that generate the crystalline lattice.

In a crystal lattice, the unit cell is a volume of space containing atoms, capable of reproducing the entire crystalline structure of the solid through translation, without overlaps or voids. When the volume of the unit cell is minimized, it is called primitive. (ASHCROFT et al., 1976)

#### 2.3.1 Bravais Lattices

There are five types of planar lattices, each one characterized by an angle and the relation between the lattice vectors:

Oblique Lattice:  $|a_1| \neq |a_2|$ ,  $\gamma \neq \frac{\pi}{2}$ .

Rectangular Lattice, p (primitive) mode:  $|a_1| \neq |a_2|$ ,  $\gamma = \frac{\pi}{2}$ .

Rectangular Lattice, c (centered) mode:  $|a_1| \neq |a_2|$ ,  $\gamma \neq \frac{\pi}{2}$ .

Square Lattice, p mode:  $|\boldsymbol{a_1}| = |\boldsymbol{a_2}|, \ \gamma = \frac{\pi}{2}$ .

Hexagonal Lattice:  $|\boldsymbol{a_1}| = |\boldsymbol{a_2}|, \ \gamma = \frac{2\pi}{3}$ .

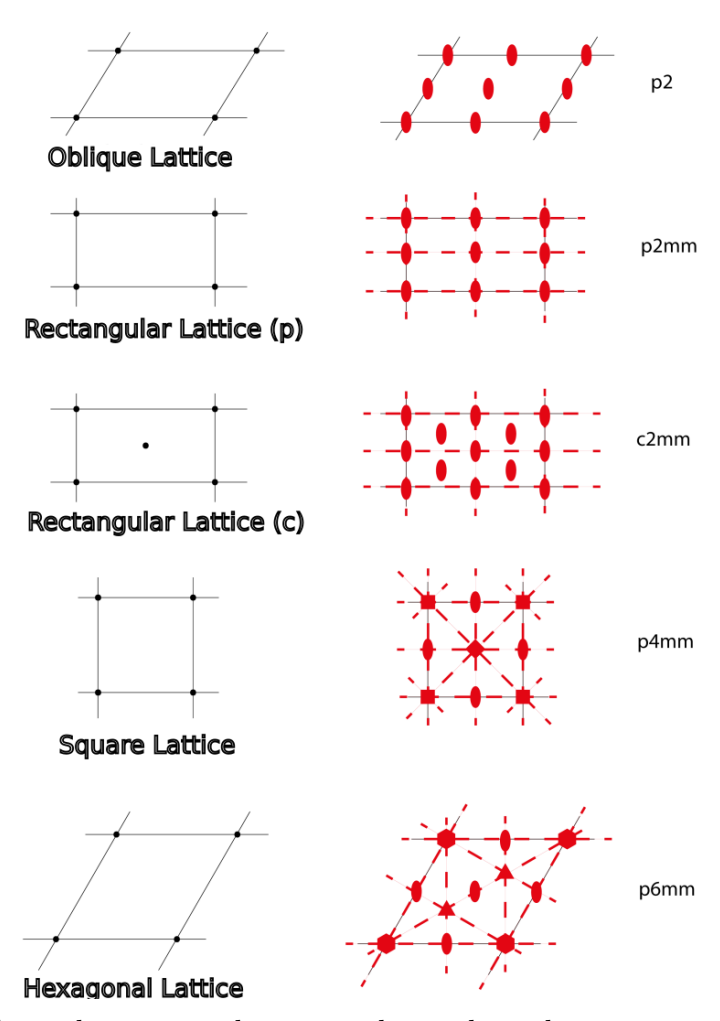


Figure 6 – The planar lattices, and next to them, their characterizations based on their respective symmetry elements.

To represent all fourteen 3D Bravais lattices, seven crystal systems are used, which may have multiple types. These are: Primitive (P), Base Centered (C), Body Centered (I) and Face Centered (F). To characterize each crystal system, we use the vectors  $\boldsymbol{a}, \boldsymbol{b}$ , and  $\boldsymbol{c}$ , which have between them the angles  $\alpha_{ab}, \alpha_{bc}$ , and  $\alpha_{ca}$ . These vectors are lattice

vectors in the case of type P lattices.

Triclinic System (P):  $|a| \neq |b| \neq |c|$ ,  $\alpha_{ab} \neq \alpha_{bc} \neq \alpha_{ca}$ 

Monoclinic System (P), (I):  $|\boldsymbol{a}| \neq |\boldsymbol{b}| \neq |\boldsymbol{c}|$ ,  $\alpha_{bc} = \alpha_{ca} = \frac{\pi}{2}$ ,  $\alpha_{ab} \neq \frac{\pi}{2}$ 

Orthorhombic System (P), (I), (C), (F):  $|\boldsymbol{a}| \neq |\boldsymbol{b}| \neq |\boldsymbol{c}|$ ,  $\alpha_{ab} = \alpha_{bc} = \alpha_{ca} = \frac{\pi}{2}$ 

Tetragonal System (P), (I):  $|a| = |b| \neq |c|$ ,  $\alpha_{ab} = \alpha_{bc} = \alpha_{ca} = \frac{\pi}{2}$ 

Trigonal System (P):  $|\boldsymbol{a}| = |\boldsymbol{b}| = |\boldsymbol{c}|, \ \alpha_{ab} = \alpha_{bc} = \alpha_{ca} < \frac{2\pi}{3}$ 

Cubic System (P), (I), (F):  $|\boldsymbol{a}| = |\boldsymbol{b}| = |\boldsymbol{c}|, \ \alpha_{ab} = \alpha_{bc} = \alpha_{ca} = \frac{\pi}{2}$ 

Tetragonal System (P), (I):  $|\boldsymbol{a}| = |\boldsymbol{b}| \neq |\boldsymbol{c}|, \ \alpha_{bc} = \alpha_{ca} = \frac{\pi}{2}, \ \alpha_{ab} = \frac{2\pi}{3}$ 

### 2.3.2 Lattice Planes and Crystalline Directions

The crystalline directions are characterized by indices [uvw], which correspond, in terms of the crystal axes, to the smallest integers proportional to any point contained in the direction vector. The vector representing this direction is written as:

$$\boldsymbol{r}_{uvw} = u\boldsymbol{a} + v\boldsymbol{b} + w\boldsymbol{c}. \tag{2.3}$$

The opposite direction of [uvw] is characterized as  $[\bar{u}\bar{v}\bar{w}]$ .

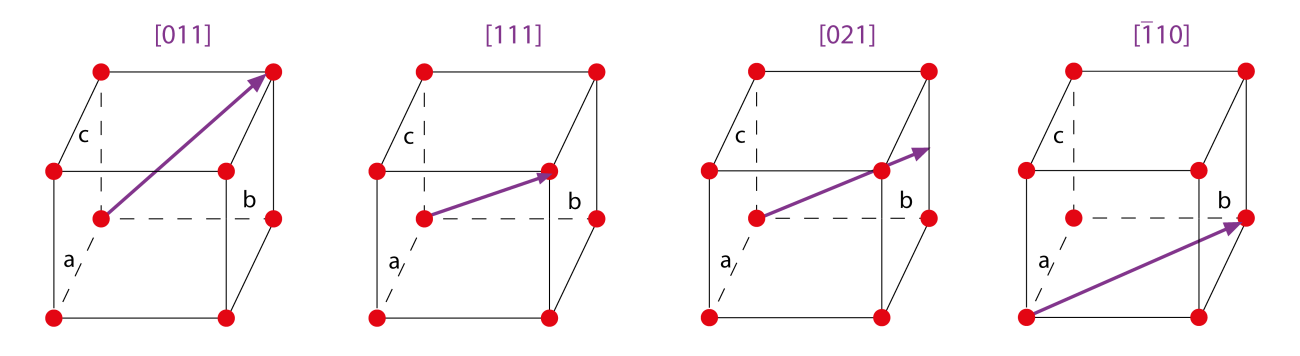


Figure 7 – Some examples of crystalline directions.

To characterize a plane, or a family of parallel and equidistant planes, we use a

2.4. Diffraction 59

similar index. This time, we determine the points where the plane intercepts the crystal axes and then find the set of smallest integers (hkl) that maintain the same proportion as the reciprocals of the intercepts. These indices are known as Miller Indices.

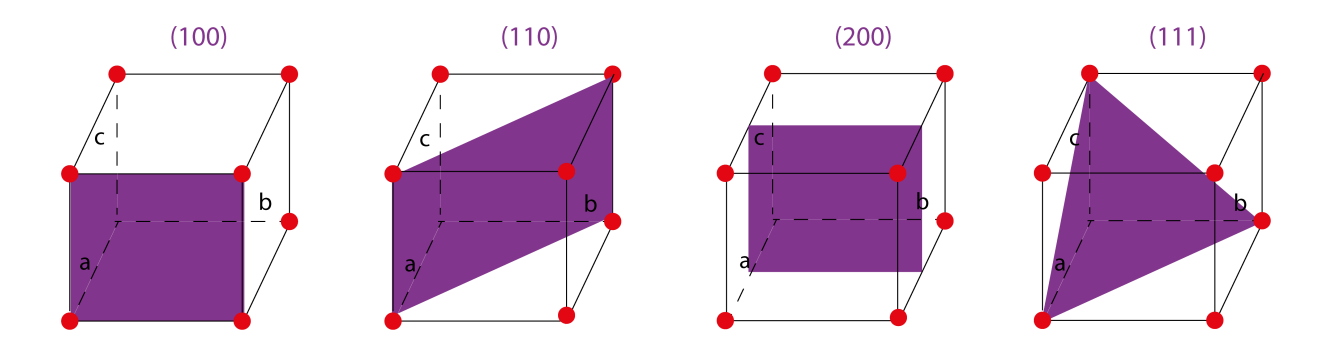


Figure 8 – Examples of crystalline planes.

We indicate the spacing between planes of the same family using the vector  $d_{hkl}$ .

### 2.4 Diffraction

The crystalline structure can be studied through the diffraction of photons, electrons, and neutrons. The behavior of diffraction will depend on the crystalline structure and the wavelength of the incident rays.

To understand the concept behind Bragg's law, we suppose that a fraction of the incident waves are reflected at an angle equal to the angle of incidence by each crystalline plane, spaced by  $d_{hkl}$ . The reflection caused by each crystalline plane has an optical path difference of  $2d_{hkl}\sin(\theta)$ , causing an interference in the reflected ray due to the wave vectors being in different phases. The diffracted rays are those whose wavelength satisfies Bragg's law, ensuring that the interference between the waves reflected by each plane is constructive, i.e., the optical path difference corresponds to a multiple of the wavelength. For this, we consider the wavelength  $\lambda \leq 2d_{hkl}$ , and the scattering of the rays is elastic, implying no energy loss. Using  $d_{hkl}$  simply as d, Bragg's law is expressed as: (KITTEL, 2004)

$$2d\sin\theta = n\lambda\tag{2.4}$$

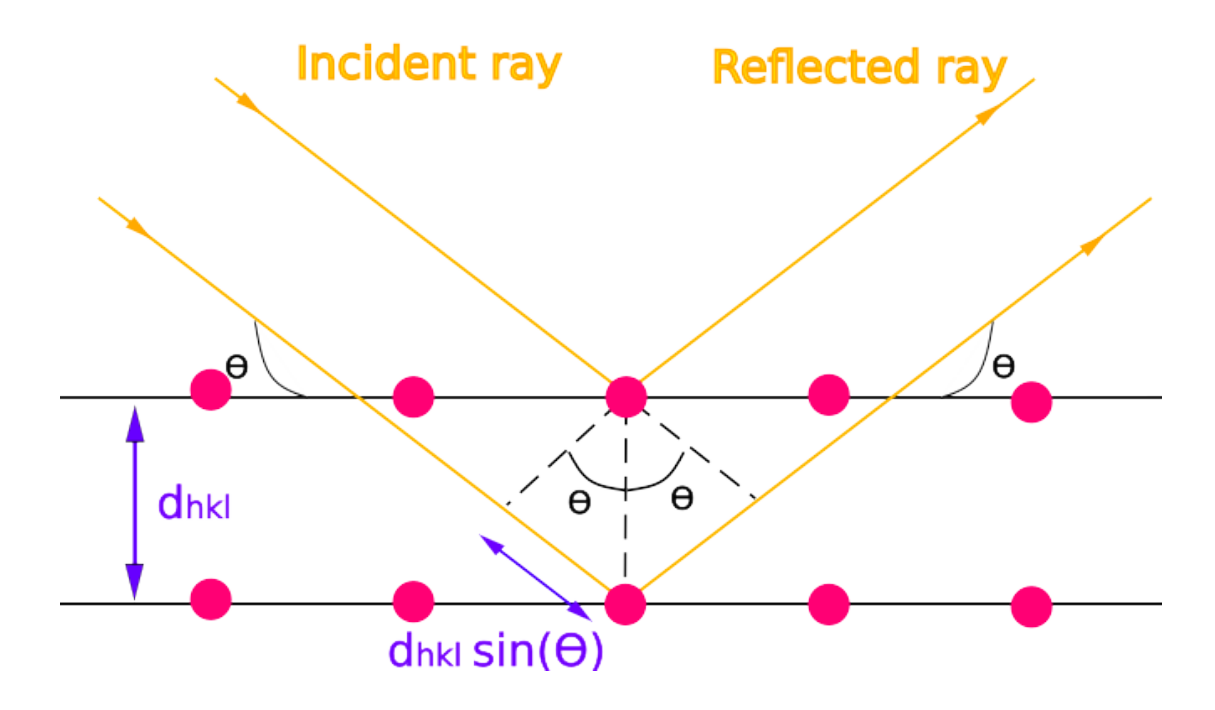


Figure 9 – Illustration showing the optical path difference in the process of crystalline diffraction.

If each plane were completely reflective, only one would suffice to reflect all radiation at all wavelengths. However, due to atomic spacing, only about  $10^{-3}$  to  $10^{-5}$  of the incident radiation is reflected by each plane, meaning that diffraction can include contributions from up to  $10^5$  planes of a perfect crystal. Bragg's law is a consequence of the periodicity of crystalline structures and is independent of the lattice or the elements composing the crystal. To perform a deeper analysis of the scattering intensity, it is necessary to consider the spatial distribution of electrons in the crystal cell.

## 2.5 Fourier Analysis

All physical properties of a perfect crystal must be invariant under lattice translations, these being characterized by a translation vector of the type  $\mathbf{l} = u_1 \mathbf{a_1} + u_2 \mathbf{a_2} + u_3 \mathbf{a_3}$ , where each  $u_i$  is an integer, and all  $\mathbf{a}_i$  being the lattice base vectors. As e.g., the electronic density at some position  $n(\mathbf{r})$  must be the same as  $n(\mathbf{r} + \mathbf{l})$ . Since we are dealing with periodic functions  $f(\mathbf{r}) = f(\mathbf{r} + \mathbf{l})$ , it is suggestive to investigate a Fourier analysis. We start with the one-dimensional case  $f(\mathbf{x})$ :

$$f(\mathbf{x}) = f_0 + \sum_{n>0} \left[ C_n \cos\left(n\frac{2\pi x}{a}\right) + S_n \sin\left(n\frac{2\pi x}{a}\right) \right], \tag{2.5}$$

where  $C_n$  and  $S_n$  are Fourier coefficients, and the factor  $\frac{2\pi}{a}$  is what guarantees the periodicity of the function  $f(\boldsymbol{x})$  with period a, as we can verify:

$$f(\boldsymbol{x}+\boldsymbol{a}) = f_0 + \sum_{n>0} \left[ C_n \cos\left(n\frac{2\pi(x+a)}{a}\right) + S_n \sin\left(n\frac{2\pi(x+a)}{a}\right) \right]$$

$$f(\boldsymbol{x}+\boldsymbol{a}) = f_0 + \sum_{n>0} \left[ C_n \cos\left(n\frac{2\pi x}{a} + 2\pi n\right) + S_n \sin\left(n\frac{2\pi x}{a} + 2\pi n\right) \right]$$

$$f(\boldsymbol{x}+\boldsymbol{a}) = f_0 + \sum_{n>0} \left[ C_n \cos\left(n\frac{2\pi x}{a}\right) + S_n \sin\left(n\frac{2\pi x}{a}\right) \right] = f(\boldsymbol{x}).$$
(2.6)

The space that contains the points allowed in the Fourier expansion consistent with the lattice periodicity is such that contains the points  $n\frac{2\pi}{a}$ . In this one-dimensional example, these points distribute themselves into a line, distanced of  $\frac{2\pi}{a}$ . Not far bellow, we shall generalize this in three dimensions, where these points will also form a lattice which depends inversely on the lattice vectors  $\mathbf{a}_i$ . We call this new pattern as the reciprocal lattice, and it will be better described latter using the new defined vectors  $\mathbf{b}_i$ , but first, we must finish the Fourier analysis.

It is convenient to express equation (2.5) in a more compact form, using  $g = \frac{2\pi n}{a}$ ,

$$f(x) = \sum_{n} A_n e^{igx}, \qquad (2.7)$$

being the sum over all integers n being positive, negative, or zero. The  $A_n$  coefficients are complex numbers that obey  $A_n = A_{-n}^*$ , in such a way that the sum over all n is a real number. For generalization in three dimensions, we consider  $g_i = \frac{2\pi n_i}{a_i}$ , so

$$f(\mathbf{r}) = \sum_{g_1, g_2, g_3} A_{g_1 g_2 g_3} e^{i(g_1 x_1 + g_2 x_2 + g_3 x_3)}, \tag{2.8}$$

that can be simplified as

$$f(\mathbf{r}) = \sum_{G} A_G e^{i\mathbf{G}\cdot\mathbf{r}}.$$
 (2.9)

As intended, this expression respects the translational symmetry of the crystal, as we can verify in

$$f(\mathbf{r} + \mathbf{l}) = \sum_{G} A_{G} e^{i\mathbf{G} \cdot (\mathbf{r} + \mathbf{l})}$$
(2.10)

$$= \sum_{G} A_{G} e^{i\mathbf{G}\cdot\mathbf{r}} e^{i\mathbf{G}\cdot\mathbf{l}} \tag{2.11}$$

$$= \sum_{G} A_G e^{i\mathbf{G}\cdot\mathbf{r}} e^{i2\pi \frac{n_i}{a_i} l_i a_i} \tag{2.12}$$

$$= \sum_{G} A_G e^{iG \cdot r} e^{i2\pi N}, \qquad (2.13)$$

where N is an integer, thus  $f(\mathbf{r}+\mathbf{l}) = f(\mathbf{r})$ . It is useful to keep in mind the relation we just used,  $e^{i\mathbf{G}\cdot\mathbf{l}} = 1$ .

Not to forget the Fourier coefficients, which can be obtained as integrals over the unity cell volume ((ZIMAN, 1972)),

$$A_G = \frac{1}{V_{uc}} \int_{cell} d^3 \mathbf{r} f(\mathbf{r}) e^{-i\mathbf{G}\cdot\mathbf{r}}.$$
 (2.14)

The Fourier analysis is now over, however, we must see in more depth how to define reciprocal lattice vectors G, which are of great importance for the crystal description in Fourier space, or as we shall call it, reciprocal space.

### 2.6 Reciprocal Lattice

In this section, the relationship between reciprocal space and wave vectors  $\mathbf{k}$  will become clear, with the space of wave vectors being the space of momentum vectors. Heisenberg's uncertainty principle is a beautiful expression of the duality that exists between momenta and positions, just like the duality between wave and particle. The reciprocal space corresponds to a wave representation of objects, dual to its corpuscular representation.

### 2.6.1 Vectors in the Reciprocal Lattice

The construction of the basis vectors of the reciprocal lattice is defined as (KIT-TEL, 2004):

$$\boldsymbol{b_1} = 2\pi \frac{\boldsymbol{a_2} \times \boldsymbol{a_3}}{V} \qquad \boldsymbol{b_2} = 2\pi \frac{\boldsymbol{a_3} \times \boldsymbol{a_1}}{V} \qquad \boldsymbol{b_3} = 2\pi \frac{\boldsymbol{a_1} \times \boldsymbol{a_2}}{V}, \tag{2.15}$$

where  $V = a_1 \cdot (a_2 \times a_3)$  is the volume of the unit cell. An equivalent and generalized definition for an arbitrary number of dimensions is expressed as

$$\mathbf{a}_i \cdot \mathbf{b}j = 2\pi \delta ij. \tag{2.16}$$

In this way, it is possible to map any point in the reciprocal lattice through the vector:

$$G = v_1 b_1 + v_2 b_2 + v_3 b_3, (2.17)$$

where  $v_i$  is an integer. With this we can verify the invariance of equation (2.9) under a translation  $T = u_1 \mathbf{a_1} + u_2 \mathbf{a_2} + u_3 \mathbf{a_3}$ ,

$$f(\mathbf{r} + \mathbf{T}) = \sum_{G} A_{G} e^{i\mathbf{G} \cdot (\mathbf{r} + \mathbf{T})}$$

$$= \sum_{G} A_{G} e^{i\mathbf{G} \cdot \mathbf{r}} e^{i\mathbf{G} \cdot \mathbf{T}}$$

$$= \sum_{G} A_{G} e^{i\mathbf{G} \cdot \mathbf{r}} e^{i(v_{1}b_{1} + v_{2}b_{2} + v_{3}b_{3}) \cdot (u_{1}a_{1} + u_{2}a_{2} + u_{3}a_{3})}$$

$$= \sum_{G} A_{G} e^{i\mathbf{G} \cdot \mathbf{r}} e^{i2\pi(v_{1}u_{1} + v_{2}u_{2} + v_{3}u_{3})}$$

$$= \sum_{G} A_{G} e^{i\mathbf{G} \cdot \mathbf{r}} = f(\mathbf{r}).$$

$$(2.18)$$

The step taken for the last line occurs because all the terms  $u_i$  and  $v_i$  are integers, so any combination of these will still result in a multiple of  $2\pi$  within the exponential. Thus, we verify that the mapping of the reciprocal lattice through the vector  $\mathbf{G}$  is equivalent to a mapping of the Fourier space in a crystalline solid.

As an example for the construction of reciprocal lattice vectors from the vectors of the real lattice, we now follow this process for the 2D hexagonal lattice of some  $M_2X$  material in Cartesian coordinates.

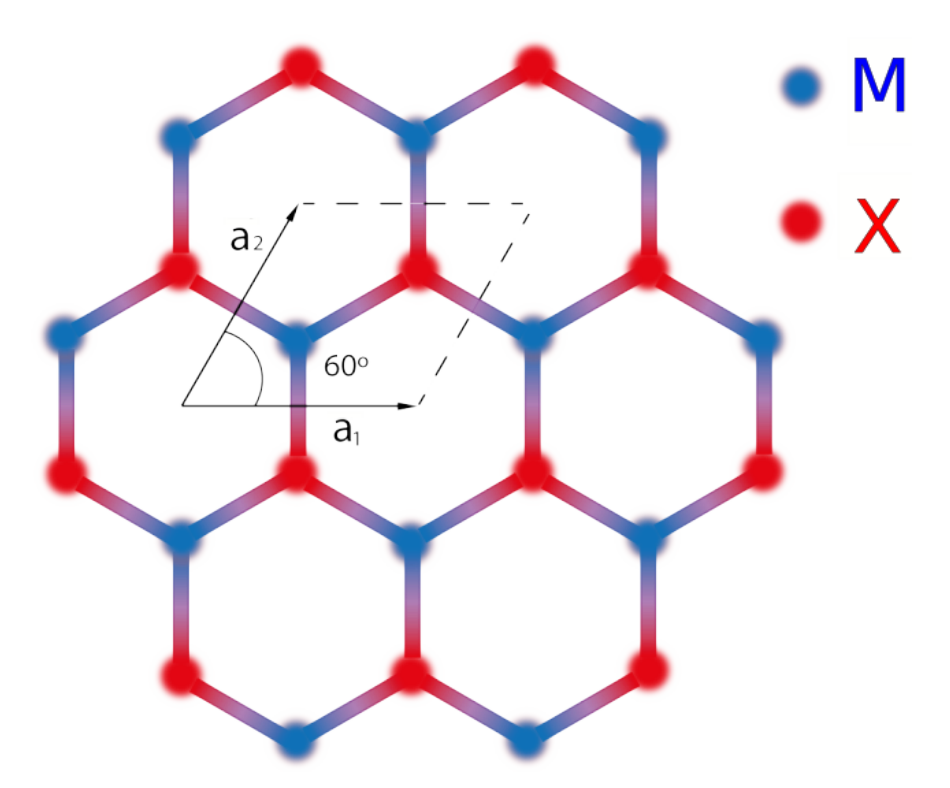


Figure 10 – Illustration of the planar hexagonal crystal lattice of M<sub>2</sub>X.

It is possible to obtain the two-dimensional lattice from equation (2.16), where in matrix form we can write:

$$\begin{pmatrix} a_{1x} & a_{1y} \\ a_{2x} & a_{2y} \end{pmatrix} \begin{pmatrix} b_{1x} & b_{1y} \\ b_{2x} & b_{2y} \end{pmatrix} = 2\pi \begin{pmatrix} 1 & 0 \\ 0 & 1 \end{pmatrix}$$
 (2.19)

Here, it would be sufficient to find and multiply on the left the inverse matrix of the real vectors  $\mathbf{a}_i$  to obtain the matrix with the reciprocal vectors  $\mathbf{b}_i$  in Cartesian coordinates. However, we can obtain the reciprocal vectors in a simpler way, using only equations (2.22) and assuming the vector  $\mathbf{a}_3 = 0\hat{i} + 0\hat{j} + 1\hat{k}$ . Thus, we have the vectors:

$$\mathbf{a}_{1} = |\mathbf{a}_{1}|\hat{i} + 0\hat{j} + 0\hat{k}$$

$$\mathbf{a}_{2} = |\mathbf{a}_{2}|\frac{1}{2}\hat{i} + |\mathbf{a}_{2}|\frac{\sqrt{3}}{2}\hat{j} + 0\hat{k}$$

$$\mathbf{a}_{3} = 0\hat{i} + 0\hat{j} + 1\hat{k}$$
(2.20)

and the operations

$$\mathbf{a}_{2} \times \mathbf{a}_{3} = |\mathbf{a}_{2}| \frac{\sqrt{3}}{2} \hat{i} - |\mathbf{a}_{2}| \frac{1}{2} \hat{j}$$

$$V = |\mathbf{a}_{1}| |\mathbf{a}_{2}| \frac{\sqrt{3}}{2}$$

$$\mathbf{a}_{3} \times \mathbf{a}_{1} = |\mathbf{a}_{1}| \hat{j}$$

$$(2.21)$$

which used in equation (2.22) result in:

$$\boldsymbol{b_1} = 2\pi \left( \frac{1}{|\boldsymbol{a}_1|} \hat{i} - \frac{\sqrt{3}}{3|\boldsymbol{a}_1|} \hat{j} \right) \qquad \boldsymbol{b_2} = 2\pi \frac{2\sqrt{3}}{3|\boldsymbol{a}_2|} \hat{j}$$
 (2.22)

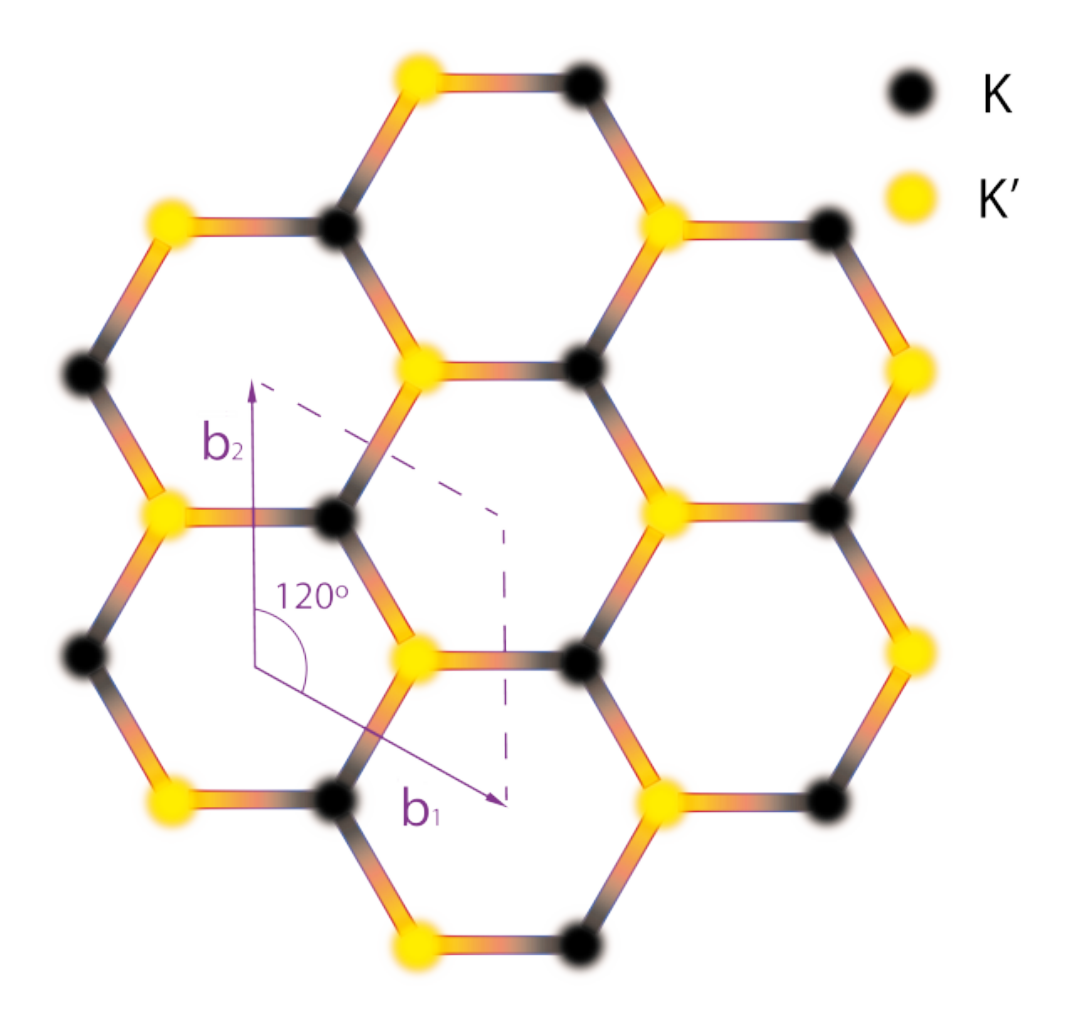


Figure 11 – Illustration of the reciprocal lattice of M<sub>2</sub>X, containing the K and K' points.

As in the real hexagonal lattice, where  $|\boldsymbol{a}_1| = |\boldsymbol{a}_2|$ , we also have  $|\boldsymbol{b}_1| = |\boldsymbol{b}_2|$  for the reciprocal lattice. Together with the angle of  $\frac{2\pi}{3}$  obtained, we also have a hexagonal configuration for the reciprocal lattice. If the real lattice was defined with an angle of  $\frac{2\pi}{3}$ , we would obtain  $\frac{\pi}{3}$  for the reciprocal lattice. The black dots (K points) and yellow dots (K' points) are obtained in the reciprocal lattice by transforming the coordinates of the positions of the M and X atoms.

#### 2.6.2 Diffraction Condition

To analyze a crystal volume, we consider volume units dV positioned at a distance  $\boldsymbol{r}$  from the origin. The optical path difference between the incident waves generates a phase difference  $e^{i2\pi(\boldsymbol{k}\cdot\boldsymbol{r})}$ , while the optical path difference for refracted waves generates a phase difference  $e^{i2\pi(-\boldsymbol{k}'\cdot\boldsymbol{r})}$ . Thus, the wave scattered by the volume dV at  $\boldsymbol{r}$  has a phase factor  $e^{i2\pi(\boldsymbol{k}-\boldsymbol{k}')\cdot\boldsymbol{r}}$  relative to the wave scattered at the origin.

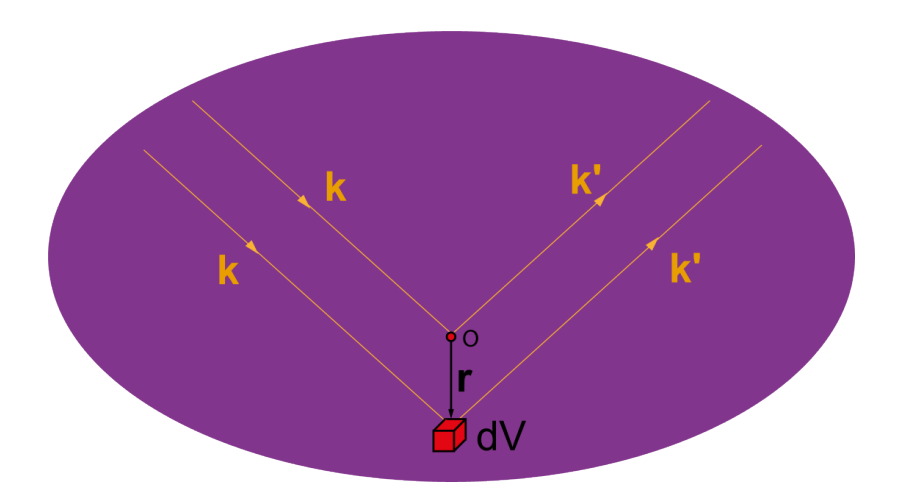


Figure 12 – Wave scattering at the origin and in a volume positioned at r.

We assume that the amplitude of the wave scattered in a volume dV is proportional to the local electronic density n(r). The total amplitude scattered in the direction k' is given by the integral, over the crystal volume, of the local electronic density multiplied by the phase factor, such as that we define A as the scattering amplitude: (KITTEL, 2004)

$$A = \int dV n(\mathbf{r}) e^{i2\pi(\mathbf{k} - \mathbf{k}') \cdot \mathbf{r}} = \int dV n(\mathbf{r}) e^{-i2\pi\Delta\mathbf{k} \cdot \mathbf{r}}$$
(2.23)

Where  $-\Delta \mathbf{k} = \mathbf{k} - \mathbf{k}'$ .  $\Delta \mathbf{k}$  measures the change in the wave vector, and it is called the scattering vector.

We can substitute  $n(\mathbf{r})$  with its Fourier representation (2.9), and then obtain:

$$A = \sum_{G} \int dV N_{G} e^{i2\pi \mathbf{G} \cdot \mathbf{r}} e^{-i2\pi \Delta \mathbf{k} \cdot \mathbf{r}} = \sum_{G} \int dV N_{G} e^{i2\pi (\mathbf{G} - \Delta \mathbf{k}) \cdot \mathbf{r}}$$
(2.24)

Thus, when the scattering vector is equivalent to a reciprocal lattice vector  $G = \Delta k$ , the exponential contribution disappears and the scattering amplitude simply becomes  $A = N_G V$ . Similarly, when the scattering vector significantly differs from the reciprocal lattice vector, the scattering amplitude becomes negligible regardless of r, and this equality is therefore called the scattering condition.

We consider elastic scattering, hence the energies and frequencies of the waves k and k' are conserved, such that their magnitudes are identical. Thus,  $k^2 = k'^2$ , and the scattering condition can be rewritten as:

$$\Delta \mathbf{k} = \mathbf{G}$$

$$\mathbf{k} + \mathbf{G} = \mathbf{k}'$$

$$(\mathbf{k} + \mathbf{G})^2 = \mathbf{k}^2$$

$$2\mathbf{k} \cdot \mathbf{G} + \mathbf{G}^2 = 0$$
(2.25)

If G represents a reciprocal lattice vector, it is evident that the same is true for -G, and from this we arrive at the final form of the diffraction condition:

$$2\mathbf{k} \cdot \mathbf{G} = \mathbf{G}^2 \tag{2.26}$$

#### 2.6.3 The First Brillouin Zone

Now we seek a geometric interpretation for the diffraction condition, so we divide equation (2.26) by four, obtaining:

$$\mathbf{k} \cdot \left(\frac{\mathbf{G}}{2}\right) = \left(\frac{\mathbf{G}}{2}\right)^2. \tag{2.27}$$

It becomes evident that any wave vector  $\mathbf{k}$ , whose projection relative to the reciprocal lattice vector  $\frac{\mathbf{G}}{2}$  has a magnitude  $\left|\frac{\mathbf{G}}{2}\right|$ , satisfies the diffraction condition. That is, if we draw lines between points in reciprocal space, separated by  $\mathbf{G}$ , the planes perpendicular to these lines, positioned precisely at the midpoints of each line, contain points where a wave vector  $\mathbf{k}$  originating from the origin satisfies the diffraction condition. These planes are called Bragg planes. The regions represented by these sets of planes are known as Brillouin zones, which contain points in reciprocal space where all wave vectors are diffracted.

The first Brillouin zone (BZ) corresponds to the smallest volume entirely contained by planes that satisfy the diffraction condition. It is of essential importance for the study of electronic band structures in crystals, as it represents a primitive cell in reciprocal space, centered at a lattice point. Figure 13 illustrates the construction of the first BZ in a hexagonal symmetry crystal, such as of the  $M_2X$  materials we work with in this study. The vector  $\mathbf{G}$  is considered as the reciprocal lattice vectors and their symmetry equivalents.

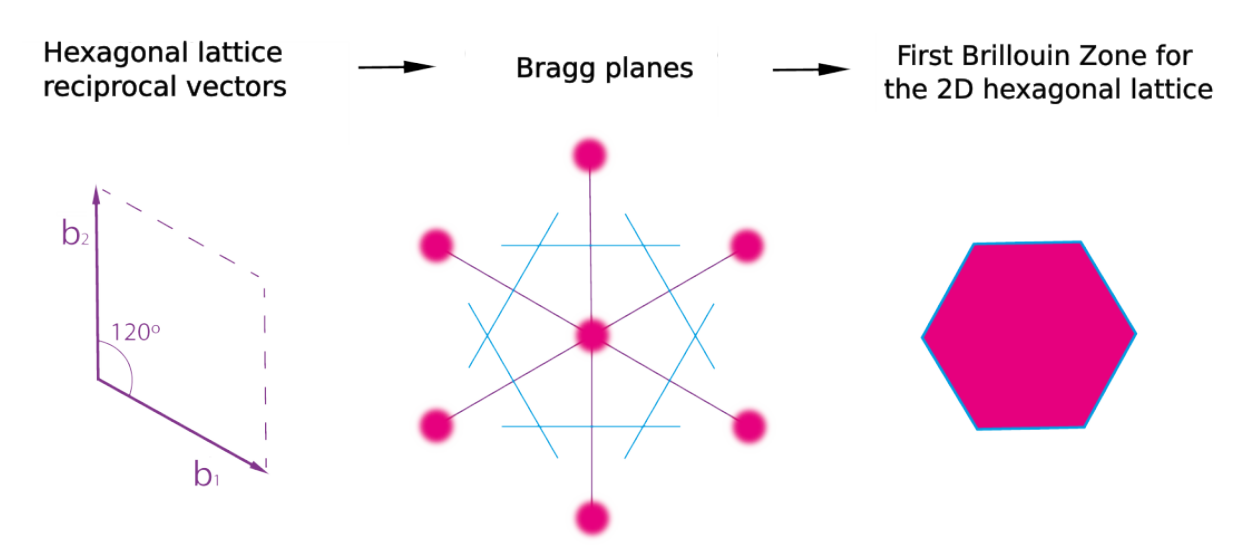


Figure 13 – Generation of the first Brillouin zone for the hexagonal lattice.

#### 2.7 Periodic Functions

#### 2.7.1 Lattice Translations

Now that we are exploring solids using quantum mechanics, the periodicity of the lattice incites us to explore the translation operator with a displacement equal to some lattice vector  $\boldsymbol{a}_i$ .

$$\hat{T}(\boldsymbol{a}_i) = e^{-i\frac{\boldsymbol{a}_i}{\hbar}\cdot\hat{\boldsymbol{p}}},\tag{2.28}$$

where  $\hat{p}$  is the momentum operator, which can be understood as the generator of spatial translations. The translation operator is a unitary transformation that acts on a position state vector  $|r\rangle$  as such:

$$\hat{T}(\boldsymbol{a}_i)|\boldsymbol{r}\rangle = |\boldsymbol{r} + \boldsymbol{a}_i\rangle.$$
 (2.29)

We notice that

$$\hat{T}^{\dagger}(\boldsymbol{a}_i) = \hat{T}^*(\boldsymbol{a}_i) = e^{i\frac{\boldsymbol{a}_i}{\hbar} \cdot \hat{p}} = \hat{T}(-\boldsymbol{a}_i); \tag{2.30}$$

and now, we are in a good position to find an important relation for the translation operator wave functions. Being  $|\Psi_n\rangle$  an eigenvector from  $\hat{T}(a_i)$ ,

2.7. Periodic Functions 69

$$\langle \boldsymbol{r} | \hat{T}(\boldsymbol{a}_i) | \Psi_n \rangle = \langle \boldsymbol{r} | \hat{T}(\boldsymbol{a}_i) | \Psi_n \rangle$$
 (2.31)

$$\langle \boldsymbol{r} - \boldsymbol{a}_i | \Psi_n \rangle = \lambda_{na_i} \langle \boldsymbol{r} | \Psi_n \rangle \tag{2.32}$$

$$\Psi_n(\mathbf{r} - \mathbf{a}_i) = \lambda_{na_i} \Psi_n(\mathbf{r}), \tag{2.33}$$

where  $\lambda_{na_i}$  is the correspondent eigenvalue of  $\hat{T}(\boldsymbol{a}_i)$ . Since  $\hat{T}(\boldsymbol{a}_i)$  is a unitary operator, the transformation should be unitary  $|\lambda_{na_i}| = 1$ . Then, we may write this eigenvalue in its most general form:

$$\lambda_{na_i} = e^{ik_i}. (2.34)$$

We may also hide the minus sign in the argument of the wave function by considering it on the exponential term  $k_i$ ,

$$\Psi_n(\mathbf{r} + \mathbf{a}_i) = e^{ik_i}\Psi_n(\mathbf{r}). \tag{2.35}$$

This relation says that a space translation of some lattice vector  $a_i$  in a wave function of the translation operator can be written as the original wave function multiplied by a phase factor.

#### 2.7.2 Bloch's Theorem

We now consider the translation operator with a displacement equal to some general vector that respects the same periodicity of the solid, i.e.  $\mathbf{l} = \sum_{i=1}^{d} n_i \mathbf{a}_i = n_i \mathbf{a}_i$ , being  $n_i$  integers, and d the total number of dimensions in the crystal:

$$\Psi_n(\mathbf{r} + \mathbf{l}) = \Psi_n(\mathbf{r} + n_i \mathbf{a}_i) = (e^{ik_i})^{n_i} \Psi_n(\mathbf{r})$$
(2.36)

$$\Psi_n(\mathbf{r} + \mathbf{l}) = e^{in_i k_i} \Psi_n(\mathbf{r}). \tag{2.37}$$

Conveniently, we define a general vector in the reciprocal space,  $\mathbf{k} = k_i \mathbf{b}_i$ , so that using the relation  $\mathbf{a}_i \cdot \mathbf{b}_i = 2\pi \delta_{ij}$ , we may write  $e^{in_i k_i} = e^{i\frac{\mathbf{k} \cdot \mathbf{l}}{2\pi}} = e^{i\mathbf{k} \cdot \mathbf{l}}$ , to finally obtain

$$\Psi_n(\mathbf{r} + \mathbf{l}) = e^{i\mathbf{k}\cdot\mathbf{l}}\Psi_n(\mathbf{r}). \tag{2.38}$$

The important insight this relation reveals to us is that any spatial translation in a wave function of the translation operator may be represented by a phase factor described

by the product of the displacement vector with some vector in reciprocal space.

This translational symmetry must be contained in the Hamiltonian itself, being invariant under lattice translation, where we take the important assumption that the potential term has the same periodicity of the solid, i.e.  $V(\mathbf{r}+\mathbf{l}) = V(\mathbf{r})$ . Figure 14 illustrates a periodic potential for the case of a one-dimensional lattice with some lattice parameter a.

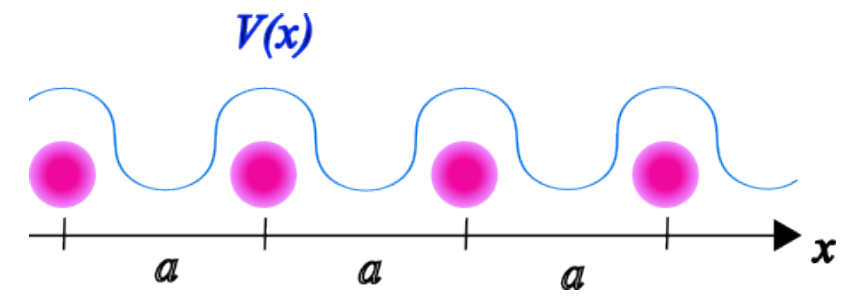


Figure 14 – Illustration of a periodic potential in an one-dimensional lattice.

Since the displacement is according to the periodicity of the lattice, we observe that this operator commutes with the potential term from the Hamiltonian,

$$\hat{T}(\boldsymbol{l})(\hat{V}(\boldsymbol{r})\Psi(\boldsymbol{r})) = \hat{V}(\boldsymbol{r} + \boldsymbol{l})\Psi(\boldsymbol{r} + \boldsymbol{l}) = \hat{V}(\boldsymbol{r})\hat{T}(\boldsymbol{l})\Psi(\boldsymbol{r}). \tag{2.39}$$

The translation operator obviously commutes with the kinetic energy term, since both are composed by no other than the momentum operator. Thus, we conclude that the translation operator commutes with the Hamiltonian of the system, or more generally,  $\hat{H}$  commutes with all powers of  $\hat{T}(\boldsymbol{l})$ ,  $\hat{T}(\boldsymbol{l})^n = \hat{T}(n\boldsymbol{l})$ , which is equivalent to consider that it commutes with the entire group of symmetry operations generated by  $\hat{T}(\boldsymbol{l})$ . This commutation relation demands the existence of a common set of eigenvectors.

The final result of the Bloch theorem is hardly overestimated. What we obtained for the plane wave functions of the translation operator is also true for any wave function or state vector that satisfies the Schrödinger equation in a periodic system. There exists a vector  $\mathbf{k}$  in the reciprocal space such that translations in the real space  $\hat{T}(\mathbf{l})$  are equivalent to multiplying the state by a phase factor  $e^{i\mathbf{k}\cdot\mathbf{l}}$ . In the case of electron waves, it means that we can label every wave function by its wave vector  $\mathbf{k}$ , i.e.

$$\Psi_{\mathbf{k}}(\mathbf{r} + \mathbf{l}) = e^{i\mathbf{k}\cdot\mathbf{l}}\Psi_{\mathbf{k}}(\mathbf{r}). \tag{2.40}$$

What is usually called Bloch functions is a more convenient way to write what we just done:

2.7. Periodic Functions 71

$$\Psi_{k}(\mathbf{r}) = e^{i\mathbf{k}\cdot\mathbf{r}}u_{k}(\mathbf{r}),\tag{2.41}$$

where  $u_{\mathbf{k}}(\mathbf{r}) = u_{\mathbf{k}}(\mathbf{r} + \mathbf{l})$ .

$$u_{\mathbf{k}}(\mathbf{r}) \times e^{i\mathbf{k}\cdot\mathbf{r}} = \Psi_{\mathbf{k}}(\mathbf{r})$$

Figure 15 – Illustration of the real part of a Bloch wave function.

Now, we label the electron wave function by its wave vector  $\mathbf{k}$ , but is this vector well defined? We can write  $\mathbf{k} = \mathbf{k}' + \mathbf{G}$ , where  $\mathbf{G}$  is some reciprocal lattice vector, and  $\mathbf{k}'$  is another wave vector. We already know that  $e^{i\mathbf{G}\cdot l} = 1$ , then Bloch theorem (2.40) states that

$$\Psi_{\mathbf{k}}(\mathbf{r} + \mathbf{l}) = e^{i(\mathbf{k}' + \mathbf{G}) \cdot \mathbf{l}} \Psi_{\mathbf{k}}(\mathbf{r})$$
(2.42)

$$= e^{i\mathbf{k}'\cdot\mathbf{l}}e^{i\mathbf{G}\cdot\mathbf{l}}\Psi_{\mathbf{k}}(\mathbf{r}) = e^{i\mathbf{k}'\cdot\mathbf{l}}\Psi_{\mathbf{k}}(\mathbf{r}). \tag{2.43}$$

The state  $\Psi_k$  satisfies Bloch's theorem as if it has the wave vector k', i.e., the electron wave function is not defined by a unique wave vector but instead includes all possible lattice translations in reciprocal space. This is a hint for the uncertainty principle of position and momentum in crystalline states, which shall be discussed later,

The second quantization of electron states in Bloch's form can be defined in terms of the field operators (1.78):

$$\hat{\Psi}^{\dagger}(\boldsymbol{r}\boldsymbol{\sigma}) = \sum_{n\boldsymbol{k}} \Psi_{n\boldsymbol{k}}(\boldsymbol{r}\boldsymbol{\sigma})\hat{c}_{n\boldsymbol{k}}^{\dagger} \qquad \qquad \hat{\Psi}(\boldsymbol{r}\boldsymbol{\sigma}) = \sum_{n\boldsymbol{k}} \Psi_{n\boldsymbol{k}}(\boldsymbol{r}\boldsymbol{\sigma})\hat{c}_{n\boldsymbol{k}}, \qquad (2.44)$$

where  $\sigma$  are the spin coordinates, n is the electron energy level,  $\hat{c}_{n\mathbf{k}}^{\dagger}$  and  $\hat{c}_{n\mathbf{k}}$  are the fermionic creation and annihilation operators, which obey the anticommutation relations (1.72).

### 2.7.3 Counting States

Let us consider more carefully the reciprocal lattice vector

$$G = n_i b_i = n_i \frac{2\pi}{a_i}. (2.45)$$

Any electron wave function, or electron state, is then assigned by a wave number in the set  $\mathbf{k} = \mathbf{k}' + n_i \frac{2\pi}{a_i}$ , i.e., all points  $\mathbf{k}$  can be mapped into the region

$$-\frac{\pi}{\boldsymbol{a}_i} < \boldsymbol{k}_i < \frac{\pi}{\boldsymbol{a}_i},\tag{2.46}$$

or

$$-\frac{\boldsymbol{b}_i}{2} < k_i \boldsymbol{b}_i < \frac{\boldsymbol{b}_i}{2} \tag{2.47}$$

$$-\frac{1}{2} < k_i < \frac{1}{2}.\tag{2.48}$$

This result is exactly what we got before entering quantum theory. All wave vectors  $\mathbf{k}$  in reciprocal space are equivalent to some vector inside the Brillouin zone.

In our consideration for translational symmetry, we have not included yet any boundary condition. A real solid system is periodic until it ends; it has a finite number of unit cells. The most feasible way to deal with this problem is to treat the solid with Born-von Kármán boundary conditions, i.e. a cyclic system:

$$\Psi_{k}(\mathbf{r} + L_{i}\mathbf{a}_{i}) = \Psi_{k}(\mathbf{r}), \tag{2.49}$$

where  $L_i$  is the total amount of unit cells along the i axis.

We must still restrict ourselves to Bloch's theorem, so the relation

$$\Psi_{k}(\mathbf{r} + L_{i}\mathbf{a}_{i}) = e^{i(k_{i}\mathbf{b}_{i}\cdot L_{i}\mathbf{a}_{i})}\Psi_{k}(\mathbf{r}) = e^{i(2\pi k_{i}L_{i})}\Psi_{k}(\mathbf{r})$$
(2.50)

demands the condition  $k_i = \frac{m_i}{L_i}$ , with  $m_i$  integers. Considering the Brillouin zone relation stated in (2.48), we find that the allowed wave vectors are the ones that satisfies

$$\mathbf{k} = \frac{m_i}{L_i} \mathbf{b}_i, \tag{2.51}$$

with integers  $m_i$  respecting  $-\frac{1}{2}L_i < m_i < \frac{1}{2}L_i$ . Thus, we obtain a fine grid of evenly distributed k-points inside the Brillouin zone. There are exactly as many allowed wave vectors in a Brillouin zone as there are unit cells in the solid system;  $N = \prod_{i=1}^{d} L_i$ , where

2.7. Periodic Functions 73

d is the number of dimensions of the system and N is the total number of unit cells, or allowed wave vectors.

Now we concern with the density of states in reciprocal space. Having N unit cells in a 2D crystal of total area  $A_{\rm C}$  implies that the area of each unity cell is  $a_{\rm uc} = \frac{A_{\rm C}}{N}$ . Since the Brillouin zone is a unit cell in reciprocal space, its area is  $A_{\rm BZ} = |\boldsymbol{b_1} \times \boldsymbol{b_2}| = \frac{4\pi^2}{a_{uc}}$ . Thus, the number of allowed k-vectors per unit area of reciprocal space is

$$\frac{N}{A_{\rm BZ}} = N \frac{a_{\rm uc}}{4\pi^2} = \frac{A_{\rm C}}{4\pi^2}.$$
 (2.52)

In real systems, N is very large so that this distribution is nearly continuous. We often express the sum over the k-vectors as an integral

$$\sum_{\mathbf{k}} \to \frac{A_{\rm C}}{4\pi^2} \int d^2 \mathbf{k}. \tag{2.53}$$

For simplicity, is usually assume that  $A_{\rm C}=1$ , so that N is the number of cells per unit area of the crystal and  $\frac{1}{N}$  is the area of a unit cell.

#### 2.7.4 Plane Wave Basis

Expanding the Bloch wave function in a Fourier transform (2.9) would require a sum over every wave vector in the reciprocal lattice, which is unfeasible in practical calculations. However, the coefficients  $A_k$  of plane waves with small kinetic energies are more important than those with large kinetic energies. Thus, we set a cutoff energy that limits the kinetic energy of the wave vectors taken as basis:

$$\frac{\hbar^2}{2m_e} |\boldsymbol{k}|^2 \le E_{\text{cut}} \tag{2.54}$$

The Fourier transform (2.9) of a squared function in real space results in squared Fourier coefficients, and reciprocal space vectors with double the length. The density matrix formalism explored in (1.18) contains a squared wave function in the operator, so the resulting reciprocal vector gives a factor of four to the cutoff energy in charge density calculations:

$$\frac{\hbar^2}{2m_{\rm e}} |\mathbf{k}|^2 \le 4E_{\rm cut}$$

$$|\mathbf{k}| \le \frac{2}{\hbar} \sqrt{2m_{\rm e}E_{\rm cut}} = |\mathbf{k}_{\rm cut}|.$$
(2.55)

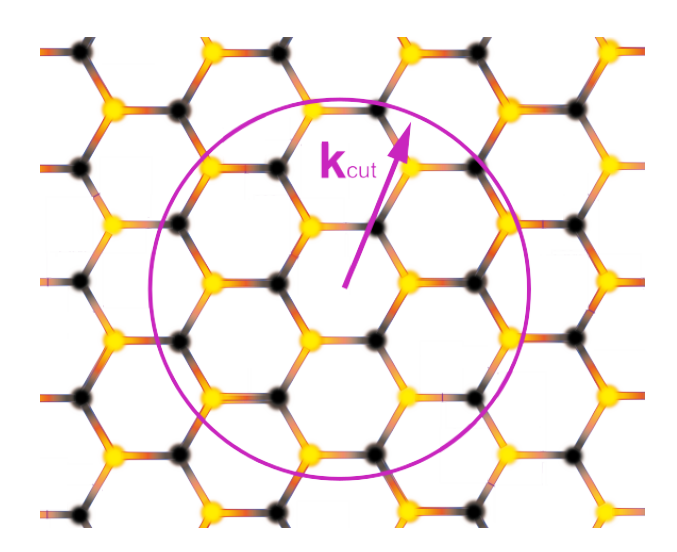


Figure 16 – Cutoff vector representation

#### 2.7.5 Wannier Functions

We have defined a form for wave functions in a periodic lattice potential. Now we ought to think of wave functions for the different energy levels an electron might occupy. We define  $\chi_n(\mathbf{r})$  as a construction tool for a function in the Bloch form (2.40) as:

$$\Psi_{n,k}(\boldsymbol{r}) = \frac{1}{\sqrt{N}} \sum_{\boldsymbol{l}e^{i\boldsymbol{k}\cdot\boldsymbol{l}}\chi_n(\boldsymbol{r}-\boldsymbol{l}),(2.56)}$$

where it exists a function  $\chi_n(\mathbf{r})$  for each energy level n of our system. These momentum-independent functions are called Wannier functions.

The wave function given in (2.56) can be understood as constituted of a sum of contributions from localized energy levels multiplied by a phase factor. We might think of a Wannier function  $\chi_n(\mathbf{r} - \mathbf{l})$  as somewhat analogous to an atomic orbital for a free atom centered at l,  $\phi_n(\mathbf{r} - \mathbf{l})$ ; but from the orthogonality of Bloch functions of different energy levels,  $\Psi_{n,k}(\mathbf{r})$ ,  $\Psi_{n',k}(\mathbf{r})$ , we have that  $\chi_n(\mathbf{r})$  must be orthogonal to  $\chi_{n'}(\mathbf{r})$  (ZIMAN, 1972).

Wannier functions are coefficients in a Fourier form (2.9) of Bloch functions, which can be directly expressed by inversion,

$$\sum_{\mathbf{k}} e^{-i\mathbf{k}\cdot\mathbf{l}'} \Psi_{n,k}(\mathbf{r}) = \frac{1}{\sqrt{N}} \sum_{\mathbf{k}\mathbf{l}} e^{i\mathbf{k}\cdot(\mathbf{l}-\mathbf{l}')} \chi_n(\mathbf{r} - \mathbf{l})$$

$$= \sqrt{N} \sum_{\mathbf{l}} \delta_{\mathbf{l}\mathbf{l}'} \chi_n(\mathbf{r} - \mathbf{l})$$

$$= \sqrt{N} \sum_{\mathbf{l}} \chi_n(\mathbf{r} - \mathbf{l}'), \qquad (2.57)$$

as

$$\chi_n(\mathbf{r} - \mathbf{l}) = \frac{1}{\sqrt{N}} \sum_{\mathbf{k}} e^{-i\mathbf{k} \cdot \mathbf{l}} \Psi_{n,k}(\mathbf{r}).$$
 (2.58)

Equations (2.56) and (2.58) are a perfect demonstration of the crystal version of the uncertainty principle. As seen in the construction of Bloch functions, translational symmetry along lattice vectors in crystalline quantum states implies that all possible lattice-translated states must be equivalent up to a phase factor, for a certain momentum. The Bloch wave function is then a state defined in momentum, but constructed as a superposition of lattice-translated states. Thus, certainty in momentum is associated with uncertainty in position; while the Wannier functions, electron states localized in real space, are constructed as a superposition of states with different momentum coordinates. So certainty in position gives uncertainty in momentum.

In the second quantization format, the creation and annihilation operators for Bloch and Wannier states are written as:

$$\hat{c}_{n\mathbf{k}} = \frac{1}{\sqrt{N}} \sum_{\mathbf{R}} e^{-i\mathbf{k}\cdot\mathbf{R}} \hat{c}_{n\mathbf{R}}, \quad \hat{c}_{n\mathbf{k}}^{\dagger} = \frac{1}{\sqrt{N}} \sum_{\mathbf{R}} e^{i\mathbf{k}\cdot\mathbf{R}} \hat{c}_{n\mathbf{R}}^{\dagger}; \tag{2.59}$$

$$\hat{c}_{n\mathbf{R}} = \frac{1}{\sqrt{N}} \sum_{\mathbf{k}} e^{i\mathbf{k}\cdot\mathbf{R}} \hat{c}_{n\mathbf{k}}, \quad \hat{c}_{n\mathbf{R}}^{\dagger} = \frac{1}{\sqrt{N}} \sum_{\mathbf{k}} e^{-i\mathbf{k}\cdot\mathbf{R}} \hat{c}_{n\mathbf{k}}^{\dagger}. \tag{2.60}$$

# 2.8 Discrete Symmetries

### 2.8.1 Space Inversion

The space inversion operator  $\hat{\pi}$ , also known as parity operator, is a unitary and hermitian operator that acts on vector states to produce space-inverted states  $|\Psi_n\rangle \rightarrow \hat{\pi} |\Psi_n\rangle$ . i.e. all spatial coordinates are mirrored over their axis, as in

$$\langle \Psi_n | \hat{\pi}^{\dagger} \hat{r} \hat{\pi} | \Psi_n \rangle = - \langle \Psi_n | \hat{r} | \Psi_n \rangle.$$
 (2.61)

$$\hat{\pi}^{\dagger} \hat{\boldsymbol{r}} \hat{\pi} = -\hat{\boldsymbol{r}} \tag{2.62}$$

The eigenvalue of this operator can only be  $\pm 1$ ,

$$\hat{\pi} |\Psi_n\rangle = \pm |\Psi_n\rangle. \tag{2.63}$$

When acting on a spatial vector state  $|r\rangle$ ,

$$\pi \left| \mathbf{r} \right\rangle = e^{i\theta} \left| -\mathbf{r} \right\rangle,\tag{2.64}$$

where  $e^{i\theta} |-r\rangle$  is just some phase factor, which for simplicity we consider  $e^{i\theta} |-r\rangle=1$ .

The momentum operator is the generator of translation, but translations should also be inverted in the space-inverted scheme, thus, momentum is too inverted. (SAKU-RAI; TUAN; COMMINS, 1995)

$$\hat{\pi}^{\dagger} \hat{\boldsymbol{p}} \hat{\pi} = -\hat{\boldsymbol{p}}. \tag{2.65}$$

It's useful to remember that the Brillouin zone is set in reciprocal space, so the space inversion operator acting on a wave vector inside the Brillouin zone gives the wave vector with mirrored momentum coordinates.

For angular momentum  $\hat{J}$ , being it an orbital angular momentum  $\hat{L}$  or a spin angular momentum  $\hat{S}$ , we make a similar argument. Angular momentum is generator of rotation, but rotation commutes with inversion, i.e., applying rotation after inversion is the same as inversion after rotation, thus angular momentum commutes with the space inversion operator,

$$\hat{\pi}^{\dagger} \hat{J} \hat{\pi} = \hat{J}. \tag{2.66}$$

The parity operator has this as one of its names because it indicates the parity of functions. Let us take the wave function

$$\Psi_n(\mathbf{r}) = \langle \mathbf{r} | \Psi_n \rangle. \tag{2.67}$$

The wave function of the space inverted state is then

$$\langle \boldsymbol{r} | \hat{\pi} | \Psi_n \rangle = \langle -\boldsymbol{r} | \Psi_n \rangle = \Psi_n(-\boldsymbol{r}).$$
 (2.68)

But we also have (2.63), so the wave functions can be divided by their parity:

$$\Psi_n(-\boldsymbol{r}) = \begin{cases} \Psi_n(\boldsymbol{r}), & \text{if even parity,} \\ -\Psi_n(\boldsymbol{r}), & \text{if odd parity.} \end{cases}$$
 (2.69)

#### 2.8.2 Time Reversion

For the time-reversal operator  $\hat{\Theta}$ , we should think of its action on a state vector as reversing the motion of this state,

$$\hat{\Theta} \left| \Psi_n \right\rangle = \left| \tilde{\Psi}_n \right\rangle, \tag{2.70}$$

where  $|\tilde{\Psi}_n\rangle$  is the time-reversed  $|\Psi_n\rangle$ , which is equivalent to a flip in the sign of the momentum coordinates, including spin;  $|\tilde{\Psi}_{n\mathbf{k}\uparrow}\rangle = |\Psi_{n-\mathbf{k}\downarrow}\rangle^*$ . This operator is quite different from all previously discussed operators, as it is an anti-unitary operator: (SAKURAI; TUAN; COMMINS, 1995)

$$\left\langle \tilde{\Psi}_{n'} \middle| \tilde{\Psi}_n \right\rangle = \left\langle \Psi_{n'} \middle| \Psi_n \right\rangle^*$$
 (2.71)

$$\hat{\Theta}(c_n | \Psi_n \rangle + c_{n'} | \Psi_{n'} \rangle) = c_n^* \hat{\Theta} | \Psi_n \rangle + c_{n'}^* \hat{\Theta} | \Psi_{n'} \rangle.$$
 (2.72)

We say that a Hermitian observable  $\hat{O}$  is even or odd under time reversal according to the signal

$$\hat{\Theta}\hat{O}\hat{\Theta}^{-1} = \pm \hat{O}. \tag{2.73}$$

As e.g., the momentum  $\hat{p}$  and angular momentum  $\hat{J}$  operators are odd, but the position operator  $\hat{x}$  is even, as we might expect by intuition;

$$\hat{\Theta}\hat{p}\hat{\Theta}^{-1} = -\hat{p},\tag{2.74}$$

$$\hat{\Theta}\hat{J}\hat{\Theta}^{-1} = -\hat{J},\tag{2.75}$$

$$\hat{\Theta}\hat{x}\hat{\Theta}^{-1} = \hat{x}.\tag{2.76}$$

For the wave function, we consider the spinless state vector being act as

$$\hat{\Theta} |\Psi_{n}\rangle = \int d^{3}x \hat{\Theta} |\mathbf{x}\rangle \langle \mathbf{x}|\Psi_{n}\rangle$$

$$= \int d^{3}x \langle \mathbf{x}|\Psi_{n}\rangle^{*} \hat{\Theta} |\mathbf{x}\rangle$$

$$= \int d^{3}x \Psi_{n}^{*}(\mathbf{x}) |\mathbf{x}\rangle. \qquad (2.77)$$

The wave function transformation indicates that the time reversion of a state has to do with the complex coefficients of the expansion,

$$\Psi_n(\boldsymbol{x}) \to \Psi_n^*(\boldsymbol{x}).$$
 (2.78)

We may notice that a second application of the operator gives back the original state,

$$\hat{\Theta}^2 = 1. \tag{2.79}$$

This is also valid for any integer spin states, but different for half-integer spin states, (SAKURAI; TUAN; COMMINS, 1995)

$$\hat{\Theta}^2 = -1. \tag{2.80}$$

# 2.8.3 High Symmetry Points and Degeneracy

When we analyze the BZ for the two-dimensional hexagonal lattice, we may find special points containing the symmetries described in Figure 5. We call those as high symmetry points, which are illustrated in Figure 17. At the center of the zone, we have the  $\Gamma$  point, which contains both a  $C_6$ , and a intercept of 6 mirrors, being then a  $D_6$  symmetry. Each K point have  $C_3$  symmetry, and M points are intercepts of two mirror lines.

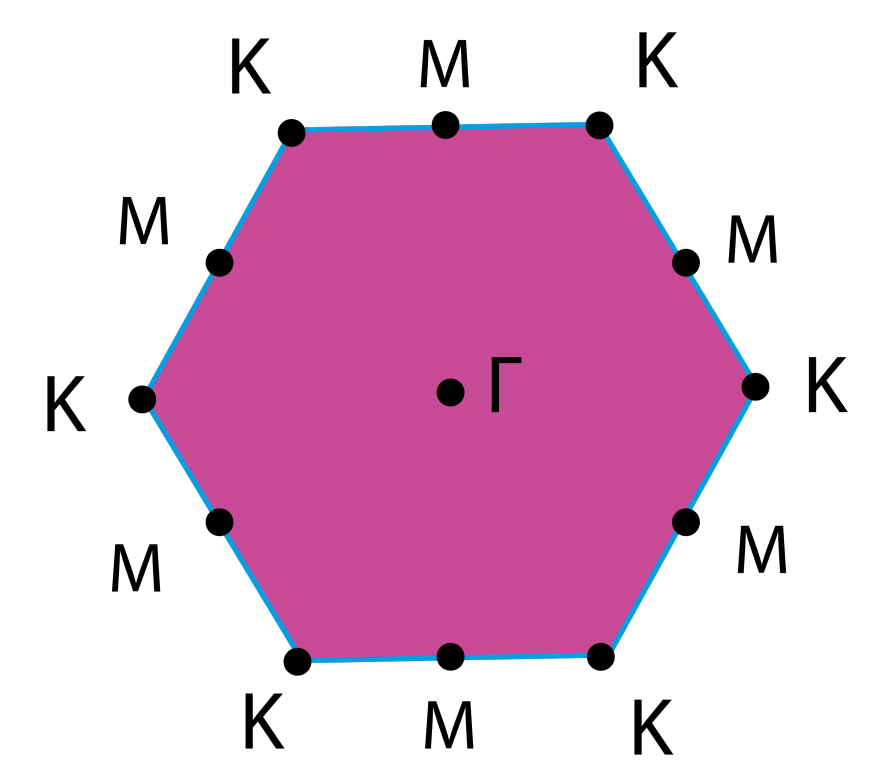


Figure 17 – High symmetry points of the two-dimensional hexagonal lattice Brillouin zone.

Symmetry is of great importance when calculating the band structure, as the energy function in the BZ has the full point group of the crystal. Any symmetry operation that leaves the crystal invariant, as discussed above, also transforms the function  $E(\mathbf{k})$  into itself (ZIMAN, 1972). This means that in every equally named point of the Brillouin zone, the energy levels are the same. We have degenerated states for every K point or every M point, thus, it is unnecessary to perform calculations for the whole zone but only enough to contemplate one of each point.

In heavy atoms we know the existence of strong spin-orbit interaction (ZIMAN, 1972), where the Hamiltonian of the system includes a term like  $\hat{H}_{SO} = \lambda \hat{L} \cdot \hat{S}$ . Since both  $\hat{L}$  and  $\hat{S}$  are invertible under time-reversion, this Hamiltonian still maintains time-reversal symmetry,  $[\hat{H}, \hat{\Theta}] = 0$ . However, electrons with opposite spins in the same orbit will have opposite energy displacements, breaking their degeneracy.

High symmetry points are not the only symmetry-concerned factors for degeneracy. Time-reversal symmetry of the system will always lead any electron Bloch state  $|\Psi_k\rangle$  degenerated with its time-reversed state  $\hat{\Theta} |\Psi_k\rangle$ . One can argue that this might be just the same state, with a phase factor  $e^{i\delta}$  difference, therefore not a pair of degenerated states. This is a valid argument, but it fails when it comes to half-integer spin systems, as

$$\hat{\Theta}^{2} |\Psi_{\mathbf{k}}\rangle = \hat{\Theta}e^{i\delta} |\Psi_{\mathbf{k}}\rangle = e^{-i\delta}\hat{\Theta} |\Psi_{\mathbf{k}}\rangle$$

$$= e^{-i\delta}e^{i\delta} |\Psi_{\mathbf{k}}\rangle = |\Psi_{\mathbf{k}}\rangle. \tag{2.81}$$

This is in contradiction with equation (2.80). Thus, for half-integer spin systems, we call this pair of degenerated states as a Kramer degeneracy. Time reversal symmetry of a system with odd number of electrons will always lead to electron Bloch functions  $\Psi_{k}(\mathbf{r})$  degenerated with their complex conjugated  $\Psi_{k}^{*}(\mathbf{r})$ , where both the wave vector  $\mathbf{k}$  and the spin  $\sigma$  have been reversed. In the hexagonal Brillouin zone, we have then that K points that are momentum-inverted must have opposite spin separation, so it conserves time-reverse symmetry. We distinguish those as K and K' points.  $\Gamma$  and M points are centers of inversion, thus they keep the energy levels as degenerated.

# 2.9 Schrödinger Equation for Many-electron Systems

The band structure, i.e. the energy levels of the electron in the Brillouin zone, is central along this study. It is from the band structure that our material's optical and electrical properties are calculated; properties such as electrical conductivity, optical absorption, and excitonic description.

A type of approach to calculate such properties is called *ab initio*. This name comes from the fact that the approach is based on the fundamental Hamiltonian of the system, with no additional and adjustable physical parameters. It is good remembering that an *ab initio* approach does not demand an absence of approximations.

First, we consider a system formed by m nuclei and n electrons. The state of the system is described by the it's wave function, which must satisfy the non-relativistic time independent Schrödinger equation. For this problem, we consider the electrons positions as  $\mathbf{r}_i$ , where i = 1, ..., n; and the nuclei positions as  $\mathbf{R}_A$ , where A = 1, ..., m.

Then, the stationary Schrödinger equation is:

$$\hat{H} |\Psi (\{\mathbf{R}\}, \{\mathbf{r}\})\rangle = E |\Psi (\{\mathbf{R}\}, \{\mathbf{r}\})\rangle.$$
(2.82)

The Hamiltonian of the system is given by the sum of kinetic energies of all electrons and nuclei, and the sum of all nucleus-electron, nucleus-nucleus and electron-electron interactions. It is also possible to add an external electromagnetic field which interacts with electrons and nuclei,

$$\hat{H} = \hat{T}_{e} + \hat{T}_{n} + \hat{V}_{nn} + \hat{V}_{en} + \hat{V}_{ee} + \hat{V}_{n-field} + \hat{V}_{e-field}.$$
 (2.83)

Being  $R_{AB}$  the distance between nucleus A and nucleus B,  $R_{Ai}$  the distance between nucleus A and electron i, and  $r_{ij}$  the distance between electron i and electron j,

$$\hat{H} = -\frac{\hbar^2}{2m_e} \sum_{i}^{n} \nabla_i^2 - \frac{\hbar^2}{2} \sum_{A}^{m} \frac{\nabla_A^2}{M_A} + \sum_{A>B}^{m} \frac{K_e Z_A Z_B e^2}{R_{AB}} - \sum_{A=1}^{m} \sum_{i=1}^{n} \frac{K_e Z_A e^2}{R_{Ai}} + \sum_{i>j}^{n} \frac{K_e e^2}{r_{ij}} + \hat{V}_{\text{n-field}} + \hat{V}_{\text{e-field}}. \quad (2.84)$$

For the external field interactions, we have

$$V_{\text{n-field}} = \sum_{A}^{m} \left[ Z_A e \Phi_{\text{ext}}(\mathbf{R}_A t) + i \frac{Z_A e \hbar}{M_A c} \mathbf{A}_{\text{ext}}(\mathbf{R}_A t) \cdot \nabla_A - \mathbf{I}_A \cdot \mathbf{B}_{\text{ext}}(\mathbf{R}_A t) \right]$$
(2.85)

$$V_{\text{e-field}} = \sum_{i}^{n} \left[ -e\Phi_{\text{ext}}(\boldsymbol{r}_{i}t) - 2i\mu_{\text{B}}\boldsymbol{A}_{\text{ext}}(\boldsymbol{r}_{i}t) \cdot \nabla_{i} + \mu_{\text{B}}\hat{\sigma}_{i} \cdot \boldsymbol{B}_{\text{ext}}(\boldsymbol{r}_{i}t) \right].$$
 (2.86)

Here,  $\Phi_{\text{ext}}$  and  $\boldsymbol{A}_{\text{ext}}$  are the scalar and vector field potentials corresponding to the external electromagnetic field,

$$\mathbf{E}_{\text{ext}}(\mathbf{r}t) = -\nabla \Phi_{\text{ext}}(\mathbf{r}t) - \frac{1}{c} \frac{\partial \mathbf{A}_{\text{ext}}(\mathbf{r}t)}{\partial t}$$
(2.87)

$$\boldsymbol{B}_{\text{ext}}(\mathbf{r}t) = \nabla \times \boldsymbol{A}_{\text{ext}}(\mathbf{r}t),$$
 (2.88)

 $I_A$  is the magnetic moment of the A-th nucleus,  $\mu_B = \frac{e\hbar}{2mc}$  is the Bohr magneton, and  $\hat{\sigma}_i$  is the spin operator corresponding to the *i*-th electron.

For all this, we have considered the motion of both electrons and nuclei as non-relativistic. We also characterize each nucleus as a point particle with mass, charge, and magnetic moment. All this treatment is not problematic for the concerns of this study, but if heavy atoms are under consideration, relativistic effects become not negligible. For the external field, it can be either static or time-dependent, e.g. a laser pulse. The coupling of the field with the quantized particles is specified assuming the Coulomb gauge,  $\nabla \cdot A_{ext}(\mathbf{r}t) = 0$ . Despite all this discussion, which aims only to open our minds to possibilities, the continuation of this study will assume no external fields, giving us back to:

$$\hat{H} = -\frac{\hbar^2}{2m_e} \sum_{i}^{n} \nabla_i^2 - \frac{\hbar^2}{2} \sum_{A}^{m} \frac{\nabla_A^2}{M_A} + \sum_{A>B}^{m} \frac{K_e Z_A Z_B e^2}{R_{AB}} - \sum_{A=1}^{m} \sum_{i=1}^{n} \frac{K_e Z_A e^2}{R_{Ai}} + \sum_{i>i}^{n} \frac{K_e e^2}{r_{ij}}.$$
 (2.89)

For shortening and clarity of text, we use from now on a simpler notation, where  $|\Psi(\{\mathbf{R}\}, \{\mathbf{r}\})\rangle = \Psi$ , and considering also the atomic units,  $K_{\rm e} = \hbar = e = m_{\rm e} = 1$ , we may rewrite equation (2.82) as

$$\left(-\frac{1}{2}\sum_{i}^{n}\nabla_{i}^{2} - \frac{1}{2}\sum_{A}^{m}\frac{\nabla_{A}^{2}}{M_{A}} + \sum_{A>B}^{m}\frac{Z_{A}Z_{B}}{R_{AB}} - \sum_{A=1}^{m}\sum_{i=1}^{n}\frac{Z_{A}}{R_{Ai}} + \sum_{i>j}^{n}\frac{1}{r_{ij}}\right)\Psi = E\Psi.$$
(2.90)

Concerning a molecular system, we treat the movement of the nuclei as an adiabatic process (KOLSOS, 1970), i.e., they move extremely slow with regards to movement of the electrons, enabling a separate description for the movement of electrons and nuclei. If we consider a solid system, this argument is even stronger. This separate description is made by separating the wave function of the system into two independent functions,  $\Psi(\{R\}, \{r\}) = \phi(\{R\}, \{r\})\chi(\{R\})$ , or in condensed notation,  $\Psi = \phi \chi$ . We have then:

$$-\frac{\chi}{2} \sum_{i}^{n} \nabla_{i}^{2} \phi - \frac{1}{2} \sum_{A}^{m} \frac{\nabla_{A}^{2}}{M_{A}} \phi \chi + \sum_{A>B}^{m} \frac{Z_{A} Z_{B}}{R_{AB}} \phi \chi - \sum_{A=1}^{m} \sum_{i=1}^{n} \frac{Z_{A}}{R_{Ai}} \phi \chi + \sum_{i>j}^{n} \frac{1}{r_{ij}} \phi \chi = E \phi \chi. \quad (2.91)$$

Now we take a moment to develop the second term of the equation in an isolated manner, which can be expanded as

$$-\frac{1}{2} \sum_{A=1}^{m} \frac{\nabla_{A}^{2}}{M_{A}} (\phi \chi) = -\frac{1}{2} \sum_{A=1}^{m} \frac{1}{M_{A}} (\boldsymbol{\nabla}_{A} \cdot (\chi \boldsymbol{\nabla}_{A} \phi + \phi \boldsymbol{\nabla}_{A} \chi))$$

$$= -\frac{1}{2} \sum_{A=1}^{m} \frac{1}{M_{A}} (\chi \boldsymbol{\nabla}_{A} \cdot \boldsymbol{\nabla}_{A} \phi + \boldsymbol{\nabla}_{A} \chi \cdot \boldsymbol{\nabla}_{i} \phi + \phi \boldsymbol{\nabla}_{A} \cdot \boldsymbol{\nabla}_{A} \chi + \boldsymbol{\nabla}_{A} \phi \cdot \boldsymbol{\nabla}_{A} \chi) \qquad (2.92)$$

$$= -\frac{1}{2} \left( \sum_{A=1}^{m} \frac{\chi \nabla_{A}^{2} \phi}{M_{A}} + 2 \frac{\boldsymbol{\nabla}_{A} \phi \cdot \boldsymbol{\nabla}_{A} \chi}{M_{A}} + \frac{\phi \nabla_{A}^{2} \chi}{M_{A}} \right).$$

At this point, we shall use the Born-Oppenheimer approximation (BORN; OP-PENHEIMER, 1927), where  $\nabla_A \phi$  is considered extremely small, as the adiabatic movement of the nuclei is irrelevant for the electron dynamics. This way, we treat  $\{R\}$  as fixed parameters in  $\phi(\{R\}, \{r\})$ . By this approximation, the first two terms in the sum are equal to zero, giving

$$-\frac{1}{2} \sum_{A=1}^{m} \frac{\nabla_A^2}{M_A} (\phi \chi) \approx -\frac{1}{2} \sum_{A=1}^{m} \frac{\phi \nabla_A^2 \chi}{M_A}.$$
 (2.93)

Using this result in the Schrödinger equation (2.91):

$$-\frac{\chi}{2} \sum_{i}^{n} \nabla_{i}^{2} \phi - \frac{\phi}{2} \sum_{A}^{m} \frac{\nabla_{A}^{2}}{M_{A}} \chi + \sum_{A>B}^{m} \frac{Z_{A} Z_{B}}{R_{AB}} \phi \chi - \sum_{A=1}^{m} \sum_{i=1}^{n} \frac{Z_{A}}{R_{Ai}} \phi \chi + \sum_{i>j}^{n} \frac{1}{r_{ij}} \phi \chi = E \phi \chi. \quad (2.94)$$

It is now possible to separate the complete Schrödinger equation of the system into nuclear and electronic equations, and for this we divide both sides by  $\phi \chi$ ,

$$-\frac{1}{2\phi}\sum_{i}^{n}\nabla_{i}^{2}\phi - \sum_{A=1}^{m}\sum_{i=1}^{n}\frac{Z_{A}}{R_{Ai}} + \sum_{i>i}^{n}\frac{1}{r_{ij}} = E + \frac{1}{2\chi}\sum_{A}^{m}\frac{\nabla_{A}^{2}}{M_{A}}\chi - \sum_{A>B}^{m}\frac{Z_{A}Z_{B}}{R_{AB}} = \epsilon(\{\mathbf{R}\}). \quad (2.95)$$

The isolated electronic equation is then:

$$-\frac{1}{2\phi} \sum_{i}^{n} \nabla_{i}^{2} \phi - \sum_{A=1}^{m} \sum_{i=1}^{n} \frac{Z_{A}}{R_{Ai}} + \sum_{i>j}^{n} \frac{1}{r_{ij}} = \epsilon(\{\mathbf{R}\})$$

$$-\frac{1}{2} \sum_{i}^{n} \nabla_{i}^{2} \phi - \sum_{A=1}^{m} \sum_{i=1}^{n} \frac{Z_{A}}{R_{Ai}} \phi + \sum_{i>j}^{n} \frac{\phi}{r_{ij}} = \epsilon(\{\mathbf{R}\}) \phi,$$
(2.96)

that can be rewritten isolating  $\phi$ , as

$$\left(-\frac{1}{2}\sum_{i}^{n}\nabla_{i}^{2}-\sum_{A=1}^{m}\sum_{i=1}^{n}\frac{Z_{A}}{R_{Ai}}+\sum_{i>j}^{n}\frac{1}{r_{ij}}\right)\phi(\{\mathbf{R}\},\{\mathbf{r}\})=\epsilon(\{\mathbf{R}\})\phi(\{\mathbf{R}\},\{\mathbf{r}\}),$$
 (2.97)

being this, finally, the Schrödinger equation for the electronic Hamiltonian, which gives us the electronic properties of the system:

$$\hat{H}_{el} |\Phi(\{\mathbf{R}\}, \{\mathbf{r}\})\rangle = \epsilon(\{\mathbf{R}\}) |\Phi(\{\mathbf{R}\}, \{\mathbf{r}\})\rangle. \tag{2.98}$$

The nuclear equation is obtained as:

$$E + \frac{1}{2\chi} \sum_{A}^{m} \frac{\nabla_{A}^{2}}{M_{A}} \chi - \sum_{A>B}^{m} \frac{Z_{A}Z_{B}}{R_{AB}} = \epsilon(\{\mathbf{R}\})$$

$$E\chi + \frac{1}{2} \sum_{A}^{m} \frac{\nabla_{A}^{2}}{M_{A}} \chi - \sum_{A>B}^{m} \frac{Z_{A}Z_{B}}{R_{AB}} \chi = \epsilon(\{\mathbf{R}\}) \chi$$

$$-\frac{1}{2} \sum_{A}^{m} \frac{\nabla_{A}^{2}}{M_{A}} \chi + \sum_{A>B}^{m} \frac{Z_{A}Z_{B}}{R_{AB}} \chi + \epsilon(\{\mathbf{R}\}) \chi = E\chi,$$

$$(2.99)$$

where the second and third terms of the equation are regarded as the potential  $\hat{V}(\{R\})$ . Giving form to the final Schrödinger equation for the nuclear Hamiltonian

$$-\frac{1}{2} \sum_{A}^{m} \frac{\nabla_{A}^{2}}{M_{A}} \chi + \hat{V}(\{\mathbf{R}\}) \chi = E \chi$$

$$\hat{H}_{n} |\chi(\{\mathbf{R}\})\rangle = E |\chi(\{\mathbf{R}\})\rangle,$$
(2.100)

being the one responsible for the description of the system's dynamics.

To obtain the second quantization of the electronic Hamiltonian, the one of most interest in this study, we shall expand it as the sum of one-body and two-body field operators:

$$\hat{H} = \hat{T} + \hat{V}_{ext} + \hat{W}, \tag{2.101}$$

where  $\hat{T}$ ,  $\hat{V}_{ext}$  and  $\hat{W}$  are operators that represent the kinetic energy, the external potential interaction and the electron-electron interaction, respectively. These become:

$$\hat{T} = \sum_{i=1}^{N} \frac{(-i\hbar \nabla_i)^2}{2} = -\frac{\hbar^2}{2} \sum_{\boldsymbol{\sigma} = \uparrow, \downarrow} \int d^3 r \hat{\Psi}^{\dagger}(\boldsymbol{r}\boldsymbol{\sigma}) \nabla^2 \hat{\Psi}(\boldsymbol{r}\boldsymbol{\sigma}), \qquad (2.102)$$

$$\hat{W} = \frac{1}{2} \sum_{\substack{i,j=1\\i\neq j}}^{N} w(\boldsymbol{r}_i, \boldsymbol{r}_j) = \frac{1}{2} \sum_{\boldsymbol{\sigma}, \boldsymbol{\sigma}' = \uparrow, \downarrow} \int d^3 r \int d^3 r' \hat{\Psi}^{\dagger}(\boldsymbol{r}\boldsymbol{\sigma}) \hat{\Psi}^{\dagger}(\boldsymbol{r}'\boldsymbol{\sigma}') w(\boldsymbol{r}, \boldsymbol{r}') \hat{\Psi}(\boldsymbol{r}'\boldsymbol{\sigma}') \hat{\Psi}(\boldsymbol{r}\boldsymbol{\sigma}),$$
(2.103)

and,

$$\hat{V}_{ext} = \sum_{i=1}^{N} v_{ext}(\boldsymbol{r}_i) = \int d^3 r v_{ext}(\boldsymbol{r}) \hat{n}(\boldsymbol{r}). \tag{2.104}$$

Here, all we are doing is the zero-temperature formalism. We used the field operators, previously discussed in the quantum theory section,  $\hat{\Psi}(r\sigma)$ , which describes the creation and annihilation operators of particles with spin  $\sigma$  and position r. Also, the electron density is represented as:

$$\hat{n}(\mathbf{r}) = \sum_{i}^{N} \delta^{3}(\mathbf{r} - \mathbf{r}_{i}) = \sum_{\sigma = \uparrow, \downarrow} \hat{\Psi}^{\dagger}(\mathbf{r}\boldsymbol{\sigma})\hat{\Psi}(\mathbf{r}\boldsymbol{\sigma}). \tag{2.105}$$

The solution for the electronic equation (2.98), as well as for the nuclear equation (2.100), demands a formidable computational cost as we increase the number of nuclei and electrons in the system. A variety of approaches have been developed to obtain approximate solutions, the oldest, the Hartree-Fock approximation (HARTREE; HARTREE, 1935). Density functional theory (DFT) is a more recent and computationally accessible method, and it is the core methodology of this research. Before further exploration into this subject, there are still some necessary concepts to be understood about solids.

The vacuum state of the fermionic Fock space, where the electrons are usually represented, is called the zero-electron vacuum, but here we work with a different approach; the Fermi vacuum. Also called the Fermi sea, it is the independent-electron ground state in which all the electrons occupy the lowest-energy spin-orbitals. In a ground state configuration, the Fermi level separates occupied from unoccupied states.

In that approach, the independent-particle excited states are described by the difference of their occupation number with respect to the highest occupied state vector in the Fermi sea. This perspective leads to the notion of holes under the Fermi sea when an electron is affected by the annihilation operator below the Fermi level. The same operator that annihilates an electron over the Fermi level is equivalent to a creation operator of a quasi-particle called "electron hole", of positive charge e. An excitation of an electron from under the Fermi level to a state above it is described by the annihilation of that electron state and the creation of the excited state, but the annihilation in the Fermi sea is equivalent to a hole creation, so the result is a neutral pair composed of an electron and a hole that interacts electrostatically, which is considered a bosonic quasi-particle called "exciton". Quasi-particles are very common in the quantum description of matter, and another essential one is discussed in the following, when we explore the vibrations of the lattice.

2.10. Phonons 85

### 2.10 Phonons

Of great importance when discussing real solids is to not simply consider them as a lattice of atoms with fixed positions, as in reality those atoms are vibrating in constant search for equilibrium, the lowest energy configuration. This vibrating system can be best understood as a coupled harmonic oscillator (KITTEL, 2004), which for simplicity of first approach we shall discuss as a one-dimensional set of equally spaced atoms with equal mass. The Hamiltonian of this system is written as

$$H = \sum_{s}^{n} \left[ \frac{1}{2M} \hat{p}_{s}^{2} + \frac{1}{2} C(\hat{q}_{s+1} - \hat{q}_{s})^{2} \right], \qquad (2.106)$$

where  $\hat{q}_s$  and  $\hat{p}_s$  are the position and momentum of the s-th atom, and C is the elastic force constant of the system.

The energy of a lattice vibration is quantized. In analogy with the quantization of the electromagnetic wave, we call the lattice vibrational quanta as a bosonic quasi-particle called "phonon". For further discussion, we must express the position and momentum operators in Bloch form (2.40),

$$\hat{q}_s = \frac{1}{\sqrt{N}} \sum_k \hat{Q}_k e^{iksa}$$
  $\hat{p}_s = \frac{1}{\sqrt{N}} \sum_k \hat{P}_k e^{-iksa},$  (2.107)

where  $\hat{Q}_k$  and  $\hat{P}_k$  are phonon coordinates correspondent to the displacement and momentum of the lattice vibration in the reciprocal space. From that we observe that a phonon is a collective mode of the entire lattice instead of being associated with single atoms.

The inverse transformations are:

$$\hat{Q}_k = \frac{1}{\sqrt{N}} \sum_s \hat{q}_s e^{-iksa} \qquad \qquad \hat{P}_k = \frac{1}{\sqrt{N}} \sum_s \hat{p}_s e^{iksa}, \qquad (2.108)$$

such that the commutation relations are respected:

$$[\hat{Q}_{k'}, \hat{P}_{k}] = \frac{1}{N} \left[ \sum_{s'} \hat{q}_{s'} e^{-ik's'a}, \sum_{s} \hat{p}_{s} e^{iksa} \right]$$

$$= \frac{1}{N} \sum_{s'} \sum_{s} [q_{s'} p_{s}] e^{-i(k's'-ks)a}$$

$$= \frac{1}{N} i\hbar \sum_{s} e^{-i(k'-k)sa} = i\hbar \delta_{k,k'}.$$
(2.109)

Now, the Hamiltonian (2.106) can be expressed in phonon coordinates as

$$H = \frac{1}{N} \sum_{s}^{n} \sum_{k} \sum_{k'} \left[ \frac{1}{2M} \hat{P}_{k} \hat{P}_{k'} e^{-i(k+k')sa} + \frac{1}{2} C(\hat{Q}_{k} e^{ik(s+1)a} - \hat{Q}_{k} e^{iksa}) (\hat{Q}_{k'} e^{ik'(s+1)a} - \hat{Q}_{k'} e^{ik'sa}) \right]$$

$$= \frac{1}{N} \sum_{s}^{n} \sum_{k} \sum_{k'} \left[ \frac{1}{2M} \hat{P}_{k} \hat{P}_{k'} e^{-i(k+k')sa} + \frac{1}{2} C\hat{Q}_{k} \hat{Q}_{k'} e^{iksa} (e^{ika} - 1) e^{ik'sa} (e^{ik'a} - 1) \right]$$

$$= \sum_{k} \left[ \frac{1}{2M} \hat{P}_{-k} \hat{P}_{k} + C\hat{Q}_{-k} \hat{Q}_{k} (1 - \cos(ka)) \right].$$

$$(2.110)$$

The angular frequency is now introduced as

$$\omega_k \equiv \sqrt{\frac{2C}{M}(1 - \cos(ka))},\tag{2.111}$$

so the final form of the Hamiltonian in phonon coordinates can be written as

$$\hat{H} = \sum_{k} \left[ \frac{1}{2M} \hat{P}_{-k} \hat{P}_{k} + \frac{1}{2} M \omega_{k}^{2} \hat{Q}_{-k} \hat{Q}_{k} \right]. \tag{2.112}$$

The equations of motion are then found using the commutation relations,

$$[\hat{Q}_k, H] = i\hbar \dot{\hat{Q}}_k,$$
  $[\dot{\hat{Q}}_k, H] = i\hbar \dot{\hat{Q}}_k,$ 

so we may find

$$\ddot{\hat{Q}}_k + \omega_k^2 \hat{Q}_k = 0, \tag{2.113}$$

which is the equation of motion for a harmonic oscillator of frequency  $\omega_k$ . The energy of such mode of vibration is

$$E_k = \left(n_k + \frac{1}{2}\right)\hbar\omega_k,\tag{2.114}$$

where  $n_k$  is the occupation number of the vibrational mode, i.e., the number of phonons in that state. The term  $\frac{1}{2}\hbar\omega_k$  is the contribution of frequency  $\omega_k$  to the zero point energy, which is the vibrational energy of the system at zero Kelvin. That is not a statement to be left unnoticed, that due to the uncertainty relation between position and momentum, a system vibrates even at zero Kelvin.

As seen in the quantum theory section, the occupation number operator may be written in terms of creation and annihilation operators. In that perspective, we may rewrite the Hamiltonian (2.112) as

2.10. Phonons 87

$$\hat{H} = \sum_{k} \left( \hat{a}_k^{\dagger} \hat{a}_k + \frac{1}{2} \right) \hbar \omega_k, \tag{2.115}$$

where the bosonic creation and annihilation operators are responsible for creating and annihilating phonon states in each mode of vibration. They are thus defined as

$$\hat{a}_{k}^{\dagger} = \frac{1}{\sqrt{2\hbar}} \left( \sqrt{M\omega_{k}} \hat{Q}_{-k} - i \frac{1}{\sqrt{M\omega_{k}}} \hat{P}_{k} \right) \qquad \hat{a}_{k} = \frac{1}{\sqrt{2\hbar}} \left( \sqrt{M\omega_{k}} \hat{Q}_{k} + i \frac{1}{\sqrt{M\omega_{k}}} \hat{P}_{-k} \right). \tag{2.116}$$

We might also write the phonon coordinates in terms of creation and annihilation operators;

$$\hat{Q}_k = \sqrt{\frac{\hbar}{2M\omega_k}} \left( \hat{a}_k + \hat{a}_{-k}^{\dagger} \right) \qquad \hat{P}_k = i\sqrt{\frac{\hbar M\omega_k}{2}} \left( \hat{a}_k^{\dagger} - \hat{a}_{-k} \right). \tag{2.117}$$

# 3 DFT

# 3.1 What is Density Functional Theory

# 3.2 The Many-Body Problem

To begin our discussion on the foundations of DFT, we first recall something explored in the solid state chapter: The second quantized form of the nonrelativistic Hamiltonian of a stationary system of N interacting electrons or, in general, spin- $\frac{1}{2}$  particles.

$$\hat{H} = \hat{T} + \hat{W} + \hat{V}_{\text{ext}},\tag{3.1}$$

where  $\hat{T}$ ,  $\hat{W}$  and  $\hat{V}_{\text{ext}}$  are operators for the kinetic energy, electron-electron interaction, and external potential interaction, respectively. Those are:

$$\hat{T} = \sum_{i=1}^{N} \frac{(-i\hbar \nabla_i)^2}{2m} = -\frac{\hbar^2}{2m} \sum_{\sigma=\uparrow,\downarrow} \int d^3 r \hat{\Psi}^{\dagger}(\boldsymbol{r}\boldsymbol{\sigma}) \nabla^2 \hat{\Psi}(\boldsymbol{r}\boldsymbol{\sigma}), \tag{3.2}$$

$$\hat{W} = \frac{1}{2} \sum_{\substack{i,j=1\\i\neq j}}^{N} w(\boldsymbol{r}_{i}, \boldsymbol{r}_{j}) = \frac{1}{2} \sum_{\boldsymbol{\sigma}, \boldsymbol{\sigma}' = \uparrow, \downarrow} \int d^{3}r \int d^{3}r' \hat{\Psi}^{\dagger}(\boldsymbol{r}\boldsymbol{\sigma}) \hat{\Psi}^{\dagger}(\boldsymbol{r}'\boldsymbol{\sigma}') w(\boldsymbol{r}, \boldsymbol{r}') \hat{\Psi}(\boldsymbol{r}'\boldsymbol{\sigma}') \hat{\Psi}(\boldsymbol{r}\boldsymbol{\sigma}'),$$
(3.3)

and,

$$\hat{V}_{\text{ext}} = \sum_{i=1}^{N} v_{\text{ext}}(\boldsymbol{r}_i) = \int d^3 r v_{\text{ext}}(\boldsymbol{r}) \hat{n}(\boldsymbol{r}).$$
 (3.4)

Being the electron density,

$$\hat{n}(\mathbf{r}) = \sum_{i}^{N} \delta^{3}(\mathbf{r} - \mathbf{r}_{i}) = \sum_{\boldsymbol{\sigma} = \uparrow \perp} \hat{\Psi}^{\dagger}(\mathbf{r}\boldsymbol{\sigma})\hat{\Psi}(\mathbf{r}\boldsymbol{\sigma}). \tag{3.5}$$

The form of the electron-electron interaction, characterized by  $w(\mathbf{r}, \mathbf{r}')$ , is not relevant for the DFT formalism. We only assume that  $w(\mathbf{r}, \mathbf{r}')$  is symmetric and independent of spin, as we see in Coulomb interaction. The external potential interaction  $v_{\text{ext}}$  is also an arbitrary function of  $\mathbf{r}$ , but we usually work with the electron-nuclei interaction present in (2.83). Latter, we shall include the presence of external electromagnetic fields, and beyond that, we shall redefine this external potential operator when we start working with

pseudopotentials. (ENGEL; DREIZLER, 2011)

# 3.3 Hohenberg-Kohn Theorem

The eigenstates  $|\Psi_k\rangle$  for the many-body Hamiltonian are then obtained as the solution of the stationary Schrödinger equation,

$$\hat{H} |\Psi_k\rangle = E_K |\Psi_k\rangle. \tag{3.6}$$

From the resulting eigenstates, there is one in particular to which we shall focus our attention. The ground state  $|\Psi_0\rangle$ .

In this first approach, we consider only non-degenerate ground states. Those states can be obtained by a set of possible Hamiltonians, i.e., a set of local potentials  $v_{\rm ext}$ . Fundamentally, this set of potentials includes not only physical potentials, but an infinity of pure mathematical constructs. Also, we must keep in mind that adding a constant to any potential  $v_{\rm ext}(\mathbf{r})$  leads to the same ground state, so both potentials are physically equivalent. In a similar way, any ground state  $|\Psi_0\rangle$  is physically equivalent to itself multiplied by a phase factor  $e^{i\theta} |\Psi_0\rangle$ .

The solution of the Scrödinger equation is therefore a map A between the set  $\mathscr{V}$  of potentials  $v_{\rm ext}$ , and the set  $\mathscr{G}$  of ground states  $|\Psi_0\rangle$ ; (ENGEL; DREIZLER, 2011)

$$A: \mathcal{V} \to \mathcal{G}. \tag{3.7}$$

This mapping process can be extended. Let us now introduce the ground state electron density,

$$n_{0}(\mathbf{r}) = \langle \Psi_{0} | \hat{n}(\mathbf{r}) | \Psi_{0} \rangle = \sum_{\sigma = \uparrow \downarrow} \int d^{3}r \, \langle \Psi_{0} | \hat{\Psi}^{\dagger}(\mathbf{r}\boldsymbol{\sigma}) \hat{\Psi}(\mathbf{r}\boldsymbol{\sigma}) | \Psi_{0} \rangle$$

$$= \sum_{\sigma,\sigma',\sigma''=\uparrow\downarrow} \int d^{3}r d^{3}r' \, d^{3}r'' \, \langle \Psi_{0} | \mathbf{r}'\boldsymbol{\sigma}' \rangle \, \langle \mathbf{r}'\boldsymbol{\sigma}' | \hat{\Psi}^{\dagger}(\mathbf{r}\boldsymbol{\sigma}) \hat{\Psi}(\mathbf{r}\boldsymbol{\sigma}) | \mathbf{r}''\boldsymbol{\sigma}'' \rangle \, \langle \mathbf{r}''\boldsymbol{\sigma}'' | \Psi_{0} \rangle$$

$$= \sum_{\sigma,\sigma',\sigma''=\uparrow\downarrow} \int d^{3}r \, d^{3}r' \, d^{3}r'' \, \langle \Psi_{0} | \mathbf{r}'\boldsymbol{\sigma}' \rangle \, \delta_{\sigma,\sigma'}\delta_{\sigma,\sigma''}\delta(\mathbf{r} - \mathbf{r}') \delta(\mathbf{r} - \mathbf{r}'') \, \langle \mathbf{r}''\boldsymbol{\sigma}'' | \Psi_{0} \rangle$$

$$= \sum_{\sigma=\uparrow\downarrow} \int d^{3}r \, |\langle \mathbf{r}\boldsymbol{\sigma} | \Psi_{0} \rangle|^{2}, \qquad (3.8)$$

where for a system of N particles, we write:

$$n_0(\boldsymbol{r}_1, ..., \boldsymbol{r}_N) = \sum_{\sigma_1, ..., \sigma_N} \int d^3 r_1 ... d^3 r_N |\langle \boldsymbol{r}_1 \boldsymbol{\sigma}_1 | \otimes ... \otimes \langle \boldsymbol{r}_N \boldsymbol{\sigma}_N | \Psi_0 \rangle|^2.$$
(3.9)

This indicates we may define a second map B between the set  $\mathscr{G}$  and the set  $\mathscr{N}$  of all ground state electron densities  $n_0$ ;

$$B: \mathcal{G} \to \mathcal{N}.$$
 (3.10)

Both maps A and B are surjective by construction, but they are also injective (ENGEL; DREIZLER, 2011), thus unique. Figure 18 illustrates these maps.

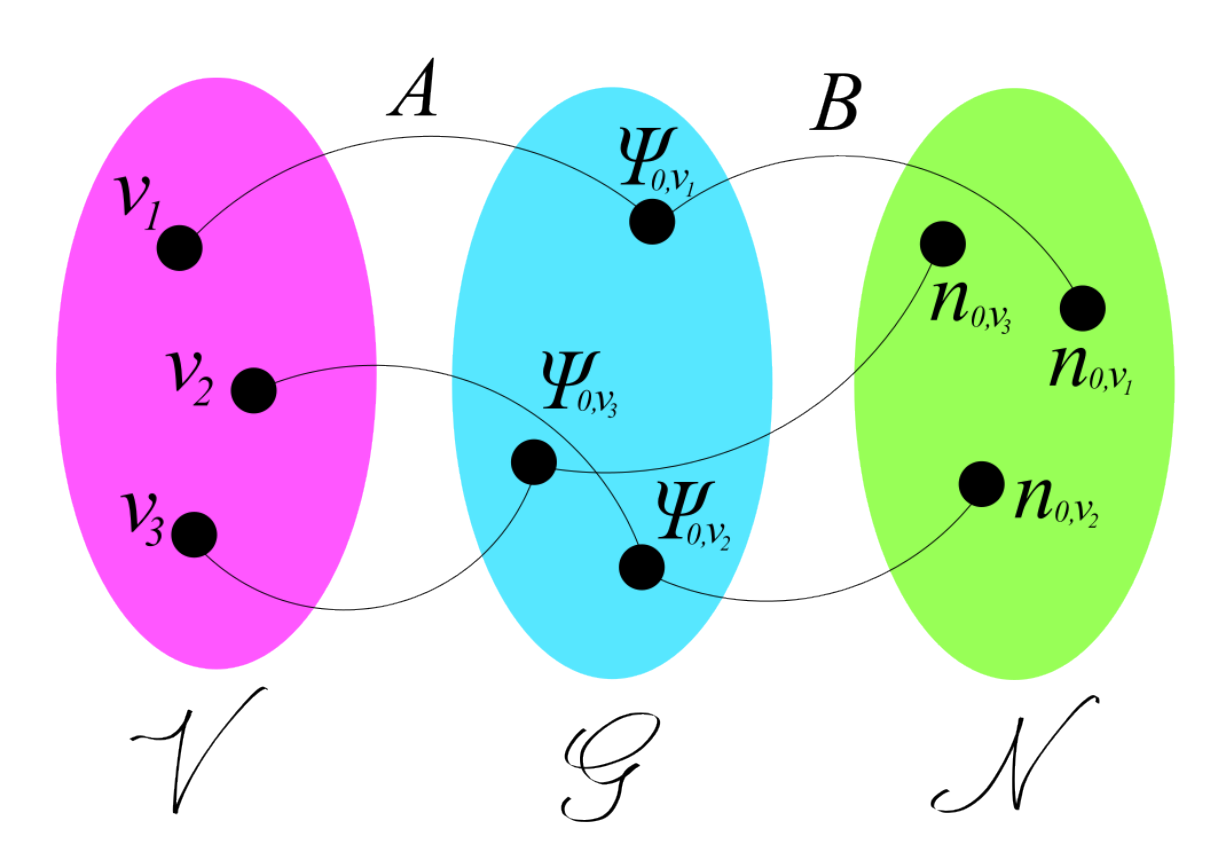


Figure 18 – Mapping between potentials, ground states, and ground state electron densities sets.

Now, we are ready to discuss the fundamental statements of the Hohenberg-Kohn theorem:

As illustrated in Figure 18,  $v_{\text{ext}}$ ,  $|\Psi_0\rangle$ , and  $n_0$  uniquely determine each other. The first Hohenberg-Kohn theorem states that the ground state can be obtained as a unique functional of the ground state electron density,

$$|\Psi_0\rangle = |\Psi[n_0]\rangle. \tag{3.11}$$

This functional is a realization of the map  $B^{-1}$ , and it applies to atoms, molecules, or solids, i.e., it is a universal functional.

As a consequence of the above, we also have that any observable ground state is a density functional, in particular, the ground state energy,

$$E_0 = E[n_0] := \langle \Psi[n_0] | \hat{H} | \Psi[n_0] \rangle = \langle \Psi[n_0] | \hat{T} + \hat{W} | \Psi[n_0] \rangle + \int d^3 r v_{\text{ext}}(\boldsymbol{r}) n_0(\boldsymbol{r}). \quad (3.12)$$

From the variational principle, the second Hohenberg-Kohn theorem states that the true ground state is the one that has the minimum value for E[n], i.e.,

$$E_0 = \min_{n \in \mathcal{N}} E[n]. \tag{3.13}$$

Having seen both Hohenberg-Kohn theorems, we entered into DFT theory knowing that there is a mapping between ground states, external potentials, and ground state electron densities. The choice of an external potential is uniquely tied to some ground state configuration. Ritz variational principle (RITZ, 1909) states that the ground state energy of the system is minimized when the electron distribution is such that it is the exact ground state density. In this scenario, the goal of DFT is to find the electron density that minimizes the ground state energy. Because of the co-dependency of the ground state and the ground state electron density, we feel invited to an iterative method in search for the minimum ground state energy (3.13).

Nevertheless, all the arguments so far have considered the inexistence of degenerate ground states. The elaboration is not that different, but to grasp the complete picture of DFT, we must start redefining the set of possible  $v_{\text{ext}}$ ,  $\mathcal{V}$ .

$$\mathscr{V} = \{ v_{\text{ext}} \mid v_{\text{ext}} \text{ multiplicative}, v_{\text{ext}}(\mathbf{r}) \neq v'_{\text{ext}}(\mathbf{r}) + const \}, \tag{3.14}$$

that can generate a set  $\mathscr{G}$  composed of  $n_g$  degenerate ground states  $|\Psi_{0,i}\rangle$ :

$$\mathscr{G} = \bigcup_{v_{\text{ext}}} \mathscr{G}_{v_{\text{ext}}}, \qquad \mathscr{G}_{v_{\text{ext}}} = \left\{ |\Psi\rangle \mid |\Psi_0\rangle = \sum_{i=1}^{n_g} c_i |\Psi_{0,i}\rangle \right\}. \tag{3.15}$$

The set of ground states is then associated with a set of ground state electron densities  $\mathcal{N}$ :

$$\mathcal{N} = \bigcup_{v_{\text{ext}}} \mathcal{N}_{v_{\text{ext}}}, \qquad \mathcal{N}_{v_{\text{ext}}} = \left\{ n(\boldsymbol{r}) \mid n(\boldsymbol{r}) = \langle \Psi_0 | \hat{n}(\boldsymbol{r}) | \Psi_0 \rangle, |\Psi_0 \rangle \in \mathcal{G}_{v_{\text{ext}}} \right\}.$$
(3.16)

Despite considering degenerate ground states, there still exists a one-to-one correspondence between any potential  $v_{\text{ext}}$  to a subset  $\mathcal{G}_{v_{\text{ext}}}$  of all the correspondent ground states, as well as to the subset  $\mathcal{N}_{v_{\text{ext}}}$  of ground state electron densities, generated from these ground states. The mapping between these sets is represented in Figure 19:

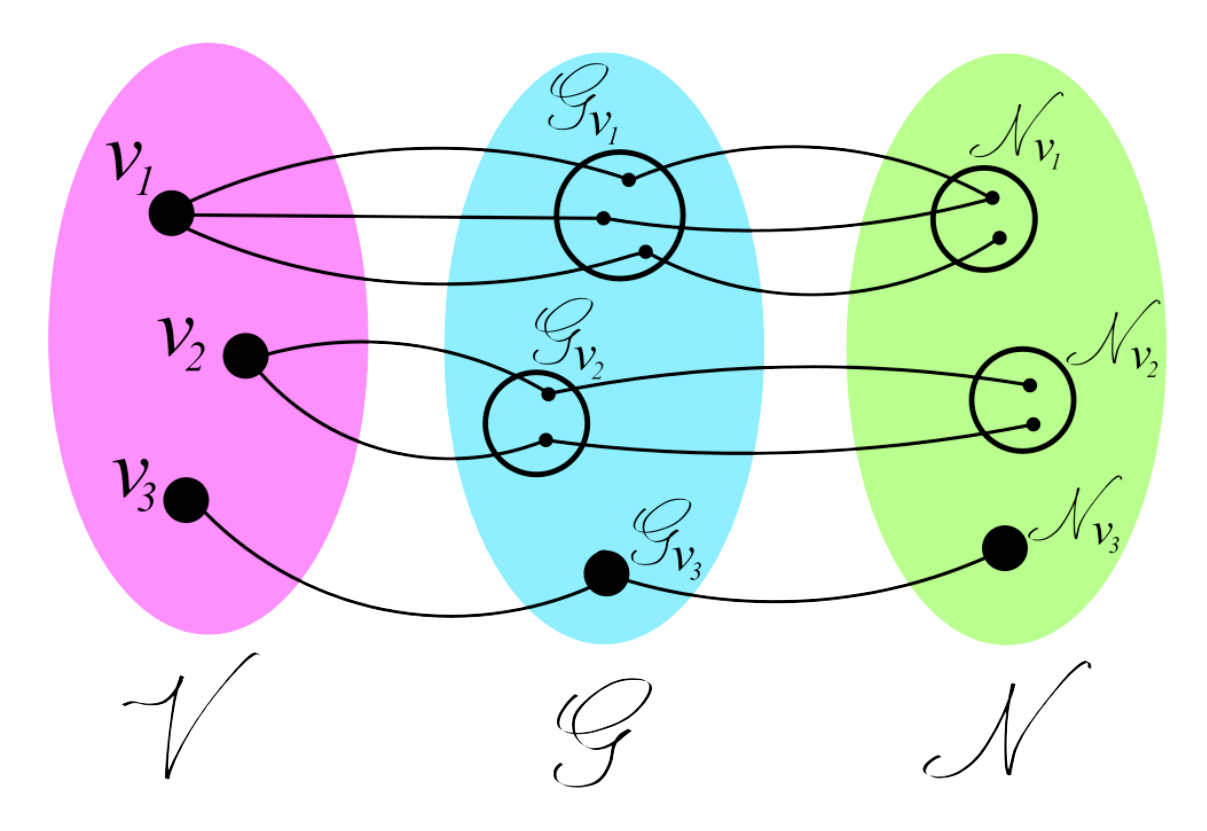


Figure 19 – Mapping between the external potentials and the corresponding set of ground states and ground state densities, considering degenerate cases.

The subsets  $\mathscr{G}_{v_{\text{ext}}}$  and  $\mathscr{N}_{v_{\text{ext}}}$  for different  $v_{\text{ext}}$  are disjoint, and from each element in  $\mathscr{N}_{v_{\text{ext}}}$  we can identify the corresponding  $\mathscr{G}_{v_{\text{ext}}}$  and  $v_{\text{ext}}$ . However, we note that it is not impossible to obtain the same density from two different elements in a subset  $\mathscr{G}_{v_{\text{ext}}}$ , but that is not a problem since we are only concerned with obtaining an energy functional  $E[n_0]$ , and the energy of any ground state is equal by definition.

$$E[n_0(\mathbf{r})] = \langle \Psi[n_0(\mathbf{r})] | \hat{H} | \Psi[n_0(\mathbf{r})] \rangle, \qquad (3.17)$$

which is unambiguous for all  $n_0(\mathbf{r})$  in the set. The second Hohenberg-Kohn theorem, the minimum principle 3.13, is still valid for the degenerate energy functional.

The fact that a ground state electron density  $n_0(\mathbf{r})$  corresponds to a unique external potential implies that finding the ground state density also determines all excited states, which is due to the solutions of the Schrödinger equation being unambiguously defined by  $v_{ext}$ :

$$n_0(\mathbf{r}) \to v_{\text{ext}} \to |\Psi_i\rangle, i = 0, 1, ..., \infty.$$
 (3.18)

The formalism being developed so far can be extended to include not only the electrostatic external potential  $v_{\text{ext}}$ , but also an external magnetic field  $\mathbf{B}_{\text{ext}}$ . Now we work on spin-polarized systems, which are described by the Hamiltonian:

$$\hat{H} = \hat{T} + \hat{W} + \int d^3r \{v_{\text{ext}}(\mathbf{r})\hat{n}(\mathbf{r}) + \mathbf{B}_{\text{ext}}(\mathbf{r}) \cdot \hat{\mathbf{m}}(\mathbf{r})\}, \tag{3.19}$$

where the operator of magnetization density,  $\hat{\boldsymbol{m}}(\boldsymbol{r}) = \mu_{\beta} \sum_{i=1}^{N} \sigma_{i} \delta^{(3)}(\boldsymbol{r} - \boldsymbol{r}_{i})$ , can be written in terms of field operators as:

$$\hat{\boldsymbol{m}}(\boldsymbol{r}) = \mu_{\beta} \sum_{\boldsymbol{\sigma}, \boldsymbol{\sigma}' = \uparrow, \downarrow} \hat{\Psi}^{\dagger}(\boldsymbol{r}\boldsymbol{\sigma}) \boldsymbol{\sigma}_{\boldsymbol{\sigma}, \boldsymbol{\sigma}'} \hat{\Psi}(\boldsymbol{r}\boldsymbol{\sigma}'), \tag{3.20}$$

being the Bohr magneton,  $\mu_{\beta} = \frac{|e|\hbar}{2mC}$ , and the vector of Pauli matrices,  $\sigma_{\sigma,\sigma'}$ , whose components can be expressed as:

$$\sigma_{x,\sigma\sigma'} = \delta_{\sigma',-\sigma}; \qquad \sigma_{y,\sigma\sigma'} = isign(\sigma')\delta_{\sigma',-\sigma}; \qquad \sigma_{\sigma\sigma'} = sign(\sigma)\delta_{\sigma',\sigma}.$$
 (3.21)

Just as the ground state electron density, we may define the ground state magnetization density,

$$\hat{\boldsymbol{m}}_0(\boldsymbol{r}) = \langle \Psi_0 | \, \hat{\boldsymbol{m}}(\boldsymbol{r}) \, | \Psi_0 \rangle \,. \tag{3.22}$$

Two different ground states  $|\Psi_0\rangle$  and  $|\Psi'_0\rangle$  from the set of all possible ground states will always lead to  $(n_0, \mathbf{m}_0)$  and  $(n'_0, \mathbf{m}'_0)$  with the condition  $\delta_{n_0, n'_0} \delta_{\mathbf{m}_0, \mathbf{m}'_0} = 0$ , i.e.,  $|\Psi_0\rangle$  is a unique functional of  $(n_0, \mathbf{m}_0)$ ,

$$|\Psi_0\rangle = |\Psi[n_0, \boldsymbol{m}_0]\rangle. \tag{3.23}$$

We can use the functional  $|\Psi[n_0, \boldsymbol{m}_0]\rangle$  to define the spin-polarized energy functional

$$E[n, \mathbf{m}] = \langle \Psi[n_0, \mathbf{m}_0] | \hat{T} + \hat{W} | \Psi[n_0, \mathbf{m}_0] \rangle + \int d^3 r \{ v_{ext}(\mathbf{r}) \hat{n}(\mathbf{r}) + \mathbf{B}_{ext}(\mathbf{r}) \cdot \hat{\mathbf{m}}(\mathbf{r}) \},$$
(3.24)

which satisfies the minimum principle

$$E[n_0, \boldsymbol{m}_0] < E[n, \boldsymbol{m}] \quad \forall \quad (n, \boldsymbol{m}) \neq (n_0, \boldsymbol{m}_0).$$
 (3.25)

# 3.4 Kohn-Sham Equations

So far, we have discussed the fundamental concepts that led us to the electronic ground state by minimization of  $E[n_0, \mathbf{m}_0]$ . The Schrödinger equation (3.6), which gives the electronic states used in the construction of the electron density (3.5), consists of a many-body problem that is computationally demanding beyond our current capabilities. Maybe in the future, quantum computation may help us in this approach (SEELEY; RICHARD; LOVE, 2012), but to the present day we still need a simplification of the question. The Kohn-Sham equations (KOHN; SHAM, 1965) provide us with a substitute system of single-particle nature, which converges to the same electron density of the Schrödinger problem, still accounting for the electron-electron interactions. The answer we seek is from an interacting system, but instead we obtain a single-particle system that mimics the electron density of the interacting one. The identical electron density can thus be mapped to the exact ground state energy and used to evaluate physical properties.

To first begin the construction of the Kohn-Sham equations, let us simply start defining a system of noninteracting electrons,

$$\hat{H}_{KS} = \hat{T}_{KS} + \hat{V}_{KS},$$
 (3.26)

with a multiplicative effective potential  $v_{\rm KS}$  given in

$$\hat{V}_{KS} = \int d^3 r \hat{n}(\mathbf{r}) v_{KS}. \tag{3.27}$$

An N-particle ground state for this system, first assumed as nondegenerate, is defined as a determinant of single-particle states, a Slater determinant,

$$\Phi_{0}(\boldsymbol{r}_{1}\boldsymbol{\sigma}_{1},...,\boldsymbol{r}_{N}\boldsymbol{\sigma}_{N}) \equiv \langle \boldsymbol{r}_{1}\boldsymbol{\sigma}_{1} | \otimes ... \otimes \langle \boldsymbol{r}_{N}\boldsymbol{\sigma}_{N} | \Phi_{0} \rangle 
= \frac{1}{\sqrt{N!}} \det \begin{pmatrix} \phi_{1}(\boldsymbol{r}_{1}\boldsymbol{\sigma}_{1}) & \dots & \phi_{N}(\boldsymbol{r}_{1}\boldsymbol{\sigma}_{1}) \\ \vdots & \ddots & \vdots \\ \phi_{1}(\boldsymbol{r}_{N}\boldsymbol{\sigma}_{N}) & \dots & \phi_{N}(\boldsymbol{r}_{N}\boldsymbol{\sigma}_{N}) \end{pmatrix},$$
(3.28)

which is constructed from the lowest solutions  $\phi_i$  of the single-particle Schrödinger equation:

$$\left(-\frac{\hbar^2 \nabla^2}{2m} + v_{KS}\right) \phi_i(\boldsymbol{r}\boldsymbol{\sigma}) = E_i \phi_i(\boldsymbol{r}\boldsymbol{\sigma}). \tag{3.29}$$

The lowest solutions are considered as such for being the occupied states, i.e., the ones with eigenvalues below the Fermi level,  $E_i < \epsilon_F$ . The energy of the highest occupied state is often called the Fermi energy  $E_F$ . (ENGEL; DREIZLER, 2011)

The ground state electron density of such a system is given by

$$n_{0 \text{ KS}}(\boldsymbol{r}) = \sum_{\boldsymbol{\sigma}=\uparrow,\downarrow} \sum_{i=1}^{N} \Theta_{i} |\phi_{i}(\boldsymbol{r}\boldsymbol{\sigma})|^{2},$$
 (3.30)

where, for zero-temperature calculations, the theta function  $\Theta_i$  is defined as

$$\Theta_i = \delta(\epsilon_F - E_i) = \begin{cases} 1 & \text{for } E_i < \epsilon_F \\ 0 & \text{elsewhere} \end{cases}$$
 (3.31)

In the case of systems with T > 0, the theta function becomes a Fermi distribution,

$$\Theta_i = \left[1 + e^{\left(\frac{E_i - \mu}{k_{\rm B}T}\right)}\right],\tag{3.32}$$

being  $\mu$  the chemical potential, chosen to result in  $\sum_i \Theta_i = N$ .

Using the ground state electron density, the ground state energy is written as:

$$E_{0 \text{ KS}} = \sum_{i=1}^{N} \Theta_{i} \sum_{\boldsymbol{\sigma} = \uparrow, \downarrow} \int d^{3}r \phi_{i}^{*}(\boldsymbol{r}\boldsymbol{\sigma}) \frac{-\hbar^{2} \nabla^{2}}{2m} \phi_{i}(\boldsymbol{r}\boldsymbol{\sigma}) + \int d^{3}r v_{\text{KS}}(\boldsymbol{r}) n_{0 \text{ KS}}(\boldsymbol{r}).$$
(3.33)

As seen in the Hohenberg-Kohn theorems, this ground state can be obtained through the minimization of the functional:

$$E_{KS}[n] = \langle \Phi[n] | \hat{T}_{KS} + \hat{V}_{KS} | \Phi[n] \rangle. \tag{3.34}$$

An important implication is that  $\phi_i$  themselves are functionals of the density, which is uniquely defined by the effective potential  $v_{\rm KS}$ . Thus, the orbitals that compose the Slater determinant depend on  $v_{\rm KS}$  and can also be expressed as density functionals,  $\phi_i(\boldsymbol{r}\boldsymbol{\sigma}) = \phi_i[n](\boldsymbol{r}\boldsymbol{\sigma})$  (ENGEL; DREIZLER, 2011).

Considering that we want to find a  $v_{KS}$  that reflects the nature of the original interacting system, we decompose E[n] in a convenient form:

$$E[n] = T_{KS}[n] + E_{H}[n] + E_{ext}[n] + E_{xc}[n], \tag{3.35}$$

where the kinetic functional is

$$T_{KS}[n] = \sum_{i=1}^{N} \Theta_{i} \sum_{\boldsymbol{\sigma} = \uparrow, \downarrow} \int d^{3}r \phi_{i}^{*}(\boldsymbol{r}\boldsymbol{\sigma}) \frac{-\hbar^{2} \nabla^{2}}{2m} \phi_{i}(\boldsymbol{r}\boldsymbol{\sigma});$$
(3.36)

the classical energy from self-interactions and interactions between the N-particles is included in the Hartree term,

$$E_{\rm H} = \frac{1}{2} \int d^3r \int d^3r' n(\mathbf{r}) w(\mathbf{r}, \mathbf{r}') n(\mathbf{r}'); \qquad (3.37)$$

and the coupling between particles and the usual external potential is given in

$$E_{\text{ext}}[n] = \int d^3 r v_{\text{ext}}(\mathbf{r}) n(\mathbf{r}). \tag{3.38}$$

The last term, known as the exchange-correlation energy functional, is defined by construction as the term that absorbs all the so far neglected many-body effects, as the Pauli exclusion principle. We can declare  $E_{\rm xc}[n]$  as a density functional considering that the energy itself is a density functional, as well as all the other terms. In a rigorous approach, this decomposition could only be defined for densities that are noninteracting v-representable; discussion that will be left for the reference (ENGEL; DREIZLER, 2011). Further exploration of this convenient functional will be left to the next section.

To complete our construction of the method, we must still find a form for the  $v_{\rm KS}$  term, which uniquely defines the ground state density. For doing so, we start by proofing that the total energy functional is considerably insensitive to errors in the electron density. This fact is important for practical applications and should not be left unseen.

In order to evaluate the ground state energy functional of some electron density that is close to the ground state,

$$n(\mathbf{r}) = n_0(\mathbf{r}) + \delta n(\mathbf{r}), \tag{3.39}$$

we use a variational method:

$$E[n] = E[n_0] + \int d^3r \frac{\delta E}{\delta n(\mathbf{r})} \Big|_{n=n_0} \delta n(\mathbf{r}) + \mathcal{O}(\delta n^2).$$
 (3.40)

A fixed particle number N implies

$$\int d^3r n(\mathbf{r}) = \int d^3r n_0(\mathbf{r}) = N \to \int d^3r \delta n(\mathbf{r}) = 0, \tag{3.41}$$

which finally gives the result we intended to demonstrate, i.e., the sensitivity of the ground state energy functional due to small density variations is of second order:

$$E[n_0 + \delta n] - E[n_0] = \mathcal{O}(\delta n^2). \tag{3.42}$$

This result makes physical sense, since our approach intends to find a stable ground state configuration corresponding to the minimum of some functional.

Now, in order to find the final form of  $v_{KS}$ , we must only write equation (3.42) in a more explicit manner. The Hartree term (3.37) and the external potential energy functional (3.38) are quite straightforward:

$$E_{\mathrm{H}}[n_0 + \delta n] - E_{\mathrm{H}}[n_0] = \int d^3 \int d^3 r' \delta n(\mathbf{r}) w(\mathbf{r}, \mathbf{r}') n_0(\mathbf{r}') + \mathcal{O}(\delta n^2); \qquad (3.43)$$

$$E_{\text{ext}}[n_0 + \delta n] - E_{\text{ext}}[n_0] = \int d^3 r v_{\text{ext}}(\mathbf{r}) \delta n(\mathbf{r}). \tag{3.44}$$

The kinetic term (3.36) is explicitly dependent of the orbitals, which are unique functionals of the density,

$$T_{KS}[n_0 + \delta n] - T_{KS}[n_0] =$$
 (3.45)

$$= \frac{(-i\hbar)^2}{2m} \sum_{i,\sigma} \Theta_i \int d^3r \left\{ \delta \phi_i^*(\boldsymbol{r}\boldsymbol{\sigma}) \nabla^2 \phi_i(\boldsymbol{r}\boldsymbol{\sigma}) + \phi_i^*(\boldsymbol{r}\boldsymbol{\sigma}) \nabla^2 \delta \phi_i(\boldsymbol{r}\boldsymbol{\sigma}) \right\} + \mathscr{O}(\delta \phi^2)$$
(3.46)

The second term, integrated by parts, becomes

$$\frac{(-i\hbar)^2}{2m} \sum_{i,\sigma} \Theta_i \int d^3r \Big\{ \nabla \cdot (\phi_i^*(\boldsymbol{r}\boldsymbol{\sigma})\nabla\delta\phi_i(\boldsymbol{r}\boldsymbol{\sigma})) - \nabla\phi_i^*(\boldsymbol{r}\boldsymbol{\sigma}) \cdot \nabla\delta\phi_i(\boldsymbol{r}\boldsymbol{\sigma}) \Big\} = (3.47)$$

$$= \frac{(-i\hbar)^2}{2m} \sum_{i,\sigma} \Theta_i \Big\{ \iint d\mathbf{S} \cdot (\phi_i^*(\mathbf{r}\boldsymbol{\sigma})\nabla\delta\phi_i(\mathbf{r}\boldsymbol{\sigma})) - \int d^3r \nabla\phi_i^*(\mathbf{r}\boldsymbol{\sigma}) \cdot \nabla\delta\phi_i(\mathbf{r}\boldsymbol{\sigma}) \Big\}, \quad (3.48)$$

where, assuming zero surface contributions, the first term will vanish and the second can be written with partial integration, which reveals another surface contribution that can be neglected. The kinetic term can then be written as

$$T_{KS}[n_0 + \delta n] - T_{KS}[n_0] = (3.49)$$

$$= \frac{(-i\hbar)^2}{2m} \sum_{i,\sigma} \Theta_i \int d^3r \left\{ \delta \phi_i^*(\boldsymbol{r}\boldsymbol{\sigma}) \nabla^2 \phi_i(\boldsymbol{r}\boldsymbol{\sigma}) + \delta \phi_i(\boldsymbol{r}\boldsymbol{\sigma}) \nabla^2 \phi_i^*(\boldsymbol{r}\boldsymbol{\sigma}) \right\} + \mathcal{O}(\delta \phi^2). \tag{3.50}$$

Using the single-particle equations (3.29) inside the kinetic term gives:

$$T_{KS}[n_0 + \delta n] - T_{KS}[n_0] =$$
 (3.51)

$$= \sum_{i,\sigma} \Theta_i \int d^3r \left[ E_i - v_{KS}(\boldsymbol{r}) \right] \left\{ \delta \phi_i^*(\boldsymbol{r}\boldsymbol{\sigma}) \phi_i(\boldsymbol{r}\boldsymbol{\sigma}) + \delta \phi_i(\boldsymbol{r}\boldsymbol{\sigma}) \phi_i^*(\boldsymbol{r}\boldsymbol{\sigma}) \right\} + \mathcal{O}(\delta^2). \tag{3.52}$$

Before further progress, aiming to explicitly write the kinetic term variation as a function of the density variation, we may use the Kohn-Sham electron density definition (3.30) inside  $n(\mathbf{r}) = n_0(\mathbf{r}) + \delta n$  to obtain

$$\sum_{\boldsymbol{\sigma}=\uparrow,\downarrow} \sum_{i=1}^{N} \Theta_{i} |\phi_{i}(\boldsymbol{r}\boldsymbol{\sigma}) + \delta\phi_{i}(\boldsymbol{r}\boldsymbol{\sigma})|^{2} = \sum_{\boldsymbol{\sigma}=\uparrow,\downarrow} \sum_{i=1}^{N} \Theta_{i} |\phi_{i}(\boldsymbol{r}\boldsymbol{\sigma})|^{2} + \delta n,$$
(3.53)

SO

$$\delta n = \sum_{i=1}^{N} \Theta_{i} \sum_{\boldsymbol{\sigma} = \uparrow, \downarrow} \left\{ \delta \phi_{i}^{*}(\boldsymbol{r}\boldsymbol{\sigma}) \phi_{i}(\boldsymbol{r}\boldsymbol{\sigma}) + \phi_{i}^{*}(\boldsymbol{r}\boldsymbol{\sigma}) \delta \phi_{i}(\boldsymbol{r}\boldsymbol{\sigma}) \right\} + \mathcal{O}(\delta^{2}). \tag{3.54}$$

This expression is conveniently contained in the kinetic term variation, so we can use it and the fact that  $\int d^3r \delta n = 0$ , to finally obtain:

$$T_{KS}[n_0 + \delta n] - T_{KS}[n_0] = = \sum_{i,\sigma} \Theta_i \int d^3r - v_{KS}(\boldsymbol{r})\delta n + \mathcal{O}(\delta^2).$$
 (3.55)

The remaining exchange-correlation functional is explicitly undefined, so we keep it in Taylor form:

$$E_{\rm xc}[n_0 + \delta n] - E_{\rm xc}[n_0] = \int d^3 r \frac{\delta E_{\rm xc}[n]}{\delta n(\mathbf{r})} \Big|_{n=n_0} \delta n(\mathbf{r}) + \mathcal{O}(\delta^2). \tag{3.56}$$

The last step towards the Kohn-Sham equations is to construct equation (3.42) explicitly writing all the terms as functions of the density variation, but neglecting second-order contributions,

$$\int d^{3} \left\{ v_{KS}(\boldsymbol{r}) - v_{ext}(\boldsymbol{r}) - \int d^{3}r'w(\boldsymbol{r}, \boldsymbol{r}')n_{0}(\boldsymbol{r}') - \frac{\delta E_{xc}[n]}{\delta n(\boldsymbol{r})} \Big|_{n=n_{0}} \right\} \delta n(\boldsymbol{r}) = 0, \quad (3.57)$$

which is equivalent to

$$v_{KS}(\mathbf{r}) = v_{ext}(\mathbf{r}) + v_{H}[n_0](\mathbf{r}) + v_{xc}[n_0](\mathbf{r}). \tag{3.58}$$

Inserting (3.58) into (3.29) returns the final Kohn-Sham equations:

$$\left\{-\frac{\hbar^2 \nabla^2}{2m} + v_{\text{ext}}(\boldsymbol{r}) + v_{\text{H}}[n_0](\boldsymbol{r}) + v_{\text{xc}}[n_0](\boldsymbol{r})\right\} \phi_i(\boldsymbol{r}\boldsymbol{\sigma}) = E_i \phi_i(\boldsymbol{r}\boldsymbol{\sigma}).$$
(3.59)

It should be noted that the Kohn-Sham potential,  $v_{\rm KS}$ , is also a density functional. For obtaining the solutions  $\phi_i$  one must resolve to a self-consistent implementation, where  $v_{\rm KS}$  is first constructed from some trial density, then fed into the Kohn-Sham equations to result in an improved set of Slater orbitals, thus an improved density and an improved potential. This iterative process must be repeated until some convergence criterion is achieved. The final Slater orbitals are not the exact ground state of the interacting system but serve as a mathematical tool to represent the electron density, which uniquely maps the exact ground state energy. It is an important remark that since the interacting ground state is never obtained, the Kohn-Sham approach does not provide all the information about the final system, but enough to evaluate most of the structural and electrical properties of the system. (ENGEL; DREIZLER, 2011)

An important information that can be obtained directly from the eigenvalues of the Kohn-Sham converged system is the ionization potential, which is equivalent to the energy of the highest occupied state (ALMBLADH, 1985).

# 3.5 Exchange and Correlation

#### 3.5.1 The Exact Functionals

The aim of DFT is to map the many-body system onto an effective single-particle system. In practice, we cannot perform exact calculations of the exchange-correlation en-

ergy functional, as it would require the solution of the many-body problem. Nevertheless, we start our approach by deriving the exact representation of the solution to serve as a guideline into the approximation methods.

We begin dividing the the exchange-correlation energy functional,  $E_{xc}[n]$ , into the correlation  $E_{c}[n]$  and the exchange  $E_{x}[n]$  parts

The exchange energy functional is defined as (ENGEL; DREIZLER, 2011),

$$E_{\mathbf{x}}[n] := \langle \Phi_0 | \hat{W} | \Phi_0 \rangle - E_{\mathbf{H}}[n], \tag{3.60}$$

where  $|\Phi_0\rangle$  is the KS Slater determinant (3.28). This equation can be explicitly written as:

$$E_{\mathbf{x}}[n] = -\frac{1}{2} \sum_{ij} \Theta_i \Theta_j \sum_{\sigma \sigma'} \int d^3r \int d^3r' \phi_i^*(\boldsymbol{r}\boldsymbol{\sigma}) \phi_j(\boldsymbol{r}\boldsymbol{\sigma}) w(\boldsymbol{r}, \boldsymbol{r}') \phi_j^*(\boldsymbol{r}\boldsymbol{\sigma}) \phi_i(\boldsymbol{r}\boldsymbol{\sigma}).$$
(3.61)

The definition above is an implicit density functional, as the slater orbitals are themselves functionals of the electron density. The definition of the correlation energy functional is then constructed as

$$E_{\rm c}[n] := E_{\rm xc}[n] - E_{\rm x}[n].$$
 (3.62)

The exchange energy functional definition given in (3.61) contains important properties, such as the cancelation of the self-interaction energy present in  $E_{\rm H}$ , i.e., the terms where i=j:

$$E_{\mathrm{H}}^{\mathrm{SI}} = \frac{1}{2} \sum_{i} \Theta_{i}^{2} \sum_{\sigma \sigma'} \int d^{3}r \int d^{3}r' |\phi_{i}(\boldsymbol{r}\boldsymbol{\sigma})|^{2} w(\boldsymbol{r}, \boldsymbol{r}') |\phi_{i}(\boldsymbol{r}\boldsymbol{\sigma})|^{2} = -E_{\mathrm{x}}^{\mathrm{SI}}.$$
 (3.63)

Another property present in (3.61) is its additivity with respect to the spin orientations. Using  $w(\mathbf{r}, \mathbf{r}') = \frac{e^2}{|\mathbf{r} - \mathbf{r}'|}$ ,

$$E_{\mathbf{x}}[n\uparrow,n\downarrow] = -\frac{e^2}{2} \sum_{\sigma} \sum_{\alpha\beta} \Theta_{\alpha\sigma} \Theta_{\beta\sigma} \int d^3r \int d^3r' \frac{\phi_{\alpha\sigma}^*(\mathbf{r})\phi_{\beta\sigma}(\mathbf{r})\phi_{\beta\sigma}^*(\mathbf{r}')\phi_{\alpha\sigma}(\mathbf{r}')}{|\mathbf{r}-\mathbf{r}'|}.$$
 (3.64)

The expression above can be thought of as two separate energy functionals, each for a distinct spin orientation;  $E_{x\uparrow}$  and  $E_{x\downarrow}$ .

Now, we aim the full  $E_{\rm xc}[n]$  exact representation. To reach such a form, we describe the exact many-body Hamiltonian in terms of the Kohn-Sham Hamiltonian and a correction Hamiltonian, i.e.,  $\hat{H} = \hat{H}_{\rm KS} + \hat{H}'$ . The elements that substantiate  $\hat{H}'$  are representatives of the electron-electron interactions  $\hat{W}$  that are not contained in  $\hat{H}_{\rm KS}$ , so we write

$$\hat{H}' = \hat{W} - \int d^3r \hat{n}(\mathbf{r}) \left\{ v_{\rm H}(\mathbf{r}) + v_{\rm xc}(\mathbf{r}) \right\}. \tag{3.65}$$

To make an adiabatic connection between  $\hat{H}$  and  $\hat{H}_{\mathrm{KS}}$ , we follow the approach of defining

$$\hat{H}(\lambda) = \hat{H}_{KS} + \lambda \hat{H}', \tag{3.66}$$

where  $\lambda \in [0,1]$  is a coupling constant. The Schrödinger equation for this system is

$$\hat{H}(\lambda) |\Psi_0(\lambda)\rangle = E_0(\lambda) |\Psi_0(\lambda)\rangle \tag{3.67}$$

The Hohenberg-Kohn theorems ensure that  $\hat{H}_{\text{KS}}$  is constructed from the same ground state electron density that represents the interacting system  $\hat{H}$ , however, we cannot easily assume the conservation of the ground state electron density through the path that connects these two systems,  $\hat{H}(\lambda)$ . The adiabatic connection must then enforce the preservation of this property. For this, we consider some external potential  $u_{\lambda}(\mathbf{r})$  such that

$$u_{\lambda}(\mathbf{r}) = \begin{cases} v_{KS}(\mathbf{r}) & \text{if } \lambda = 0\\ \text{unknown} & \text{if } 0 < \lambda < 1 \ ,\\ v_{\text{ext}}(\mathbf{r}) & \text{if } \lambda = 1 \end{cases}$$
(3.68)

which can be used to write the Hamiltonian

$$\hat{H}(\lambda) = \hat{T} + \int d^3 r u_{\lambda}(\mathbf{r}) \hat{n}(\mathbf{r}) + \lambda \hat{W}. \tag{3.69}$$

This procedure maintains the endpoints of the variation,

$$\hat{H}(\lambda) = \begin{cases} \hat{H}_{KS} & \text{for } \lambda = 0\\ \hat{H} & \text{for } \lambda = 1 \end{cases}$$
 (3.70)

For the unknown region of  $u_{\lambda}$ , we must use the condition

$$n_{\lambda}(\mathbf{r}) = \langle \Psi_0(\lambda) | \hat{n}_{\lambda}(\mathbf{r}) | \Psi_0(\lambda) \rangle \equiv n(\mathbf{r}) \text{ for all } 0 \le \lambda \le 1.$$
 (3.71)

The ground state energy through the variation path is given as

$$E_0(\lambda) = \langle \Psi_0(\lambda) | \hat{H}(\lambda) | \Psi_0(\lambda) \rangle, \qquad (3.72)$$

which can be differentiated with respect to  $\lambda$ :

$$\frac{d}{d\lambda}E_{0}(\lambda) = (3.73)$$

$$= \left\langle \frac{d\Psi_{0}(\lambda)}{d\lambda} \middle| \hat{H}(\lambda)\Psi_{0}(\lambda) \middle| + \right\rangle \left\langle \Psi_{0}(\lambda) \middle| \hat{H}(\lambda) \middle| \frac{d\Psi_{0}(\lambda)}{d\lambda} \right\rangle + \left\langle \Psi_{0}(\lambda) \middle| \frac{d\hat{H}(\lambda)}{d\lambda} \middle| \Psi_{0}(\lambda) \right\rangle = (3.74)$$

$$= E_{0}(\lambda) \left( \left\langle \frac{d\Psi_{0}(\lambda)}{d\lambda} \middle| \Psi_{0}(\lambda) \right\rangle + \left\langle \Psi_{0}(\lambda) \middle| \frac{d\Psi_{0}(\lambda)}{d\lambda} \right\rangle \right) + \left\langle \Psi_{0}(\lambda) \middle| \frac{d\hat{H}(\lambda)}{d\lambda} \middle| \Psi_{0}(\lambda) \right\rangle. (3.75)$$

Normalization ensures  $\langle \Psi_0(\lambda)|\Psi_0(\lambda)\rangle=1$ , and thus  $\frac{d}{d\lambda}\langle \Psi_0(\lambda)|\Psi_0(\lambda)\rangle=0$ . Equation (3.75) then becomes:

$$\frac{d}{d\lambda}E_0(\lambda) = \left\langle \Psi_0(\lambda) \middle| \frac{d\hat{H}(\lambda)}{d\lambda} \middle| \Psi_0(\lambda) \right\rangle. \tag{3.76}$$

which can be integrated from 0 to 1 with respect to  $\lambda$ , giving

$$E_{0} - E_{KS 0} = \int_{0}^{1} d\lambda \left\langle \Psi_{0}(\lambda) \left| \frac{d\hat{H}(\lambda)}{d\lambda} \right| \Psi_{0}(\lambda) \right\rangle$$

$$= \int_{0}^{1} d\lambda \left\langle \Psi_{0}(\lambda) \left| \int d^{3}r \hat{n}(\mathbf{r}) \frac{du_{\lambda}(\mathbf{r})}{d\lambda} + \hat{W} \right| \Psi_{0}(\lambda) \right\rangle$$

$$= \int d^{3}r [u_{\lambda=1}(\mathbf{r}) - u_{\lambda=0}(\mathbf{r})] n(\mathbf{r}) + \frac{1}{2} \sum_{\sigma,\sigma'} \int d^{3}r \int d^{3}r' w(\mathbf{r}, \mathbf{r}') \int_{0}^{1} d\lambda$$

$$\times \left\langle \Psi_{0}(\lambda) \right| \hat{\Psi}^{\dagger}(\mathbf{r}\sigma) \hat{\Psi}^{\dagger}(\mathbf{r}'\sigma') \hat{\Psi}(\mathbf{r}'\sigma') \hat{\Psi}(\mathbf{r}\sigma) \left| \Psi_{0}(\lambda) \right\rangle.$$

$$(3.79)$$

Using the anticommutation relations of the fermionic field operators (1.82), we have that

$$\hat{\Psi}^{\dagger}(\boldsymbol{r}\sigma)\hat{\Psi}^{\dagger}(\boldsymbol{r}'\sigma')\hat{\Psi}(\boldsymbol{r}'\sigma')\hat{\Psi}(\boldsymbol{r}\sigma) \qquad (3.80)$$

$$= \hat{\Psi}^{\dagger}(\boldsymbol{r}\sigma)\hat{\Psi}(\boldsymbol{r}\sigma)\hat{\Psi}^{\dagger}(\boldsymbol{r}'\sigma')\hat{\Psi}(\boldsymbol{r}'\sigma') - \delta^{(3)}(\boldsymbol{r}-\boldsymbol{r}')\delta_{\sigma\sigma'}\hat{\Psi}^{\dagger}(\boldsymbol{r}\sigma)\hat{\Psi}(\boldsymbol{r}\sigma), \tag{3.81}$$

$$E_{0} - E_{KS 0} = \int d^{3}r [u_{\lambda=1}(\mathbf{r}) - u_{\lambda=0}(\mathbf{r})] n(\mathbf{r}) + \frac{1}{2} \int d^{3}r \int d^{3}r' w(\mathbf{r}, \mathbf{r}') \int_{0}^{1} d\lambda$$
$$\times \langle \Psi_{0}(\lambda) | \hat{n}(\mathbf{r}) \hat{n}(\mathbf{r}') - \delta^{(3)}(\mathbf{r} - \mathbf{r}') \hat{n}(\mathbf{r}) | \Psi_{0}(\lambda) \rangle. \tag{3.82}$$

The second term of this equation defines the exchange-correlation energy functional, which can be expressed using the density-density response function of the interacting system (ENGEL; DREIZLER, 2011):

$$E_{\rm xc}[n] = \frac{1}{2} \int d^3r \int d^3r' w(\boldsymbol{r}, \boldsymbol{r}') \int_0^1 d\lambda \left[ i\hbar \chi_{\lambda}(\boldsymbol{r}0, \boldsymbol{r}'0) - \hat{n}(\boldsymbol{r}) \delta^{(3)}(\boldsymbol{r} - \boldsymbol{r}') \right]. \tag{3.83}$$

Response functions are a major concept inside DFT, but it's details will be left for reference, (ENGEL; DREIZLER, 2011). Conceptually, what must be known is that the response function used above is a time-ordered response function at the limit  $t \to 0$ . A time-ordered response function uses the Heisenberg form of the density function to construct a description of how an observable responds over time to the perturbation generator of such causality.

Equation (3.83) represents the adiabatic connection formula for  $E_{xc}[n]$ , but as previously discussed, it does not serve as a tool for practical calculations, but rather as a concept to sustain our understanding of the exchange-correlation energy functional.

### 3.5.2 The Approximated Functionals

Far from being useless, the adiabatic connection format (3.83) has a major application that can be seen in the homogeneous electron gas (HEG). The HEG is a well-known interacting system in which the electron density is contained in the response function  $\chi_{\lambda}$ . This hypothetical system can be defined as an infinite set of interacting electrons that do not experience a spatially varying external potential, such as a smooth positive background charge density,  $n_+$ , instead of a discrete set of atomic nuclei. This positive charge is necessary to cancel the divergence in the energy density of an infinite set of negative charges due to long-range Coulomb interactions.

This concept implies that the exchange-correlation energy density  $\epsilon_{\rm xc}^{\rm HEG} = E_{\rm xc}^{\rm HEG} n_0$  of the system becomes a simple function of the ground state electron density  $n_0$ , which is now spatially constant. The translational and rotational symmetries of the HEG simplify the response function and the electron-electron interactions to depend only on the distance between the particles,  $|\mathbf{r} - \mathbf{r}'|$ . The adiabatic connection then becomes:

$$\epsilon_{\rm xc}^{\rm HEG}(n_0) = \frac{1}{2} \int d^3r \int d^3r' w(\boldsymbol{r} - \boldsymbol{r}') \int_0^1 d\lambda \left[ i\hbar \chi_{\lambda}(\boldsymbol{r} - \boldsymbol{r}', 0; n_0) - n_0 \delta^{(3)}(\boldsymbol{r} - \boldsymbol{r}') \right]. \quad (3.84)$$

The Fourier transformation (2.9), very present in solid-state physics, simplify the system to:

$$\epsilon_{\rm xc}^{\rm HEG}(n_0) = \frac{1}{2} \int \frac{d^3k}{(2\pi)^3} w(\mathbf{k}) \left[ i\hbar \int_0^1 d\lambda \int \frac{d\omega}{2\pi} \chi_{\lambda}(\mathbf{k}, \omega; n_0 - n_0) \right]. \tag{3.85}$$

where the Fourier version of the electron-electron interaction and the responsefunction are:

$$w(\mathbf{k}) = \int d^3r e^{-i\mathbf{k}\cdot\mathbf{r}} w(\mathbf{r} - \mathbf{r}')$$
 (3.86)

$$\chi_{\lambda}(\mathbf{k},\omega) = \int dt \int d^3r e^{i\omega t} e^{-i\mathbf{k}\cdot\mathbf{r}} \chi_{\lambda}(\mathbf{r} - \mathbf{r}', t - t'). \tag{3.87}$$

Considering  $w(\mathbf{k})$  only as a Coulomb interaction, we obtain an explicit format

$$w(\mathbf{k}) = \frac{4\pi e^2}{\mathbf{k}^2}. (3.88)$$

In reality, the systems we want to simulate are not homogeneous, but locally this is not a bad approximation. That is the main idea of the local density approximation (LDA) technique, where the energy per particle  $\epsilon_{xc}$  of a system with density  $n(\mathbf{r})$  is locally approximated to  $\epsilon_{xc}^{HEG}$  of a homogeneous gas with  $n_0 = n(\mathbf{r})$ . The LDA exchange-correlation functional is defined as

$$E_{\rm xc}^{\rm LDA}[n] = \int d^3r n(\boldsymbol{r}) \epsilon_{\rm xc}^{\rm HEG}(n_0 = n(\boldsymbol{r})), \qquad (3.89)$$

and the local spin-density approximation (LSDA) variant is

$$E_{\rm xc}^{\rm LSDA}[n\uparrow,n\downarrow] = \int d^3r n(\boldsymbol{r})\epsilon_{\rm xc}^{\rm HEG}(n\uparrow,n\downarrow). \tag{3.90}$$

The LDA and LSDA functionals are universal first-principles functionals of n, since they do not require any free parameters. Despite being easily used in the DFT formalism, the short-range approximation leaves room for further improvements of the functional.

The predominant idea of an improvement to local approximations is represented in generalized gradient approximations (GGA) (BECKE, 1988). Still based on the LDA and

LSDA, the GGA approach considers not only the local density, but also the local density gradient, gathering information about the change in the local density. The general format of such approximations is as follows:

$$E_{\rm xc}^{\rm GGA}[n\uparrow, n\downarrow] = \int d^3r f(n\uparrow, n\downarrow, \nabla n\uparrow, \nabla n\downarrow). \tag{3.91}$$

In this study, we focus our discussion on the Perdew-Burke-Ernzerhof (PBE) (PERDEW; BURKE; ERNZERHOF, 1996) variant of the GGA format, which was developed within a decade of research from the first attempt of a GGA potential; a long path we shall not see entirely. We begin our discussion from the correlation energy potential in the form (PERDEW; BURKE; WANG, 1996a):

$$E_{\rm c}^{\rm GGA}[n_{\uparrow}, n_{\downarrow}] = \int d^3r \, n \left[ \epsilon_{\rm c}^{\rm HEG}(r_{\rm S}, \zeta) + G(r_{\rm S}, \zeta, t) \right], \tag{3.92}$$

where G is the gradient contribution,  $r_{\rm S}$  is the local Seitz radius, defined as the average distance between electrons around  $\boldsymbol{r}$ ,  $\frac{4\pi r_{\rm S}^3}{3}=\frac{1}{n}=\frac{3\pi^2}{k_{\rm F}};\;\zeta=\frac{(n_\uparrow-n_\downarrow)}{n}$  is the relative spin polarization;  $t=\frac{|\nabla n|}{2\phi(\zeta)k_sn}$  is a dimensionless density gradient, where  $\phi(\zeta)=\frac{[(\zeta+1)^{2/3}+(\zeta-1)^{2/3}]}{2}$  is a spin-scaling factor and  $k_s=\sqrt{\frac{4k_{\rm F}e}{\pi a_0}}$  is the Thomas-Fermi screening wave number.  $a_0=\frac{\hbar^2}{me}$  and  $k_{\rm F}$  is the radius of the Fermi surface of free electrons, this spherical surface is the Fermi level  $\epsilon_{\rm F}$  of noninteracting electrons in a constant potential.

The gradient contribution must be constructed under three conditions:

- 1. The slowly varying density limit  $(t \to 0)$  causes the gradient term to approach the second-order contribution (WANG; PERDEW, 1991),  $G \to (\frac{e^2}{a_0})\beta\phi^3t^2$ . Here,  $\beta \approx 0.066725$ .
- 2. The rapidly varying density limit  $t \to \infty$  gives  $G \to -\epsilon_c^{HEG}$ , which is equivalent to the absence of correlation effects.
- 3. In a path uniformly scaling the density to its high limit, the correlation energy must scale to a constant. To achieve this, G must cancel the logarithmic singularity of  $\epsilon_{\rm c}^{\rm HEG}$  (LEVY, 1989) in the limit:  $\epsilon_{\rm c}^{\rm HEG}(r_{\rm S},\zeta) \to (\frac{e^2}{a_0})\phi^3 \left[\gamma ln\left(\frac{r_{\rm S}}{a_0}\right) \omega\right]$ , where  $\gamma$  and  $\omega$  are weak functions of  $\zeta$  which shall be considered in their  $\zeta=0$  values,  $\gamma = \frac{1-ln(2)}{\pi^2} \approx 0.031091$  and  $\omega \approx 0.046644$ . The form we must construct to respect the high-density scaling condition must scale to  $G \to \frac{e^2}{a_0} \gamma \phi^3 ln(t^2)$ .

All the above conditions are satisfied with the ansatz:(PERDEW; BURKE; ERNZ-ERHOF, 1996)

$$G = \frac{e^2 \gamma \phi^3}{a_0} ln \left[ 1 + \frac{\beta}{\gamma} t^2 \left( \frac{1 + At^2}{1 + At^2 + A^2 t^4} \right) \right], \tag{3.93}$$

with

$$A = \frac{\beta}{\gamma} \left( exp \left\{ \frac{-\epsilon_{\rm c}^{\rm HEG} a_0}{\gamma \phi^3 e^2} \right\} - 1 \right)^{-1}. \tag{3.94}$$

Equation (3.93) shows a gradient contribution that scales from the lower limit  $t \to 0$  as a second-order expansion to the higher limit  $t \to \infty$  as the necessary cancellation of  $\epsilon_c^{\text{HEG}}$ , thus satisfying the first two conditions. The third condition is too satisfied, as scaling to the high-density limit leads to

$$E_{\rm c}^{\rm GGA\text{-}PBE} \to \frac{e^2}{a_0} \int d^3r n \gamma \phi^3 ln \left( 1 + \frac{1}{\frac{\chi s^2}{\phi^2} + \left(\frac{\chi s^2}{\phi^2}\right)^2} \right),$$
 (3.95)

where 
$$s = \frac{|\nabla n|}{2nk_{\rm F}}$$
,  $\chi = \frac{\beta c^2}{\gamma} e^{\frac{-\omega}{\gamma}} \approx 0.72161$ , and  $c = \left(\frac{3\pi^2}{16}\right)^{\frac{1}{3}} \approx 1.2277$ .

Four new conditions are imposed into the exchange energy:

1. Under uniform density scaling, the  $E_{\rm x}$  must scale alike. Thus, with  $\zeta \to 0$ , we must obtain

$$E_{\mathbf{x}}^{\text{GGA-PBE}} = \int d^3 n \epsilon_x^{\text{HEG}}(n) F_{\mathbf{x}}(s), \qquad (3.96)$$

where  $\epsilon_x^{\text{HEG}} = \frac{-2e^2k_{\text{F}}}{4\pi}$ , so the uniform gas limit is recovered when  $F_x(0) = 1$ .

2. For small density variations around the uniform density, we must recover the LSDA linear response, which in this situation is a good approximation to the exact exchange-correlation energy, while the gradient expansion is not. For that, as  $s \to 0$ 

$$F_{\rm x}(s) \to 1 + \mu s^2,$$
 (3.97)

where  $\mu = \frac{\beta \pi^2}{3} \approx 0.21951$ .

3. The exact exchange energy follows the spin-scaling form

$$E_{\mathbf{x}}[n\uparrow, n\downarrow] = \frac{E_{\mathbf{x}}[2n\uparrow] + E_{\mathbf{x}}[2n\downarrow]}{2}.$$
 (3.98)

4. The Lieb-Oxford bound

$$E_{\mathbf{x}}[n\uparrow, n\downarrow] \ge E_{\mathbf{x}\mathbf{c}}[n\uparrow, n\downarrow] \ge -1.679e^2 \int d^3r n^{\frac{4}{3}}$$
 (3.99)

must be satisfied, which requires  $F_{\rm x}(s) \leq 1.804$ .

108 Chapter 3. DFT

To satisfy the second and fourth requirements, we use the format

$$F_{\mathbf{x}}(s) = 1 + \kappa - \frac{\kappa}{\left(1 + \frac{\mu s^2}{\kappa}\right)},\tag{3.100}$$

with  $\kappa = 0.804$ .

Considering all the above, the final form of the GGA-PBE energy functional is given by  $E_{\rm xc}^{\rm GGA-PBE} = E_{\rm c}^{\rm GGA-PBE} + E_{\rm x}^{\rm GGA-PBE}$ , which is conveniently written as

$$E_{\rm xc}^{\rm GGA-PBE} = \int d^3 n \epsilon_x^{\rm HEG}(n) F_{\rm xc}(r_{\rm S}, \zeta, s), \qquad (3.101)$$

where the enhancement factor (BHATTACHARJEE; KOSHI; LEE, 2024),

$$F_{\rm xc}(r_{\rm S},\zeta,s) = F_{\rm x}(s) + \frac{\epsilon_{\rm c}^{\rm HEG}(r_{\rm S},\zeta)}{\epsilon_{\rm x}(n)} F_{\rm c}(r_{\rm S},\zeta,t), \qquad (3.102)$$

is defined to consider the nonlocality of GGA in local exchange while still preserving the correct features of the LSDA. (PERDEW; BURKE; ERNZERHOF, 1996)

The GGA-PBE is one of the best and most well-known potentials to this day, but, at some additional computational cost, there are some not purely DFT exchange-correlation energy functionals that give better results for some physical properties, as the electronic structure. This new type of functional is called the hybrid exchange-correlation energy functional, which combines DFT functionals and non-DFT elements such as the exact Hartree-Fock (HF) exchange energy (HARTREE, 1928; Fock, 1930).

A very popular hybrid functional that has been giving excellent results for the energy gap of insulators and semi-conductors is the Heyd-Scuseria-Ernzerhof 2003 (HEYD; SCUSERIA; ERNZERHOF, 2003) (HSE03), which was in 2006 corrected by the own authors into the HSE06 version. The HSE03 and HSE06 functionals are based on a screened Coulomb operator for the HF exchange interaction, and combine it to the GGA-PBE exchange-correlation energy functional.

Part II

Materials

#### 3.6 Of Two-Dimensional Materials

"Upward, not Northward" —represents the confusion between a circle and a sphere, creatures of different dimensions, as discussed in the romance by Edwin A. Abbott, "Flatland". Reducing the dimensions of physical systems is not only a simplification, but brings with it its own features. Other than being highly transparent, mechanically strong and flexible, two-dimensional (2D) materials also benefit from confining electrons in the lower dimension, reducing the electronic screening and scattering effects; leading to enhanced or even unique electronic properties.

This lower dimension revolution began with the discovery of graphene (NOVOSELOV et al., 2004; NOVOSELOV et al., 2005; NOVOSELOV et al., 2007), which was only the beginning, rapidly followed by the family of transition metal dichalcogenides (TMDs), widening the range of possible monolayers (CHHOWALLA et al., 2013a; GANATRA; ZHANG, 2014). It became clear that more atomic combinations were possible to be constructed as 2D crystalline systems, and now, the scientific community has opened its eyes to a whole new class of 2D materials: Transition metal carbides, nitrides, and carbonitrides (MXenes) (ANASORI; LUKATSKAYA; GOGOTSI, 2017; PERSSON; ROSEN, 2019); where most of the conceivable monolayers have not yet been synthesized, leaving a wide range of physical properties unexplored.

In this study, we focus on the most recent families, TMDs and MXenes. The attention given to each of these is related to their position in the present time. MXenes are yet considered a newborn class of materials, which incites us to explore unsynthesized structures. For that, we focus on the important properties for synthesis, such as the stability and characterization of the materials, without sacrificing important electronic properties such as the band structure, excitonic properties, and the effective mass of the charge carrier states. TMDs are not that new anymore, so we leave the stability calculations out of consideration and use an already synthesized material, MoS<sub>2</sub> (MAK et al., 2010), to head towards further development of computational methods to calculate advanced electronic properties such as exciton states, valleytronics, and topological quantities.

# 3.7 Of Transition Metal Dichalcogenides

The crystal structure of 2D TMDs is of a quasi-2D type, where a few atomic layers of specific geometry are combined. We can classify them according to the symmetries associated with layer sequencing and the coordination geometry of the transition metal. The main polymorphs representing TMD crystals are: 1T, 2H, and 3R. The numbers 1, 2, and 3 indicate the number of layers in the unit cell, while the letters indicate the crystal

112 Chapter 3. DFT

system:  $T \to \text{tetragonal}$ ,  $H \to \text{hexagonal}$ ,  $R \to \text{rhombohedral}$ . While the 1T form exhibits metallic behavior associated with octahedral coordination between the transition metal and its chalcogen ligands, the 2H and 3R forms behave as semiconductors due to trigonal prismatic coordination (CHHOWALLA et al., 2013b).

In the case of monolayer TMDs, only two forms are present: 2H, with trigonal prismatic coordination and semiconducting behavior; and 1T, with octahedral coordination and metallic behavior. The crystal structure of 2H-MX<sub>2</sub> (semiconductor) consists of a plane of transition metals sandwiched between two planes of chalcogens. Each M atom is coordinated in a trigonal prismatic geometry with six X atoms, while each X atom is bonded to three M atoms. This characterizes a structure with inversion asymmetry, as there is no inversion center in trigonal prisms. Figure 20 illustrates this configuration applied to MoS<sub>2</sub>.

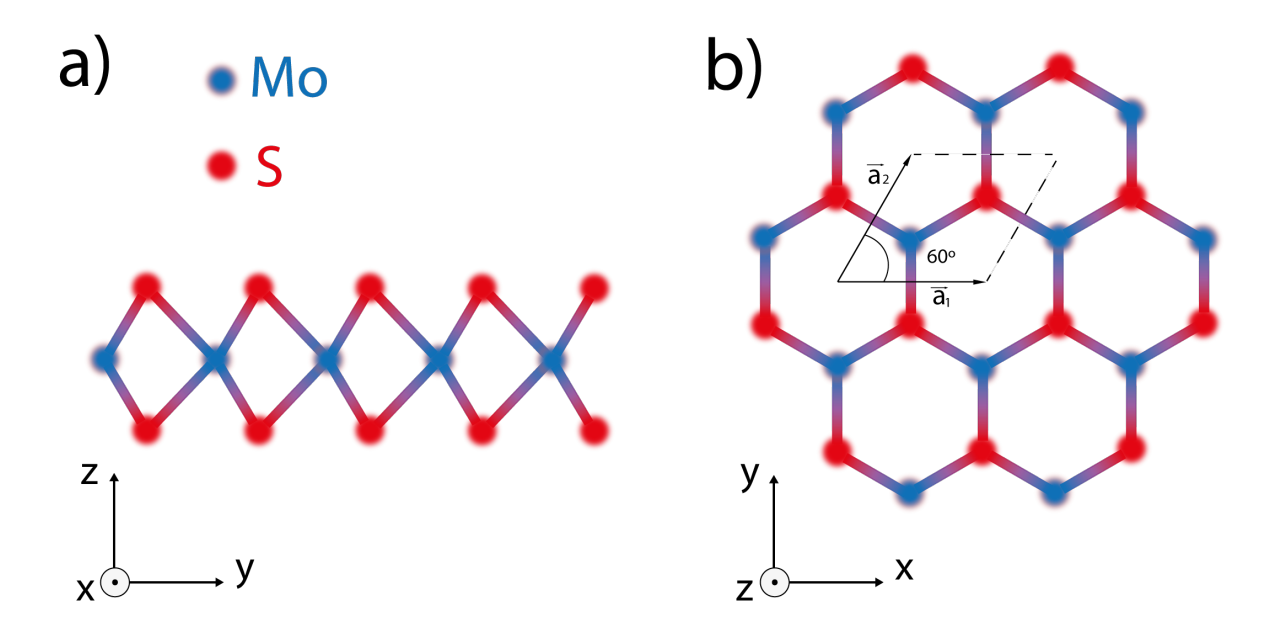


Figure 20 – a) Crystal structure of 2H-MoS<sub>2</sub> viewed along the x-axis. b) Crystal structure of 2H-MoS<sub>2</sub> viewed along the z-axis.

A semiconductor is defined by an energy gap between the highest occupied state and the lowest unoccupied state, with that energy gap being large enough to deny the usual conductor behavior, but insufficient for the material to be considered as an insulator. This, and more sophisticated properties of materials can be studied from its band structure, which is the core of our discussion in MoS<sub>2</sub>.

tially filled d bands from Mo energetically between Mo-S s-p bonding and antibonding bands. The s contribution to the states near Fermi level is rather negligible (RIDOLFI; LEWENKOPF; PEREIRA, 2018), where the Mo d orbitals are prominent. The trigonal prismatic symmetry splits these d bands into three groups (XIAO et al., 2012a):  $A_1$  symmetry  $\rightarrow$  lobes along  $\hat{z}$ ,  $[d_{z^2}]$ ; E symmetry  $\rightarrow$  in-plane orbitals  $[d_{xz}, d_{x^2-y^2}]$ ; and E' symmetry  $\rightarrow$  out-of-plane orbitals  $[d_{xz}, d_{yz}]$ . There is also a mirror symmetry in the  $\hat{z}$  plane to be considered, which denies hybridization of the out-of-plane orbitals. The hybridization between  $A_1$  and E orbitals is responsible for opening a direct band gap located at the K and K' points of the first Brillouin zone (BZ) (MATTHEISS, 1973), meaning the valence band maximum aligns with the conduction band minimum. In both valleys where the direct gap occurs, the band energies are identical (degenerate) but from non-equivalent states. The non-equivalence arises from the absence of inversion symmetry (2.63).

Preservation of time-reversal symmetry (2.70) implies  $\hat{\Theta}\hat{J}\hat{\Theta}^{-1} = -\hat{J}$ . Graphene satisfies this symmetry without breaking inversion symmetry by having  $L_z(K) = 0$ , but  $MoS_2$  does not. The orbital angular momentum quantum number of the valence energy state at K valley is +2 and for the valence state at K' valley is -2. The spin separation of bands must also be opposite in each valley. In the next chapter, we discuss that the valence energy band that peaks at K is not the same band that peaks at K', but its spin counterpart. These different valley configurations are responsible for decoupled optical transitions at K and K', where circular polarization to the right selectively excites electrons at K' valence states, while left polarization excites electrons at K valence states. These optical selection rules are a result of angular momentum conservation in the transition from  $\pm 2$  angular momentum states into the 0 angular momentum conduction band.

The spin-orbit interaction is a relativistic effect that considers the coupling between the electron's spin and the magnetic field generated by the orbital motion of the nucleus from the electron's perspective. Strong spin-orbit coupling splits both valence and conduction bands into two non-degenerate subbands with opposite spin polarizations and energy differences of 0.45 eV in the valence bands and 0.15 eV in the conduction bands for MoX<sub>2</sub> materials, while only a few meV for WX<sub>2</sub> materials. Moreover, time-reversal symmetry in TMDs requires that spin splitting in different valleys must be opposite, maintaining energy degeneracy between valleys despite their opposite momentum numbers. As a result, spin-up orbitals in the K valley's valence band have higher energy than spin-down orbitals, while the relationship is inverted in the K' valley.

These unique features of 2H-type monolayer TMD band structures lead to spinvalley coupling, where the total angular momentum emerges from individual momenta. 114 Chapter 3. DFT

This structure also enables valley-selective optical transitions: left-circularly polarized light can only excite the K valley, while right-circularly polarized light excites only the K' valley. Furthermore, when electrons recombine with holes in the K and K' valleys, they emit light with polarization matching their absorption. An electron in a valley can be excited from the valence to the conduction band by absorbing a photon with energy equal to the gap. In this process, the excited electron leaves behind a hole in the valence band-a quasiparticle with opposite charge that is also a fermion. The electron and hole can then form a Coulomb-bound pair called an exciton, which is a composite boson (JOE, 2021). This valley-selective excitation underpins valleytronics, where information is encoded in valley polarization rather than charge or spin. These excitons inherit the valley degree of freedom (valley excitons), and their high binding energies (up to hundreds of meV) make them remarkably stable even at room temperature (XIAO et al., 2012b).

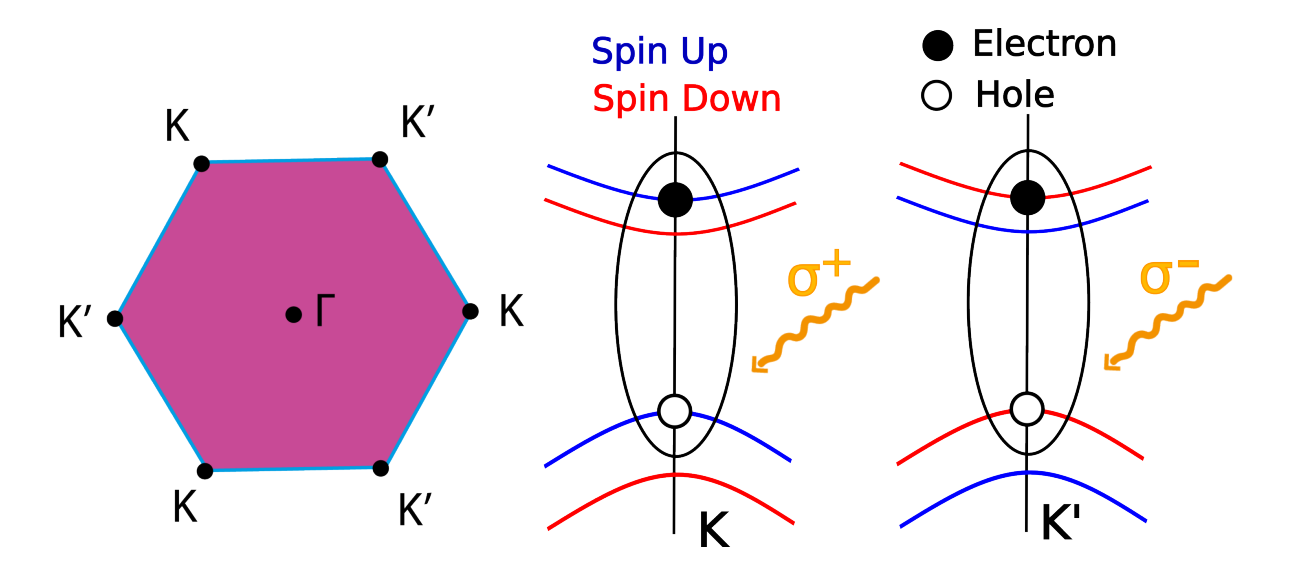


Figure 21 – First Brillouin zone of  $MoS_2$  and its distinct K and K' valleys, where bright exciton states are formed with opposite spins, induced by different light polarization.

Due to spin-valley coupling, intervalley scattering only occurs when the spins in each valley are simultaneously flipped, thereby transferring a momentum equivalent to the difference between the K and K' point momenta. The difficulty of this scattering process results in long valley polarization times, enabling exciton valley qubits in TMDs to operate without polarization flipping. Valley coherence has been experimentally demonstrated (JONES et al., 2013), showing these qubits won't be limited by decoherence. Finally, spin-valley qubit control has been theoretically proposed (BROOKS; BURKARD, 2019). Thus, valley excitons in TMD monolayers have tremendous potential as quantum information carriers (BORGES et al., 2023).

3.8. Of MXenes 115

#### 3.8 Of MXenes

A general MXene is described by the formula  $M_{n+1}X_nT_x$ , where n ranges from 1 to 3, M is a transition metal, X is carbon, nitrogen, or carbonitride, and  $T_x$  represents x termination groups. The exact composition of these terminations is not fully standardized and depends on the synthesis method (ANASORI; LUKATSKAYA; GOGOTSI, 2017).

Conductive MXenes have found applications in technologies such as photovoltaic cells (SAEED et al., 2022), energy storage (AMPONG et al., 2023), electromagnetic interference shielding (LIU; XIAO; III, 2016; HUANG et al., 2025), water purification (ALHADITHY et al., 2024), and gas sensors (ZHANG CHENGCHENG TAO, 2025). However, the semiconductor section of MXenes remains less explored, leaving many physical properties to be discovered. Nevertheless, previous studies have shown that  $Y_2CF_2$  is a stable semiconductor that could be synthesized from yttrium-carbon-based MAX phases (HONG; KLIE; ÖĞÜT, 2016; ALIAKBARI; AMIRI; DEZFULI, 2023), and also its three-dimensional stacking has already been achieved (DRUFFEL et al., 2019). In this work, we theoretically investigate the effect of changing carbon for nitrogen in this structure, and also, mainly, we investigate the effects of different terminations (T = F, Cl, Br) on  $Y_2CT_2$  MXenes.

MXenes are synthesized by selectively etching atomic layers from their parent MAX phases, which consist of alternating layers of transition metal carbides or nitrides and A-element layers, having the formula  $M_{n+1}AX_n$ , where A typically belongs to groups 13 or 14 of the periodic table. The etching process involves wet-chemical exfoliation, where A atoms are removed and some atoms from the etching solution become termination groups on the resulting MXene (PERSSON; ROSEN, 2019). The chemical bond between transition metals M and A atoms in MAX phases is primarily metallic, making it unfeasible to separate these layers through simple mechanical shearing due to their mechanical strength, while in contrast, the M-X bonds exhibit a more mixed covalent/ionic character (BARSOUM, 2000). This difference in bonding nature enables the selective etching of A-layers through chemical reactions that target the weaker M-A metallic bonds while preserving the stronger M-X network. The resulting  $M_{n+1}X_n$  layers then form MXenes with surface terminations.

The first and still most common synthesis method uses aqueous fluoride-containing solutions like hydrofluoric acid (HF) at 55°C (NAGUIB et al., 2014). The specific conditions vary for different materials, but in general, MXenes with heavier transition metals M or higher n values in  $M_{n+1}X_nT_x$  require higher concentrations in etching solutions and longer reaction times. After etching, the exposed transition metal surfaces react with the

116 Chapter 3. DFT

solution to form a mixture of -O, -OH, and -F terminations. While still an emerging field, post-synthesis processes can now produce MXenes with controlled terminations (LAI et al., 2015). As an example, the chemical reactions to obtain the material present in this study,  $Y_2CF_2$ , from a MAX phase precursor  $Y_2AC$ , are:

$$Y_2AC + 3HF \to Y_2C + AF_3 + \frac{3}{2}H_2$$
 (3.103)

$$Y_2C + 2H_2O \to Y_2C(OH)_2 + H_2$$
 (3.104)

$$Y_2C + 2HF \to Y_2CF_2 + H_2$$
 (3.105)

The general picture is given in Figure 22:

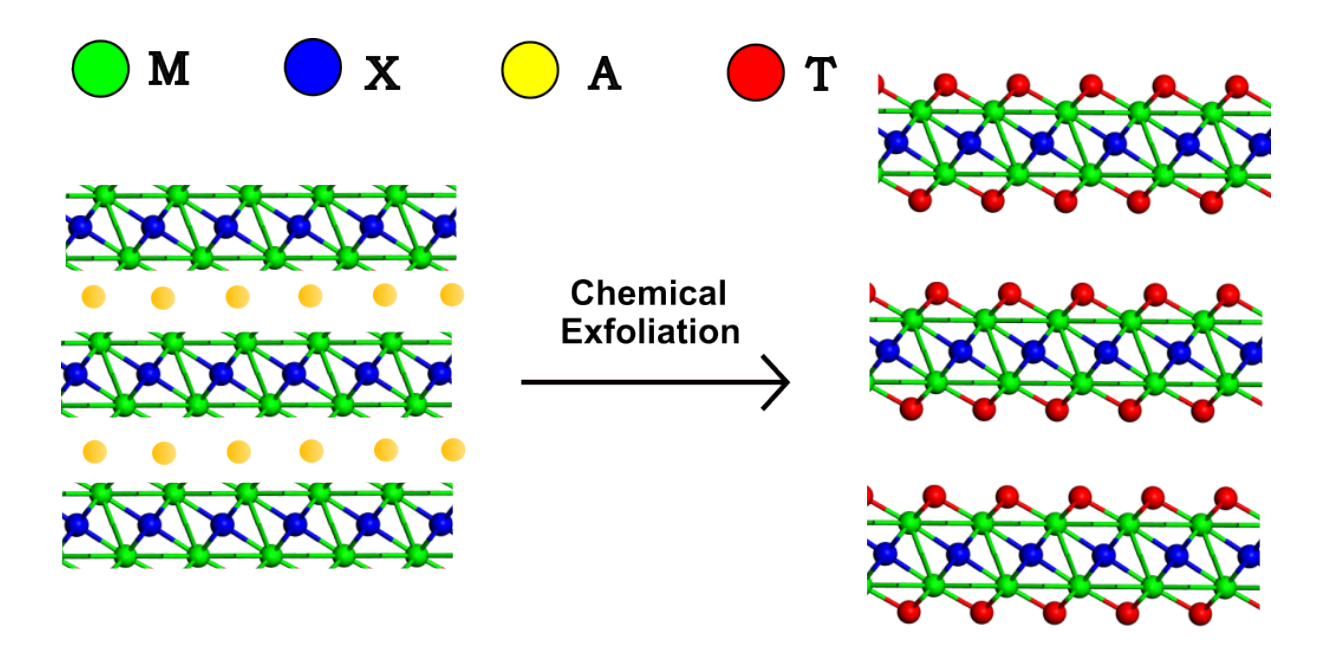


Figure 22 – General chemical exfoliation for the synthesis process of an  $M_2XT_2$  MXene derived from its precursor MAX phase.

Regardless of the termination group, the crystal structure of an MXene inherits its hexagonal symmetry directly from the parent MAX phase. Most MAX phases crystallize in the  $P6_3/mmc$  space group, resulting in MXenes where M atoms adopt a hexagonal close-packed arrangement with X atoms occupying octahedral interstitial sites. For Y<sub>2</sub>CT<sub>2</sub> (illustrated in Figure 23) and other M<sub>2</sub>XT<sub>2</sub> MXenes, this leads to a TMXMT-TMXMT stacking sequence where termination groups (T) bridge the interlayer gaps. The monolayer symmetry consequently reduces to the trigonal  $P\overline{3}m1$  space group.

The 2D hexagonal unit cell in real space transforms into a rotated  $(\pi/4)$  hexagonal cell in reciprocal space. The high symmetry points of interest in this configuration are

3.8. Of MXenes 117

the  $\Gamma$ , M, and K points, as illustrated in Figure 23 b), along with the unit cells in both spaces.

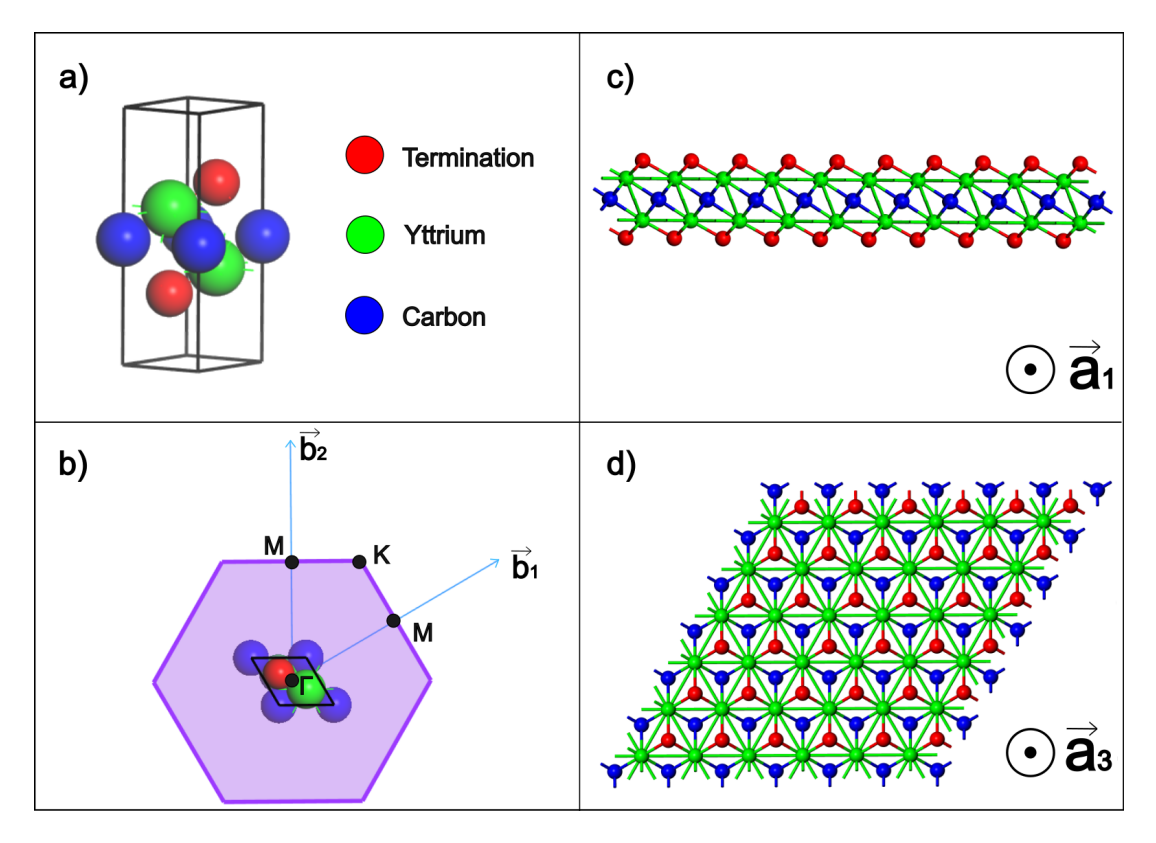


Figure 23 – a) Real space unit cell for  $Y_2C_1T_2$  MXenes in the trigonal p-3m1 space-group. b) First Brillouin zone representation, showing  $\Gamma$ , M and K points of high symmetry (the top view of the real lattice in the center is not in true proportion in relation to the reciprocal lattice). c) Side view of the  $Y_2CT_2$  monolayer. d) Top view of the  $Y_2CT_2$  monolayer.

This study dedicates to push further the limits of our current knowledge over this futuristic class of 2D materials. Not neglecting the basic, but essential, stability and electronic properties, we head towards a more in depth exploration of the electronic structure. This exploratory posture was reinforced during the study, after realizing we were gifted with exotic results for  $Y_2CCl_2$ , which is discussed in the next section.

# Part III Of Computational Simulations

# 4 Novel MXenes Predictions

#### 4.1 DFT with CASTEP

The simulations of materials from the MXene family will be the first here presented. For such materials, which have not yet been synthesized, we focus on the stability, characterization, and basic electronic properties, such as the band structure and the effective mass of the band states. Conduced by these properties, we choose to work with the CASTEP (Cambridge Sequential Total Energy Package) (SEGALL et al., 2002a; CLARK et al., 2005), which uses the DFT formalism (3) to calculate physical properties of materials.

DFT is a method for calculating the electron density that minimizes the total energy of a many-body system, relying solely on the fundamental laws of quantum mechanics, thus being called an *ab initio* method. For such minimization, an exchange-correlation functional is necessary to perform the calculations. The Generalized Gradient Approximation (GGA), proposed by Perdew, Burke, and Ernzerhof (PBE) (CORSO et al., 1996; PERDEW; BURKE; WANG, 1996b), was used for the geometry optimization of the crystal, within a norm-conserved pseudopotential to replace the core electrons in each atomic species (LIN et al., 1993). The electronic configuration explicitly considered in calculations for each atom is shown in Table 1.

Atom	Configuration
Y	$4d^1 \ 5s^2$
$\overline{C}$	$2s^2 2p^2$
F	$2s^2 \ 2p^5$
Br	$4s^2 4p^5$
Cl	$3s^2 \ 3p^5$

Table 1 – Pseudo atoms configurations used for geometry optimization.

The first Brillouin zone (BZ) is the unit cell in reciprocal space; thus, integration over the BZ is necessary for calculations. This integration was performed as a sum over a 9x9x1 k-point Monkhorst-Pack grid (MONKHORST; PACK, 1976), which was found to be sufficient for electron density convergence.

DFT calculations are a self-consistent methodology. The parameters used for the convergence of both monolayers were: Total energy change less than  $1\times10^{-5}\,\mathrm{eV/atom}$ , maximum force on each atom below  $0.03\,\mathrm{eV/Å}$ , pressure less than  $0.05\,\mathrm{GPa}$ , and maximum

atomic displacement not greater than  $1\times10^{-3}$  Å, using the Broyden–Fletcher–Goldfarb–Shanno (BFGS) algorithm (PFROMMER et al., 1997) for the minimization. The cut-off energy for the plane-wave basis, necessary for representing the Kohn-Sham orbitals, was set as  $680\,\mathrm{eV}$  for  $Y_2\mathrm{CBr}_2$  and  $750\,\mathrm{eV}$  for  $Y_2\mathrm{CCl}_2$ .

All materials studied here belong to the same hexagonal structure, represented in Figure 23. However, geometry optimization revealed distinct lattice parameters for each system. Consequently, the reciprocal lattice and thus the BZ will have different sizes for each material. The resulting lattice parameters, obtained by minimizing the system energy using the GGA-PBE approach, are presented in Table 2.

System	Lattice Parameters (Å)
	a = 3.479
$Y_2CF_2$	b = 3.479
	c = 20.422
	a = 3.620
$Y_2CCl_2$	b = 3.620
	c = 19.270
	a = 3.669
$Y_2CBr_2$	b = 3.669
	c = 18.965

Table 2 – Lattice parameters for the studied systems, according to the DFT GGA-PBE geometry optimization.

The GGA-PBE approach is known to underestimate the energy gap of semiconductors, which invites us to perform a second calculation using a hybrid functional. Based on the geometry optimization already calculated, we conducted an additional single point calculation using the HSE06 hybrid functional (HEYD; SCUSERIA; ERNZERHOF, 2003). This step aims to achieve a more experimentally precise prediction of the energy gap contained in the band structure of the materials.

## 4.2 Lattice Stability and Characterization

#### 4.2.1 Cohesive Energy

Cohesive energy is a measure that indicates the strength with which atoms are bonded within a crystal structure. Verifying the effect of terminations on cohesive energy means observing how the termination groups affect one of the main stability indicators. The formal definition of cohesive energy,  $E_{\rm coh}$ , is the difference between the energy summation of the pseudo atoms and the total energy of the system, divided by the number of atoms in the system. For  $Y_2CT_2$  MXenes we have:

$$E_{\rm coh} = \frac{2E_{\rm Y}^{\rm pseudo} + E_{\rm C}^{\rm pseudo} + 2E_{\rm T}^{\rm pseudo} - E_{\rm Y_2CT_2}^{\rm tot}}{5}.$$
 (4.1)

Applying the values obtained after geometry optimization of the primitive cells, we found the resulting cohesive energies:

System	$E_{coh}(eV)$
$Y_2CF_2$	7.462
$Y_2CCl_2$	6.513
$\overline{\mathrm{Y_{2}CBr_{2}}}$	6.249

Table 3 – Cohesive energy  $(E_{coh})$  for the studied systems, according to the DFT GGA-PBE geometry optimization.

Higher cohesive energy was obtained for termination groups with greater electronegativity. These large cohesive energies, overall, are good indicators of stability for the proposed systems, closely resembling the results found for graphene (SHIN et al., 2013) and other MXenes (ZHANG et al., 2018).

#### 4.2.2 Phonon Energy States

The Born-Oppenheimer energy surface is defined as the ground state energy of an electronic system in a field of fixed nuclei. We can obtain these energy states from the Schrödinger equation:

$$H_{\text{BO}}(\{\mathbf{R}\}, \{\mathbf{r}\})\Phi(\{\mathbf{R}\}, \{\mathbf{r}\}) = E(\{\mathbf{R}\}, \{\mathbf{r}\})\Phi(\{\mathbf{R}\}, \{\mathbf{r}\}),$$
 (4.2)

where the Born-Oppenheimer Hamiltonian is (BARONI et al., 2001)

$$H_{BO}(\{\mathbf{R}\}, \{\mathbf{r}\}) = -\frac{1}{2} \sum_{i}^{n} \nabla_{i}^{2} + \sum_{A>B}^{m} \frac{Z_{A}Z_{B}}{R_{AB}} - \sum_{A=1}^{m} \sum_{i=1}^{n} \frac{Z_{A}}{R_{Ai}} + \sum_{i>i}^{n} \frac{1}{r_{ij}}.$$
 (4.3)

The system's geometry equilibrium is reached when the force acting on each nucleus is zero, i.e.

$$\mathbf{F}_{A} \equiv -\frac{\partial E(\{\mathbf{R}\}, \{\mathbf{r}\})}{\partial \mathbf{R}_{A}} = 0. \tag{4.4}$$

For understanding the vibrations of the lattice we might think of the Hamiltonian response to small lattice displacements  $u_{\nu}^{n} = \chi_{\nu}^{n} - R_{\nu}^{n}$ , where  $\chi_{\nu}^{n}$  is the position of the *n*th

atom in the  $\nu$  axis, and  $R^n_{\nu}$  is its equilibrium position. Despite similarities, this notation is not representing covariance nor contravariance, as the number of atoms is not a quantity related to any metric. The expanded potential is thus

$$V = V_0 + \sum_{n,\nu} u_{\nu}^n \frac{\partial V}{\partial u_{\nu}^n} + \sum_{n,m,\nu,\mu} u_{\nu}^n u_{\mu}^m \frac{\partial^2 V}{\partial u_{\nu}^n \partial u_{\mu}^m} + \dots$$
 (4.5)

In the harmonic approximation we might neglect all terms beyond the third, and the second is also zero as we are concerned with oscillations near equilibrium. The matrix of force constants is defined from the third term as

$$\Phi_{\nu,\mu}^{n,m} \equiv \frac{\partial^2 V}{\partial u_{\nu}^n \partial u_{\mu}^m}.$$
(4.6)

From Hamilton equation  $\dot{p}_{\nu}^{n} = -\frac{\partial H}{\partial u_{\nu}^{n}}$  we obtain 3N equations of motion,

$$M_n \ddot{u}_{\nu}^n = -\sum_{m,\mu} u_{\mu}^m \Phi_{\nu,\mu}^{n,m}, \tag{4.7}$$

which can be understood as each term on the sum being the force acting on the  $\nu$ th axis of the nth atom due to a displacement  $u_{\mu}^{m}$  of the mth atom in the  $\mu$ th axis.

From translational symmetry, we might write a guess solution for the small displacement as a function of time as

$$u_{\nu}^{n} = U_{\nu}^{n} e^{i(q_{\nu}R_{\nu}^{n} - \omega t)} \tag{4.8}$$

where  $q_{\nu}$  is the  $\nu$ th component of the phonon wave vector  $\boldsymbol{q}$ ,  $U_{\nu}^{n}$  is the amplitude of the vibration, and  $\omega$  is the respective angular frequency. Using this solution in equation 4.7,

$$M_n \omega^2 U_{\nu}^n e^{i(q_{\nu} R_{\nu}^n - \omega t)} = \sum_{m,\mu} U_{\mu}^m e^{i(q_{\mu} R_{\mu}^m - \omega t)} \Phi_{\nu,\mu}^{n,m}.$$
 (4.9)

Only the relative position  $\mathbb{R}^m - \mathbb{R}^n$  is relevant, so we might take  $\mathbb{R}^m$  as the origin without loss of generality, to obtain:

$$M_{n}\omega^{2}U_{\nu}^{n} = \sum_{m,\mu} U_{\mu}^{m} e^{-i(q_{\mu}R_{\mu}^{n})} \Phi_{\nu,\mu}^{n,m}$$

$$\omega^{2}U_{\nu}^{n} = \sum_{m,\mu} U_{\mu}^{m} D_{\nu,\mu}^{n,m}(\mathbf{q}),$$
(4.10)

where  $D_{\nu,\mu}^{n,m}(\boldsymbol{q}) \equiv \frac{1}{M_n} \Phi_{\nu,\mu}^{n,m} e^{-i(q_{\mu}R_{\mu}^n)}$  is the dynamical matrix, which contains all the information about the lattice vibrations. The dynamical matrix can be seen as the mass-reduced Fourier transform of the force constants matrix, and is hermitian by construction, giving real eigenvalues. Non-trivial solutions are obtained from

$$|D_{\nu,\mu}^{n,m}(\mathbf{q}) - \omega^2 \delta_{\nu\mu} \delta^{nm}| = 0. \tag{4.11}$$

The lattice vibration frequencies are obtained as the square roots of the eigenvalues, and the eigenvectors give the pattern of atomic displacements belonging to each mode (SEGALL et al., 2002b). It is important to notice that negative eigenvalues will give imaginary frequencies, which is more than nonsense; when these imaginary frequencies are used in the displacement function (4.8) they result in a real component of the exponential term, i.e., indicates instability of the system due to increasing displacement with time.

For computing the matrix of force constants, we obtain the potential term as the ground state expectation value of the potential operator,  $V = \langle \Phi(\{\mathbf{R}\}, \{\mathbf{r}\}) | \hat{V} | \Phi(\{\mathbf{R}\}, \{\mathbf{r}\}) \rangle$ , so we can write

$$\frac{\partial^{2}V}{\partial u_{\nu}^{n}\partial u_{\mu}^{m}} = \frac{\partial}{\partial u_{\mu}^{m}} \left( \frac{\partial V}{\partial u_{\nu}^{n}} \right) 
= \frac{\partial}{\partial u_{\mu}^{m}} \left( \left\langle \frac{\partial \Phi}{\partial u_{\nu}^{n}} \middle| \hat{V} \middle| \Phi \right\rangle + \left\langle \Phi \middle| \hat{V} \middle| \frac{\partial \Phi}{\partial u_{\nu}^{n}} \right\rangle + \left\langle \Phi \middle| \frac{\partial \hat{V}}{\partial u_{\nu}^{n}} \middle| \Phi \right\rangle \right) 
= \frac{\partial}{\partial u_{\mu}^{m}} \left( \epsilon \left\langle \frac{\partial \Phi}{\partial u_{\nu}^{n}} \middle| \Phi \right\rangle + \epsilon \left\langle \Phi \middle| \frac{\partial \Phi}{\partial u_{\nu}^{n}} \right\rangle + \left\langle \Phi \middle| \frac{\partial \hat{V}}{\partial u_{\nu}^{n}} \middle| \Phi \right\rangle \right) 
= \frac{\partial}{\partial u_{\mu}^{m}} \left\langle \Phi \middle| \frac{\partial \hat{V}}{\partial u_{\nu}^{n}} \middle| \Phi \right\rangle 
= \left\langle \frac{\partial \Phi}{\partial u_{\mu}^{m}} \middle| \frac{\partial \hat{V}}{\partial u_{\nu}^{n}} \middle| \Phi \right\rangle + \left\langle \Phi \middle| \frac{\partial \hat{V}}{\partial u_{\nu}^{n}} \middle| \frac{\partial \Phi}{\partial u_{\mu}^{m}} \right\rangle + \left\langle \Phi \middle| \frac{\partial^{2} \hat{V}}{\partial u_{\mu}^{m} u_{\nu}^{n}} \middle| \Phi \right\rangle.$$
(4.12)

ab initio methods for solving this equation may vary. Our solution comes from linear response, or, density functional perturbation theory (DFPT); an analytical way of computing the second derivative of the total energy with respect to a given perturbation. The nature of the perturbation can vary when obtaining different properties, but for the dynamical matrix we only need a perturbation in the atomic positions, giving the linear response of the wave function  $\frac{\partial \Phi}{\partial \lambda}$  due to a displacement  $\lambda$ .

Phonon dispersion is the relation between the squared vibrational frequency and the phonon wave vector, which can be mapped inside the first BZ. Figure 24 shows phonon dispersion curves for  $Y_2CF_2, Y_2CCl_2$  and  $Y_2CBr_2$  along the  $\Gamma$ -K-M- $\Gamma$  symmetry path in BZ.

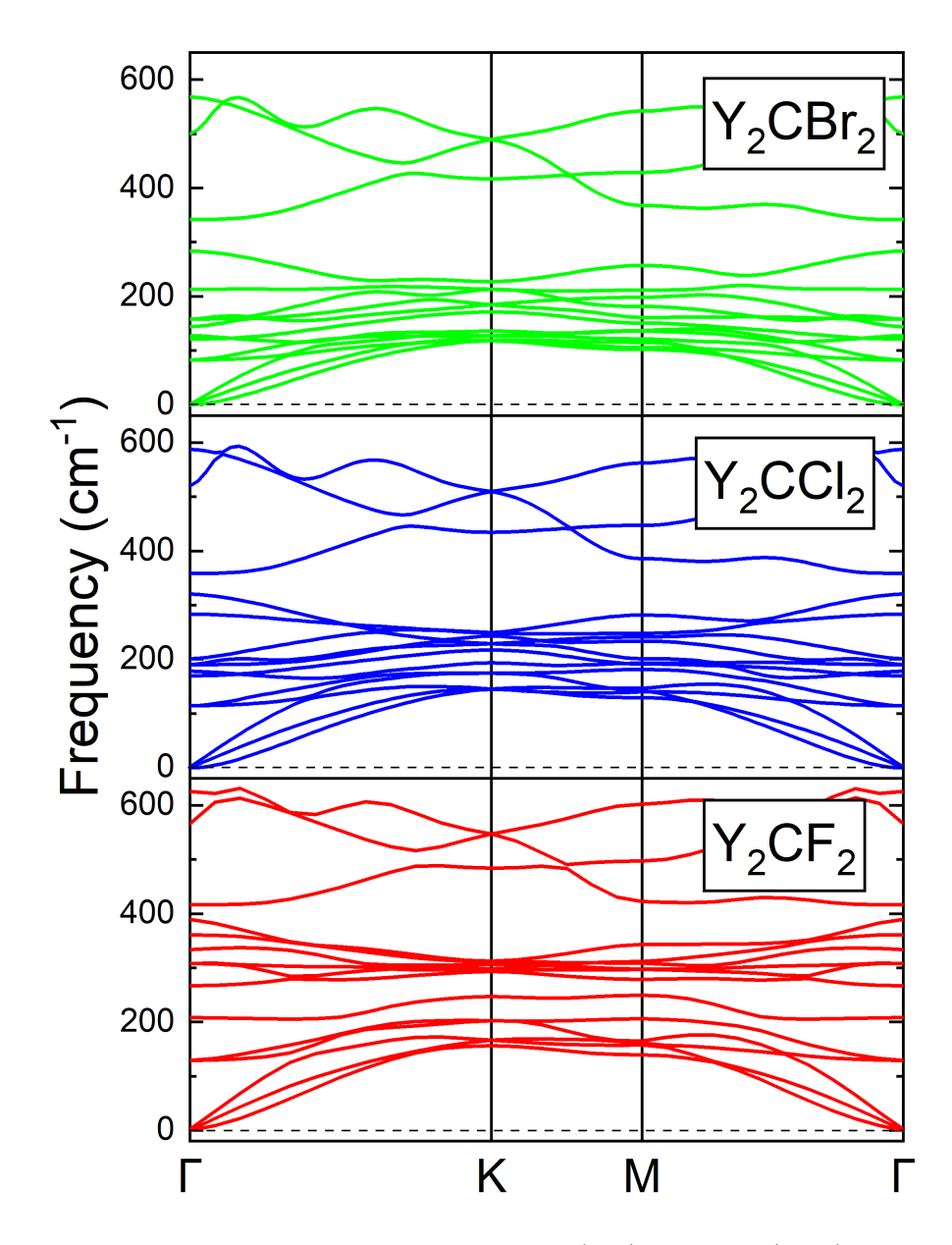


Figure 24 – Phonon dispersion curves of  $Y_2CF_2$  (red),  $Y_2CCl_2$  (blue) and  $Y_2CBr_2$  (green) in the frequency range from 0 to  $600\,\mathrm{cm^{-1}}$ , calculated with the GGA-PBE exchange-correlation functional.

According to the phonon dispersion curves shown in Figure 24, all materials examined here presented positive squared frequencies throughout the entire path, meaning absence of imaginary frequencies, hence a strong indication of high dynamic stability. We also observed that the three acoustic branches of each material are very similar to their counterparts, though differently, the decrease in the termination group mass (Br > Cl > F) correlated with a decrease in the energy of the optical branches. This behavior is strongly related to the presence of the atomic mass in the dynamical tensor, where heavier

systems produce lower vibrational energy states. We also remark that  $Y_2CF_2$  presented two small phonon band gaps (247–265 and 390–417 cm<sup>-</sup>1),  $Y_2CCl_2$  presented one slightly bigger (320–358 cm<sup>-</sup>1), and  $Y_2CBr_2$  presented a more robust one (284–342 cm<sup>-</sup>1). These phonon band gaps represent forbidden vibrational states in these structures, which implicates the reduction of thermal conductivity and suppression of electron-phonon scattering within that vibrational range, enhancing electron mobility.

For further exploration into physical properties that derive from lattice interactions, we shall first grasp the concept of phonon density of states (DOS), which can be understood as the amount of vibrational modes in each frequency range. The DOS is calculated as

$$N(\omega) = \frac{1}{4\pi^3} \sum_{i} \int \delta(\omega - \omega_i(\mathbf{q})) d\mathbf{q}, \qquad (4.13)$$

where  $\omega_i(\mathbf{q})$  is the *i*th band frequency of a phonon vector  $\mathbf{q}$  in reciprocal space.

#### 4.2.3 Thermodynamics

The total vibrational energy of the lattice, as a quantum harmonic oscillator, is expressed as

$$E = \sum_{\mathbf{q}} E_{\mathbf{q}} = \sum_{\mathbf{q}} \left( n_{\mathbf{q}} + \frac{1}{2} \right) \hbar \omega_{\mathbf{q}}, \tag{4.14}$$

where  $n_q$  is the occupation number of phonon states of momentum vector q.

The part of this energy that is independent of occupied phonon states is called zero-point energy  $E_{zp}$  and may be written in integral form using the DOS:

$$E_{\rm zp} = \frac{1}{2} \int \hbar \omega N(\omega) d\omega. \tag{4.15}$$

The obtained results for the zero-point energy of each monolayer are presented in Table 4

System	$E_{zp}(eV)$
$Y_2CF_2$	0.248
$\overline{Y_2CCl_2}$	0.188
$\overline{\mathrm{Y_{2}CBr_{2}}}$	0.196

Table 4 – Zero-point energy  $(E_{zp})$  for the studied systems.

The average occupancy of phonons with wave vector q in thermal equilibrium is given by the Planck distribution,

$$\langle n_{\mathbf{q}} \rangle = \frac{1}{exp(\frac{\hbar \omega_{\mathbf{q}}}{k_{\mathrm{B}}T}) - 1},$$
 (4.16)

so the energy fraction that comes from the occupied states, E<sub>phonon</sub> is

$$E_{\text{phonon}} = \sum_{\mathbf{q}} \langle n_{\mathbf{q}} \rangle \hbar \omega_{\mathbf{q}}; \tag{4.17}$$

which can also be written in integral form:

$$E_{\text{phonons}} = \int \frac{\hbar\omega}{exp(\frac{\hbar\omega}{k_{\text{P}}T}) - 1} N(\omega) d\omega. \tag{4.18}$$

In thermodynamics, the heat capacity at a constant volume is defined as  $C_{\rm V} = \left(\frac{dU}{dT}\right)_v$ , where T is the temperature and U is the internal energy. The contribution from the lattice to the heat capacity, i.e., the lattice heat capacity at constant volume is thus calculated from the derivative with respect to the temperature of the lattice vibrational energy:

$$C_{\rm V}(T) = \left(\frac{dE}{dT}\right)_v = k_B \int d\omega N(\omega) \frac{\left(\frac{\hbar\omega}{k_B T}\right)^2 exp\left(\frac{\hbar\omega}{k_B T}\right)}{\left[exp\left(\frac{\hbar\omega}{k_B T}\right) - 1\right]^2}.$$
 (4.19)

For our system, isolated from interactions, the enthalpy becomes just the internal energy

$$H(T) = E_{\rm zp} + E_{\rm phonon},\tag{4.20}$$

and the entropy may be obtained from the heat capacity at constant volume, as

$$S(T) = \int \frac{C_{\rm V}}{T} dT = \frac{E_{phonon}}{T} - k_B \int N(\omega) ln \left[ 1 - exp \left( -\frac{\hbar \omega}{K_{\rm B} T} \right) \right] d\omega. \tag{4.21}$$

Gibbs free energy as a function of temperature can then be easily calculated as the difference between enthalpy and entropy times temperature, G(T) = H(T) - TS(T).

Figure 25 shows the calculated curves of enthalpy H(T), free energy G(T), and temperature times entropy, TS(T), as a function of temperature. The most important

prediction of these properties is that G(T) remains negative across all temperature values and decreases with rising temperatures, being a crucial aspect for consideration in material stability studies. Our results indicate that for terminations exhibiting higher electronegativity and increased atomic mass, the free energy experiences a more rapid decline with rising temperature.

We also observe that, at low temperatures, the heat capacity of all materials is consistent with the third law of thermodynamics, being proportional to  $T^3$ . At high temperatures, Y<sub>2</sub>CF<sub>2</sub> and Y<sub>2</sub>CCl<sub>2</sub> converged to near 24 cal/cell · K, while Y<sub>2</sub>CBr<sub>2</sub> went close to 30 cal/cell · K, significantly higher than its counterparts and close to the Duolong-Petit limit (ASHCROFT; MERMIN, 2022), i.e.,  $C_V = 3R$  for  $T \to \infty$ . For conversion, considering the unit cell containing 5 atoms, 30 cal/cell · K  $\approx 25$  J/mol · K.

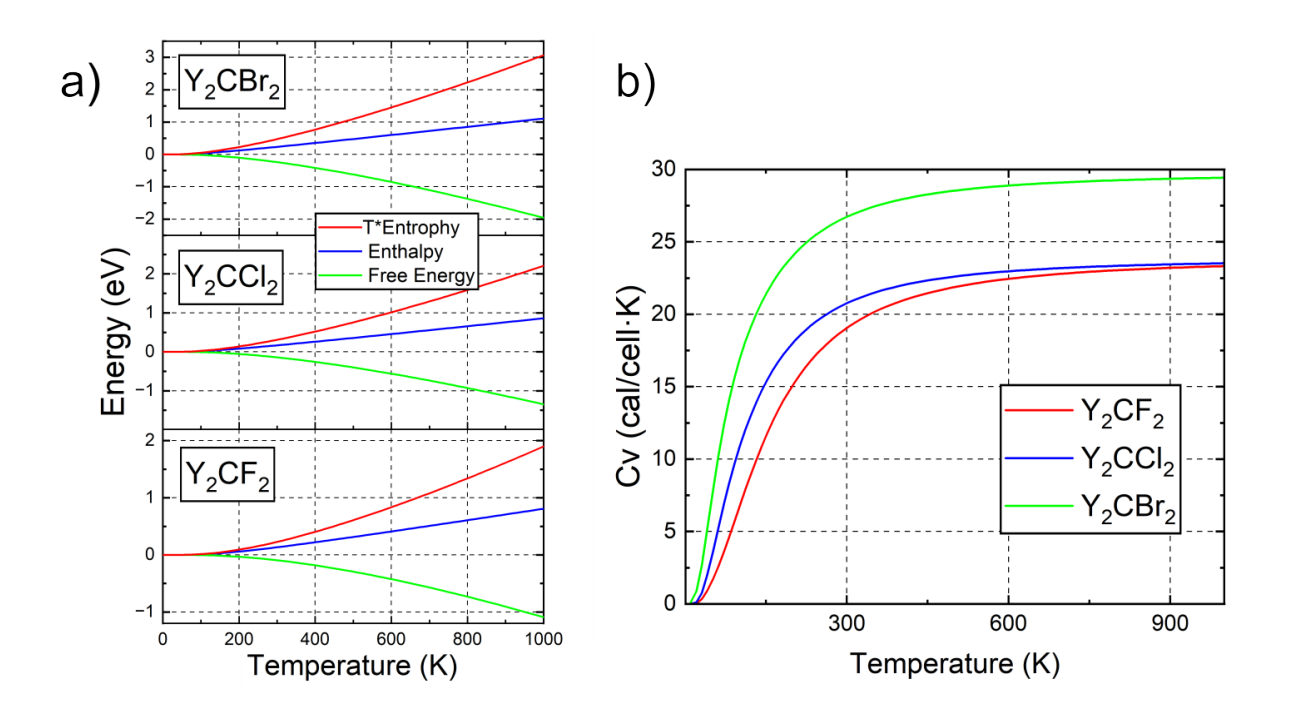


Figure 25 – a) Thermodynamic properties for  $Y_2CT_2$  MXenes: Enthalpy [H(T)] (blue), temperature times entropy,  $T \times S(T)$  (red), and free energy [G(T)] (green). b) Constant volume heat capacity,  $C_V$ , for the  $Y_2CF_2$  (red),  $Y_2CCl_2$  (blue) and  $Y_2CBr_2$  (green) monolayers as a function of the temperature (K), using the GGA-PBE functional.

## 4.2.4 Vibrational Spectroscopy

In condensed matter physics, infrared (IR) and Raman spectra are useful for studying and identifying chemical substances or functional groups and their low-frequency vibrational modes. It can be used to characterize new materials so that they can be identified in future samples. The following discussion explores IR and Raman spectroscopy, where the spectra are calculated from the vibrational eigenmode frequencies of the optical phonons at  $\Gamma$ , i.e.,  $\omega_i(\mathbf{q}=0)$ . From now on, we consider  $\omega_i \equiv \omega_i(\mathbf{q}=0)$ .

In IR absorption, an electron state is annihilated, and a higher energy electron state is created; the energy difference is absorbed from an annihilated photon in the IR range. That excited state can eventually decay back into the lower energy state, releasing the energy difference as a lattice vibration, i.e., the creation of a phonon state with the same energy and momentum as in the absorbed photon. This process is illustrated in Figure 26.

The formalism presented in (POREZAG; PEDERSON, 1996) considers that a displacement  $U^i_{\mu}$  in the direction of the *i*th eigenvector  $v^i_{\mu}$  can then be written as  $U^i_{\mu} = Q^i v^i_{\mu}$ , with  $Q^i$  being a normal-mode coordinate. The first-order IR intensity is then evaluated as:

$$I_{\rm IR}^i = \frac{\mathcal{N}\pi}{3c} \left| \frac{d\boldsymbol{\mu}}{dQ^i} \right|^2,\tag{4.22}$$

where  $\mathcal{N}$  is the particle density in the sample, c is the speed of light, and  $\boldsymbol{\mu}$  is the dipole moment of the system, which can be calculated as (GRYCIUK; GÓRECKI, 2002):

$$\boldsymbol{\mu} = \sum_{m} \boldsymbol{r}_{m} q_{m} + \iiint_{C} \boldsymbol{r} \hat{n}(\boldsymbol{r}) \, dV, \tag{4.23}$$

where  $r_m$  and  $q_m$  are the position and charge, respectively, of the *m*th atom.  $\hat{n}$  is the electron density and the integration is taken over the cell C.

For each material, the calculated infrared spectrum shown in Figure 27 predicts four peaks of light absorption, with six modes of vibration within. These modes are equivalent for every  $Y_2CT_2$  MXene, where only the atomic specimen present in the vibration is different. Nevertheless, as a consequence of the differences in the termination groups, not only in electronegativity but more importantly in mass, the positions and sizes of the peaks are significantly different for each material. Structures with heavier termination groups presented lower vibration frequencies for all modes.

Table 5 shows the resulting modes of vibration. The first and third energy peaks correspond to two degenerate in-plane asymmetric stretching modes of vibration  $(E_u)$ , while the second and the fourth correspond to non-degenerate asymmetric out-of-plane modes  $(A_{2u})$ .

System	$\mathbf{E}_u$	$A_{2u}$	$\mathbf{E}_u$	$A_{2u}$
$Y_2CF_2$	288	384	422	653
$Y_2CCl_2$	170	283	359	587
$Y_2CBr_2$	121	213	342	568

Table 5 – Frequency of the modes of vibration generated from infrared light absorption in MXenes, in  $cm^{-1}$ .

Within a crystalline environment, the interaction of light with the lattice results in a probability of the light being scattered. Given an interaction, the greatest probability is of an elastic scattering, though it is possible to happen an energy shift of the scattered photons, where an electron is excited into a virtual state that immediately decays into an electron state different from before. The energy and momentum difference between the previous and new electron states is compensated by the creation or annihilation of a phonon state that matches the difference. That is known as the Raman effect of inelastic scattering of monocromatic light, where the case of phonon creation is known as Stokes scattering, and anti-Stokes scattering happens when a phonon state is annihilated. Figure 26 illustrates these processes.

For calculations, we follow the formalism in (MIWA, 2011), where the intensity  $I_{\text{Raman}}^i$  of each *i*th eigenmode  $\omega_i$  follows a proportion relation as

$$I_{\mathrm{Raman}}^{i} \propto \left| \boldsymbol{e}_{\mathrm{in}} \cdot \boldsymbol{A}^{i} \cdot \boldsymbol{e}_{\mathrm{out}} \right|^{2} \frac{1}{\omega_{i}} \left( \frac{1}{exp\left(\frac{\hbar\omega_{i}}{k_{\mathrm{D}}T}\right) - 1} + 1 \right),$$
 (4.24)

where  $e_{in}$  ( $e_{out}$ ) is the polarization vector of the incident (scattered) photon. The Raman susceptibility tensor  $A^i$  is calculated as

$$A_{\mu\nu}^{i} = \sqrt{\Omega} \sum_{n,\xi} \frac{d\chi_{\mu\nu}}{dR_{n,\xi}} \frac{\upsilon_{n,\xi}^{i}}{\sqrt{M_{n}}},\tag{4.25}$$

where  $v_n^i$  is the *i*th vibrational eigenmode of the *n*th atom, with mass  $M_n$  and position  $R_n$ ;  $\Omega$  is the volume of the unit-cell,  $\chi$  is the electronic linear dielectric susceptibility, and Greek indices represent the Cartesian directions.

 $\chi$  derivatives are evaluated as

$$\frac{d\chi_{\mu\nu}}{dR_{n,\xi}} = -\frac{1}{\Omega} \frac{d^3 E}{d\epsilon_{\mu} d\epsilon_{\nu} dR_{n,\xi}},\tag{4.26}$$

where  $\epsilon_{\mu}$  ( $\epsilon_{\nu}$ ) is a uniform electric field in the  $\mu$ th ( $\nu$ th) direction, and E is the total energy of the system.

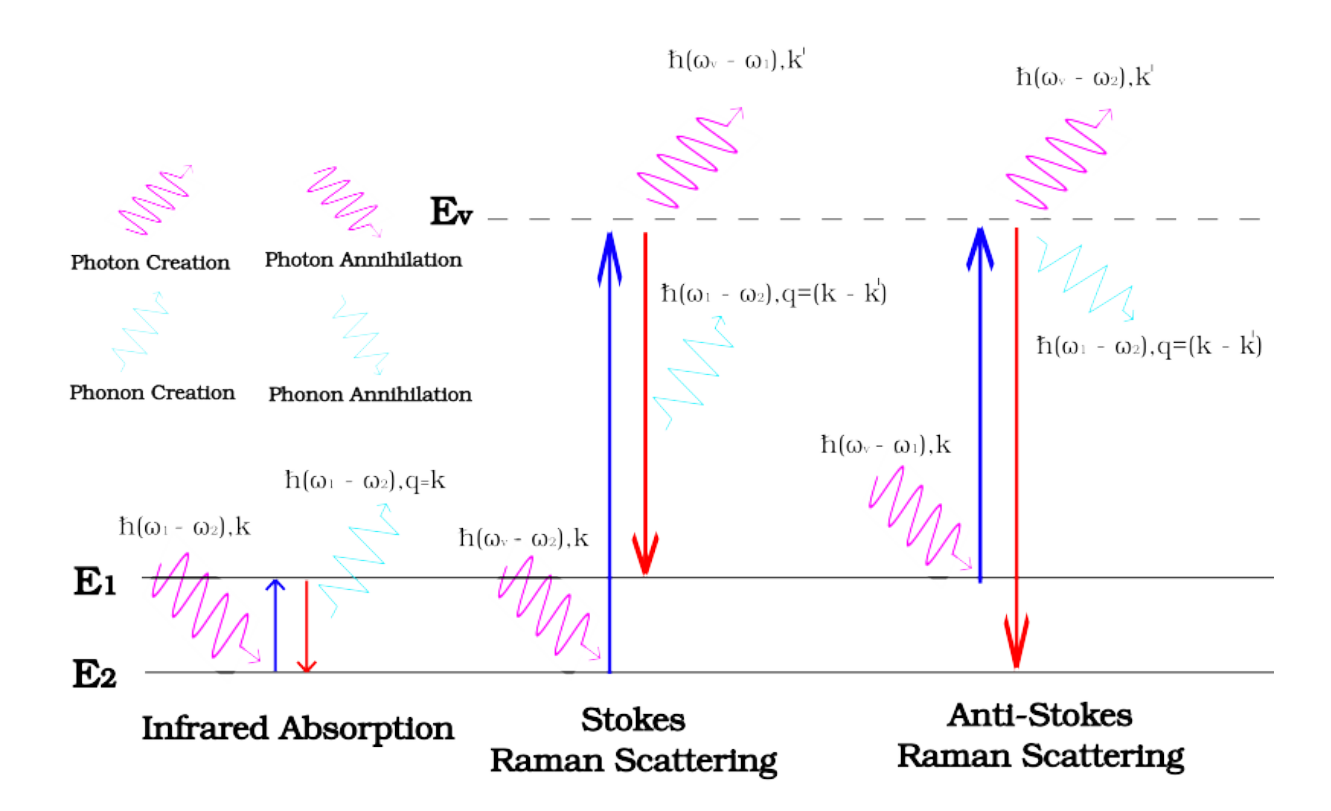


Figure 26 – Energy level diagram representing IR absorption, Stokes Raman scattering, and anti-Stokes Raman scattering.

Similarly to what was predicted in IR, the Raman spectrum shown in Figure 27 predicts four peaks of inelastic light scattering, also containing six modes of vibration within, where two of the peaks represent individual modes of vibration, and the other two are related to degenerated vibrational states. The first and third peaks both correspond to the degenerated in-plane shear modes of vibration  $(E_g)$ , while the second and fourth peaks refer to non-degenerated symmetric and asymmetric out-of-plane modes  $(A_{1g})$ , respectively.

Due to the same causes highlighted in the phonon and IR discussions, despite the fact that all materials presented in Figure 27 contain the same modes of vibration, the size and positions of the peaks are unique for each material. Again, heavier termination groups in the monolayers were correlated with lower frequencies for each mode of vibration. Table 6 contains all the predictions for the vibrational modes to be expected from light scattering in the studied systems.

System	$E_g$	$A_{1g}$	$E_g$	$\overline{\mathrm{A}_{1g}}$
$Y_2CF_2$	134	214	327	412
$Y_2CCl_2$	114	178	190	320
$Y_2CBr_2$	82	127	158	284

Table 6 – Frequency of the Raman modes of vibration for MXenes, in cm<sup>-1</sup>.

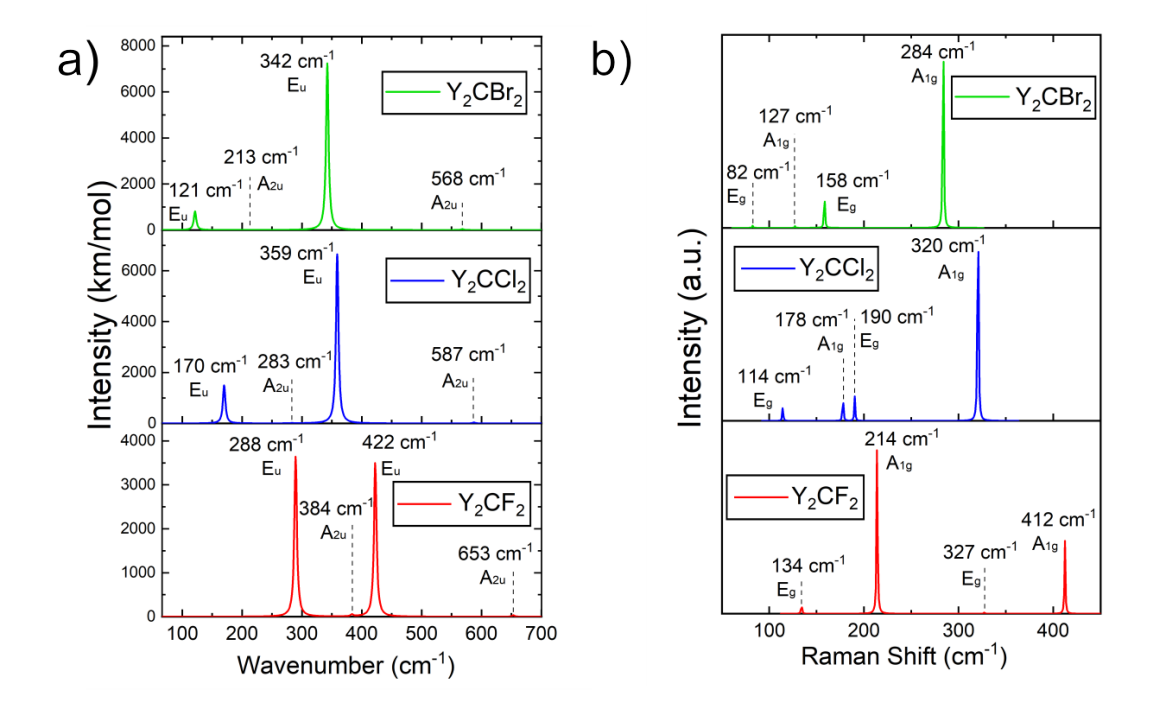


Figure 27 – a) Infrared spectrum for Y<sub>2</sub>CF<sub>2</sub> (red), Y<sub>2</sub>CCl<sub>2</sub> (blue) and Y<sub>2</sub>CBr<sub>2</sub> (green). b) Raman spectrum for the Y<sub>2</sub>CF<sub>2</sub> (red), Y<sub>2</sub>CCl<sub>2</sub> (blue) and Y<sub>2</sub>CBr<sub>2</sub> (green).

# 4.3 Electronic Properties

#### 4.3.1 Band Structure

The energy levels of electrons can be mapped in reciprocal space, generating what we call the electronic structure. To explore the regions of most interest, the mapping inside the BZ is performed in a path passing through the high symmetry points of the cell,  $\Gamma \to K \to M \to \Gamma$ , just as done in the phonon dispersion. Figure 28 presents the Kohn-Sham band structure calculated for Y<sub>2</sub>CF<sub>2</sub>, Y<sub>2</sub>CCl<sub>2</sub> and Y<sub>2</sub>CBr<sub>2</sub>, using both GGA-PBE and HSE06 functionals.

Spin-polarized calculations were also performed for all three materials, but we found only non-magnetic ground states, which is explained by the strong covalent bond between yttrium and carbon, and the attached termination groups. Other studies have

found that these non-magnetic states can be altered with the application of strain (ZHAO; KANG; XUE, 2014).

From Figure 28, we observe that for the three MXenes, the smallest energy gap corresponds to an indirect transition, with the gap size correlating to the electronegativity of the termination group. Indirect transitions require phonon assistance, meaning electrons can be excited while absorbing momentum from lattice vibrations. Therefore, direct band gaps are generally more attractive for applications.

Close analysis reveals that although the smallest gap is indirect for all three materials, direct transitions are not very energetically distant, especially for the Cl termination. This incites us to question whether the predominant transitions in these materials are direct or indirect. It is observed that for the direct transition calculated with GGA-PBE,  $Y_2CF_2$  contains an unusual flat valence band in the vicinities of the M point. We note that in  $Y_2CCl_2$ , not only are the direct (at M) and indirect (from  $\Gamma$  to M) band gaps energetically very close to each other, but with the hybrid functional we see that the energy levels between the high symmetry points do not change much, luring our attention to the verification of some "flatness effect" in that crystalline direction.

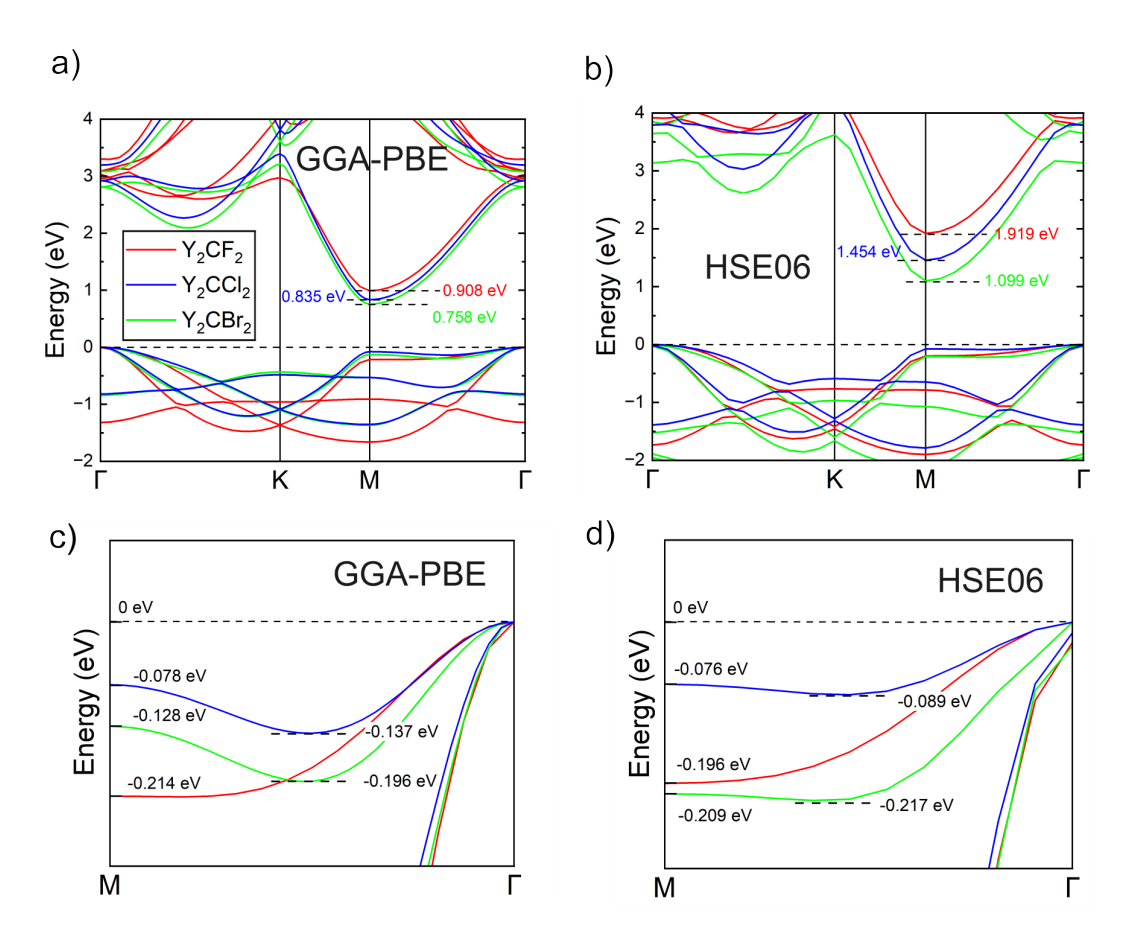


Figure 28 – Electronic band structure of  $Y_2CF_2$  (red),  $Y_2CCl_2$  (blue) and  $Y_2CBr_2$  (green). a) using GGA-PBE exchange-correlation functional along the 2D Brillouin high symmetry pathand, b) using HSE06 hybrid functional. c) and d) are the same energy bands of a) and b), but zoomed near Fermi level in  $M \to \Gamma$  path.

System	PBE Direct (eV)	PBE Indirect (eV)	HSE06 Direct (eV)	HSE06 Indirect (eV)
$\overline{Y_2CF_2}$	1.122	0.908	2.115	1.919
$\overline{Y_2CCl_2}$	0.913	0.835	1.530	1.454
$Y_2CBr_2$	0.886	0.758	1.318	1.099

Table 7 – Direct and indirect band gaps, obtained for Y<sub>2</sub>CF<sub>2</sub>, Y<sub>2</sub>CCl<sub>2</sub> and Y<sub>2</sub>CBr<sub>2</sub>, using both PBE and HSE06 functionals.

#### 4.3.2 Effective Mass

Heading into a semi-classical picture, where we preserve the Newtonian intuition of F=ma, an electron/hole in the crystal structure, in the presence of some external electromagnetic field, is not accelerated as if its inertial mass is  $m_{\rm e}$ . Instead, due to the interaction with the lattice, the electron/hole behaves as if it has an effective mass  $m^*$ , which can be anisotropic or even negative.

For that, we start from the position of the particle as a distribution probability given by the squared amplitude of the plane wave packet. In this perspective, the group velocity,  $v_{\rm g}$ , is what most closely resembles the classical intuition of velocity. This is our first important tool for investigating the particle dynamics in the lattice:

$$v_{\rm g}(\mathbf{k}) \equiv \frac{d\omega}{d\mathbf{k}} = \frac{1}{\hbar} \frac{dE(\mathbf{k})}{d\mathbf{k}}.$$
(4.27)

We take a second derivative to obtain the acceleration of the particles,

$$a_{g}(\mathbf{k}) = \frac{dv_{g}(\mathbf{k})}{dt} = \frac{1}{\hbar} \frac{d^{2}E(\mathbf{k})}{d\mathbf{k}^{2}} \frac{d\mathbf{k}}{dt}.$$
 (4.28)

We neglect not the physical intuition that we aimed from the beginning: The inclination of the energy levels in the reciprocal space, along a certain direction, gives the velocity of the particles that occupies these states, traveling in that direction. When we consider the whole curvature of the energy levels in reciprocal space, we see that the curvature itself contains all information about the effective velocity and acceleration of particles occupying energy states in a crystal. Thus, a horizontally flat energy band means that the group velocity of the electron/hole wave packet is zero, and its effective mass tends to infinity along that direction, i.e., particles are strongly localized in specific spatial locations due to high inertia. This type of structure might lead to unusual physical properties, often studied in topology (PHONG; MELE, 2023) and superconductor physics (DENG; SIMON; KöHLER, 2003; CHEN; LAW, 2024; KURLETO et al., 2023).

Going further, the work done by an external force in a wavepacket is:

$$dE(\mathbf{k}) = Fd\mathbf{r} = Fv_{g}(\mathbf{k})dt, \tag{4.29}$$

so force can be isolated to:

$$F = \frac{1}{v_{g}}(\mathbf{k}) \frac{dE(\mathbf{k})}{dt} = \frac{1}{v_{g}(\mathbf{k})} \frac{dE}{d\mathbf{k}} \frac{d\mathbf{k}}{dt} = \hbar \frac{d\mathbf{k}}{dt}.$$
 (4.30)

Finally, after having expressions for both force and acceleration, we might reconstruct the Newtonian equation,  $F = m^*a$ , where the effective mass tensor is:

$$m^*(\mathbf{k}) = \hbar^2 \frac{1}{\frac{d^2 E(\mathbf{k})}{d\mathbf{k}^2}};\tag{4.31}$$

$$m^*(\mathbf{k}) = \begin{pmatrix} m_{xx} & m_{xy} & m_{xz} \\ m_{yx} & m_{yy} & m_{yz} \\ m_{zx} & m_{zy} & m_{zz} \end{pmatrix}.$$
 (4.32)

These results can be used in the semi-classical dynamics of charge carriers in energy bands, which respond to external Lorentz forces as:

$$m^*(\mathbf{k})a_{g}(\mathbf{k}) = e(E_{ext} + v_{g}(\mathbf{k}) \times B_{ext}). \tag{4.33}$$

The sign of the effective mass ratio,  $\frac{m^*}{m_e}$ , reveals the concavity of the curvature, and we propose the absolute value of this quantity as a measurement of flatness. The energies and effective mass ratio of the valence band, calculated along the path between two  $\Gamma$  points, are shown in Figure 29.

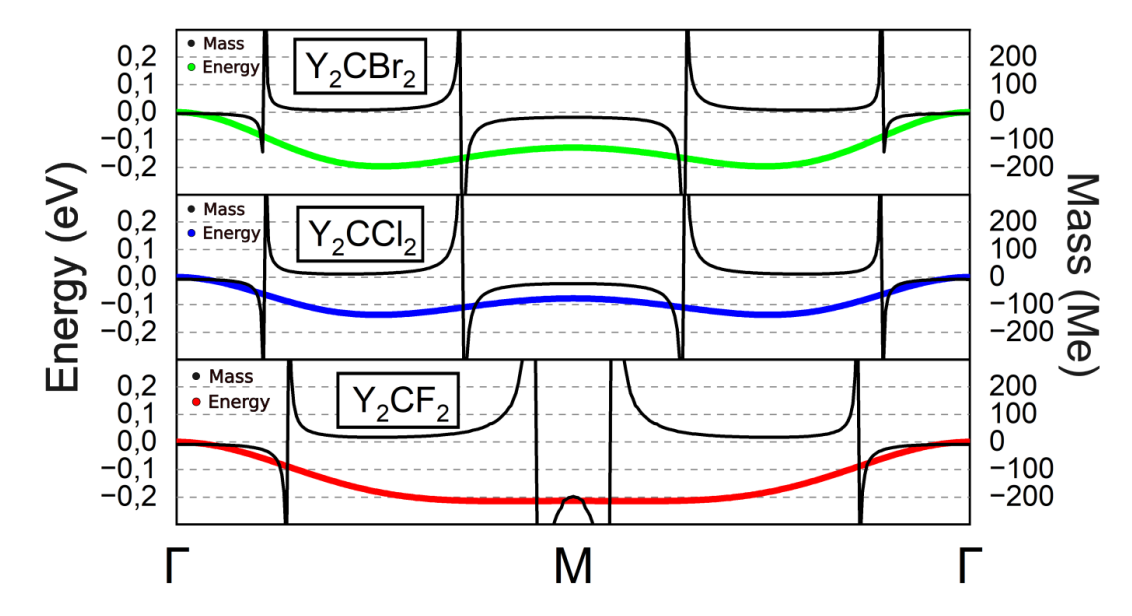


Figure 29 – Highest occupied energy bands for  $Y_2CF_2$  (red),  $Y_2CCl_2$  (blue) and  $Y_2CBr_2$  (green), between two  $\Gamma$  points, with correspondent effective mass (black) as a multiple of the electron mass  $m_e$ .

The purpose of Figure 29 is to identify peaks in the effective mass, corresponding to regions where the flatness effect is expected. This analysis allows the interpreter to determine whether the peaks in effective mass are located in a horizontal band or if they are observed in a non-zero velocity state. We see that the precision of the effective mass calculations is extremely sensitive at high values due to the singularity in 4.31, but it is completely safe to call flat any region where the absolute value of the effective mass is two orders of magnitude above the electron mass. In fact, the literature already considers  $\left|\frac{m^*}{m_e}\right| > 25$  as supermassive states (KURLETO et al., 2023).

All three materials exhibited several peaks of high effective mass, which is completely normal for non-zero velocity states. Nevertheless, a large area around the M symmetry point in Y<sub>2</sub>CF<sub>2</sub> remained a horizontal flat region. The mass ratio found at the M point is far beyond the flatness requirement we stated earlier,  $\left|\frac{m^*}{m_e}\right| \approx 200$ , implying a high flatness effect for hole states in direct transitions. The negative mass found at that

point indicates the presence of a smooth energy peak hidden in flatness. Unfortunately, the ideal scenario would be to find such massive states closer to the Fermi level, but in  $Y_2CF_2$  they are 0.2 eV below the top of the valence band.

Besides being a good measurement of flatness, the effective mass calculation can provide important information for general studies of electron/hole mobility. A pair of bands that are degenerate at the highest occupied state usually have different curvatures, resulting in heavy and light holes at that momentum coordinate. In Figure 28 we can see that each material presents two distinct curvatures in the  $\Gamma$  point, corresponding to their light and heavy hole states. Table 8 shows, for each MXene, the mass ratio for the electron at the bottom of the conduction band and for the light and heavy holes associated with the degenerate state at the top of the valence bands.

System	Electron	Light Hole	Heavy Hole
$Y_2CF_2$	1.14	-0.49	-2.51
$Y_2CCl_2$	1.00	-0.57	-2.52
$Y_2CBr_2$	1.02	-0.44	-1.64

Table 8 – Mass ratio for electron and holes associated with the indirect transition from  $\Gamma$  to M, obtained for  $Y_2CF_2$ ,  $Y_2CCl_2$  and  $Y_2CBr_2$ .

From Table 8, we observe no correlation between the termination electronegativity and resulting effective masses in the indirect transition states. The values obtained are also far from any flatness effect, being considerably similar for all materials except for the lighter heavy hole found in  $Y_2CBr_2$ .

To ensure that the code developed for this study gives reasonable results, we also performed the effective mass calculation for silicon, which is well explored in the literature. The obtained effective mass for the electron in the longitudinal direction is  $0.89m_e$ , very close to the  $0.90m_e$  obtained with the well established QuantumATK code (SMIDSTRUP et al., 2019), and still close to the experimental measurement of  $0.98m_e$  (DEXTER et al., 1954).

At this point we have almost finished our results for the novel MXenes we committed to explore, observing the effect caused by a change in the termination groups of these materials. We based all calculations on DFT methods and successfully found positive phonon frequencies and negative free energy predictions for  $Y_2CF_2$ ,  $Y_2CCl_2$ , and  $Y_2CBr_2$ , making them great candidates for future synthesis due to high dynamic stability and good thermodynamic indicators. If synthesized, one should expect semiconductor be-

havior from all of them, with an indirect band gap in the visible light range. The gap size was found to be correlated with the electronegativity of the terminations. Interestingly, for the  $Y_2CCl_2$  in particular, the direct band gap is virtually the same as the indirect one. The study included the expected characterization of the materials in terms of infrared and Raman spectra, showing similar patterns of vibration, except for higher vibration frequencies in materials with lighter termination groups. Lastly, we found an interesting quality in the  $Y_2CF_2$  energy bands, which demonstrated supermassive electronic states in a flat region of the valence band. We emphasize the fact that similar MXenes can manifest different physical properties, which incites the continuous exploration in the vast range of 2D materials in the MXene family.

# 5 Advanced Electronic Properties of MXenes and TMDs

# 5.1 Quantum Espresso and Wannier90

For obtaining more sophisticated electronic properties with denser grids and significantly less computational cost, we post-process DFT results to obtain a tight-binding Hamiltonian, but with single-particle states constructed with Wannier functions instead of atomic orbitals. The choice of Wannier functions as a basis set is justified for its similarities with atomic orbitals while being naturally connected to the Bloch functions, inheriting their orthogonality.

Our process starts with DFT calculations, then uses the Wannier90 (MOSTOFI et al., 2008) framework to obtain the tight-binding Hamiltonian, and then we construct algorithms whose computations are equivalent to solving the physical equations for the desired properties. The DFT tool compatible with the Wannier90 framework we chose to work with is the open source Quantum Espresso package (GIANNOZZI et al., 2009). From MXenes, we selected Y<sub>2</sub>CCl<sub>2</sub> as the candidate for a better electronic description, as its nearly direct band gap and nearly flat band structure are suggestive of an interesting exploration. For TMDs, we pick MoS<sub>2</sub>, which is a widely studied material and full of space for physical exploration, which is perfect for pushing our limits into developing computational tools related to valleytronics and topological properties.

To perform once again DFT calculations of  $Y_2CCl_2$ , but now using Quantum Espresso, we tightened the convergence parameter for total energy from  $1\times10^{-5}$  to  $1\times10^{-8}$  eV/atom. The cut-off energy for the plane-wave basis was reduced from 750 to 400 eV, as it was enough for convergence. The grid was drastically increased in density, from a 9x9x1 to a 20x20x3 k-point set, justified by our need for precision in the electronic levels. As we are now less interested in the band gap itself and more focused on the curvatures of the eigenstates and eigenvalues, we felt no need to perform the accurate HSE06 functional, but preferred to concentrate the computational resources into the finer grid expansion with the PBE functional.

For  $MoS_2$ , which calculation is more complex due to strong spin-orbit coupling, we spent more resources considering a cutoff energy for the plane-wave basis at 500 eV, and also a  $1\times10^{-8}$  convergency criteria. A fine grid consisting of  $32\times32\times1$  k-points is justified by the post DFT methods which greatly benefit from a fine k-sample. For this material,

we also kept the lower PBE exchange-correlation functional.

In the Y<sub>2</sub>CCl<sub>2</sub> Wannierization process, we considered a 20x20x1 grid with the  $d_{xy}$ ,  $d_{yz}$ ,  $d_{z^2}$ ,  $d_{x^2-y^2}$ ,  $p_x$ ,  $p_y$ ,  $p_z$ , and s orbitals of Y, and the sp3 hybridization for the C and Cl atoms. These orbital projections were considered to construct 30 Wannier functions, which formed 36 energy bands, of which we are only interested in the ones near the Fermi level.

For MoS<sub>2</sub> we considered 22 energy bands near the Fermi level, using also 22 Wannier functions to represent them within a 32x32x1 grid. For this material, the most significant orbitals near the Fermi level are the  $d_{xy}$ ,  $d_{yz}$ ,  $d_{z^2}$  and  $d_{x^2-y^2}$  Mo orbitals; and  $p_x$ ,  $p_y$  and  $p_z$  S orbitals.

# 5.2 Tight-Binding in Wannier Basis

The tight-binding method was originally idealized considering basis states for a single-particle system as a linear combination of the atomic orbitals of the constituent atoms. As being tightly bound to the atoms of the crystal, the atomic orbitals are localized states periodically distributed in the lattice. Another alternative for periodically localized states is the Wannier functions, which are the choice of this study, as shall be later discussed.

A basis function for the tight-binding method is then written as a normalized Bloch function:

$$|\phi_{\tau,\mathbf{k}}(\mathbf{r})\rangle = \frac{1}{\sqrt{N}} \sum_{\alpha=1}^{N} e^{i\mathbf{k}\cdot\mathbf{R}_{\alpha}} |\chi_{\tau}(\mathbf{r} - \mathbf{R}_{\alpha})\rangle,$$
 (5.1)

where  $\chi_{\tau}$  represents a Wannier or orbital function of quantum number  $\tau$ , and  $\mathbf{R}_{\alpha}$  is the position vector of each nucleus  $\alpha$ , which is summed up to all the atoms considered in our calculations. This sum over the atomic sites of a two-dimensional crystal can be written as:

$$\sum_{\alpha=1}^{N} \mathbf{R}_{\alpha} = \sum_{n_1}^{m} \sum_{n_2}^{m} n_1 \mathbf{a}_1 + n_2 \mathbf{a}_2 = \sum_{n_1}^{m} \sum_{n_2}^{m} \mathbf{R}_{n_1 n_2},$$
 (5.2)

where the sums should run the entire lattice. Figure (5.2) brings a visual representation of the atomic site position vectors.

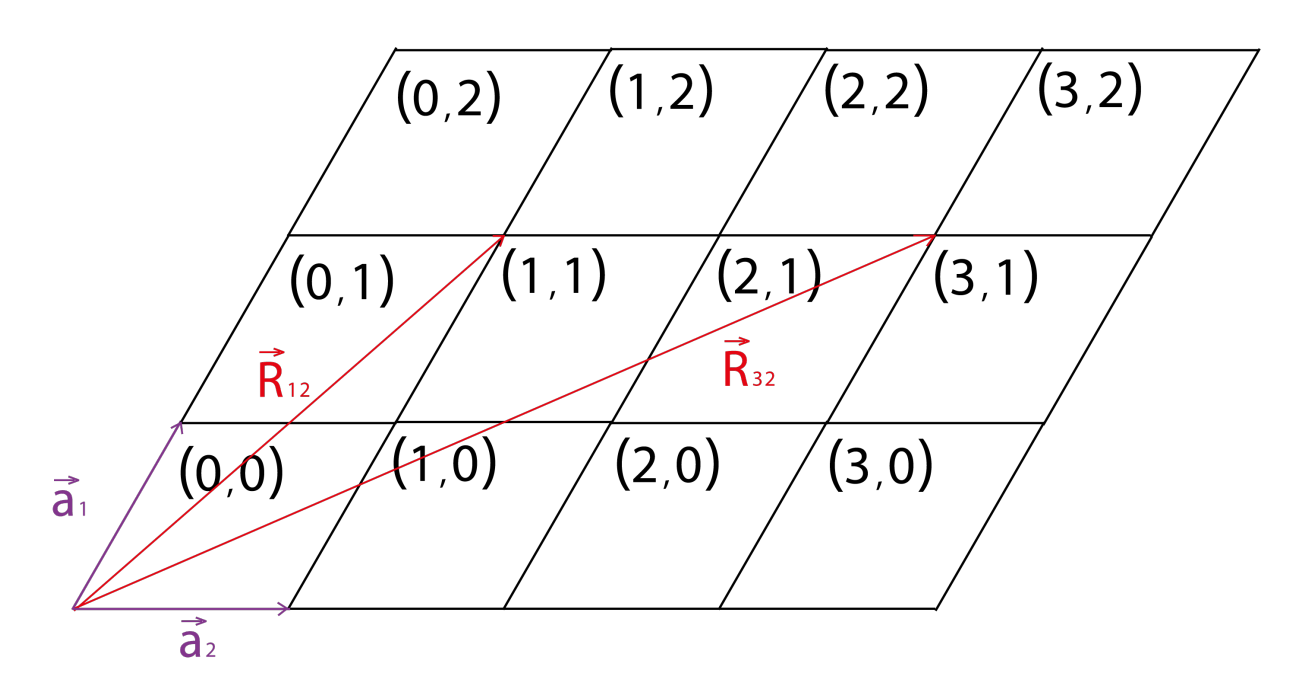


Figure 30 – Crystalline sites localized by its position vectors  $\mathbf{R}_{n_1n_2}$ . Each site correspond to the origin of a crystalline cell identified with the coordinates of it's origin.

In the tight-binding method, the localized electron states interact with their nearest neighbors. The electronic Hamiltonian for this system can be expressed as:

$$\hat{H} = \frac{p^2}{2m_e} + \sum_{\alpha} \hat{V}(\boldsymbol{r} - \boldsymbol{R}_{\alpha}), \tag{5.3}$$

where  $m_{\rm e}$  stands for the electron mass, while r and  $R_{\alpha}$  are the positions of the electron and an atomic site of index  $\alpha$ . The quantity of nuclei accounted in the sum is a choice between precision and computational cost.

To construct the Hamiltonian matrix in the basis of Bloch functions, each element is written as:

$$H_{\tau\tau'}(\mathbf{k}) = \frac{1}{N} \int d\mathbf{r} \left\langle \phi_{\tau,\mathbf{k}}(\mathbf{r}) \middle| \hat{H} \middle| \phi_{\tau',\mathbf{k}}(\mathbf{r}) \right\rangle. \tag{5.4}$$

where we integrate over the total volume of the crystal, using  $\frac{1}{N}$  as the normalization factor in units of unit cells. Substituting the Bloch functions with (5.1) we obtain:

$$H_{\tau\tau'}(\mathbf{k}) = \sum_{\mathbf{R}_{\alpha}} \sum_{\mathbf{R}_{\beta}} \frac{1}{N} \int d\mathbf{r} e^{-i\mathbf{k}\cdot\mathbf{R}_{\alpha}} \left\langle \chi_{\tau}(\mathbf{r} - \mathbf{R}_{\alpha}) | \hat{H} e^{i\mathbf{k}\cdot\mathbf{R}_{\beta}} | \chi_{\tau'}(\mathbf{r} - \mathbf{R}_{\beta}) \right\rangle. \tag{5.5}$$

Each term in the summation represents the energy from the interaction between electron states in sites  $\alpha$  and  $\beta$ . Intending to reduce the equation to a single sum, we

consider the position coordinates as the relative distance between an atomic site  $\beta$  and a site  $\alpha$ , being  $\mathbf{R} = \mathbf{R}_{\beta} - \mathbf{R}_{\alpha}$ . Substituting  $\mathbf{R}_{\beta}$  and shifting the whole system by  $\mathbf{R}_{\alpha}$ , also using  $\sum_{R_{\alpha}} \frac{1}{N} = 1$ , the equation can be rewritten as:

$$H_{\tau\tau'}(\mathbf{k}) = \sum_{\mathbf{R}} e^{i\mathbf{k}\cdot\mathbf{R}} \int d\mathbf{r} \langle \chi_{\tau}(\mathbf{r}) | \hat{H} | \chi_{\tau'}(\mathbf{r} - \mathbf{R}) \rangle = \sum_{\mathbf{R}} e^{i\mathbf{k}\cdot\mathbf{R}} t_{\tau\tau'}^{\mathbf{R}},$$
 (5.6)

where  $t_{\tau\tau'}^R$  are the hopping integrals, which describe the energy associated with the hopping of an electron from its origin to the position R, changing from an initial Wannier state of quantum number  $\tau$  into the state of quantum number  $\tau'$ . If R=0, this quantity is an on-site energy instead of a hopping energy, being the energy associated with the individual localized states. In the limiting case of considering every atomic site of the lattice, this method contemplates the energy of all possible spatial state transitions of an electron in the crystal. The hopping integrals and on-site energies can be obtained with the Wannier-90 post-DFT framework (MOSTOFI et al., 2008).

Using the creation and annihilation operators of Wannier states (2.60), we may write the Hamiltonian operator in the second quantization format, which gives a better intuition of the interactions contemplated in the system:

$$\hat{H} = \sum_{\tau,\tau',\alpha} \epsilon_{\tau\tau'}^{\alpha} \hat{c}_{\tau',\alpha}^{\dagger} \hat{c}_{\tau,\alpha} + \sum_{n,n',\alpha\neq\beta} t_{\tau\tau'}^{\alpha\beta} \hat{c}_{\tau',\beta}^{\dagger} \hat{c}_{\tau,\alpha}. \tag{5.7}$$

## 5.3 Energy States in Crystals

After adequate modeling of the system's Hamiltonian, the energy states are given by the time-independent Schrödinger equation:

$$H|\Psi_{n,k}(\mathbf{r})\rangle = E_{n,k}|\Psi_{n,k}(\mathbf{r})\rangle,$$
 (5.8)

where  $E_{n,k}$  is an energy eigenvalue of quantum number n, and momentum vector  $\mathbf{k}$ . Each eigenvalue is associated with a Bloch energy state  $|\Psi_{n,\mathbf{k}}(\mathbf{r})\rangle$ , which is represented as a linear combination of the basis functions,

$$|\Psi_{n,k}(\mathbf{r})\rangle = \sum_{\tau} c_{n,k}^{\tau} |\phi_{\tau,k}(\mathbf{r})\rangle.$$
 (5.9)

Substituting in (5.9), we obtain

$$H \sum_{\tau} c_{n,k}^{\tau} |\phi_{\tau,k}(\mathbf{r})\rangle = E_{n,k} \sum_{\tau} c_{n,k}^{\tau} |\phi_{\tau,k}(\mathbf{r})\rangle, \qquad (5.10)$$

5.4. Grids 145

and then multiplying both sides by  $\langle \phi_{\tau',k}(\mathbf{r})|$ , also considering the orthonormality of Bloch functions based on Wannier functions:

$$\sum_{\tau} \langle \phi_{\tau',k}(\boldsymbol{r}) | H | \phi_{\tau,k}(\boldsymbol{r}) \rangle c_{n,k}^{\tau} = E_{n,k} \sum_{\tau} \langle \phi_{\tau',k}(\boldsymbol{r}) | \phi_{\tau,k}(\boldsymbol{r}) \rangle c_{n,k}^{\tau}$$

$$\sum_{\tau} H_{\tau'\tau} c_{n,k}^{\tau} = E_{n,k} \sum_{\tau} \delta_{\tau'\tau} c_{n,k}^{\tau}$$

$$\sum_{\tau} H_{\tau'\tau} c_{n,k}^{\tau} = E_{n,k} c_{n,k}^{\tau'}.$$
(5.11)

In matrix notation, where the left side corresponds to a matrix-vector product, and the right side a scalar multiplication of a vector:

$$\mathbb{HC}_{n,k} = E_{n,k} \mathbb{C}_{n,k},\tag{5.12}$$

where  $\mathbb{H}$  is the Hamiltonian,  $E_{n,k}$  is an energy state, and  $\mathbb{C}_{n,k}$  is the correspondent wave function as a column vector, being its elements the coefficients for the linear combination of the basis functions, where each of which is constructed from Wannier functions of quantum numbers  $\tau$ .

## 5.4 Grids

The first step we discuss in solid simulations is the construction of grids, as they are the coordinate space in which the simulation is calculated. Here, all calculations are performed in 2D momentum space, so each point contained in the grid is called a k-point vector of dimension two. Generalizations for three dimensions are straightforward. A complete grid for electronic calculations must represent the unit cell of the reciprocal space, although some calculations might focus on specific high-symmetry points. We discuss two grids that contemplate the whole unit cell.

The first grid we've already worked with is a simple momentum space unit cell constructed with its basis vectors, also known as the Monkhorst-Pack type of grid. Here we work with uniformly distributed points, with coordinates based on fractions of the basis vectors  $\boldsymbol{b}$  of the reciprocal space. This set for an  $n \times n$  grid can be written as:

$$\mathbf{k} = \left\{ \mathbf{b}_1 \frac{(i-1)}{n} + \mathbf{b}_2 \frac{(j-1)}{n} + \mathbf{O} \mid i, j \in \{1, \dots, n\} \right\},$$
 (5.13)

where O is the origin coordinate. A 7 x 7 example is presented in Figure 31, showing a Monkhorst grid for the 2D hexagonal unit cell, as used in both cases of  $Y_2CCl_2$  and  $MoS_2$ :

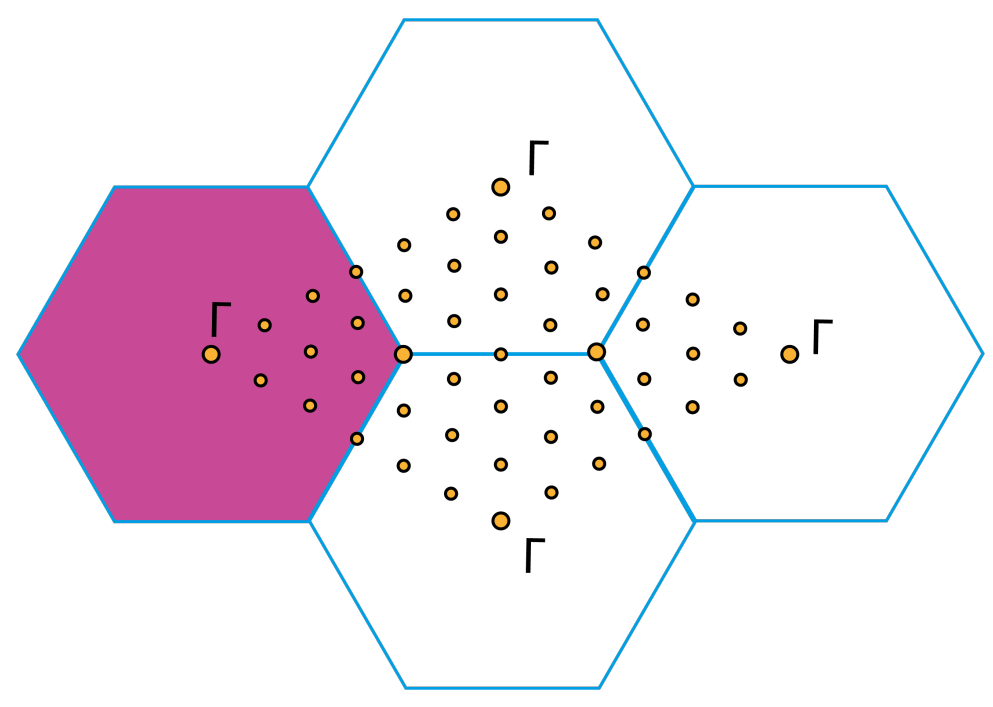


Figure 31 – Unit cell shaped grid, equivalent to the Brillouin Zone.

This type of grid is very simple to construct and brings the benefit of allowing modular arithmetic methods in calculations, as any border coordinate can be linked to the opposite border to form a system of cyclical coordinates, kp(n+1,j) = kp(1,j), which can be constructed with modular indexes. One major use of this property is seen in the gradient operator for a set of discrete circular coordinates. An element of the action of such an operator can be defined as:

$$(\nabla Q)_{k_x} = \frac{Q_{|k_x+1|_n, k_y} - Q_{|k_x-1|_n, k_y}}{2\Delta k},$$
(5.14)

Where  $|n+1|_n = n+1 \mod n \equiv 1 \mod n$ . This gradient operator can be computationally constructed as a routine or a method in object-oriented programming.

Another very useful type of grid is the hexagonal Brillouin zone grid, constructed following the hexagonal symmetry. Despite being the canonical Brillouin Zone, we may choose to dislocate the center to focus on some intended momentum coordinate. The big disadvantage of this type of grid is that it makes the use of periodic conditions difficult. Figure 32 shows this grid for a small number of k-points, while Figure 33 shows the energy levels of  $Y_2CCl_2$  represented in a denser configuration, where we call special attention

5.4. Grids 147

again to the nearly flat bands seen in the valence states.

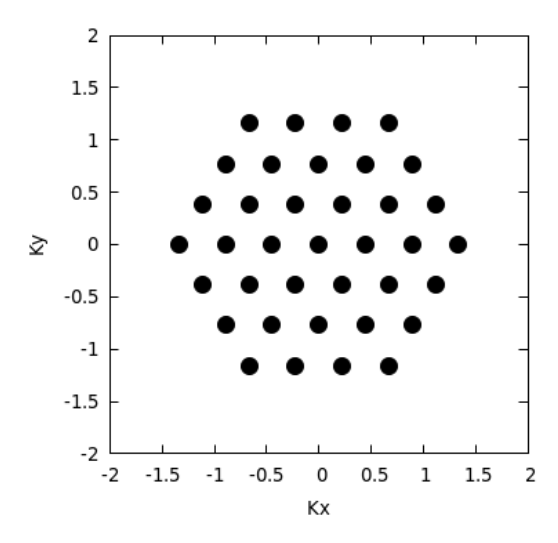


Figure 32 – Grid for the Brillouin zone in the 2D hexagonal system.

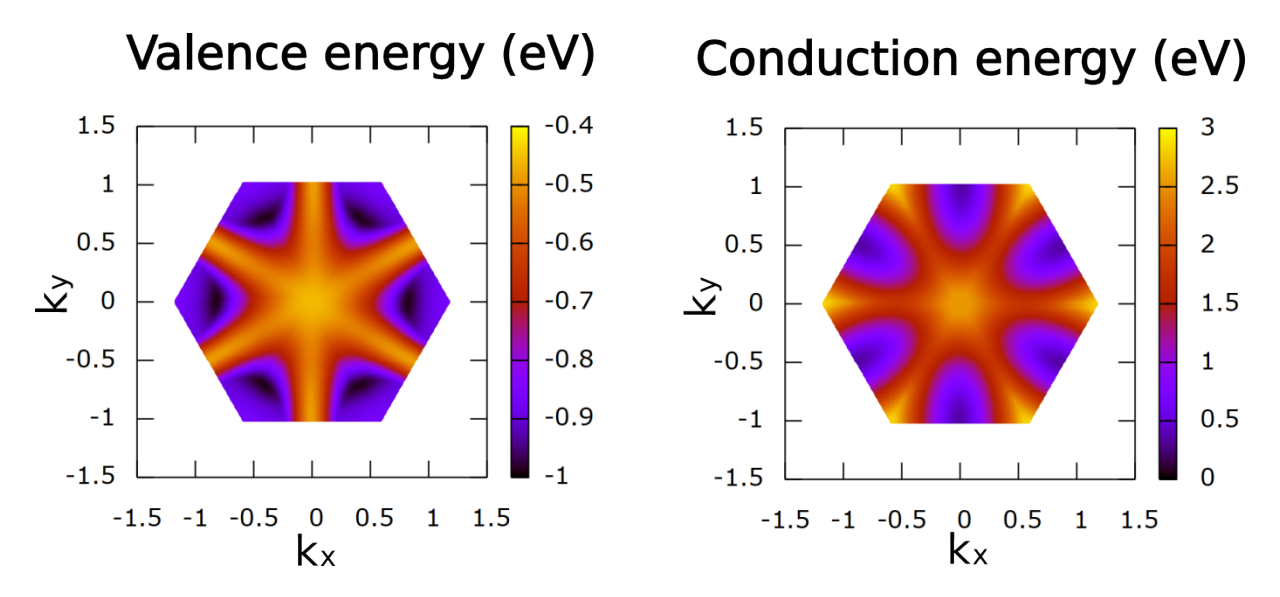


Figure 33 – Valence and conduction energy levels of Y<sub>2</sub>CCl<sub>2</sub> Brillouin Zone.

Based on these calculations we reformulated the effective mass (4.31) and group velocity (4.27) algorithms to map the higher valence electron/hole states in the entire Brillouin zone, demonstrating the flat band behavior of  $Y_2CCl_2$  in the path between  $\Gamma$  high symmetry points. Figure 34 shows the absolute value of the obtained effective mass tensor element  $m^*(\mathbf{k})_{yy}$ , and the group velocity tensor element  $v_g(\mathbf{k})_{yy}$ . We note the flat band in the  $\hat{y}$  axis composed of carrier states with an effective mass higher than 20  $m_e$ , and zero group velocity.

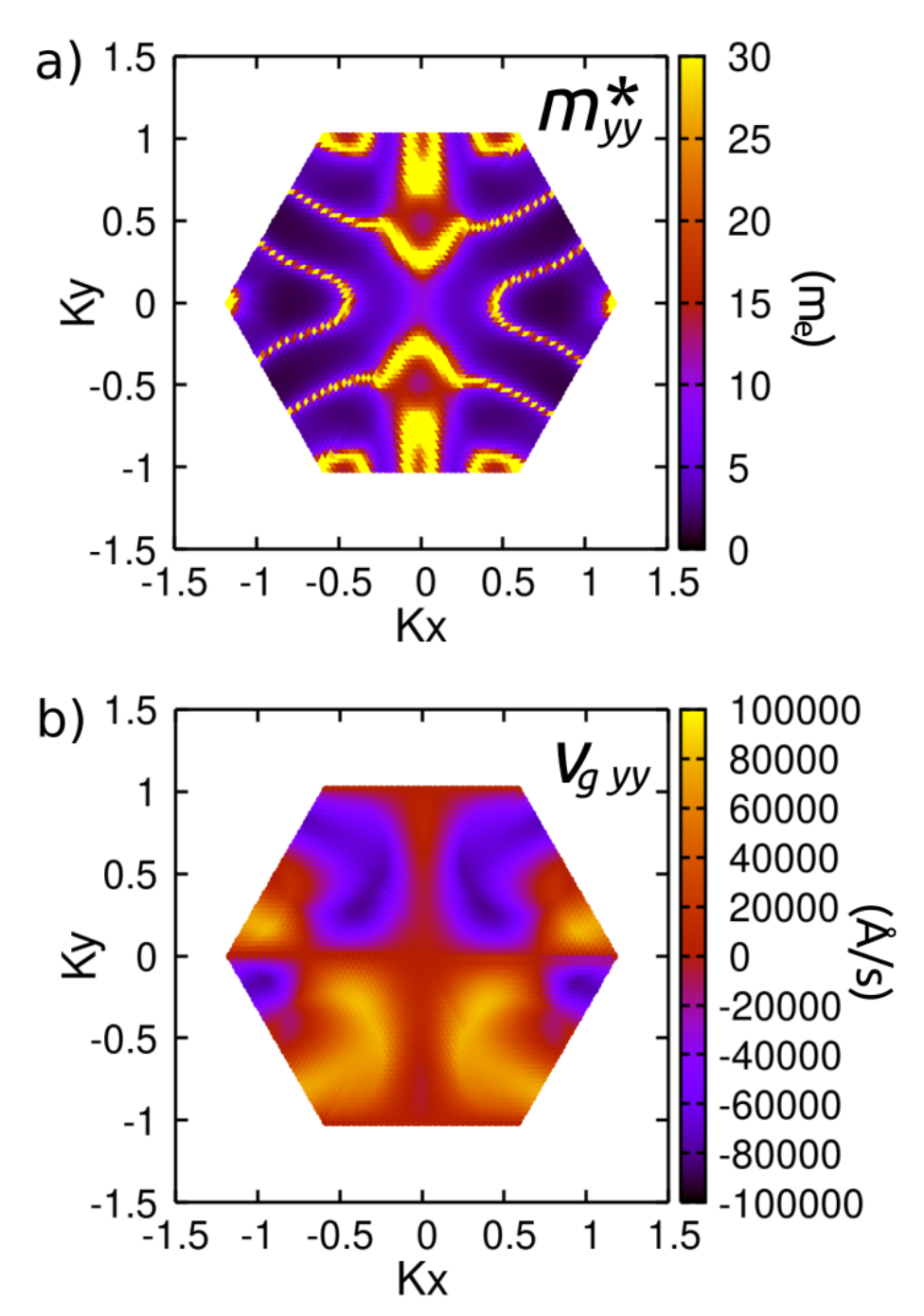


Figure 34 – a) Higher valence state effective mass along  $\hat{y}$  mapped in Y<sub>2</sub>CCl<sub>2</sub> Brillouin Zone (30  $m_e$  is set as threshold for numerical precision). b) Higher valence state group velocity along  $\hat{y}$  mapped in Y<sub>2</sub>CCl<sub>2</sub> Brillouin

## 5.5 Addressing Band-States

Zone.

We've been treating n as a general quantum number, but we must precise it to its real meaning. n should not be taken as a simple energy level index, as this relates to

a hierarchical logic of addressing the states, in which the quantum number is determining the energetic position of the states in relation to the others. In solid state systems, the energy states are distributed in energy bands. Each one is constituted of a number of energy states within the reciprocal unit cell equivalent to the number of atoms in the system, forming a nearly continuous structure, as a single entity mapped in the momentum space. One major significance of this study comes from realizing how much our description of the physical properties depends on the correct addressing of the band states.

It's common to see energy bands treated as simple energy levels along the momentum space (BIENIEK et al., 2022; DIAS et al., 2018). In this sense, energy bands can be hierarchically set from lower to higher energy bands, but we show that this method creates conflict with the definition of an energy band as a single continuous entity. In practice, the hierarchical position of an energy band may vary along reciprocal space, such that the continuity of the correspondent wave functions must be preserved. Energy bands may cross each other, causing an energy level of index m that may previously belong to some specific energy band to become part of the other. In this sense, an energy level m is not associated with a particular energy band n, but at each point in momentum space it may belong to a different band. The index for an energy band must not be mistaken for the hierarchical index of energy states.

Let us discuss the two configuration possibilities for addressing the single-particle bands index. The simple hierarchical logic is just  $E_{0,k} = E_{\min,k}$  and  $E_{n+1,k} > E_{n,k} \, \forall n, k$ . The method we propose to address the single-particle states begins with the hierarchical logic, then proceeds to the correct addressing algorithm, where  $E_{0,0} = E_{\min,0}$  and  $E_{n+1,0} > E_{n,0}$ , and then for every other momentum coordinate we set each band index according to the minimization of:

$$\delta \Psi_{n,\mathbf{k}}^{m} = ||n,\mathbf{k}\rangle - |m,\mathbf{k} + \Delta \mathbf{k}\rangle|, \qquad (5.15)$$

where n is the fixed band index that represents the band being addressed, m should be every possible band index, and  $\mathbf{k} + \Delta \mathbf{k}$  is a neighbor momentum coordinate to  $\mathbf{k}$ . The quantity  $\delta \Psi_{n,\mathbf{k}}^m$  represents the discontinuity between states, so after its calculation for every m, we state that:

$$|n, \mathbf{k} + \Delta \mathbf{k}\rangle = |n', \mathbf{k} + \Delta \mathbf{k}\rangle \quad \text{if} \quad \delta \Psi_{n, \mathbf{k}}^{n'} = \min[\delta \Psi_{n, \mathbf{k}}^{m}].$$
 (5.16)

We built a computational code that calculates all possible  $\delta \Psi_{n,k}^m$  for each momentum step, and for each momentum step it is chosen to become part of the energy band

n the energy state m whose wave function discontinuity is the lowest for that step. The results for the comparison of both index configurations are shown in Figure 35, which illustrates the energy bands calculated for  $Y_2CCl_2$ .

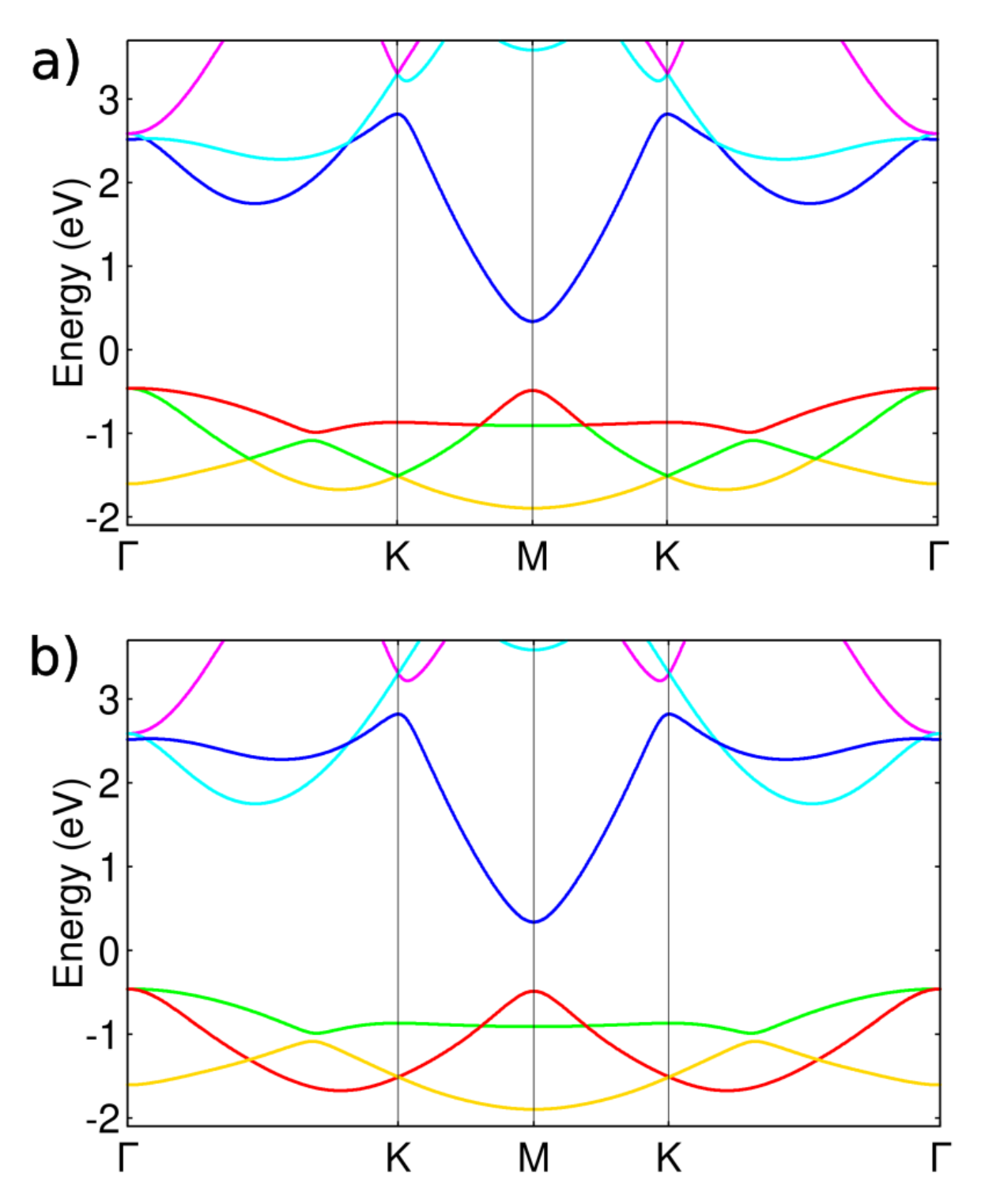


Figure 35 – Both perspectives on energy eigenstates along path in first Brillouin zone. The energy levels or bands are distinguished by color in both cases. a) Energy levels addressed according to energy hierarchy. b) Energy bands addressed according to wave function continuity. The green, red and yellow are the first to third higher valence bands, respectively; while the blue, cyan and pink bands are the first to third lower conduction bands, respectively. The ordering of the bands considered the higher/lower value of each valence/conduction band.

We can observe that when the continuity of the wave functions is considered, the energy eigenstates also demonstrate better continuity, while the hierarchically defined bands demonstrate a break of continuity in the crossing regions.

To see what happens in the wave functions for both types of index configuration, Figure 36 shows the probability coefficients  $|c_v^{\tau}(\mathbf{k})|^2$  along  $\mathbf{k}$ , for the first and third valence bands (v = 1, 3) (green and yellow in Figure 35), corresponding to the  $\tau$  Wannier states that compose the basis.

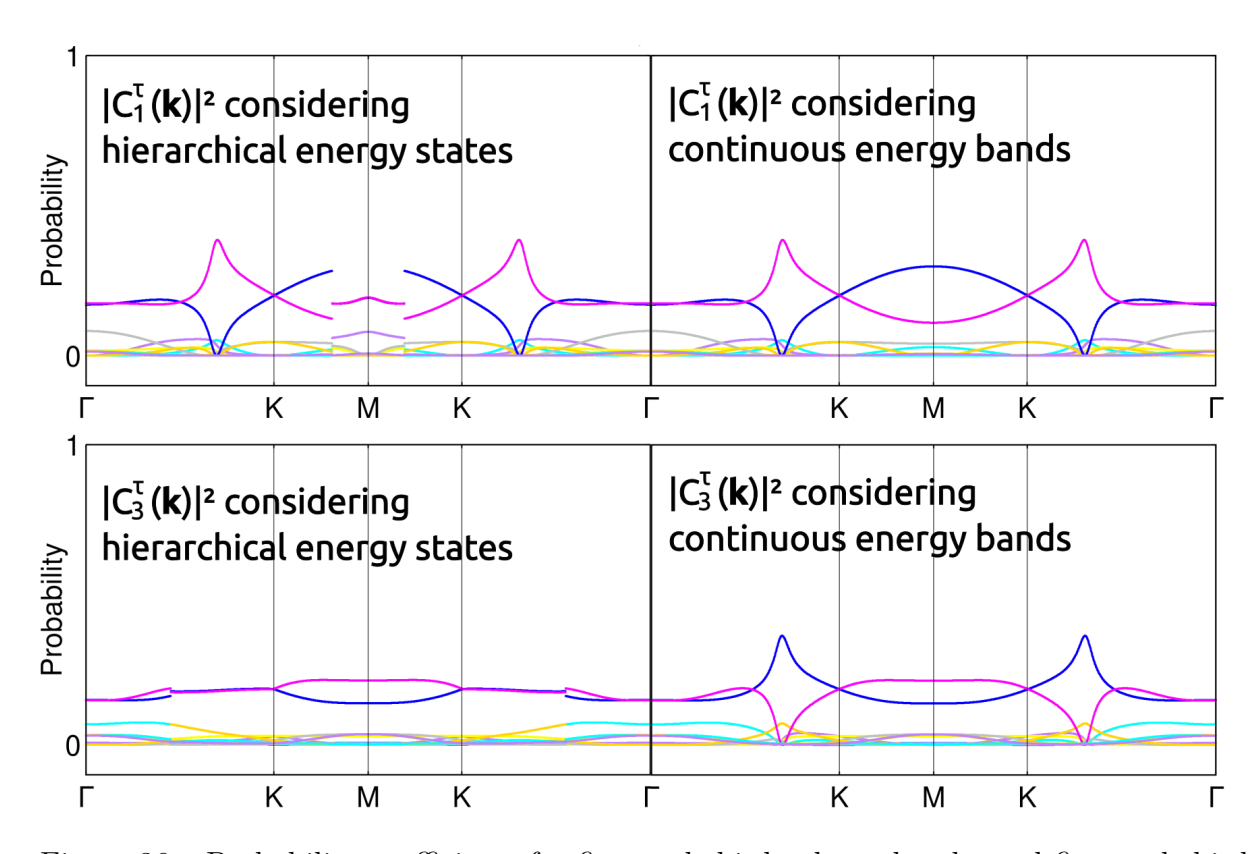


Figure 36 – Probability coefficients for first and third valence bands, and first and third hierarchical levels. Each individual coefficient is distinguished by color.

When we see the behavior of the wave function in each picture, it is observed that the hierarchical energies method contains a break of continuity exactly in the crossing regions. It becomes clear that the band state configuration is the optimal one. We chose the first (green) and third (yellow) highest energy bands in particular to observe what happens in the avoided crossing region, between  $\Gamma$  and K points. The wave function composition at these avoided crossing regions concentrates in particular Wannier functions (or orbitals);  $\left|c_1^{\text{pink}}(\boldsymbol{k})\right|^2$  grows as  $\left|c_1^{\text{blue}}(\boldsymbol{k})\right|^2$  decreases, but  $\left|c_3^{\text{pink}}(\boldsymbol{k})\right|^2$  decreases as  $\left|c_3^{\text{blue}}(\boldsymbol{k})\right|^2$  grows. We shall not go deeper into this subject, as for now we only intend to demonstrate that the wave function of the electron in a crystal asks for band labels, and not only

hierarchical energy levels.

Despite the fact that most of the physical properties calculations avoid this problem by including the sum of all bands, it is impossible to specify the band interactions by means other than correctly addressing the band index. From now on, we will be addressing band states divided in conduction and valence bands. The ordering of bands will still be given from energy hierarchy, but now we consider the higher energy value of each band to order valence bands, and the lower energy value of each to order conduction bands. The notation for the state vectors will also consider  $\mathbf{k}$  not as a label, but as a coordinate, which leaves only the band index as a label:  $|n, \mathbf{k}\rangle \to |\Psi_n(\mathbf{k})\rangle$ .

Now, we use the same method to obtain  $MoS_2$  band states, which will be crucial for the rest of the discussion, shown in Figure 37:

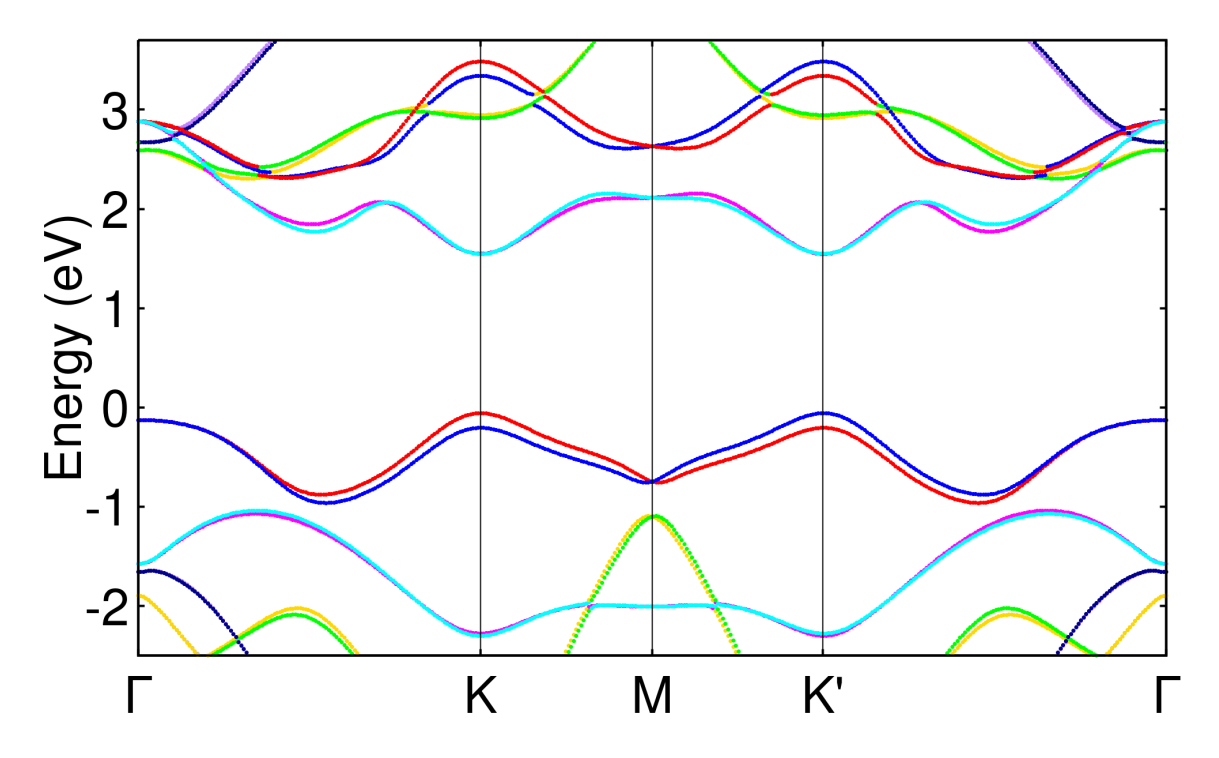


Figure  $37 - MoS_2$  energy bands after index correction.

When conserving the wave function continuity, it is possible to see that degenerate bands separated by spin-orbit coupling are not symmetric, and that's what justifies the distinction between K and K', respecting the orbital angular momentum in each point of momentum space. Still, M is a valid reflection symmetry of the energy eigenstates, but those just do not belong to the same bands. Figure 38 shows the two valence bands mapped in the 2D hexagonal unit cell, where it becomes clear the fact that each band is responsible for the highest occupied state in distinct valleys.

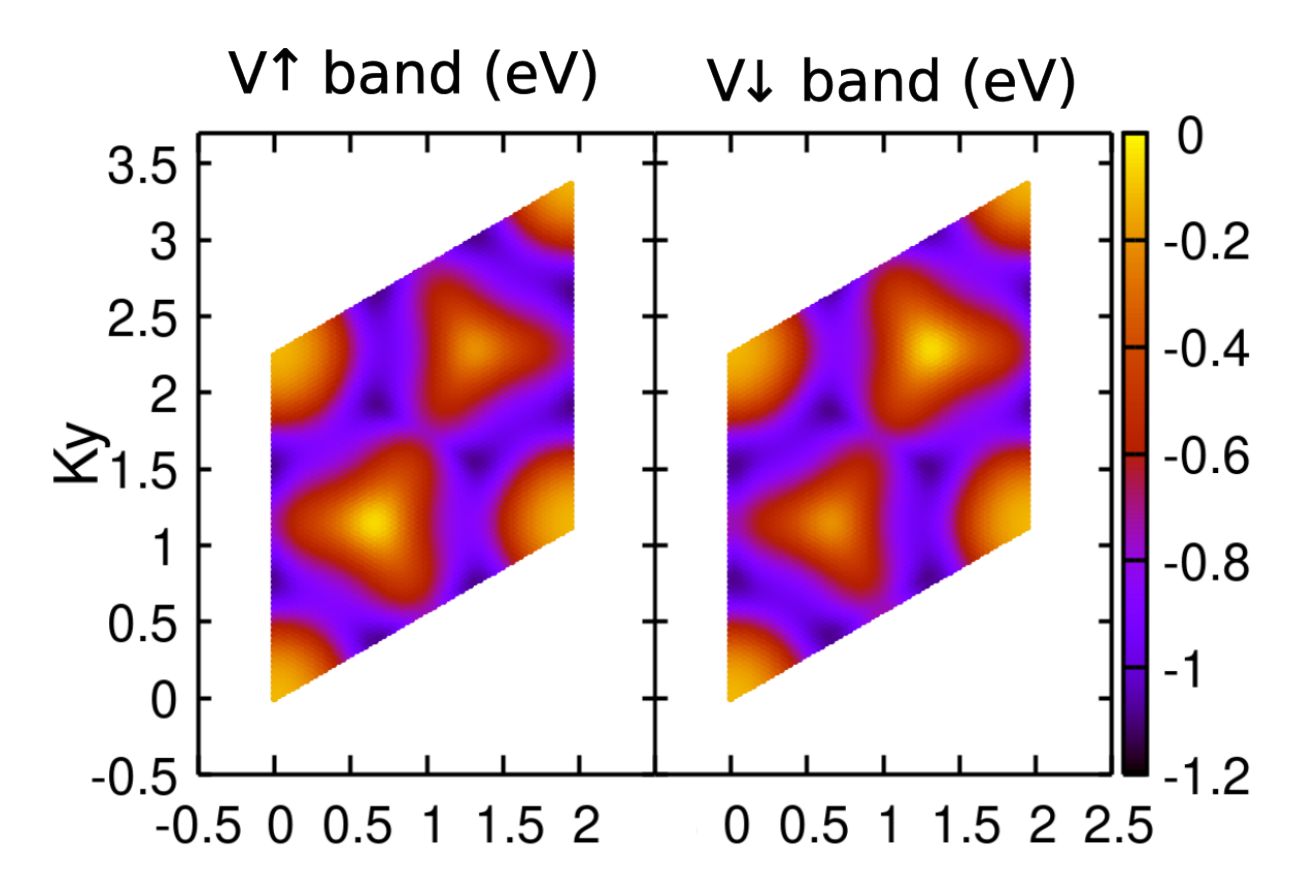


Figure 38 - 2D mapping of the  $MoS_2$  valence bands in the hexagonal unit cell.

## 5.6 Momentum Matrix

Physical properties such as optical absorption and the Berry curvature can be calculated with the canonical momentum matrix elements,  $P_{vc}^{\alpha}(\mathbf{k})$ , which give the coupling between the single-particle states  $|\Psi_v(\mathbf{k})\rangle$  and  $|\Psi_c(\mathbf{k})\rangle$ , resulting from an interaction with an electromagnetic field in the  $\alpha$  polarization. These elements are defined as:

$$P_{vc}^{\alpha}(\mathbf{k}) = \langle \Psi_c(\mathbf{k}) | \hat{p}_{\alpha} | \Psi_v(\mathbf{k}) \rangle. \tag{5.17}$$

For practical calculations, we use the commutation relation  $\hat{p} = \frac{-im_e}{\hbar}[\hat{r}, \hat{H}]$ , and the momentum space representation of the position vector  $\hat{r} = i\nabla_k$  (ZAK, 1968), which gives:

5.6. Momentum Matrix 155

$$P_{vc}(\mathbf{k}) = \frac{-im_{e}}{\hbar} \langle \Psi_{c}(\mathbf{k}) | [\hat{r}, \hat{H}] | \Psi_{v}(\mathbf{k}) \rangle$$

$$= \frac{m_{e}}{\hbar} \langle \Psi_{c}(\mathbf{k}) | [\nabla_{k} \hat{H} - \hat{H} \nabla_{k}] | \Psi_{v}(\mathbf{k}) \rangle$$

$$= \frac{m_{e}}{\hbar} \left( \langle \Psi_{c}(\mathbf{k}) | (\nabla_{k} \hat{H}) | \Psi_{v}(\mathbf{k}) \rangle + \langle \Psi_{c}(\mathbf{k}) | \hat{H} \nabla_{k} | \Psi_{v}(\mathbf{k}) \rangle - \langle \Psi_{c}(\mathbf{k}) | \hat{H} \nabla_{k} | \Psi_{v}(\mathbf{k}) \rangle \right)$$

$$= \frac{m_{e}}{\hbar} \langle \Psi_{c}(\mathbf{k}) | (\nabla_{k} \hat{H}) | \Psi_{v}(\mathbf{k}) \rangle.$$
(5.18)

For each dimension, this simplifies to:

$$P_{vc}^{\alpha}(\mathbf{k}) = \frac{m_{e}}{\hbar} \left\langle \Psi_{c}(\mathbf{k}) \middle| \frac{\partial \hat{H}}{\partial k_{\alpha}} \middle| \Psi_{v}(\mathbf{k}) \right\rangle. \tag{5.19}$$

Equation (5.19) is simple to solve, as from equation (5.6) it is trivial to find  $\frac{\partial \hat{H}}{\partial \alpha} = iR_{\alpha}\hat{H}$ . Also, it's evident that a quantity that describes the coupling of bands must correctly consider the band index in all the BZ.

Figure 39 shows the momentum matrix elements in the  $\hat{x}$  polarization corresponding to the interaction between valence and conduction bands of Y<sub>2</sub>CCl<sub>2</sub>, considering both index configurations.

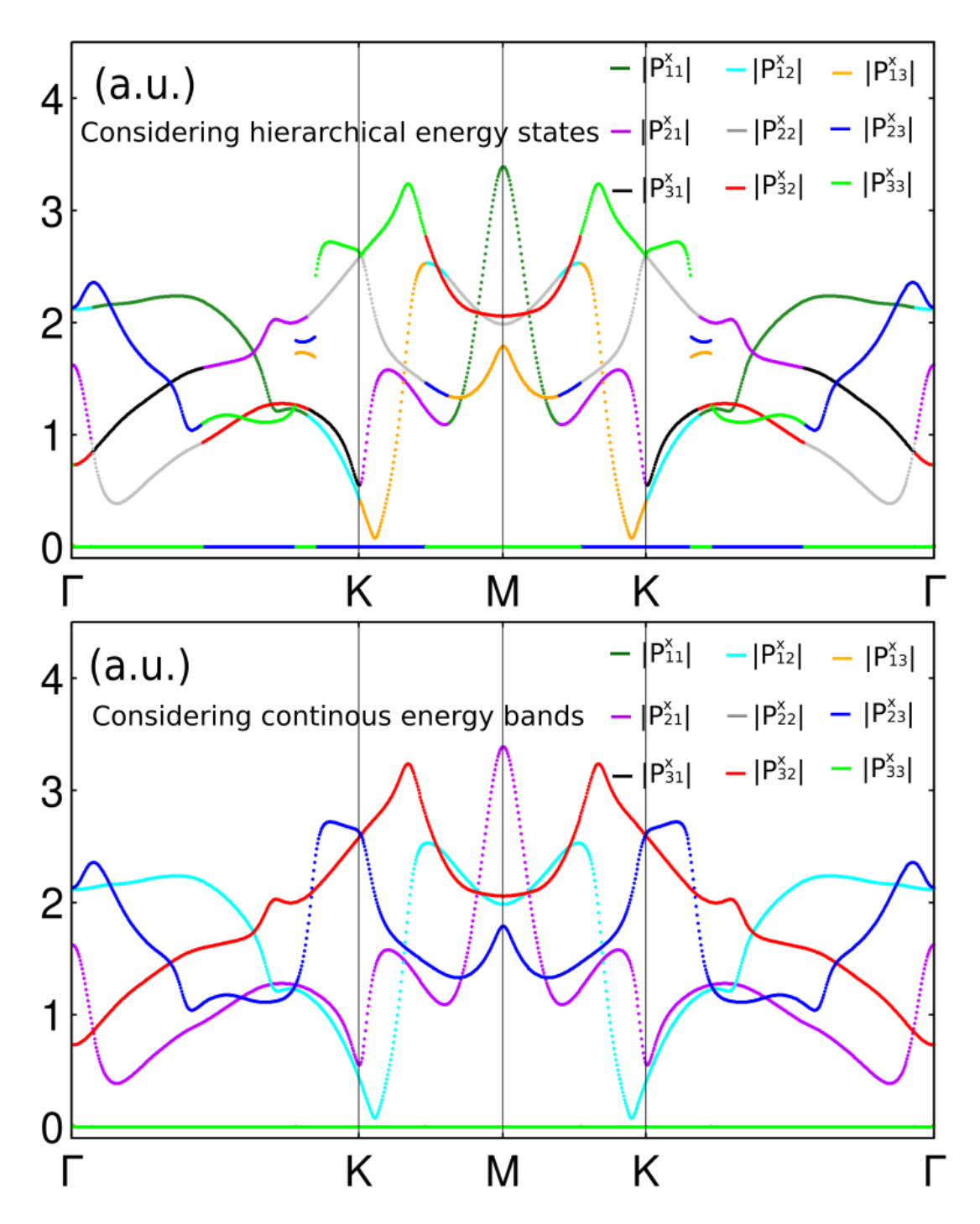


Figure 39 – Y<sub>2</sub>CCl<sub>2</sub> Momentum matrix element in both index configurations, considering the bands/levels in the vicinity of the Fermi level.

We see that the optical activity within the band structure is quite complex, where strange behavior happens in the avoided crossing regions, revealing some instances of discontinuity. This type of result invites reflection upon the limits of our simulations, being the Wannierization process or even the DFT calculation. There is something we couldn't grasp yet, but it's very unlikely that nature presents behaviors such as what is here demonstrated. Nevertheless, one important realization is that despite the smallest energy

5.6. Momentum Matrix 157

gap being indirect, from  $\Gamma$  to M high symmetry point, the large momentum element at M corresponds to the interaction of bands at this coordinate, indicating optical activity in the direct gap. The optical activity between bands near the Fermi level is constituted from transitions from the second valence band to the first and third conduction bands, while the second and third valence bands interact only with the second conduction band. This type of close analysis is crucial for avoiding misleading impressions from first sight. Correctly addressing the band states significantly improves our capacity of optical investigation in crystals. In another scenario, where avoided crossing is absent, we explore other features of optical phenomena, such as the role of spin. Figure 40 demonstrates the behavior of the momentum components in the  $\hat{x}$  polarization for v = 1, 2 and c = 1, 2, calculated with both index configurations for MoS<sub>2</sub>.

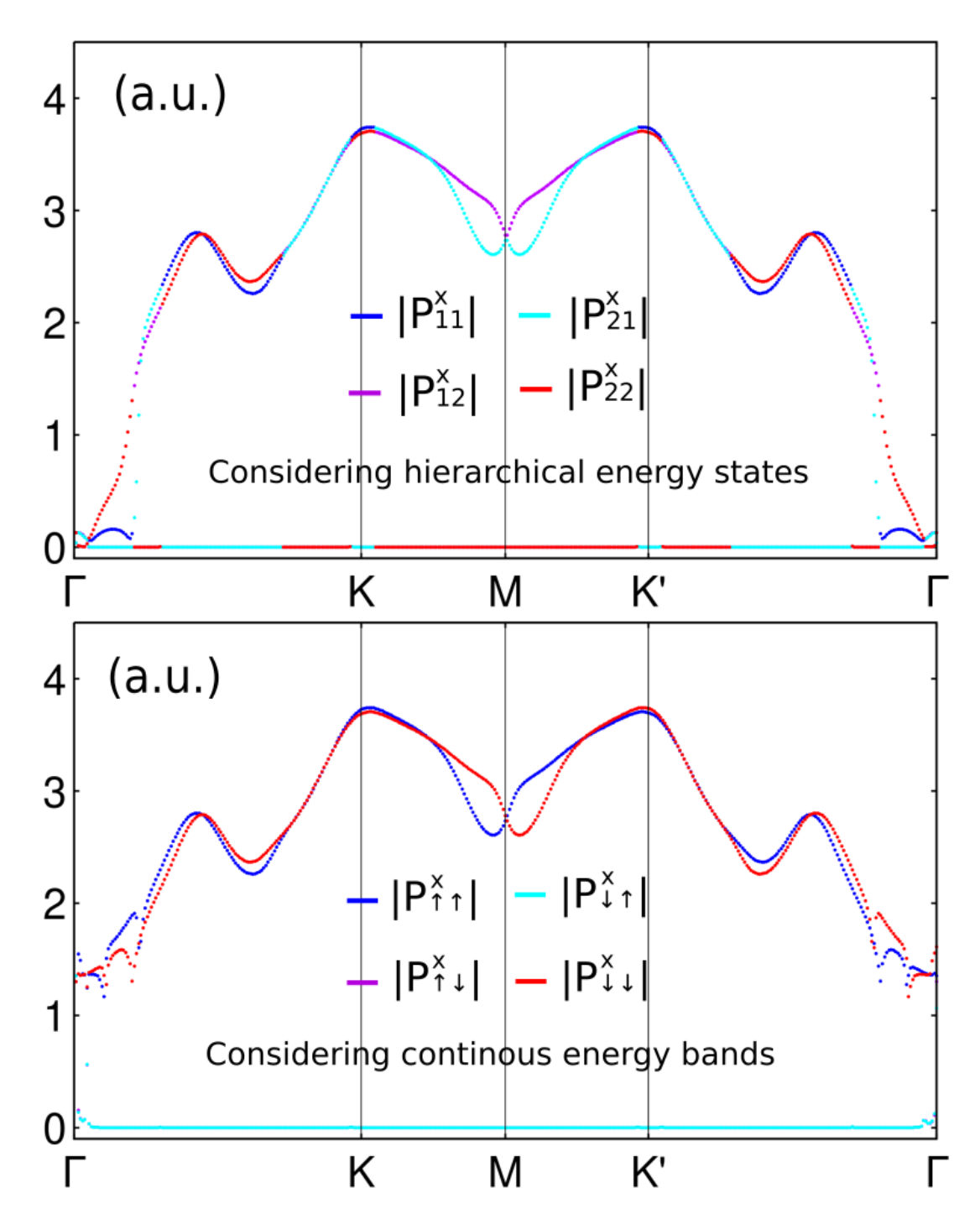


Figure 40 – MoS<sub>2</sub> Momentum matrix elements in both index configurations. Each element along the momentum space is distinguished by color.

Since the first and second bands, for both conduction and valence states, are resulted from degenerated bands splitting due to spin-orbital interaction, we may reference C1 and C2 as  $C\uparrow$  and  $C\downarrow$  respectively, and similarly with respect to the valence bands. This approach by itself is only possible if the bands are correctly addressed, and it allows us to study the optical activity between energy bands.

5.7. Optics 159

## 5.7 Optics

An optical absorption is understood as a transition of electronic states upon energy absorption from an interaction with an electromagnetic field, i.e., photons of energy equivalent to the gap between energy bands can excite electrons from the lower energy state into the higher energy state. The transition rate of these excitations is given by Fermi's Golden rule:

$$W_{i\to f} = \frac{2\pi}{\hbar} \left| \langle f | \hat{H}_{\rm int} | i \rangle \right|^2 \delta(E_f - E_i - \hbar\omega), \tag{5.20}$$

where  $\hat{H}_{int}$  is the Hamiltonian of the interaction,  $E_i$  and  $E_f$  are the energies of the initial and final states, respectively, and  $\omega$  is the frequency of the electromagnetic field.

Due to conservation of momentum, a photon can induce the transition of an electron only between states with identical momentum coordinates k, a restricted scenario which we call direct absorptions. If the interaction also considers the creation or annihilation of phonons as a way to transfer momentum between electrons and vibrational modes of the lattice, indirect absorptions become possible. Nevertheless, for this study we work only with direct transitions, which are the predominant type (KOPACZEK et al., 2019). The transition rate W between band states becomes:

$$W(\omega) = \frac{2\pi}{\hbar} \sum_{c,v,\mathbf{k}} \left| \langle \Psi_c(\mathbf{k}) | \hat{H}_{int} | \Psi_v(\mathbf{k}) \rangle \right|^2 \delta \left( E_c(\mathbf{k}) - E_v(\mathbf{k}) - \hbar \omega \right), \tag{5.21}$$

where the interaction Hamiltonian is:

$$\hat{H}_{\text{int}} = -\frac{e}{m_0} \mathbf{A} \cdot \hat{\mathbf{p}},\tag{5.22}$$

being A the vector potential of the electromagnetic field with amplitude  $A_0$  and direction  $\hat{e}$ , which can be not only  $\hat{x}$  or  $\hat{y}$  but also combinations of these, as we define circular polarizations:

$$\mathbf{A}^{\pm} = A_0 \hat{\epsilon}^{\pm}, \quad \hat{\epsilon}^{\pm} = \frac{1}{\sqrt{2}} (\hat{x} \pm i\hat{y}), \tag{5.23}$$

where  $\mathbf{A}^+$  is right-handed and  $\mathbf{A}^-$  is left-handed. Circularly polarized light does not simply excite electrons from valence to conduction states, but this polarization of light brings with it a dual sign for the angular momentum  $\pm \hbar$ .

The strength of this interaction is given by the momentum matrix in circular polarization, where  $\frac{\partial \hat{H}}{\partial k_{\alpha}} \rightarrow \frac{1}{\sqrt{2}} (\frac{\partial \hat{H}}{\partial k_{x}} \pm i \frac{\partial \hat{H}}{\partial k_{y}})$ . The results for this quantity in MoS<sub>2</sub>, mapped

not only at the valleys but in the whole BZ, are shown in Figure 41.

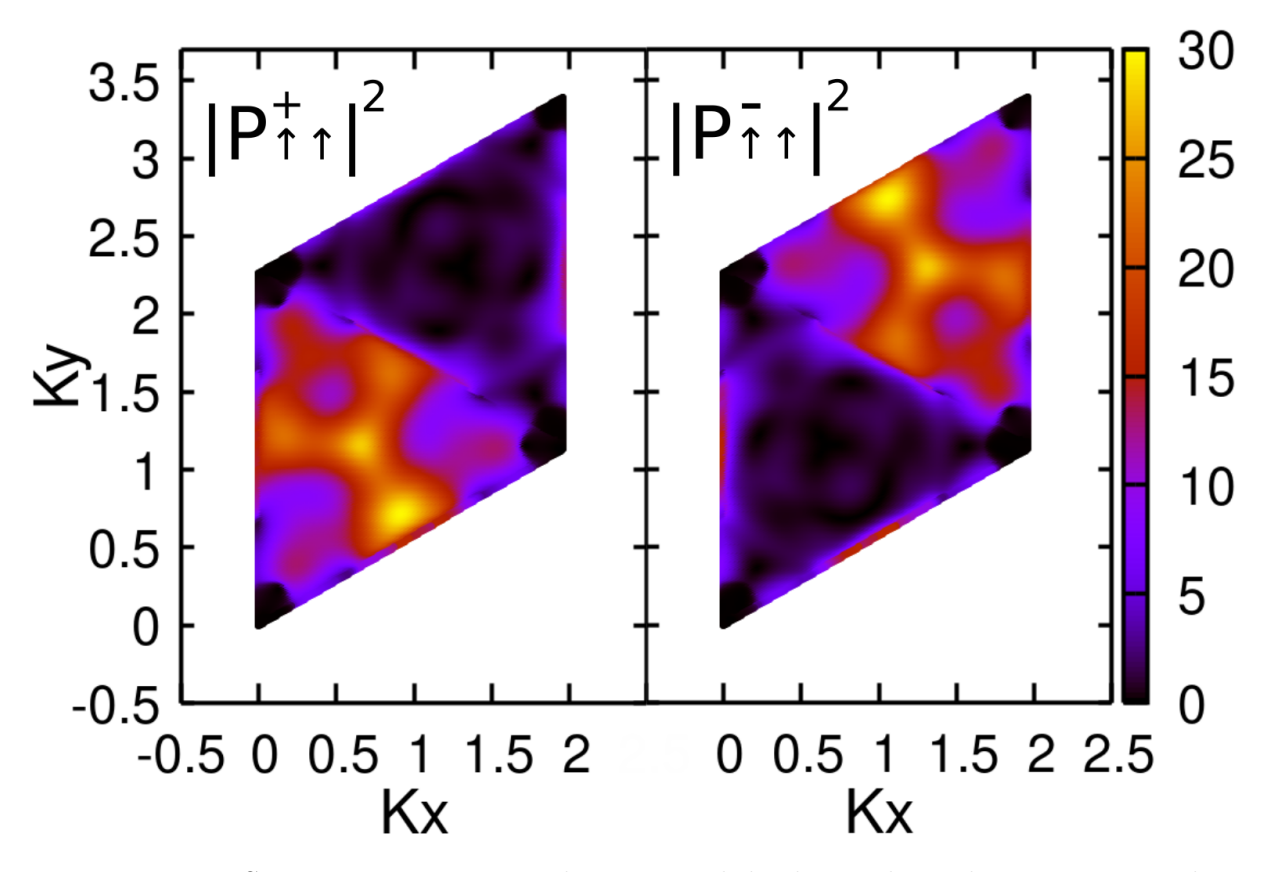


Figure  $41 - MoS_2$  momentum matrix elements with both circular polarizations, coupling spin up or spin down bands.

From Figure 41 we can clearly see the optical selection rules, affecting the coupling of states at different sides of the unit cell, which is divided by a broken mirror plane. It's important to notice an anomaly shown at one M point of each valley, giving the highest coupling rate where it shouldn't be that high. This is explained by a numerical error in the Wannierization process, most likely due to border effect, indicating space for improvement of calculations. Nevertheless, the K points are the central symmetry for the continuity of this study, and these are perfectly represented in the figure above.

Below, Figure 42 shows the unit cell mapping of the momentum matrix element with  $\hat{x}$  and  $\hat{y}$  polarizations in Y<sub>2</sub>CCl<sub>2</sub>:

5.7. Optics 161

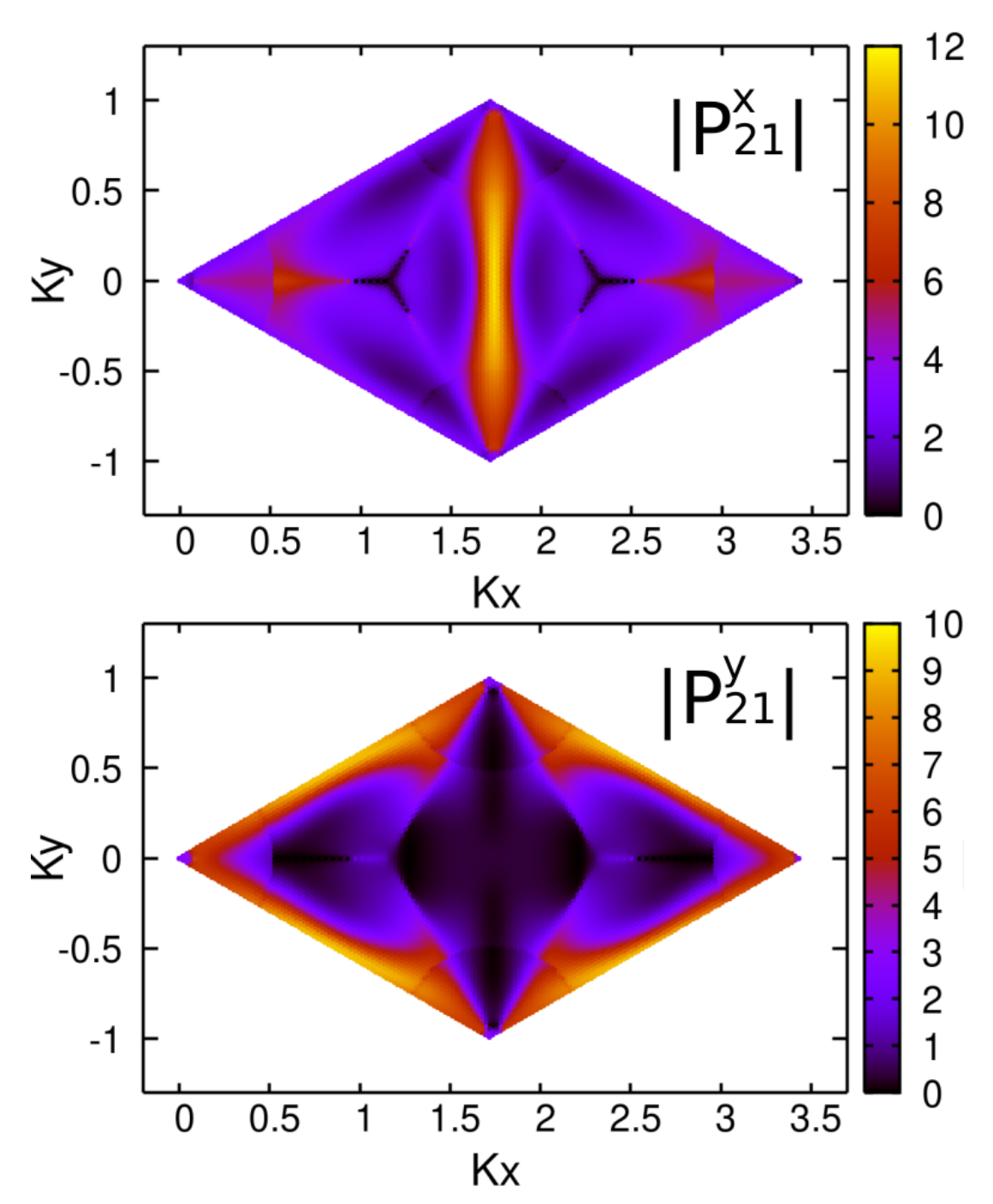


Figure 42 –  $Y_2CCl_2$  momentum matrix elements with  $\hat{x}$  and  $\hat{y}$  polarization, showing regions of optical activity.

This map of the momentum matrix elements in the unit cell confirms the peak of optical activity at the M high symmetry point, but it shows how the flat band behavior of the valence states in  $Y_2CCl_2$  gives no K valleys of optical activity as in  $MoS_2$ , but a large wall dividing the unit cell into two triangles of lesser optical activity. The optical transitions happen not in the K points, but in the path between  $\Gamma$  points. The  $\hat{x}$  polarization resulted in a  $\hat{y}$  line of activity, while the  $\hat{y}$  polarization gave lesser optical activity, but still followed the in-between between  $\Gamma$  paths, insinuating a perpendicular

relation between the photon polarization and the lines of maximal optical absorption in reciprocal space. Both momentum maps (figures 41 and 42) are still imperfect, revealing higher fragility of the wave function continuity algorithm when working in two dimensions.

The optical absorption coefficient  $\alpha_{vc}^{\pm}(\omega)$  for the transition between each pair of bands obeys the proportion relation:

$$\alpha_{vc}^{\pm}(\omega) \propto \frac{1}{\omega} \int_{BZ} \frac{d\mathbf{k}}{(2\pi)^3} \left| \mathbf{p}_{cv}^{\pm}(\mathbf{k}) \right|^2 \delta \left( \hbar \omega - \left( E_c(\mathbf{k}) - E_v(\mathbf{k}) \right) \right), \tag{5.24}$$

and the total absorption coefficient is:

$$\alpha^{\pm}(\omega) \propto \frac{1}{\omega} \sum_{c,v} \int_{BZ} \frac{d\mathbf{k}}{(2\pi)^3} \left| \mathbf{p}_{cv}^{\pm}(\mathbf{k}) \right|^2 \delta \left( \hbar \omega - \left( E_c(\mathbf{k}) - E_v(\mathbf{k}) \right) \right). \tag{5.25}$$

This model contains only single-particle states; however, in reality, exciton states are necessary to fully grasp the physical picture. The first peaks in the experimental optical spectrum are energies corresponding to the creation of excitonic quasiparticles.

## 5.8 Exciton States

The Bethe-Salpeter equation (BSE) (SALPETER; BETHE, 1951) is an approximate equation that uses perturbation theory to describe the electron-hole interaction. Through this equation, it is possible to obtain the exciton energy states and their corresponding wave functions.

An exciton is constituted by an electron and a hole coupled by an electromagnetic interaction. Thus, the exciton Hamiltonian must include contributions from the electron Hamiltonian, the hole Hamiltonian, and the electromagnetic potential:

$$\hat{H}_{\rm X} = \hat{H}_{\rm e} + \hat{H}_{\rm h} + \hat{V}.$$
 (5.26)

The exciton state vectors  $|\Psi_X^i\rangle$  are expanded as a linear combination of the basis states:

$$\left|\Psi_{X}^{i}\right\rangle = \sum_{v,c,k} A_{v,c}^{i}(\boldsymbol{k})\hat{c}_{c}^{\dagger}(\boldsymbol{k})\hat{c}_{v}(\boldsymbol{k})\left|GS\right\rangle = \sum_{v,c,k} A_{v,c}^{i}(\boldsymbol{k})\left|\Psi_{c,v}(\boldsymbol{k})\right\rangle,$$
 (5.27)

where  $|\text{GS}\rangle$  is the ground state, and  $|\Psi_{c,v}(\mathbf{k})\rangle = |\Psi_c(\mathbf{k})\rangle \otimes |\Psi_v(\mathbf{k})\rangle$ , coupling the electron and hole states. We have then  $N_v \times N_c \times N_k$  basis functions, being that the

5.8. Exciton States 163

dimension of the BSE Hamiltonian.

The eigenvalues and eigenstates are thus obtained from simple diagonalization,

$$\hat{H}_{X} \left| \Psi_{X}^{i} \right\rangle = E_{X_{i}} \left| \Psi_{X}^{i} \right\rangle. \tag{5.28}$$

This Schrödinger equation may be written as:

$$(E_{c}(\mathbf{k}) - E_{v}(\mathbf{k}))A_{v,c}^{i}(\mathbf{k}) + \frac{1}{A_{C}} \sum_{v',c',k'} V(\mathbf{q}) \left\langle \Psi_{c}(\mathbf{k}) | \Psi_{c'}(\mathbf{k}') \right\rangle \left\langle \Psi_{v'}(\mathbf{k}') | \Psi_{v}(\mathbf{k}) \right\rangle A_{v',c'}^{i}(\mathbf{k}')$$

$$= E_{X_{i}} A_{v,c}^{i}(\mathbf{k}),$$

$$(5.29)$$

with  $A_{\rm C} = A_{\rm UC}N_k$  corresponding to the total area of the crystal in real space, V(q) being the electromagnetic potential in reciprocal space, where q = k' - k. Let's assume the Keldysh (KELDYSH, 1979) form:

$$V(\mathbf{q}) = -\frac{e^2}{2\epsilon_0 \epsilon_d |\mathbf{q}| (1 + r_0 |\mathbf{q}|)}.$$
 (5.30)

$$V(\boldsymbol{q}) = -\frac{e^2}{2\epsilon_0 \epsilon_d |\boldsymbol{q}|} (1 + r_0 |\boldsymbol{q}|). \tag{5.31}$$

Here, e is the electron charge,  $\epsilon_0$  is the permittivity constant in vacuum,  $r_0$  corresponds to the 2D polarizability of the system, representing the scale at which the Coulomb potential transitions from 3D to 2D environment (13.55 Å for MoS<sub>2</sub>), and  $\epsilon_d$  is the environmental dielectric constant (2.5 for air/silica interface) (RIDOLFI; LEWENKOPF; PEREIRA, 2018). The 2D polarizability of the MXene crystal was estimated to be equal to the TMD counterpart, due to the lack of literature on this newborn material.

The nature of the electromagnetic potential includes a singularity problem when q=0. To solve this, we start by understanding that in this discrete model, each momentum vector k in our grid represents a small area that when summed up results in the full unit cell area. Each potential calculation should not be thought of as an interaction between charges with specific grid momentum coordinates k and k', but as the interaction between charges whose coordinates belong to the surroundings of the specific grid coordinates. Instead of defining another expression for the potential in the singularity, as commonly used (RIDOLFI; LEWENKOPF; PEREIRA, 2018), we solve the singularity problem using an integral form of the electromagnetic potential inside a small area around the momentum vector coordinates. This small area must be correspondent to the fraction

of the reciprocal unit cell area related to each point in the grid  $\Delta A = \frac{A_{\rm BZ}}{N_k}$ . Even for very dense grids, where each point becomes very close to each other, the integral form compensates for that by reducing the area of integration, converging the results for higher  $N_k$ .

The potential is then numerically calculated as

$$V_K(\mathbf{q} \approx 0) = -\frac{2}{\Delta A} \int_{-N_s \Delta x}^{0} \int_{-\frac{N_s \Delta y}{2}}^{\frac{N_s \Delta y}{2}} \frac{e^2}{2\epsilon_0 \epsilon_d \sqrt{k_x^2 + k_y^2 (1 + r_0 \sqrt{k_x^2 + k_y^2})}} dy dx, \qquad (5.32)$$

where  $\Delta A$  is the total area of of the small unit cell represented in Figure 43;  $N_s$  is the number of steps in the numerical integration.  $\Delta x = \frac{|b_{1x} + b_{2x}|}{2N_p N_s}$ , and  $\Delta y = \frac{|b_{1y} - b_{2y}|}{N_p N_s} \frac{x_{\text{step}}}{N_s}$ , being  $x_{\text{step}}$  the counter of steps in the  $\hat{k}_x$  direction, necessary to define  $\Delta y$  since its height varies for each  $x_{\text{step}}$ . The factor 2 in front of the integral permits a cheaper integration on only half of the total area that should be considered.

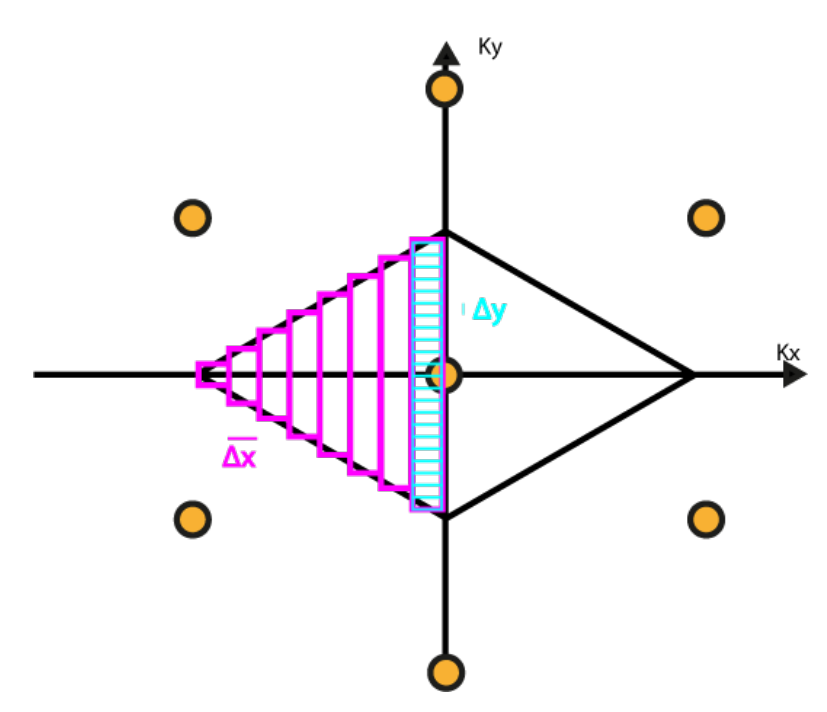


Figure 43 – Illustration of the numeric integral around the singularity point.

The exciton calculations performed for MoS<sub>2</sub> and Y<sub>2</sub>CCl<sub>2</sub> resulted in binding energies,  $E_{\rm bind} = E_{\rm gap} - E_{\rm X}$ , of 0.334 and 0.299 eV respectively, for their first exciton states, where in the case of MoS<sub>2</sub> it is a degenerate state; being both significant indicators of good exciton state stability. The squared absolute values of their wave functions are shown in figures 44 and 45, where we have considered  $\left|A_{\uparrow,\uparrow}^1(\boldsymbol{k})\right|^2$ ,  $\left|A_{\uparrow,\uparrow}^2(\boldsymbol{k})\right|^2$ ,  $\left|A_{\downarrow,\downarrow}^1(\boldsymbol{k})\right|^2$  and  $\left|A_{\downarrow,\downarrow}^2(\boldsymbol{k})\right|^2$  for MoS<sub>2</sub>, and  $\left|A_{2,1}^1(\boldsymbol{k})\right|^2$  for Y<sub>2</sub>CCl<sub>2</sub>:

5.8. Exciton States 165

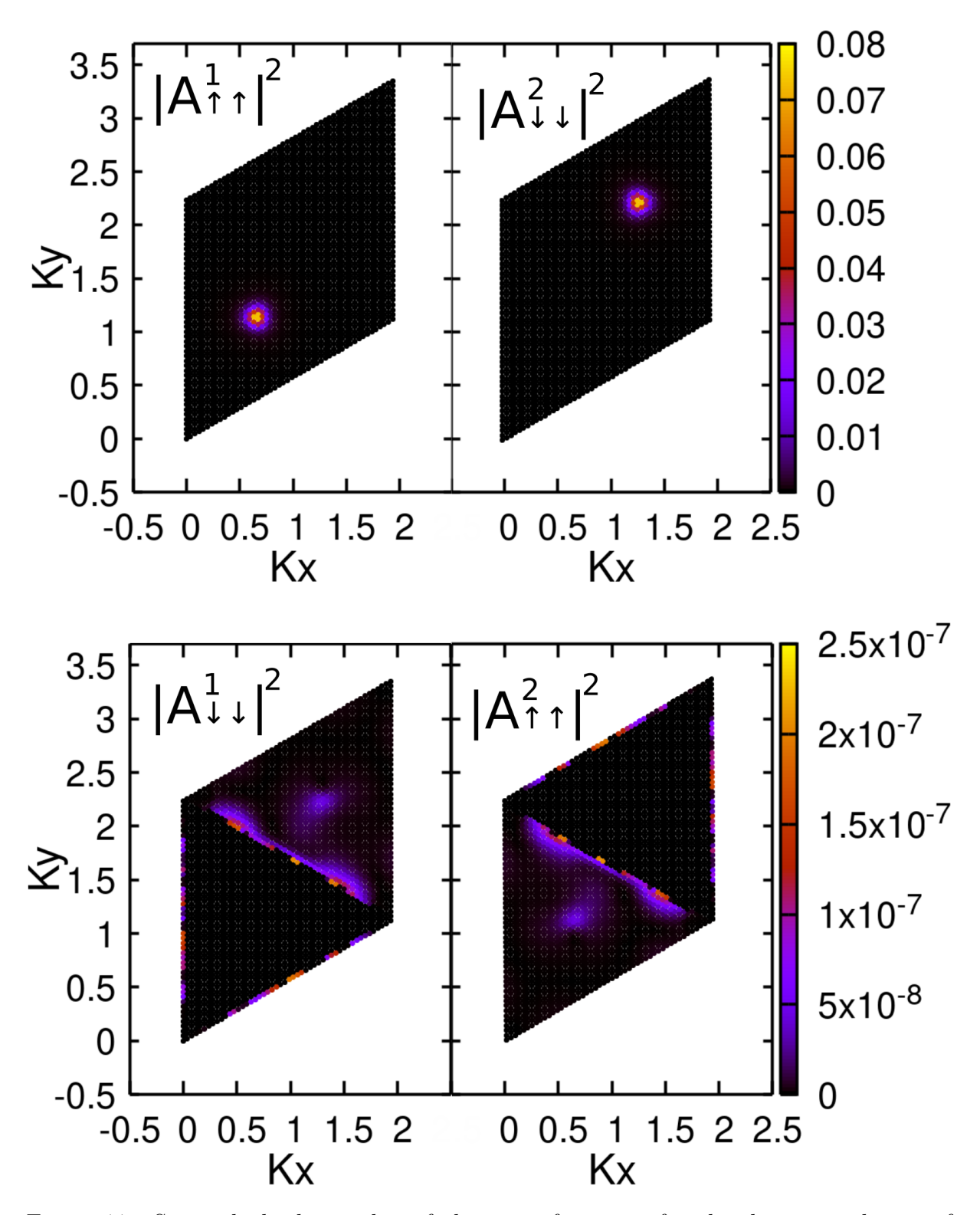


Figure 44 – Squared absolute value of the wave functions for the degenerated pair of exciton states in  $MoS_2$ .

Figure 44 shows the first pair of degenerate exciton state wave functions in MoS<sub>2</sub>,  $|\Psi_{\rm X}^1\rangle = A_{\uparrow,\uparrow}^1(\mathbf{k} \approx {\rm K})\hat{c}_{c=\uparrow}^\dagger(\mathbf{k} \approx {\rm K})\hat{c}_{v=\uparrow}(\mathbf{k} \approx {\rm K})|{\rm GS}\rangle$  and  $|\Psi_{\rm X}^2\rangle = A_{\downarrow,\downarrow}^2(\mathbf{k} \approx {\rm K}')\hat{c}_{c=\downarrow}^\dagger(\mathbf{k} \approx {\rm K}')\hat{c}_{c=\downarrow}^\dagger(\mathbf{k} \approx {\rm K}')\hat{c}_{v=\downarrow}(\mathbf{k} \approx {\rm K})\hat{c}_{v=\downarrow}(\mathbf{k} \approx {\rm K})\hat{c}_{v=\downarrow}(\mathbf{k})\hat{c}_{v=\downarrow}(\mathbf{k} \approx {\rm K})\hat{c}_{v=\downarrow}(\mathbf{k} \approx {\rm K})\hat{c}_{v=\downarrow}(\mathbf{k}$ 

K)  $|\text{GS}\rangle$  and  $|\Psi_{\text{X}}^4\rangle = A_{\uparrow,\uparrow}^4(\mathbf{k} \approx \text{K}')\hat{c}_{c=\uparrow}^\dagger(\mathbf{k} \approx \text{K}')\hat{c}_{v=\uparrow}(\mathbf{k} \approx \text{K}') |\text{GS}\rangle$ , is called "B excitons". For being constituted of electron-hole pairs sharing the same spin alignment and momentum coordinate, both A and B excitons are bright states, i.e., they can decay back to ground state by photon emission of equivalent energy and polarization.

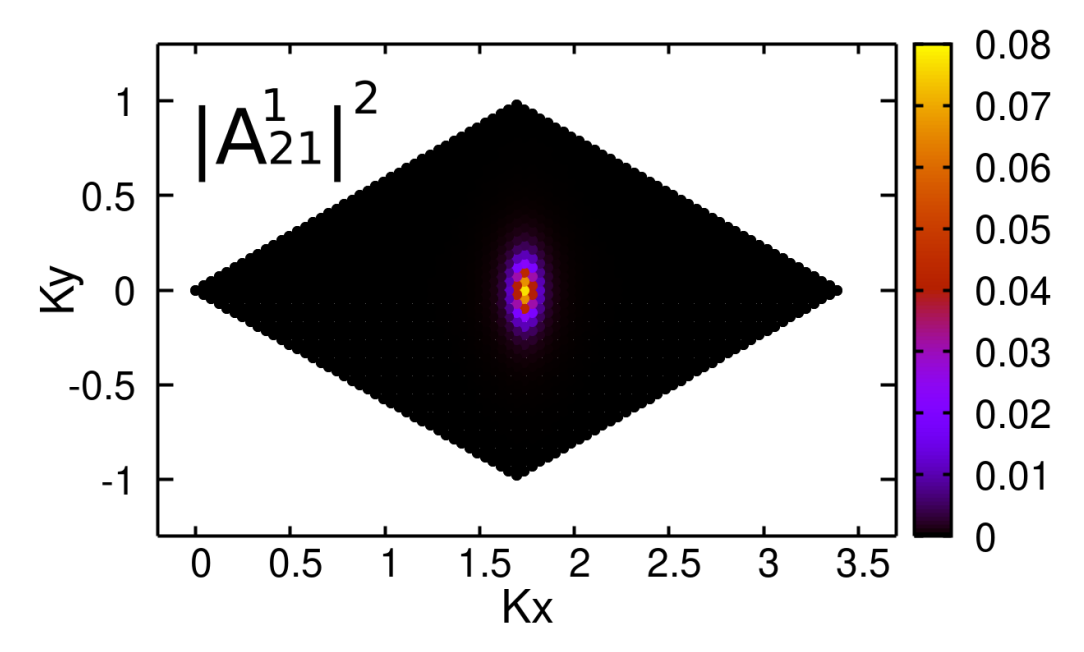


Figure 45 – Squared absolute value of the first exciton state wave function in Y<sub>2</sub>CCl<sub>2</sub>.

The first exciton state in Y<sub>2</sub>CCl<sub>2</sub>, shown in Figure 45, differs from what is seen in the TMD counterpart. Firstly, the wave function spreads in a straight line, and this line is centered in the M high symmetry point, as the momentum mapping (Figure 42) suggests. What is also important to notice is that this exciton state,  $|\Psi_{\rm X}^1\rangle = A_{2,1}^1(\mathbf{k} \approx {\rm M})\hat{c}_{c=1}^{\dagger}(\mathbf{k} \approx {\rm M})\hat{c}_{c=1}^{\dagger}(\mathbf{k} \approx {\rm M})|{\rm GS}\rangle$ , is less localized because the hole states in its constitution belong to nearly flat band states, which have an effective mass of  $\approx 20~m_{\rm e}$ . Since the effective mass of the exciton is the sum of electron and hole masses, this is a supermassive exciton.

The contribution of each band transition to the optical absorption coefficient considering excitonic effects  $\xi^{\alpha}(\omega)$  is given as:

$$\xi_{vc}^{\alpha}(\omega) = \frac{1}{\omega} \frac{\pi}{A_{\rm C}} \sum_{i,k} O_{i,v,c}^{\alpha}(k) \delta(\hbar\omega - E_{\rm X_i}). \tag{5.33}$$

And the total absorption coefficient:

$$\xi^{\alpha}(\omega) = \frac{1}{\omega} \frac{\pi}{A_{\rm C}} \sum_{i,v,c,k} O_{i,v,c}^{\alpha}(\mathbf{k}) \delta(\hbar\omega - E_{\rm X_i}), \tag{5.34}$$

5.8. Exciton States 167

where we've been using the oscillator strength  $O_{i,v,c}^{\alpha}(\mathbf{k})$ , which represents the contribution to the *i*th excitonic state given by the interaction between an electron in  $|\Psi_c(\mathbf{k})\rangle$  and a hole in  $|\Psi_v(\mathbf{k})\rangle$ , induced by an electromagnetic field in the  $\alpha$  polarization. This quantity is computed as:

$$O_{i,v,c}^{\alpha}(\mathbf{k}) = \left| A_{v,c}^{i}(\mathbf{k}) P_{vc}^{\alpha}(\mathbf{k}) \right|^{2}. \tag{5.35}$$

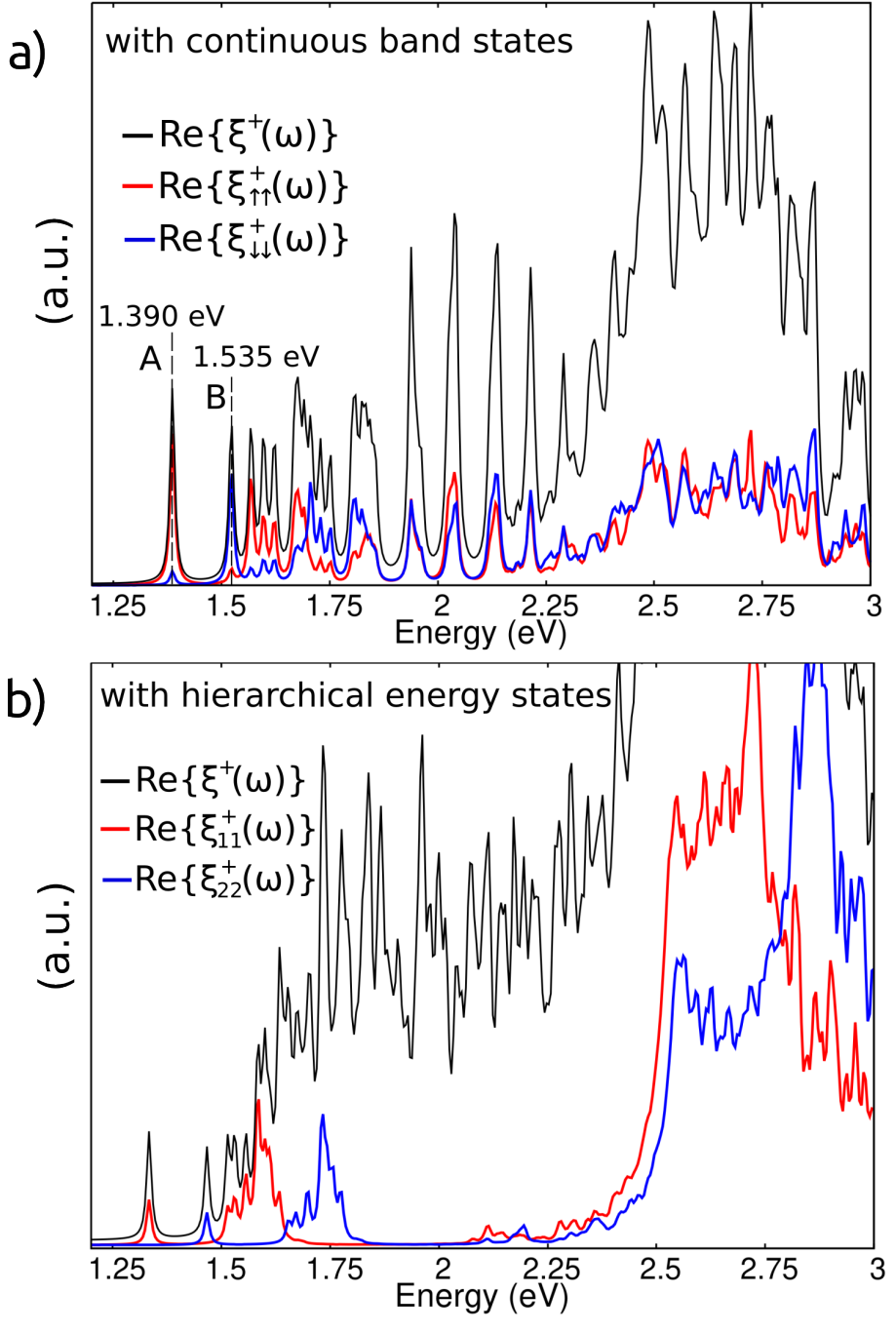


Figure 46 – Excitonic Optical absorption spectra of monolayer MoS<sub>2</sub> under right-handed circularly polarized light. a) considers hierarchical energy states, while b) considers continuous energy bands.

The spectrum shown in Figure 46 corresponds to excitation by right-handed circular polarization of light, such that the exciton states here observed are produced in the K valley, while the K' valley would be excited by left-handed circularly polarized light, producing peaks in the same energetic positions yet with opposite spins with relation to these results from positive polarization. We can see the importance of the correct index configuration for elucidating which electron-hole pair represents each exciton state, which is one step further than the most advanced methods for excitonic calculations in the literature (WU; QU; MACDONALD, 2015; RIDOLFI; LEWENKOPF; PEREIRA, 2018; DIAS et al., 2018). Each peak represents an optical excitation related to the creation of some specific exciton, the first state correspondent to the interaction between a hole in the upper valence state and an electron in the lower conduction state with the same spin, i.e., each valley is responsible for an exciton state of distinct spin orientation yet energetically degenerate. The second exciton state in each valley is of opposite spin in relation to the first exciton state, and higher states are condensed in the same energy range, resulting in an intense absorption composed of contributions from multiple exciton states.

This optical control over both valleys is the key to valleytronics, where information can be encoded in the valley degree of freedom of the exciton states. Spin up A excitons are formed in the K valley upon 1.390 eV energy absorption from right-handed circularly polarized light, while B excitons with spin down are formed if the energy of the incident photons is 1.535 eV. A and B excitons are also formed upon left-handed circularly polarized light, but they appear in the K' valley, and the spin values are also opposite from the K valley. Exciton states can be in superposition, which leads to the possibility of quantum information encoding, unlike usual binary information contained in common electronic technologies. This material is a candidate for being used as a quantum bit, the quantum information unit considered in quantum computation (BORGES et al., 2023).

Figure 47 shows the excitonic absorption spectra in  $Y_2CCl_2$ , where the first peak represents the light absorption that forms the supermassive exciton (fig. 44), light whose photon energy is 0.486 eV and polarization is in the  $\hat{x}$  axis.

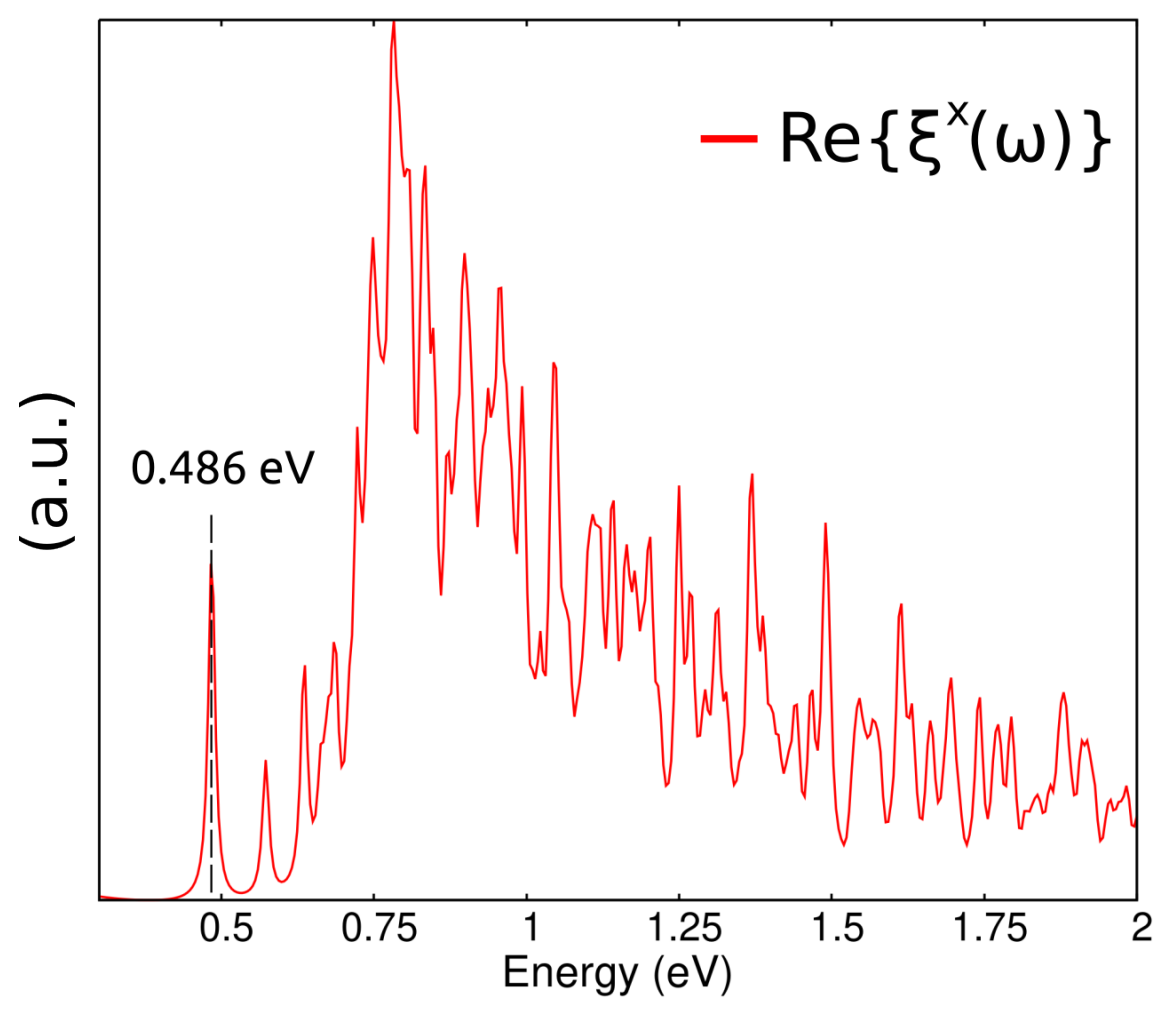


Figure 47 – Excitonic Optical absorption spectra of monolayer  $Y_2CCl_2$  under  $\hat{x}$  polarized light.

At this point, it is important to recover that all those calculations are based on DFT with GGA-PBE exchange-correlation functionals. A more experimentally accurate result would come from a calculation with the HSE06 hybrid functional, which would shift the whole spectrum at least 0.5 eV higher by opening the valence-conduction energy gap by that amount. Another consideration is that we only considered two valence and two conduction bands for the results, which are responsible for the lower energy exciton states. A more accurate result in the energetically higher states would require contributions from more band interactions.

## 5.9 Berry Curvature

The Berry curvature is a profound subject with various applications to topological condensed matter physics, impacting quantum computation, spintronics, and many emerging technologies (KöNIG et al., 2007; MOURIK et al., 2012). Chern numbers and anomalous Hall properties can be directly extracted from Berry curvature, as well as other

quantities such as the quantum metric. The anomalous Hall effect and spin Hall effect find applications in spintronic devices, such as magnetic sensors and magnetic memory devices (NAKATANI et al., 2024), where information is encoded in the spin current rather than charge current, being much more energy-efficient than common electronics. Chern numbers are one of the fundaments in topological quantum computing (CHEN et al., 2023), where quantum information is topologically protected from decoherence, which is a crucial aspect for the future of quantum computation (AASEN et al., 2025). This study merely scratches the surface, but we go far enough to understand how the calculation of these properties that are derived from Berry curvature can be impacted by proper treatment of the electronic states.

We start by pondering upon adiabatic transformations of our system, i.e., we now consider the system in an eigenstate  $|\Psi_n(\mathbf{k}(t))\rangle$ , where  $\mathbf{k}(t)$  is slowly changing. The quantum adiabatic theorem (KATO, 1950) states that a system initially in one of its eigenstates  $|\Psi_n(\mathbf{k}(0))\rangle$  remains in that instantaneous state  $|\Psi_n(\mathbf{k}(t))\rangle$  under adiabatic transformations. This state evolves in time according to the time-dependent Schrödinger equation,

$$i\hbar \frac{d}{dt} |\Psi_n(\mathbf{k}(t))\rangle = \hat{H}(\mathbf{k}(t)) |\Psi_n(\mathbf{k}(t))\rangle.$$
 (5.36)

Now we must remember that (5.8) does not uniquely determine the phase of the basis functions, as it allows an arbitrary phase factor which is usually unexplored, since observables are gauge invariant.  $|\Psi_n(\mathbf{k}(t))\rangle \to e^{i\phi(\mathbf{k})} |\Psi_n(\mathbf{k}(t))\rangle$  is a local gauge transformation, as  $\phi(\mathbf{k})$  can vary arbitrarily at each point in parameter space. This phase factor can be expanded as (XIAO; CHANG; NIU, 2010):

$$e^{i\phi(\mathbf{k})} |\Psi_n(\mathbf{k}(t))\rangle = e^{i\gamma_n(t)} exp\left[\frac{-i}{\hbar} \int_0^t dt' \epsilon_n(\mathbf{k}(t'))\right] |\Psi_n(\mathbf{k}(t))\rangle,$$
 (5.37)

where the second exponential is the dynamical phase, which is irrelevant to our discussion, while the first exponential contains the Berry phase  $\gamma_n(t)$ , which can be canceled with local gauge transformations, and hence for long neglected. The exception was noticed by (BERRY, 1984), when he considered the effect of this phase upon closed paths, where the initial and final coordinates are equal, and the  $\gamma_n(t)$  becomes a gauge-invariant quantity. To obtain the form of this phase, we consider that it must satisfy the time-dependent Schrödinger equation, so inserting (5.37) into (5.36), and multiplying both sides by  $\langle \Psi_n(\mathbf{k}(t))|$  gives:

$$\dot{\gamma}_n(t) = i \langle \Psi_n(\mathbf{k}(t)) | \nabla_{\mathbf{k}} | \Psi_n(\mathbf{k}(t)) \rangle \cdot \dot{\mathbf{k}}(t).$$
 (5.38)

Integrating in time, then considering a closed loop C after using  $\dot{\mathbf{k}}(t')dt' \to d\mathbf{k}$ , we finally obtain a geometric phase  $\gamma_n$  of the nth band state, which is not only gauge-invariant but also time-independent and brings intuition of how the physical state changes over the coordinate space:

$$\gamma_n = \oint_C d\mathbf{k} \cdot i \langle \Psi_n(\mathbf{k}) | \nabla_{\mathbf{k}} | \Psi_n(\mathbf{k}) \rangle = \oint_C d\mathbf{k} \cdot \mathbf{A}_n, \qquad (5.39)$$

where  $A_n = i \langle \Psi_n(\mathbf{k}) | \nabla_{\mathbf{k}} | \Psi_n(\mathbf{k}) \rangle$  is now called the Berry connection of the *n*th band state, being a gauge-dependent quantity. Stokes's theorem can be invoked to give a representation of the Berry phase in terms of a vector field called the Berry curvature,  $\Omega_n(\mathbf{k}) = \nabla_{\mathbf{k}} \times A_n(\mathbf{k})$ :

$$\gamma_n = \oint_C d\mathbf{k} \cdot \mathbf{A_n} = \oiint_S d\mathbf{S} \cdot \Omega_n(\mathbf{k}). \tag{5.40}$$

The Berry curvature is gauge-invariant and analogous to a magnetic field  $\boldsymbol{B}$ , but it is defined in momentum space, or any parameter space, and its nature is not magnetic; it is a local geometric description as it quantifies the non-commutativity of adiabatic parallel transport of quantum states in parameter space. This intuition is better grasped in the more generalized expression for the Berry curvature, expressed as an antisymmetric tensor  $\Omega_{\gamma}^{n} = \epsilon_{\alpha\beta\gamma}\Omega_{\alpha\beta}^{n}$ , where (XIAO; CHANG; NIU, 2010)

$$\Omega_{\alpha\beta}^{n} = \frac{d}{d\mathbf{k}^{\alpha}} A_{\beta}^{n} - \frac{d}{d\mathbf{k}^{\beta}} A_{\alpha}^{n}.$$
 (5.41)

If we were to go deeper into the subject, we could take integrals of  $\Omega_{n,xy}(\mathbf{k})$  over closed manifolds, such as the BZ, to result in topological invariants known as Chern numbers  $c_n$ , opening perspectives for many topological properties such as the quantum Hall effect (THOULESS et al., 1982). Here we will limit ourselves to compute the total Berry curvature according to a more approachable form of calculation, discussed in (WANG et al., 2006), from where we obtain:

$$\Omega_{\alpha,\beta}(\mathbf{k}) = -2i \sum_{v,c} \frac{\langle \Psi_c(\mathbf{k}) | \frac{\partial H}{\partial \alpha} | \Psi_v(\mathbf{k}) \rangle \langle \Psi_v(\mathbf{k}) | \frac{\partial H}{\partial \beta} | \Psi_c(\mathbf{k}) \rangle}{(E_c(\mathbf{k}) - E_v(\mathbf{k}))^2}.$$
 (5.42)

This expression brings the intuition that the curvature relates to band interactions, and can be easily calculated using the momentum matrix elements  $P_{vc}^{\alpha}(\mathbf{k})$ . These results for the total Berry curvature are perfectly obtained using any addressing method for the energy states, as the sum over all valence and conduction bands will include interactions of all combinations regardless of the index configuration. Nevertheless, if we fix the conduction and valence band indices, we have the expression that brings the curvature contribution from each band interaction:

$$\Omega_{\alpha,\beta}^{v,c}(\mathbf{k}) = -2i \frac{\langle \Psi_c(\mathbf{k}) | \frac{\partial H}{\partial \alpha} | \Psi_v(\mathbf{k}) \rangle \langle \Psi_v(\mathbf{k}) | \frac{\partial H}{\partial \beta} | \Psi_c(\mathbf{k}) \rangle}{(E_c(\mathbf{k}) - E_v(\mathbf{k}))^2}.$$
 (5.43)

This result can be properly calculated only if we correctly address the band states, as we show by comparison in Figure 48, where we consider = x and  $\beta = y$  in both scenarios:

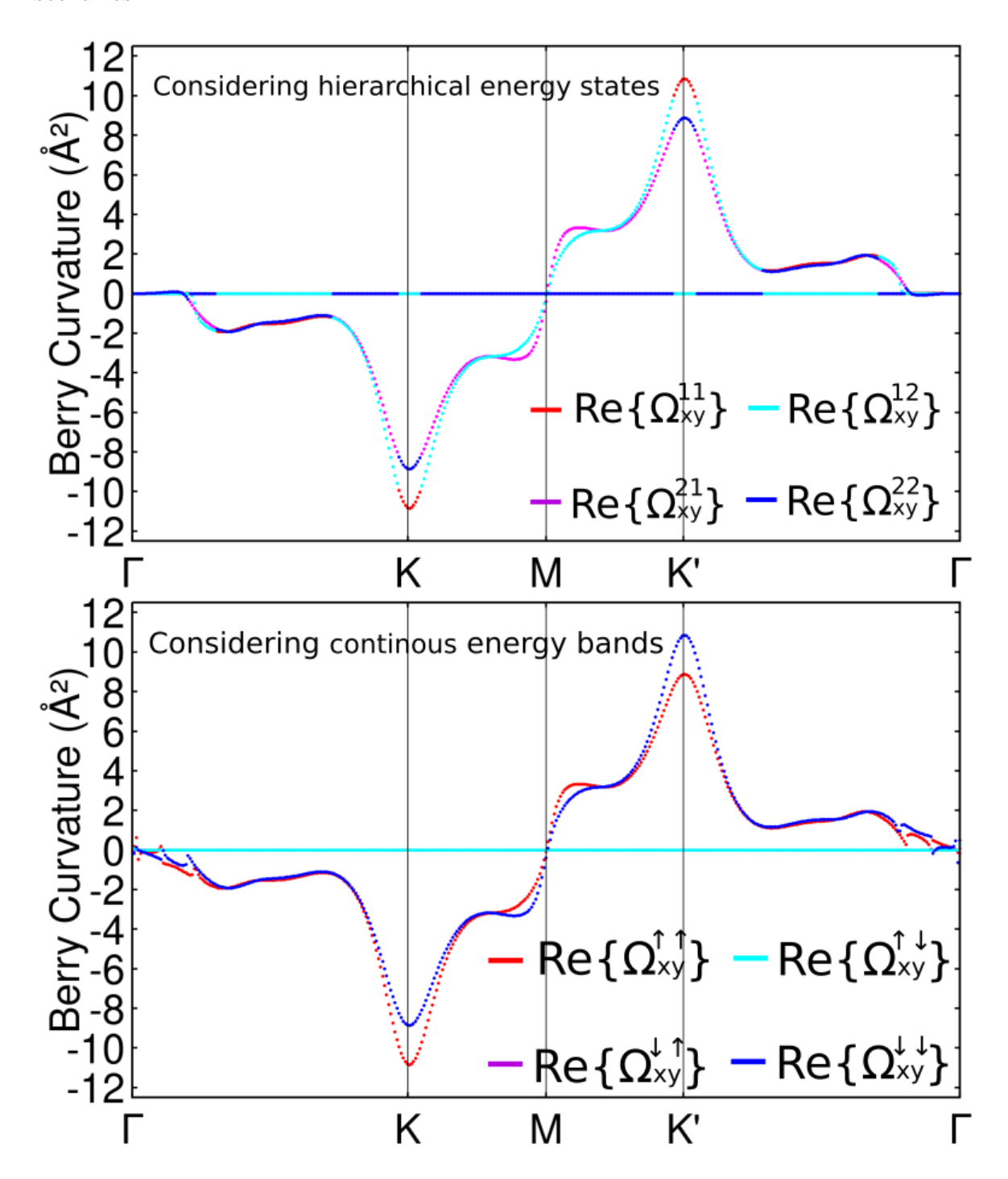


Figure 48 – Real part of Berry curvature contributions for each band interactions in both pictures of index configurations. The contribution from each pair of bands is distinguished by color, and both scenarios considers = x and  $\beta = y$ .

We see that without the correct index configuration, the Berry curvatures for particular interactions are nonsense, but it is a meaningful result when we properly consider the band index configuration, being associated with the optical selection rules and valley-dependent topology (ZHOU et al., 2021). This approach gives a finer view of the band interactions at a topological level, showing spin dependency in the band contribution to the total Berry curvature, being an elucidating information for valleytronics physics. Figure 49 shows the Berry curvatures considering  $\alpha = x, y$  and  $\beta = x, y$ , where we verify the antisymmetric nature of the Berry tensor:

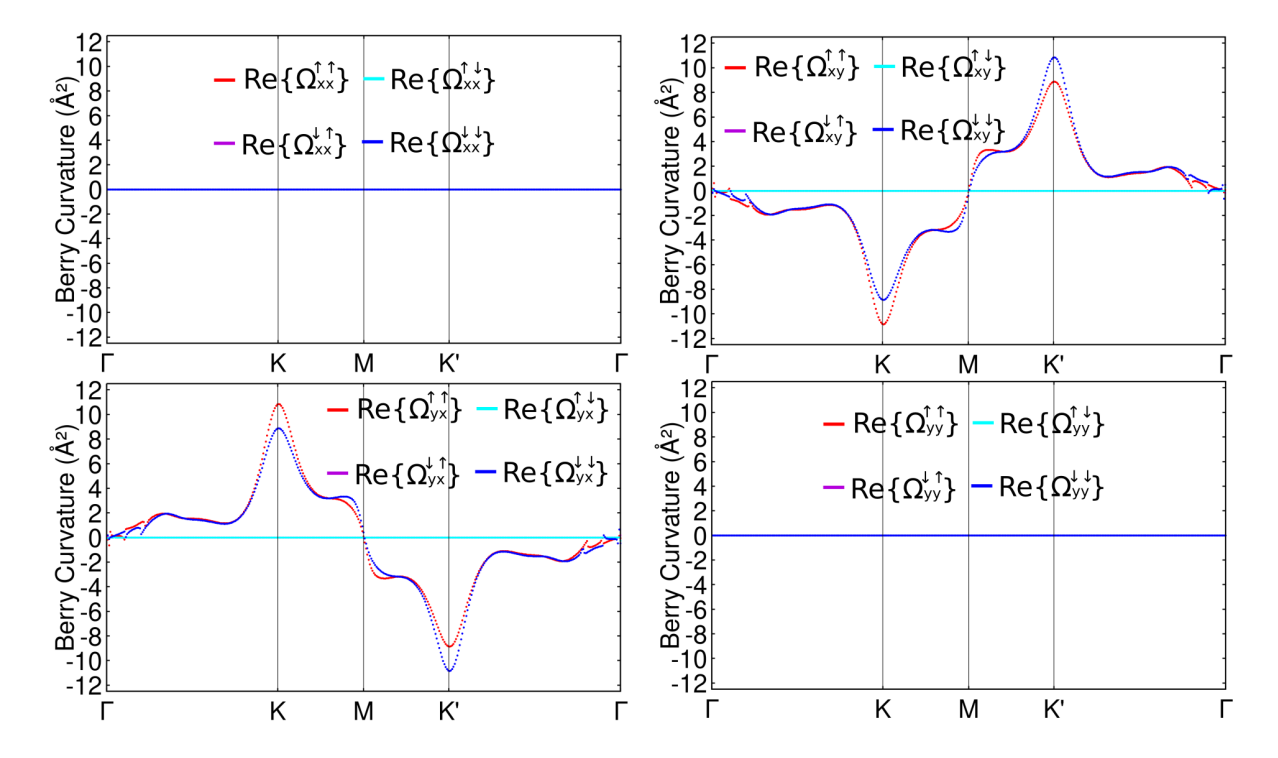


Figure 49 – Real part of Berry curvature tensor components.

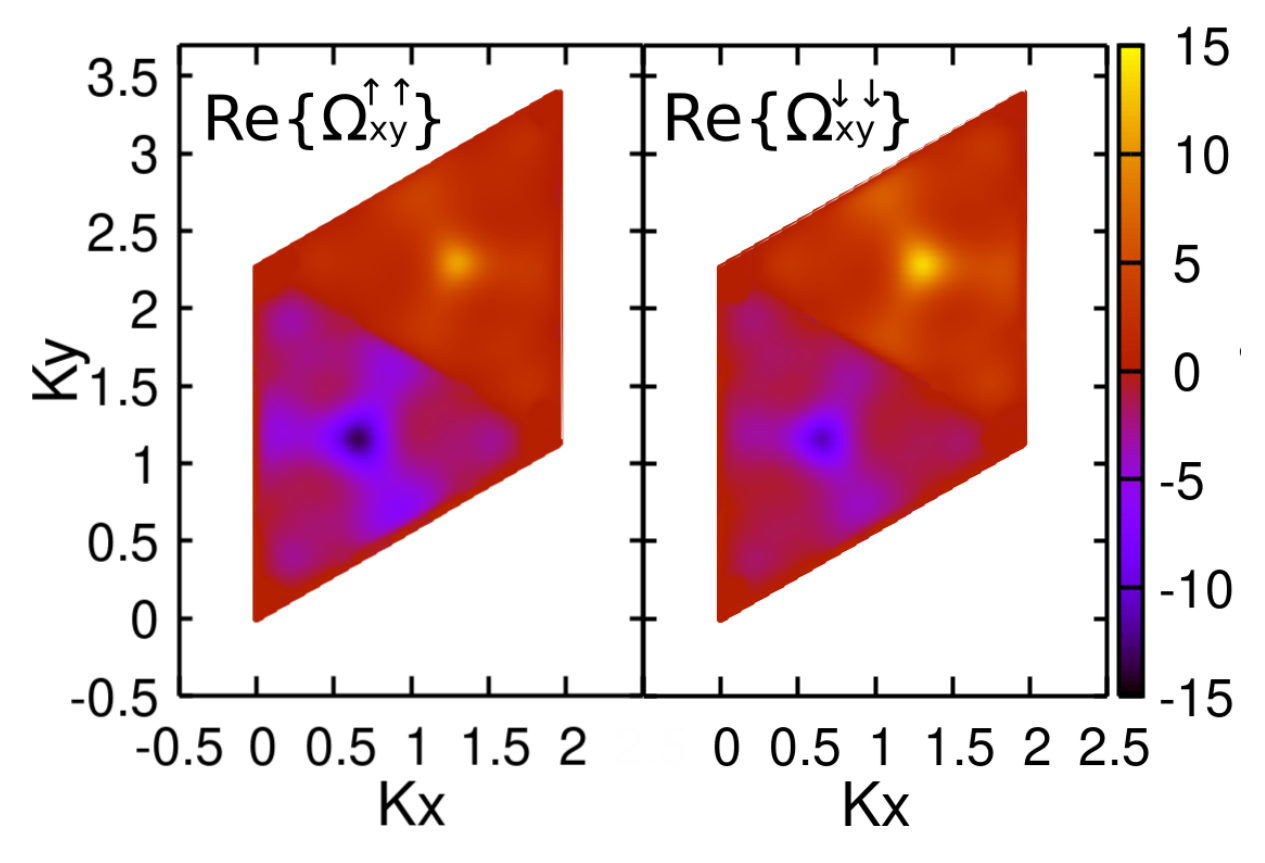


Figure 50 – Spin up and down contributions to the Berry curvature within the unit cell (Berry curvature units in  $\mathring{A}^2$ ).

# Conclusions

I cannot conclude without first emphasizing the importance of the gradual construction of knowledge both as a personal pursuit and as a collective human goal. This study represents the best contribution my present self can offer to the community, and I recognize that much work is yet to be done. This study was able to accomplish a journey through the understanding of the fundamental properties of physics, until achieving great practical methodologies and results of the quantum mechanical behavior in realistic solid systems.

We explored two of the most modern classes of materials, TMDs and MXenes, giving the individual attention each material deserved. For the MXene family, we used DFT to explore unsynthesized crystals, starting by simulating their stability and vibrational properties. Our results predict viable synthesis conditions for Y<sub>2</sub>CF<sub>2</sub>, Y<sub>2</sub>CCl<sub>2</sub> and Y<sub>2</sub>CBr<sub>2</sub> by obtaining positive phonon band states and using the phonon density to find good thermodynamic indicators of the materials' stability. The vibrational description of the materials also permitted the calculation of the lattice interaction with light, resulting in the infrared and Raman spectra, which will be valuable for future characterization of the synthesized materials. Having assured the materials' condition to exist, we dived into their electronic properties. All three MXenes exhibited a semiconductor band structure, all with an indirect band gap. Our attention was caught by the flatness of the highest valence band in each material, which called for further investigation into the effective mass of charge carriers in those electronic states. We found an impressive effective mass in the M high symmetry coordinate of the Y<sub>2</sub>CF<sub>2</sub> reciprocal lattice, two orders of magnitude higher than the electron mass, confidently indicating a real flat band region. Y<sub>2</sub>CCl<sub>2</sub> also called for special attention, as we noticed that more than a strip of flatness effect, the almost flat region located in the direct band gap was energetically close to the top of the valence band. For that reason, the electronic structure of Y<sub>2</sub>CCl<sub>2</sub> was chosen for a deeper analysis alongside MoS<sub>2</sub>, a widely studied TMD known for its valleytronic properties.

We pushed the limits of computational simulation by constructing advanced algorithms capable of threatening the wave function of the electron states one step further than simple DFT calculations. Using Wannier functions, we were capable of correctly finding the coupling of the electronic states, and with it calculate optical and topological interactions, finding their absorption spectrum with excitonic effects, analyzing the optical transitions in detail and the effect of the coupling of states in topological phenomena by the prediction of the Berry curvature. We were able to demonstrate the valleytronic structure of MoS<sub>2</sub> in more depth than what is done in the current literature. Also, we found massive states with one order of magnitude higher than the electron mass in the va-

176 Conclusions

lence band of Y<sub>2</sub>CCl<sub>2</sub>, states which are also in a region of high optical activity, indicating direct optical transitions from massive states. These were predicted to majorly contribute to excitonic behavior, resulting in a massive exciton state whose binding energy is similar to the recognized stable excitons in MoS<sub>2</sub>, but differently from the K valley localization and radial distribution of the wave function, its wave is distributed in a linear shape in the center of the reciprocal unit cell.

Despite achieving groundbreaking results with our methodology, we notice the eternal incompletion of knowledge as we see a clear path for deeper investigation. There is much more to be explored in topological properties, spintronics, and valleytronics; applications in quantum technology. Everything done in this study can be pushed even further beyond, and we finish this document with open doors.

# References

- AASEN, D. et al. Roadmap to fault tolerant quantum computation using topological qubit arrays. arXiv preprint arXiv:2502.12252, 2025. 170
- ALHADITHY, Z. E. et al. Advancements in water treatment with mxene-enhanced membranes: A review of current progress and future directions. *Water*, *Air*, & *Soil Pollution*, Springer, v. 235, n. 809, 2024. Disponível em: <a href="https://link.springer.com/article/10.1007/s11270-024-07628-x">https://link.springer.com/article/10.1007/s11270-024-07628-x</a>. 115
- ALIAKBARI, A.; AMIRI, P.; DEZFULI, A. G. Stability and physical properties of yttrium-based new max phases y2ax (a= al, si, ga, and ge; x= c and n): a first-principles prediction. *Applied Physics A*, Springer, v. 129, n. 7, p. 476, 2023. 115
- ALMBLADH, C.-O. Exact results for the charge and spin densities, exchange-correlation potentials, and density-functional eigenvalues. *Physical review. B, Condensed matter*, v. 31, p. 3231–3244, 04 1985. 100
- AMPONG, D. N. et al. Mxene: fundamentals to applications in electrochemical energy storage. *Discover Nano*, Springer, v. 18, n. 3, 2023. Disponível em: <a href="https://link.springer.com/article/10.1186/s11671-023-03786-9">https://link.springer.com/article/10.1186/s11671-023-03786-9</a>. 115
- ANASORI, B.; LUKATSKAYA, M. R.; GOGOTSI, Y. 2d metal carbides and nitrides (mxenes) for energy storage. *Nature Reviews Materials*, Nature Publishing Group, v. 2, n. 2, p. 1–17, 2017. 111, 115
- ASHCROFT, N. et al. *Solid State Physics*. [S.l.]: Holt, Rinehart and Winston, 1976. (HRW international editions). ISBN 9780030839931. 56
- ASHCROFT, N. W.; MERMIN, N. D. Solid state physics. [S.l.]: Cengage Learning, 2022. 129
- BARONI, S. et al. Phonons and related crystal properties from density-functional perturbation theory. *Rev. Mod. Phys.*, American Physical Society, v. 73, p. 515–562, Jul 2001. Disponível em: <a href="https://link.aps.org/doi/10.1103/RevModPhys.73.515">https://link.aps.org/doi/10.1103/RevModPhys.73.515</a>. 123
- BARSOUM, M. W. The mn+1axn phases: A new class of solids: Thermodynamically stable nanolaminates. *Progress in Solid State Chemistry*, v. 28, n. 1, p. 201–281, 2000. ISSN 0079-6786. Disponível em: <a href="https://www.sciencedirect.com/science/article/pii/S0079678600000066">https://www.sciencedirect.com/science/article/pii/S0079678600000066</a>. 115
- BECKE, A. D. Density-functional exchange-energy approximation with correct asymptotic behavior. *Phys. Rev. A*, American Physical Society, v. 38, p. 3098–3100, Sep 1988. Disponível em: <a href="https://link.aps.org/doi/10.1103/PhysRevA.38.3098">https://link.aps.org/doi/10.1103/PhysRevA.38.3098</a>>. 105
- BERRY, M. V. Quantal phase factors accompanying adiabatic changes. *Proceedings of the Royal Society of London. A. Mathematical and Physical Sciences*, The Royal Society London, v. 392, n. 1802, p. 45–57, 1984. 170

BHATTACHARJEE, S.; KOSHI, N. A.; LEE, S.-C. Customizing pbe exchange—correlation functionals: a comprehensive approach for band gap prediction in diverse semiconductors. *Phys. Chem. Chem. Phys.*, The Royal Society of Chemistry, v. 26, p. 26443–26452, 2024. 108

- BIENIEK, M. et al. Theory of excitons in atomically thin semiconductors: Tight-binding approach. *Nanomaterials*, v. 12, n. 9, 2022. ISSN 2079-4991. Disponível em: <a href="https://www.mdpi.com/2079-4991/12/9/1582">https://www.mdpi.com/2079-4991/12/9/1582</a>. 149
- BORGES, H. S. et al. Persistent entanglement of valley exciton qubits in transition metal dichalcogenides integrated into a bimodal optical cavity. *Phys. Rev. B*, American Physical Society, v. 107, p. 035404, Jan 2023. Disponível em: <a href="https://link.aps.org/doi/10.1103/PhysRevB.107.035404">https://link.aps.org/doi/10.1103/PhysRevB.107.035404</a>. 114, 168
- BORN, M.; OPPENHEIMER, R. Zur quantentheorie der molekeln annalen der physik, v. 84. 1927. 82
- BROOKS, M.; BURKARD, G. Electronic dipole spin resonance of 2d semiconductor spin qubits. In: *APS March Meeting Abstracts*. [S.l.: s.n.], 2019. v. 2019, p. A15–014. 114
- CHEN, C. et al. Berry curvature and bulk-boundary correspondence from transport measurement for photonic chern bands. *Phys. Rev. Lett.*, American Physical Society, v. 131, p. 133601, Sep 2023. Disponível em: <a href="https://link.aps.org/doi/10.1103/PhysRevLett.131.133601">https://link.aps.org/doi/10.1103/PhysRevLett.131.133601</a>. 170
- CHEN, S. A.; LAW, K. Ginzburg-landau theory of flat-band superconductors with quantum metric. *Physical Review Letters*, APS, v. 132, n. 2, p. 026002, 2024. 136
- CHHOWALLA, M. et al. The chemistry of two-dimensional layered transition metal dichalcogenide nanosheets. *Nature Chemistry*, Nature Publishing Group UK London, v. 5, n. 4, p. 263–275, 2013. 111
- CHHOWALLA, M. et al. The chemistry of two-dimensional layered transition metal dichalcogenide nanosheets. *Nature chemistry*, Nature Publishing Group UK London, v. 5, n. 4, p. 263–275, 2013. 112
- CLARK, S. J. et al. First principles methods using castep. Zeitschrift Für Kristallographie Crystalline Materials, v. 220, n. 5-6, p. 567–570, 2005. 121
- CORSO, A. D. et al. Generalized-gradient approximations to density-functional theory: A comparative study for atoms and solids. *Physical Review B*, APS, v. 53, n. 3, p. 1180, 1996. 121
- DENG, S.; SIMON, A.; KöHLER, J. The origin of a flat band. *Journal of Solid State Chemistry*, Elsevier, v. 176, n. 2, p. 412–416, 2003. 136
- DEXTER, R. et al. Effective masses of electrons in silicon. *Physical Review*, APS, v. 96, n. 1, p. 222, 1954. 138
- DIAS, A. et al. Band structure of monolayer transition-metal dichalcogenides and topological properties of their nanoribbons: Next-nearest-neighbor hopping. *Physical Review B*, APS, v. 98, n. 7, p. 075202, 2018. 149, 168

References 179

DRUFFEL, D. L. et al. Synthesis and electronic structure of a 3d crystalline stack of mxene-like sheets. *Chemistry of Materials*, ACS Publications, v. 31, n. 23, p. 9788–9796, 2019. 115

- ENGEL, E.; DREIZLER, R. Density Functional Theory: An Advanced Course. [S.l.]: Springer Berlin Heidelberg, 2011. (Theoretical and Mathematical Physics). ISBN 9783642140907. 29, 36, 40, 50, 90, 91, 96, 97, 100, 101, 104
- FLEMING, I. Molecular orbitals and organic chemical reactions. [S.l.]: John Wiley & Sons, 2011. 54
- Fock, V. Näherungsmethode zur Lösung des quantenmechanischen Mehrkörperproblems. Zeitschrift fur Physik, v. 61, n. 1-2, p. 126–148, jan. 1930. 108
- GANATRA, R.; ZHANG, Q. Few-layer mos2: a promising layered semiconductor. *ACS Nano*, ACS Publications, v. 8, n. 5, p. 4074–4099, 2014. 111
- GIANNOZZI, P. et al. Quantum espresso: a modular and open-source software project for quantum simulations of materials. *Journal of Physics: Condensed Matter*, v. 21, n. 39, p. 395502, sep 2009. Disponível em: <a href="https://dx.doi.org/10.1088/0953-8984/21/39/395502">https://dx.doi.org/10.1088/0953-8984/21/39/395502</a>>. 141
- GRYCIUK, M.; GÓRECKI, J. On calculations of the dipole moment from the electron density data. *TASK Quarterly*, v. 6, n. 4, p. 661–668, 2002. 130
- HARTREE, D. R. The wave mechanics of an atom with a non-coulomb central field. part ii. some results and discussion. *Mathematical Proceedings of the Cambridge Philosophical Society*, v. 24, p. 111 132, 1928. Disponível em: <a href="https://api.semanticscholar.org/CorpusID:121520012">https://api.semanticscholar.org/CorpusID:121520012</a>>. 108
- HARTREE, D. R.; HARTREE, W. Self-consistent field, with exchange, for beryllium. *Proceedings of the Royal Society of London. Series A-Mathematical and Physical Sciences*, The Royal Society London, v. 150, n. 869, p. 9–33, 1935. 84
- HEISENBERG, W. Über den anschaulichen inhalt der quantentheoretischen kinematik und mechanik. Zeitschrift für Physik, Springer, v. 43, n. 3, p. 172–198, 1927. 27
- HEYD, J.; SCUSERIA, G. E.; ERNZERHOF, M. Hybrid functionals based on a screened coulomb potential. *The Journal of chemical physics*, American Institute of Physics, v. 118, n. 18, p. 8207–8215, 2003. 108, 122
- HONG, L.; KLIE, R. F.; ÖĞÜT, S. First-principles study of size-and edge-dependent properties of mxene nanoribbons. *Physical Review B*, APS, v. 93, n. 11, p. 115412, 2016. 115
- HUANG, W. et al. Ultra-broadband and ultra-high electromagnetic interference shielding performance of aligned and compact mxene films. *Nano-Micro Letters*, Springer, v. 17, n. 1, p. 150, 2025. Disponível em: <a href="https://link.springer.com/article/10.1007/s40820-025-01750-z">https://link.springer.com/article/10.1007/s40820-025-01750-z</a>. 115
- JOE, A. Y. Interlayer Excitons in Atomically Thin van der Waals Semiconductor Heterostructures. Tese (Doutorado) Harvard University, 2021. 114

180 References

JONES, A. M. et al. Optical generation of excitonic valley coherence in monolayer wse 2. *Nature nanotechnology*, Nature Publishing Group, v. 8, n. 9, p. 634–638, 2013. 114

- KATO, T. On the adiabatic theorem of quantum mechanics. *Journal of the Physical Society of Japan*, v. 5, n. 6, p. 435–439, 1950. Disponível em: <a href="https://doi.org/10.1143/JPSJ.5.435">https://doi.org/10.1143/JPSJ.5.435</a>. 170
- KELDYSH, L. V. Coulomb interaction in thin semiconductor and semimetal films. *JETP Letters*, v. 29, p. 658–661, 1979. Original Russian: *Pis'ma Zh. Eksp. Teor. Fiz.* **29**, 716 (1979). 163
- KITTEL, C. *Introduction to Solid State Physics*. 8. ed. [S.l.]: Wiley, 2004. ISBN 9780471415268. 59, 62, 66, 85
- KOHN, W.; SHAM, L. J. Self-consistent equations including exchange and correlation effects. *Physical review*, APS, v. 140, n. 4A, p. A1133, 1965. 95
- KOŁSOS, W. Adiabatic approximation and its accuracy. In: Advances in Quantum Chemistry. [S.l.]: Elsevier, 1970. v. 5, p. 99–133. 81
- KOPACZEK, J. et al. Direct and indirect optical transitions in bulk and atomically thin mos2 studied by photoreflectance and photoacoustic spectroscopy. *Journal of Applied Physics*, v. 125, n. 13, p. 135701, 04 2019. ISSN 0021-8979. Disponível em: <a href="https://doi.org/10.1063/1.5080300">https://doi.org/10.1063/1.5080300</a>. 159
- KURLETO, R. et al. Flat bands at the fermi level in unconventional superconductor yfe2ge2. arXiv preprint arXiv:2311.09492, 2023. 136, 137
- KöNIG, M. et al. Quantum spin hall insulator state in hgte quantum wells. *Science*, v. 318, n. 5851, p. 766–770, 2007. Disponível em: <a href="https://www.science.org/doi/abs/10.1126/science.1148047">https://www.science.org/doi/abs/10.1126/science.1148047</a>>. 169
- LAI, S. et al. Surface group modification and carrier transport property of layered transition metal carbides (ti2ctx, t: -oh, -f and -o). *Nanoscale*, v. 7, 11 2015. 116
- LEVY, M. Asymptotic coordinate scaling bound for exchange-correlation energy in density-functional theory. *International Journal of Quantum Chemistry*, Wiley Online Library, v. 36, n. S23, p. 617–619, 1989. 106
- LIN, J. et al. Optimized and transferable nonlocal separable ab initio pseudopotentials. *Physical Review B*, APS, v. 47, n. 8, p. 4174, 1993. 121
- LIU, Y.; XIAO, H.; III, W. A. G. Schottky-barrier-free contacts with two-dimensional semiconductors by surface-engineered mxenes. *Journal of the American Chemical Society*, ACS Publications, v. 138, n. 49, p. 15853–15856, 2016. 115
- MAK, K. F. et al. Atomically thin mos: A new direct-gap semiconductor. *Physical Review Letters*, American Physical Society, v. 105, n. 13, p. 136805, 2010. 111
- MANZANO, D. A short introduction to the lindblad master equation. AIP Advances, AIP Publishing LLC, v. 10, n. 2, p. 025106, 2020. 27, 28, 32
- MATTHEISS, L. F. Band structures of transition-metal-dichalcogenide layer compounds. *Phys. Rev. B*, American Physical Society, v. 8, p. 3719–3740, Oct 1973. Disponível em: <a href="https://link.aps.org/doi/10.1103/PhysRevB.8.3719">https://link.aps.org/doi/10.1103/PhysRevB.8.3719</a>. 112, 113

MIWA, K. Prediction of raman spectra with ultrasoft pseudopotentials. *Physical Review B*, APS, v. 84, n. 9, p. 094304, 2011. 131

- MONKHORST, H. J.; PACK, J. D. Special points for brillouin-zone integrations. *Physical review B*, APS, v. 13, n. 12, p. 5188, 1976. 121
- MOSTOFI, A. A. et al. wannier90: A tool for obtaining maximally-localised wannier functions. *Computer physics communications*, Elsevier, v. 178, n. 9, p. 685–699, 2008. 141, 144
- MOURIK, V. et al. Signatures of majorana fermions in hybrid superconductor-semiconductor nanowire devices. *Science*, v. 336, n. 6084, p. 1003–1007, 2012. Disponível em: <a href="https://www.science.org/doi/abs/10.1126/science.1222360">https://www.science.org/doi/abs/10.1126/science.1222360</a>. 169
- NAGUIB, M. et al. Two-dimensional materials: 25th anniversary article: Mxenes: a new family of two-dimensional materials (adv. mater. 7/2014). *Advanced Materials*, Wiley Online Library, v. 26, n. 7, p. 982–982, 2014. 115
- NAKATANI, T. et al. Perspective on nanoscale magnetic sensors using giant anomalous hall effect in topological magnetic materials for read head application in magnetic recording. *Applied Physics Letters*, AIP Publishing, v. 124, n. 7, 2024. 170
- NOVOSELOV, K. S. et al. Room-temperature electric field effect and carrier-type inversion in graphene films.  $arXiv\ preprint\ cond-mat/0410631$ , 2004. 111
- NOVOSELOV, K. S. et al. Two-dimensional gas of massless dirac fermions in graphene. *nature*, Nature Publishing Group, v. 438, n. 7065, p. 197–200, 2005. 111
- NOVOSELOV, K. S. et al. Room-temperature quantum hall effect in graphene. *Science*, American Association for the Advancement of Science, v. 315, n. 5817, p. 1379–1379, 2007. 111
- PERDEW, J. P.; BURKE, K.; ERNZERHOF, M. Generalized gradient approximation made simple. *Phys. Rev. Lett.*, American Physical Society, v. 77, p. 3865–3868, Oct 1996. Disponível em: <a href="https://link.aps.org/doi/10.1103/PhysRevLett.77.3865">https://link.aps.org/doi/10.1103/PhysRevLett.77.3865</a>. 106, 108
- PERDEW, J. P.; BURKE, K.; WANG, Y. Generalized gradient approximation for the exchange-correlation hole of a many-electron system. *Phys. Rev. B*, American Physical Society, v. 54, p. 16533–16539, Dec 1996. Disponível em: <a href="https://link.aps.org/doi/10.1103/PhysRevB.54.16533">https://link.aps.org/doi/10.1103/PhysRevB.54.16533</a>. 106
- PERDEW, J. P.; BURKE, K.; WANG, Y. Generalized gradient approximation for the exchange-correlation hole of a many-electron system. *Physical review B*, APS, v. 54, n. 23, p. 16533, 1996. 121
- PERSSON, P. O.; ROSEN, J. Current state of the art on tailoring the mxene composition, structure, and surface chemistry. *Current Opinion in Solid State and Materials Science*, Elsevier, v. 23, n. 6, p. 100774, 2019. 111, 115
- PFROMMER, B. G. et al. Relaxation of crystals with the quasi-newton method. *Journal of Computational Physics*, Elsevier, v. 131, n. 1, p. 233–240, 1997. 122
- PHONG, V. T.; MELE, E. Quantum geometric oscillations in two-dimensional flat-band solids. *Physical Review Letters*, APS, v. 130, n. 26, p. 266601, 2023. 136

POREZAG, D.; PEDERSON, M. R. Infrared intensities and raman-scattering activities within density-functional theory. *Physical Review B*, APS, v. 54, n. 11, p. 7830, 1996. 130

- RIDOLFI, E.; LEWENKOPF, C. H.; PEREIRA, V. M. Excitonic structure of the optical conductivity in mos 2 monolayers. *Physical Review B*, APS, v. 97, n. 20, p. 205409, 2018. 113, 163, 168
- RITZ, W. Über eine neue methode zur lösung gewisser variationsprobleme der mathematischen physik. Walter de Gruyter, Berlin/New York Berlin, New York, 1909. 92
- SAEED, M. A. et al. 2d mxene: a potential candidate for photovoltaic cells? a critical review. *Advanced Science*, Wiley Online Library, v. 9, n. 10, p. 2104743, 2022. 115
- SAKURAI, J. J.; TUAN, S. F.; COMMINS, E. D. Modern quantum mechanics, revised edition. *American Journal of Physics*, v. 63, p. 93–95, 1995. Disponível em: <a href="https://api.semanticscholar.org/CorpusID:119727482">https://api.semanticscholar.org/CorpusID:119727482</a>. 76, 77, 78
- SALPETER, E. E.; BETHE, H. A. A relativistic equation for bound-state problems. *Physical Review*, APS, v. 84, n. 6, p. 1232, 1951. 162
- SEELEY, J. T.; RICHARD, M. J.; LOVE, P. J. The bravyi-kitaev transformation for quantum computation of electronic structure. *The Journal of chemical physics*, AIP Publishing, v. 137, n. 22, 2012. 95
- SEGALL, M. et al. First-principles simulation: ideas, illustrations and the castep code. Journal of Physics: Condensed Matter, IOP Publishing, v. 14, n. 11, p. 2717, 2002. 121
- SEGALL, M. D. et al. First-principles simulation: ideas, illustrations and the castep code. *Journal of Physics: Condensed Matter*, v. 14, n. 11, p. 2717, mar 2002. Disponível em: <a href="https://dx.doi.org/10.1088/0953-8984/14/11/301">https://dx.doi.org/10.1088/0953-8984/14/11/301</a>>. 125
- SHIN, H. et al. Cohesion energetics of carbon allotropes: Quantum monte carlo study. *The Journal of Chemical Physics*, v. 139, n. 12, p. 124701, 2013. 123
- SMIDSTRUP, S. et al. Quantumatk: an integrated platform of electronic and atomic-scale modelling tools. *Journal of Physics: Condensed Matter*, IOP Publishing, v. 32, n. 1, p. 015901, 2019. 138
- THOULESS, D. J. et al. Quantized hall conductance in a two-dimensional periodic potential. *Phys. Rev. Lett.*, American Physical Society, v. 49, p. 405–408, Aug 1982. Disponível em: <a href="https://link.aps.org/doi/10.1103/PhysRevLett.49.405">https://link.aps.org/doi/10.1103/PhysRevLett.49.405</a>. 171
- WANG, X. et al. Ab initio calculation of the anomalous hall conductivity by wannier interpolation. *Phys. Rev. B*, American Physical Society, v. 74, p. 195118, Nov 2006. Disponível em: <a href="https://link.aps.org/doi/10.1103/PhysRevB.74.195118">https://link.aps.org/doi/10.1103/PhysRevB.74.195118</a>>. 171
- WANG, Y.; PERDEW, J. P. Spin scaling of the electron-gas correlation energy in the high-density limit. *Phys. Rev. B*, American Physical Society, v. 43, p. 8911–8916, Apr 1991. Disponível em: <a href="https://link.aps.org/doi/10.1103/PhysRevB.43.8911">https://link.aps.org/doi/10.1103/PhysRevB.43.8911</a>. 106

References 183

WU, F.; QU, F.; MACDONALD, A. H. Exciton band structure of monolayer mos<sub>2</sub>. *Phys. Rev. B*, American Physical Society, v. 91, p. 075310, Feb 2015. Disponível em: <a href="https://link.aps.org/doi/10.1103/PhysRevB.91.075310">https://link.aps.org/doi/10.1103/PhysRevB.91.075310</a>. 168

- XIAO, D.; CHANG, M.-C.; NIU, Q. Berry phase effects on electronic properties. *Rev. Mod. Phys.*, American Physical Society, v. 82, p. 1959–2007, Jul 2010. Disponível em: <a href="https://link.aps.org/doi/10.1103/RevModPhys.82.1959">https://link.aps.org/doi/10.1103/RevModPhys.82.1959</a>. 170, 171
- XIAO, D. et al. Coupled spin and valley physics in monolayers of mos<sub>2</sub> and other group-vi dichalcogenides. *Phys. Rev. Lett.*, American Physical Society, v. 108, p. 196802, May 2012. Disponível em: <a href="https://link.aps.org/doi/10.1103/PhysRevLett.108.196802">https://link.aps.org/doi/10.1103/PhysRevLett.108.196802</a>>. 113
- XIAO, D. et al. Coupled spin and valley physics in monolayers of mos<sub>2</sub> and other group-vi dichalcogenides. *Phys. Rev. Lett.*, American Physical Society, v. 108, p. 196802, May 2012. 114
- ZAK, J. Dynamics of electrons in solids in external fields. *Phys. Rev.*, American Physical Society, v. 168, p. 686–695, Apr 1968. Disponível em: <a href="https://link.aps.org/doi/10.1103/PhysRev.168.686">https://link.aps.org/doi/10.1103/PhysRev.168.686</a>>. 154
- ZHANG CHENGCHENG TAO, H. Y. W. N. J. D. Y. H. . X. W. Z. Mxene materials: developments and sensor applications in modern composites. *Journal of Materials Science*, Springer, 2025. Disponível em: <a href="https://link.springer.com/article/10.1007/s10853-025-11135-7">https://link.springer.com/article/10.1007/s10853-025-11135-7</a>. 115
- ZHANG, N. et al. Superior structural, elastic and electronic properties of 2d titanium nitride mxenes over carbide mxenes: a comprehensive first principles study. 2D Materials, IOP Publishing, v. 5, n. 4, p. 045004, 2018. 123
- ZHAO, S.; KANG, W.; XUE, J. Manipulation of electronic and magnetic properties of m2c (m= hf, nb, sc, ta, ti, v, zr) monolayer by applying mechanical strains. *Applied Physics Letters*, AIP Publishing, v. 104, n. 13, 2014. 134
- ZHOU, X. et al. Sign-reversible valley-dependent berry phase effects in 2d valley-half-semiconductors. *npj Computational Materials*, Nature Publishing Group, v. 7, n. 1, p. 160, 2021. Disponível em: <a href="https://www.nature.com/articles/s41524-021-00632-3">https://www.nature.com/articles/s41524-021-00632-3</a>. 173
- ZIMAN, J. M. *Principles of the Theory of Solids*. [S.l.]: Cambridge university press, 1972. 62, 74, 79

# ANNEX A – Materials Today Communications Article:

Materials Today Communications 44 (2025) 112060



#### Contents lists available at ScienceDirect

### **Materials Today Communications**

journal homepage: www.elsevier.com/locate/mtcomm



## Flat bands in yttrium semiconductor MXenes: A first principles study

Victor R.P. Vendramini \*, D.L. Azevedo

Instituto de Física, Universidade de Brasília (UnB), Brasília, DF 70919-970, Brazil

#### ARTICLE INFO

Keywords: MXenes ab initio Semiconductor 2D Materials Effective mass Flat band. 2010 MSC: 81-XX 81-08

#### ABSTRACT

Transition metal carbides, nitrides, and carbonitrides (MXenes) represent a versatile class of two-dimensional materials that recently emerged as promising materials for electronic and quantum applications. MXenes are composed not only of the primary elements mentioned, but also feature surface terminations that vary according to the synthesis method, thereby greatly expanding the range of properties in these materials. This study theoretically investigates the anticipated structure, stability, thermodynamic, and electronic properties of yttrium-carbon-based monolayers terminated with F, Cl, and Br groups. The calculations are substantiated by density functional theory (DFT) and density functional electronic properties of GGA-PBE exchange functional and the HSE06 hybrid functional for a better prediction of the electronic structure. The findings regarding phonon dispersion, cohesive energy, and thermodynamic properties indicate good stability. Concerning electronic properties, all materials demonstrated semiconductor behavior, each characterized by a unique indirect band gap extending from  $\Gamma$  to M high symmetry points, although the direct transition is energetically close, especially in the Y<sub>2</sub>CCl<sub>2</sub> structure. Considerable focus was directed towards the effective mass of the particles within these monolayers, justified by the flat band behavior that appears as a platform for exotic quantum phenomena such as correlated insulators and superconductivity.

#### 1. Introduction

Following the discovery of graphene [1-3], two-dimensional (2D) materials have garnered significant attention in technology. Subsequently, the family of transition metal dichalcogenides (TMDs) was incorporated, facilitating the production of numerous more monolayers [4,5]. The scientific community is now recognizing a novel category of 2D materials, specifically transition metal carbides, nitrides, and carbonitrides (MXenes); the majority of potential monolayers remain unsynthesized, resulting in a vast array of physical properties yet to be investigated. Conductor MXenes have been utilized in significant technologies, including photovoltaic cells, energy storage, and gas sensors; however, the semiconductor domain remains shrouded in potential, necessitating investigation into undiscovered physical properties. A general MXene is described by the formula  $M_{n+1}X_n$   $T_x$ , where n might be from 1 to 3, M is a transition metal, X is carbon, nitrogen, or carbonitride, and  $T_x$  stands for the x number of terminations T. These terminations are not well defined in terms of viability and depend on the method used for the synthesis of the material [6].

In the synthesis processes, MXenes are obtained from selective etching of atomic layers of a parent MAX phase. MAX phases,  $M_{n+1}AX_n$ ,

are interleaved layers of transition metal carbides or nitrides, with layers of A atoms, usually belonging to the groups 13 or 14 of the periodic table of elements. For removing the A atoms, MAX phases are submitted to a wet-chemical exfoliation, where some atoms from the etching solution will end up as a termination group for the resulting MXene [7].

The most common technique used for the synthesis of MXenes is to etch the A-atoms from its precursor in an aqueous fluoride-containing solution, such as hydrofluoric acid (HF) [1]. This process can be performed by controlling the concentration of HF and the reaction time at a temperature of 55°C. The specificities of the process vary for each particular material, but in general, an increase in the atomic number of M, or a larger n in the  $M_{n+1}X_nT_x$  formula, demands stronger etching and longer time. After etching the A atoms, the exposed and highly reactive surface constituted of transition metals M forms bonds with atoms in the solution, giving rise to a mixture of -0, -0H, and -F terminations. Despite being still an emerging field of study, there are already post-synthesis processes capable of producing MXenes with chosen terminations [2].

Based on evidence from previous studies [8] that  $Y_2CF_2$  is a stable semiconductor material that could be synthesized from yttrium-carbon-based MAX phases [9], and considering that a

E-mail address: victor.vendra@gmail.com (V.R.P. Vendramini).

<sup>\*</sup> Corresponding author.

# ANNEX B - e-Boletim da Física Article:



International Centre for Physics
Instituto de Física, Universidade de Brasília
Ano 13, 2025 • http://periodicos.unb.br/index.php/e-bfis • eBFIS XIII 01-1(03)

# Insightsem efeitos de substituição em MX<br/>enes baseados em ítrio. Uma investigação utilizando DFT

Vendramini, V.R.P\* and D. L. Azevedo $^{\dagger}$  Instituto de Física, Universidade de Brasília (UnB)

Os carbetos, nitretos e carbonitretos de metais de transição, conhecidos como MXenes, constituem uma classe emergente de materiais bidimensionais (2D). A literatura científica reconhece que a maioria dos MXenes apresenta comportamento condutor. No presente estudo, empregamos cálculos ab initio para elucidar a estrutura, estabilidade, propriedades espectroscópicas, termodinâmicas e eletrônicas dos MXenes pertencentes à família do ítrio, os quais ainda não foram sintetizados experimentalmente. Todos os cálculos realizados fundamentam-se nos métodos da Teoria do Funcional da Densidade (DFT) e da Teoria do Funcional da Densidade por Perturbação (DFPT), utilizando funcional de troca-correlação GGA-PBE e o funcional híbrido HSE06 para uma estimativa mais precisa do gap de banda. Nossos resultados referentes à dispersão de fônons e às propriedades termodinâmicas indicam alta estabilidade para os materiais na fase 2H do sistema trigonal prismático. Embora o  $Y_2NF_2$  tenha sido previsto como condutor, conforme a tendência geral dos MXenes, observamos um comportamento semicondutor para o  $Y_2CF_2$ , com um gap de banda indireto de 1.908 eV, estendendo-se do ponto  $\Gamma$  ao ponto M.

Keywords: MXenes, DFT, semicondutor, 2D, monocamadas, Ítrio

## I. INTRODUÇÃO

Após o primeiro grande avanço com o grafeno, os materiais bidimensionais tornaram-se um campo de pesquisa extremamente popular, abrindo caminho para novas possibilidades tecnológicas [1–3]. Os Dicalcogenetos de Metais de Transição (TMDs) emergiram como uma classe moderna de materiais 2D, confirmando o potencial da tendência bidimensional [4, 5]. Nos últimos anos, a atenção volta-se para uma nova classe: carbetos, nitretos e carbonitretos de metais de transição (MXenes), que têm o potencial de se tornar uma das classes mais versáteis de materiais 2D, com um grande número de materiais ainda inexplorados e uma ampla gama de propriedades físicas [6, 7]. A fórmula geral para os MX<br/>enes é  $\mathbf{M}_{n+1}\mathbf{X}_{n}\mathbf{T}_{m},$ onde nvaria de 1 a 3, M<br/> representa o metal de transição, X representa os carbetos, nitretos ou carbonitretos, e  $\mathbf{T}_x$  representa o número x de terminações  $\mathbf{T}.$ Essas terminações dependem do método utilizado para a síntese do MXene [6].

Os MXenes são obtidos a partir da corrosão seletiva das camadas atômicas de algum material precursor, usualmente sintetizados por esfoliação dos materiais parentais em solução química [7]. As fases MAX,  $M_{n+1}AX_n$ , consistem em camadas hexagonais intercaladas de carbe-

tos ou nitretos de metais de transição, com camadas de átomos de A, geralmente dos grupos 13 ou 14 da tabela periódica dos elementos. A ligação química entre os metais de transição M e os átomos A é metálica, portanto, não é possível separar essas camadas das fases MAX por simples cisalhamento mecânico. No entanto, as ligações entre os elementos M-X são de natureza covalente, sendo mais fortes do que as ligações metálicas, o que possibilita a corrosão seletiva das camadas  $\mathbf{M}_{n+1}\mathbf{X}_n$  [6]. A técnica de síntese mais comumente empregada na produção de MXenes consiste em corroer os átomos de A de seu precursor em uma solução aquosa contendo flúor, como o ácido fluorídrico (HF) [8]. Este processo pode ser realizado controlando a concentração de HF e o tempo de reação, mantendo uma temperatura de 55°C. As especificidades práticas do processo variam para cada material particular, mas geralmente, o aumento do número atômico em M, ou um n maior na fórmula  $M_{n+1}X_nT_m$ , exige uma corrosão mais forte e um tempo maior. Após a corrosão dos átomos de A, a superfície exposta e altamente reativa dos metais de transição M forma ligações com átomos da solução, resultando em uma mistura de terminações de -O, -OH e -F. Apesar de ainda ser um campo emergente de estudo, já existem processos póssíntese capazes de produzir MXenes com terminações específicas [9]. Neste estudo pensamos além dos materiais já sintetizados, mas, mantemos as terminações em F pois elas resultam da técnica de corrosão mais comum, o uso de soluções de HF. Apesar de não haver ainda registro de monocamadas de Y2CF2, já é relatada a síntese de

<sup>\*</sup> victor.vendra@gmail.com

<sup>†</sup> david888azv@gmail.com